TECHNISCHE UNIVERSITÄT MÜNCHEN

Ingenieurfakultät Bau Geo Umwelt

Lehrstuhl für Hydrologie und Flussgebietsmanagement

Uncertainty quantification in modeling karst water resources and the impacts of land use changes

Daniel Christian Martin Bittner

Vollständiger Abdruck der von der Ingenieurfakultät Bau Geo Umwelt der Technischen Universität München zur Erlangung des akademischen Grades eines

Doktor Ingenieurs (Dr.-Ing.)

genehmigten Dissertation.

Vorsitzender: Prof. Dr. Florian Einsiedl
Prüfer der Dissertation: 1. Prof. Dr. Gabriele Chiogna
2. Prof. Dr.-Ing. Markus Disse
3. Prof. Dr. Andreas Hartmann
(Universität Freiburg)

Die Dissertation wurde am 11.12.2019 bei der Technischen Universität München eingereicht und durch die Ingenieurfakultät Bau Geo Umwelt am 04.05.2020 angenommen.

To Lara and Nayla

'Rein das Ding, fertig und ab nach Hause.'
(Lukas Podolski)

Abstract

About 25 % of the world's population depends either fully or patially on freshwater obtained from karst systems, making their protection and sustainable management an essential task in water resource management. Similar to most freshwater resources, also karst aquifers are affected by increasing pressures from anthropogenic activities. The dolomite-dominated karst system in Waidhofen a.d. Ybbs (Austria) represents such an example as it is affected by increasing mining activities. Mining activities cause a decrease in groundwater recharge as the surface is sealed to avoid any contamination of the aquifer. This problem was also recognized by the regional waterworks and they needed a tool that can support the future management of their water supplying systems. This dissertation aims to contribute to the challenge of safely and sustainably managing karst systems by developing a hydrologic model that is able to simulate the hydrological impacts of land use changes on karst spring discharge. Moreover, a further focus is to deal with the uncertainties that are related to a simulated spring discharge. Therefore, I decided to divide the presented thesis into two major objectives, i.e. *Model development, implementation and application* and *Uncertainty quantification*.

   Before developing mathematical approaches for the simulation of hydrological processes, a conceptual model of an aquifer of interest is needed. For the Waidhofen karst system, such an idea of the internal functioning of the aquifer was gathered from a detailed analysis of long-term hydrochemical time series. In particular, for the spring that is assumed to be most affected by increasing quarry areas, i.e. the Kerschbaum spring, an acceptable conceptual model was built that provided an appropriate starting point for the development of a mathematical simulation model. Most karst hydrologic models fall in the category of lumped parameter models, since it is challenging to apply physically-based models where little is known about the heterogeneity and order of karst conduits and how they interact with the matrix. Similarly, a lumped parameter model was developed in this study. The model, called LuKARS (Land use change modeling in KARSt systems), is based on the implementation of disctinct landscape units with similar soil and land use characteristics, defined as hydrotopes. LuKARS was intitially set-up for the Kerschbaum spring and later tested for other springs in order to ensure the transferability of the approach. It was shown that the model is able to reproduce the observed changes in karst spring discharge as a result of increasing dolomite quarries. Since this research idea evolved from a practical problem of water management in Waidhofen a.d. Ybbs, LuKARS should not only be applicable by researchers, but also by decision makers. For that reason, the model was implemented in an open source framework that uses QGIS as a graphical user interface (GUI) and consists of tools for water resource

mangement, i.e. FREEWAT.

For the second objective of this thesis, the active subspace method was applied to the Kerschbaum spring LuKARS model to investigate the model parameter and output uncertainties as well as to test for possibilities to reduce the parameter dimensions. The original space of 21 parameters was effectively reduced to a four dimensional problem. A surrogate model was fitted in this lower dimensional parameter space and used to perform a Bayesian inversion in order to quantify the parametric uncertainties in the original parameter space. The results highlighted that LuKARS in combination with the active subspace method can be used to perform land use change impact studies with an acceptable range of model output uncertainties, i.e. < 10 % with respect to the mean discharge. Finally, a comprehensive parametric study was performed to investigate the hydrological meaning of an identified active subspace. Relevant hydrological and catchment properties can be derived from an active subspace, which can be used to better interpret the model uncertainties as well as to develop tailored field campaigns for missing modeling data.

Zusammenfassung

Etwa 25 % der Weltbevölkerung hängt entweder teilweise oder komplett von der Versorgung mit Trinkwasser aus Karstsystemen ab, was deren Schutz und nachhaltige Bewirtschaftung zu einer essenziellen Aufgabe in der Wasserwirtschaft machen. Ebenso wie die meisten Frischwasserressourcen sind auch Karstgrundwasserleiter von steigendem Druck anthropogener Aktivitäten betroffen. Das von Dolomit dominierte Karstsystem in Waidhofen a.d. Ybbs (Österreich) stellt ein solches Beispiel dar, da es von zunehmenden Steinbruchaktivitäten beeinflusst wird. Durch die Versiegelung der Oberfläche in diesen Bereichen, welche eine Verschmutzung des Grundwasserleiters verhindern soll, wird gleichzeitig die Grundwasserneubildung verringert. Dieses Problem wurde auch von dem für die regionale Wasserversorgung zuständigen Wasserwerk identifiziert und es wird ein Instrument benötigt, welches sie bei der zukünftigen Bewirtschaftung ihres Wasserversorgungssystems unterstützt. Das Ziel dieser Dissertation ist es, einen Beitrag für die sichere und nachhaltige Bewirtschaftung von Karstsystemen zu leisten. Dazu soll ein hydrologisches Modell entwickelt werden, welches für die Simulation von landnutzungsbedingten Veränderungen im Karstquellabfluss benutzt werden kann. Des Weiteren liegt der Fokus auf der Quantifizierung der Unsicherheiten, welche in Bezug zu den simulierten Quellabflüssen stehen. Auf dieser Basis habe ich beschlossen, die Arbeit in zwei Hauptziele zu gliedern, zum einen die *Modellentwicklung, Implementierung und Anwendung* und zum andern die *Unsicherheitsquantifizierung*.

Bevor ein mathematischer Ansatz zur Simulation von hydrologischen Prozessen entwickelt werden kann, muss ein konzeptionelles Modell des Grundwasserleiters, welcher modelliert werden soll, erstellt werden. Für den Fall des Karstsystems in Waidhofen wurde solch eine Vorstellung der hydrologischen Funktionsweise durch eine detaillierte Analyse von Langzeithydrochemischen Zeitreihen generiert. Speziell für die Quelle, für welche davon ausgegangen wird, dass sie am meisten durch die Vergrößerung der Dolomitsteinbrüche beeinflusst wird (Kerschbaumquelle), wurde ein akzeptables Konzeptmodell generiert, welches eine angemessene Basis für die Entwicklung eines mathematischen Simulationsmodells darstellt. Die meisten karst-hydrologischen Modelle fallen in die Kategorie der *lumped* Parameter Modelle, da die Anwendung physikalisch-basierter Modellansätze eine große Herausforderung darstellt, wenn es kein Wissen über die Heterogenitäten und die Ordnung von Karströhren und deren Interaktion mit der Gesteinsmatrix gibt. Im hiesigen Fall wurde ein *lumped* Parameter Modell entwickelt, welches auf der Implementierung von unabhängigen Landschaftseinheiten mit ähnlichen Boden- und Landnutzungseigenschaften basiert, den sogenannten Hydrotopen. Dieses Modell, genannt LuKARS (Land use change modeling in KARSt systems), wurde zunächst für die Kerschbaumquelle aufgebaut und anschließend für

andere Quellen getestet um die Übertragbarkeit des Modellansatzes zu gewährleisten. Es wurde gezeigt, dass LuKARS in der Lage ist, die beobachteten Veränderungen im Quellabfluss, welche aus der Steinbruchvergrößerung resultierten, nachzubilden. Ferner, da diese Forschungsidee einem anwendungsorientierten Wasserwirtschaftsproblem entsprang, sollte LuKARS kein reines Forschungswerkzeug sein, sondern auch für Entscheidungsträger nutzbar sein. Aus diesem Grund wurde das Modell in eine frei zugängliche und verfügbare Umgebung, welche QGIS als grafische Benutzeroberfläche verwendet, implementiert. Diese Umgebung, mit dem Namen FREEWAT, verfügt über diverse Analyseinstrumente, welche speziell in der Wasserwirtschaft verwendet werden.

Für das zweite Hauptziel dieser Arbeit wurde die Methode der aktiven Unterräume für das LuKARS Modell der Kerschbaumquelle angewendet um sowohl die Unsicherheiten in den Modellparametern und den Modellergebnissen zu quantifizieren, als auch Möglichkeiten zur Reduktion der Parameterdimensionen zu testen. Der ursprüngliche, 21 dimensionale Parameterraum wurde effektiv zu einem 4 dimensionalen Problem reduziert. Ein Surrogat wurde an diesen niederdimensionalen Parameterraum angepasst und im Rahmen einer Bayes'schen Inversion verwendet um die Parameterunsicherheiten im ursprünglichen Parameterraum zu quantifizieren. Die Ergebnisse zeigen, dass LuKARS in Verbindung mit der Methode der aktiven Unterräume zur Simulation von landnutzungsbedingten Veränderungen in Karstquellabflüssen mit akzeptablen Modellergebnisunsicherheiten von $< 10\ \%$, bezogen auf den mittleren Quellabfluss, verwendet werden kann. Abschließend wurde eine umfassende Parameterstudie durchgeführt um die hydrologische Bedeutung eines identifizierten, aktiven Unterraumes zu untersuchen. Diese hat ergeben, dass relevante hydrologische, als auch gebietsabhängige Eigenschaften aus den aktiven Unterräumen abgeleitet werden können. Diese können dazu verwendet werden, um die Modellunsicherheiten besser zu interpretieren als auch um angepasste Feldkampagnen für die Erhebung fehlender Modelldaten zu entwerfen.

Affidavit

I hereby affirm that I wrote this doctoral thesis independently and on my own without illegal assistance of third parties. To the best of my knowledge, all sources that I used to prepare this dissertation are labelled as such. This dissertation has not been received by any examination board, neither in this nor in a similar form.

Munich, December 10th, 2019

Daniel Bittner

Acknowledgements

At first, I want to thank the Chair of Hydrology and River Basin Management at my alma mater, the Technical University of Munich, for providing a great research environment over the last 3 years. In this respect, I am particularly thankful to my supervisors Prof. Dr. Gabriele Chiogna and Prof. Dr.-Ing. Markus Disse who gave me the opportunity to be part of this great and inter-disciplinary research group. Both always encouraged me to enhance my personal and professional skills throughout this time and guided me in my research. I would particularly highlight that they gave me the unique opportunity to select a research topic I wanted to deal with; something that is not common and what I am more than thankful for.

Special thanks belongs to Prof. Dr. Andreas Hartmann, who became my third supervisor and who supported me to become a part of the karst community. Although I was not 'his' student, he was always open for discussions and helped me with my research. Moreover, I am indepted to Prof. Dr.-Ing. Markus Casper for accompanying me since my Bachelor studies and for giving me all opportunities that brought me to the point in my career where I am now. Furthermore, I want to thank Prof. Dr. Florian Einsiedl for taking over the role as chairman for my PhD defense.

I want to express my great gratitude to the whole team of the Chair of Hydrology and River Basin Management. In particular, I owe my colleagues Sonja Teschemacher, Matthias Kopp and Florentin Hofmeister a great debt of gratitude for being amazing office mates and for several, life-saving evening beers. Moreover, I am thankful for all topic related discussions with Mario Teixeira Parente, Monica Basilio Hazas and Pablo Merchan-Rivera and their continuous support. I further want to thank Punit Bhola and Thomas Pflugbeil for maintaining my physical health throughout the years in strong volleyball matches and the fitness club. A special thanks also belongs to Christiane Zach-Cretaine for always helping me with this hell of bureaucracy and administration.

It is important to me to thank all the great persons I met during these last 3 years and who not only became great research contacts, but also friends. In particular, I want to thank Dr. Wesley Henson and Dr. Scott Boyce from USGS California and Dr. Barbara Mahler from USGS Texas.

I further want to gratefully acknowledge the International Graduate School of Science and Engineering for providing the funding for my international research stays and for offering a great educational program during my PhD. I am especially thankful for the great and continuous support from Jo-Anna Küster and Sandra Schöngen. Moreover, I want to thank Barbara Wohlmuth and Steven Mattis for all support and research advices related to the more mathematically oriented

parts of this thesis.

Moreover, I am committed to thank Markus Hochleitner from the waterworks Waidhofen a.d. Ybbs. He supported all works I did in this beautiful area. Without his continuous support I would not have been able to conduct this research.

A special thanks belongs to all great students and friends who supported my research and project activities over these years. Without the great work they all did, I would not have been able to finish this work as quick as it was. In particular, I want to thank Anna Leuteritz, Beatrice Richieri, Tobias Klöffel, Ayla Rychlik, Agnieszka Plonczak, Sandra Zimmermann, Eleni Loulli and Joel Achenbach.

Finally, I want to thank my friends and family for all their encouragements and support during my research. I am greatly indepted to my best friend Diego Ellis Soto, aka Banana Joe. When thinking back to where it all started in Trier, it is incredible to see where we are now. I am more than happy to share the road with you. Further, I want to thank my friends Björn Klaes and Julian Struck for great times together, all past and upcoming outdoor adventures and all personal and research advices they gave me. Moreover, I gratefully acknowledge Ina Klinkhammer and Sneschana Klemmer for keeping me grounded for more than a decade of my life.

My sincere thanks goes to my mother for being the most patient and supportive person in my life. Without your lifelong advices and encouragement, I would never have reached the point where I am now. The same accounts for my brother Michael, my grandma Luise and my grandpa Harri. I miss you so much...

Since this PhD thesis is the product of sleepless nights of work, a lot of absent times and times of bad moods, I owe my wife Lara gratitude and my deepest respect for all the love, support, encouragement and advice she always gave me. You have always been the light at the end of this tunnel and you finally make me to the person who I am. I am the luckiest person to have you and our amazing daughter Nayla in my life.

I love you.

Research articles and author contributions

Presented research articles

The presented cumulative dissertation is based on five research articles. Four of them are peer-reviewed and published in relevant international journals. The works of Bittner et al. (2018a), Bittner et al. (2020b) and Bittner et al. (2020a) are first author publications, which are required for this cumulative dissertation. The works of Narany et al. (2019) and Teixeira Parente et al. (2019a) are co-author publications which were added to complete the storyline of this dissertation. All articles are presented in Chapters 2 to 6. The data needed to reproduce the results of all articles are provided on my GitHub account, i.e. github.com/dbittner87/dissertation_data

Article 1

Narany, T.S., **Bittner, D.**, Disse, M., Chiogna, G., 2019. Spatial and temporal variability in hydrochemistry of a small scale dolomite karst environment. Environmental Earth Sciences 78, 273.

- Co-author publication

- Chapter 2

- Author contributions: Tahoora Sheikhy Narany, Daniel Bittner and Gabriele Chiogna conceived the research idea. Tahoora Sheikhy Narany and Daniel Bittner analyzed the data. Tahoora Sheikhy Narany wrote the first draft of the article. All authors reviewed the first draft. Tahoora Sheikhy Narany, Daniel Bittner and Gabriele Chiogna wrote the final version of the article. Gabriele Chiogna and Markus Disse supervised this study.

Article 2

Bittner, D., Narany, T.S., Kohl, B., Disse, M., Chiogna, G., 2018. Modeling the hydrological impact of land use change in a dolomite-dominated karst system. Journal of Hydrology 567, 267-279.

- 1 of 3 required first author publications (core publication)

- Chapter 3

- Author contributions: Daniel Bittner and Gabriele Chiogna conceived the research idea. Daniel Bittner developed the model and created the software. All authors analyzed the modeling results. Daniel Bittner wrote the article. All authors reviewed the article. Daniel Bittner and Gabriele Chiogna wrote the final version of the article. Gabriele Chiogna and Markus Disse supervised this study.

Article 3

Bittner, D., Rychlik, A., Klöffel, T., Leuteritz, A., Disse, M., Chiogna, G., 2020b. A GIS-based model for simulating the hydrological effects of land use changes on karst systems – The integration of the LuKARS model into FREEWAT. Environmental Modelling and Software, 104682.

- 2 of 3 required first author publications (core publication)

- Chapter 4

- Author contributions: Daniel Bittner and Gabriele Chiogna conceived the research idea. Anna Leuteritz and Tobias Klöffel mapped the hydrotopes. Daniel Bittner, Ayla Rychlik and Tobias Klöffel created the software. Daniel Bittner, Ayla Rychlik and Tobias Klöffel tested the software. Daniel Bittner wrote the article. All authors reviewed the article. Gabriele Chiogna and Markus Disse supervised this study.

Article 4

Teixeira Parente, M., **Bittner, D.**, Mattis, S., Chiogna, G., Wohlmuth, B., 2019a. Bayesian calibration and sensitivity analysis for a karst aquifer model using active subspaces. Water Resources Research, 55, 7086-7107.

- Co-author publication

- Chapter 5

- Author contributions: All authors conceived the research idea. Mario Teixeira Parente (active subspace method) and Daniel Bittner (LuKARS model) developed the software. Mario Teixeira Parente performed the simulations. All authors analyzed the results. Mario Teixeira Parente wrote the article. All authors reviewed the article. Steven Mattis and Barbara Wohlmuth supervised this study.

Article 5

Bittner, D., Teixeira Parente, M., Mattis, S., Wohlmuth, B., Chiogna, G., 2020. Identifying relevant hydrological and catchment properties in active subspaces: An inference study of a lumped karst aquifer model. Advances in Water Resources 135, 103472.

- 3 of 3 required first author publications (core publication)

- Chapter 6

- Author contributions: All authors conceived the research idea. Daniel Bittner (LuKARS model) and Mario Teixeira Parente (active subspace method) developed the software. Daniel Bittner performed the simulations. All authors analyzed the results. Daniel Bittner wrote the article. All authors reviewed the article. Barbara Wohlmuth and Gabriele Chiogna supervised this study.

Further scientific contributions

Oral presentations

- **Bittner, D.**, Disse, M., Chiogna, G., 2017. Trinkwasserschutz und Landwirtschaft - Wie schützen wir nachhaltig unser Trinkwasser?. *Jahreshauptversammlung des NABU Vulkaneifel*, Hillesheim (Germany).

- **Bittner, D.**, Narany, T.S., Disse, D., Chiogna, G., 2018. Modelling the impact of land use change on drinking water supply in a karstic aquifer. *EGU conference*, Vienna (Austria).

- **Bittner, D.**, Chiogna, G., 2018. PROLINE-CE - Efficient Practices of Land Use Management Integrating Water Resources Protection and Non-structural Flood Mitigation Experiences. *AK Bodenschutz und Gewässerschutz*, Landesanstalt für Landwirtschaft, Freising (Germany).

- **Bittner, D.**, Teixeira Parente, M., Mattis, S., Wohlmuth, B., Disse, M., Chiogna, G., 2018. Uncertainty quantification in modeling karst water resources and the impacts of land use changes. *Forschungskolloquium der Physischen Geographie*, Trier (Germany).

- **Bittner, D.**, Teixeira Parente, M., Mattis, S., Wohlmuth, B., Chiogna, G., 2019. Parameter dimension reduction using the active subspace method for a lumped karst aquifer model. *EGU conference*, Vienna (Austria).

- **Bittner, D.**, Rychlik, A., Klöffel, T., Chiogna, G., 2019. Modeling the hydrological impact of land use change in karst systems using the LuKARS plugin for FREEWAT. *2nd International LIFE REWAT Summer School*, Pisa (Italy).

- **Bittner, D.**, Teixeira Parente, M., Mattis, S., Wohlmuth, B., Disse, M., Chiogna, G., 2019. How to model the impacts of land use changes in karstic environments: Model development, parameter dimension reduction and uncertainty quantification. *IAH conference*, Malaga (Spain).

Posters

- Basilio Hazas, M., Merchan-Rivera, P., **Bittner, D.**, Teixeira Parente, M., Mattis, S., Wohlmuth, B., Chiogna, G., 2018. UNMIX - Uncertainties due to boundary conditions in predicting mixing in groundwater. IGSSE Forum, Raitenhaslach (Germany).

- Disse, M., Plonczak, A., Chiogna, G., **Bittner, D.**, 2019. One-Water Hydrologic Flow Model: A MODFLOW Based Conjuctive Use Simulation Software. *IESP-Workshop Bewässerung in ländlichen und urbanen Räumen*, Munich (Germany).

Contents

List of Figures

List of Tables

Chapter 1

Introduction

Water is considered as one of the most important substances on our planet. We as humans are sure that life would not exist as we know it without water. Knowing about this vital importance of water, the United Nations General Assembly recognized as a human right that all of us have access to affordable and clean drinking water in 2010 (UN, 2018). The neccesity for this recognition is especially given by an unbelievable number of 2.2 billion people, i.e. about 30% of the world's population, who do not have access to safely managed drinking water services (WHO, 2017). Besides this fundamental discussion about the accessibility to fresh water, knowing about the dependence of human survival on clean drinking water makes it important to safely and sustainably manage our water resources.

From all exploited water bodies, groundwater can be regarded as the most important resource, since it provides almost half of the world's drinking water demand (Smith et al., 2016). Moreover, Siebert et al. (2010) estimated that the irrigation demand of 38% of actually irrigated lands worldwide is met by groundwater resources. Hence, this water is used to produce the food we eat and the energy we consume, i.e. energy crops. The reason why groundwater became an essential source for freshwater supply is two-fold; On the one hand, despite the freshwater stored in the global ice caps and glaciers, groundwater systems represent the second largest global freshwater storage. On the other hand, meteoric water gets purified while percolating through soil and rock layers before arriving in an aquifer system, which can ensure a good quality of the groundwater. Thus, groundwater systems are valuable freshwater sources in terms of their quantity and quality. Given that this hidden treasure is stored below our feed, every single action we undertake on the earth's surface may somehow affect groundwater reservoirs. More precisely, if we seal surfaces for urban spreading, we reduce groundwater recharge which affects the quantity of a groundwater resource (Bittner et al., 2018a). If we apply intensive farming using fertilizers, pesticides and herbicides, we may change the groundwater quality (Mencié et al., 2016). However, how anthropogenic activities interact with different types of groundwater systems is a matter of intense research (Luo et al., 2016; Narany et al., 2017; Zipper et al., 2019). Given our increasing world population, debates about human-induced climate change and an observable increasing pressure on the land surface and our freshwater supply systems, studying this interconnection between land use activities and

groundwater dynamics has never been more urgent to safeguard future water supply.

Tools that are commonly applied to investigate how land use actions affect the hydrological behavior of groundwater systems are mathematical models (Dwarakish and Ganasri, 2015; Karlsson et al., 2016). Different kinds of hydrological models exist and they mainly differ in terms of their mathematical base. So called black-box models are the most simple approaches. They use a defined function to transfer an input to an output (Labat et al., 2000; Hu et al., 2008). While those models are easy to apply and implement, they can only be considered reliable for the specific hydrological conditions of the calibration period (Hartmann et al., 2014a). Lumped models try to build a physical conceptualization of a groundwater system. They are based on transfer functions, each of them simulating a specific hydrological process in the conceptual representation of an aquifer (Fleury et al., 2007; Tritz et al., 2011; Mazzilli et al., 2017). Given that the parameters of black-box and lumped models cannot be obtained from field measurements, they need to be estimated during model calibration (Bittner et al., 2020a). This parameter estimation is prone to parameter uncertainties and depending on the total number of calibration parameters, different parameter combinations can lead to similar modeling results (Beven, 2006). To tackle this issue, it is recommended to perform global sensitivity analyses and uncertainty studies when applying this kind of models. Finally, distributed, process-based models implement physical functions that describe the different hydrological processes (Reimann and Hill, 2009). These models can account for the spatial variability of hydrological parameters and are often used to assess potential impacts of anthropogenic impacts on a groundwater reservoir (Chu et al., 2010).

How to approach questions related to the interconnection between land use activities and groundwater dynamics mainly depends on the complexity of an investigated system. In this context, the probably most complex groundwater systems are represented by karst aquifers (Bakalowicz, 2005). Worldwide, 10 to 25 % of the supplied freshwater fully or partially originates from these kind of groundwater systems (Chen et al., 2017a; Stevanović, 2019). These important but vulnerable sources for freshwater supply are mainly characterized by two types of flow, i.e. a slow flow through the rock matrix and a quickflow through conduit fracture systems. Conduits result from carbonate dissolution along existing cracks in the composite rocks (Ford and Williams, 2013). In response to precipitation events, these open channel systems in the subsurface lead to a quick discharge reaction at an outlet spring. However, the internal structure of a karst system remains a black-box since we cannot see the conduit network, how it interacts with the rock matrix and how water is stored within. This complexity makes it difficult to investigate hydrological impacts of anthropogenic activities (Hartmann et al., 2014a). In particular, the uncertainties about the internal structure of karst systems mostly do not allow to reliably parametrize physically-based models (Jukić and Denić-Jukić, 2009). Hence, it is difficult to use these models for investigating the hydrological effects of anthropogenic activities on karst systems.

For the given reasons, lumped parameter models are usually preferred simulation tools in karst hydrological research (Jukić and Denić-Jukić, 2008; Jourde et al., 2015). As already mentioned, their parameters usually cannot be obtained from field campaigns and, thus, they need to be estimated during model calibration. In most cases, the more processes we aim to implement, the more

parameters are needed which have to be calibrated (Bittner et al., 2020a). Since a high number of calibration parameters can lead to model uncertainties, the development of a lumped parameter model that can be used to perform land use change impact studies in karst systems also requires a quantification of model uncertainties and possibilities to reduce the parameter spaces dimension; This challenge is what the proposed thesis aims to tackle.

1.1 The case study problem

At the beginning of my dissertation, I was confronted with the task to perform hydrological investi-gations in one of the pilot areas of the Interreg project PROLINE-CE. This pilot area was the water supplying karst system in Waidhofen a.d. Ybbs (Austria, Fig. 1.1a). The specific problem was that the recharge area of the most important spring for the regional water supply, i.e. Kerschbaum spring, is affected by land cover changes. In particular, parts of this recharge area are used for dolomite mining. Based on spatial analysis performed using existing orthophotos from 2007 and 2010, it could be observed that the mining areas almost doubled within this period. Given this rapid increase of the quarry areas and the importance of the Kerschbaum spring, the waterworks Waidhofen a.d. Ybbs (also a project partner in PROLINE-CE) were interested to investigate how this land use change affects the Kerschbaum spring discharge.

In order to start this investigation, the first task was to collect all existing information about the study area, analyze existing data and create first conceptual ideas of the study area. From a geographical point of view, this pre-alpine region is part of the eastern foothills of the Northern Calcareous Alps, having altitudes that range between 415 to 969 m a.s.l. The surface drainage of the area is managed by two small fluvial systems, the Waidhofenbach and the Lugerbach, which drain most of the study area into the Ybbs river in Waidhofen. Analyzing the existing climate data from 1981 to 2014, the regional climate could be described as warm-moderate with an annual mean temperature of 8 °C. From December to February, mean daily temperatures below freezing can occur. An annual mean precipitation of 1379 mm was calculated from this data set, having a bimodal distribution with maxima during summer (June and July) and winter months (December and January). Taking into account the geological map of the region (Fig. 1.1b), most of the area is dominated by a lithologic sequence of dolomitic basement rocks. This leads to the assumption that typical karst phenomena like dry valleys and caves are present in the study area. Hacker (2003) found that significant sinkholes are not present in the study area, leading to the conclusion that point-infiltration plays a minor role for recharge in the study area. Furthermore, Hacker (2003) revealed that a deep karstified groundwater system exists, which extends even below the elevation level of the Waidhofenbach valley.

This basic knowledge about the study area was the starting point for the investigations in the framework of this dissertation. The formulated research hypotheses and objectives are presented in Fig. 1.2.
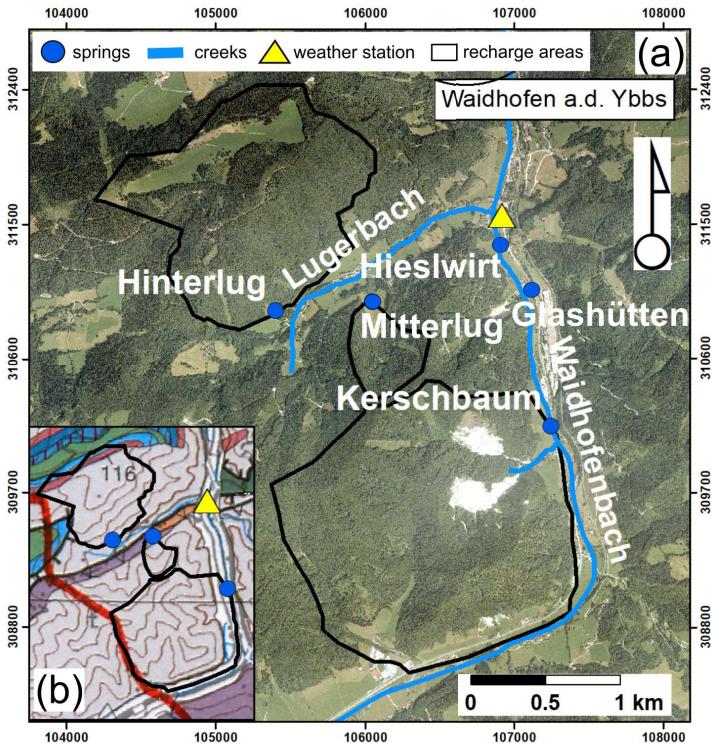
Figure 1.1: Overview of the recharge areas of the Kerschbaum, Mitterlug and Hinterlug spring. a) The location of all springs, i.e. Kerschbaum, Glashütten, Hieslwirt, Mitterlug and Hinterlug. Moreover, the Lugerbach and Waidhofenbach creeks are shown together with the location of the local climate station. The orthophoto in the background indicates that forests are the dominant land cover. b) The geological map highlights the dominance of dolomitic basement rocks (grey) in the study area (GBA, 2018).

1.2 Model development, implementation and application

1.2.1 Hypothesis 1: Dolomite aquifers can display high temporal and spatial variability in their hydrochemical signals also on a small spatial scale

In Section 1.1 it was shown that a basic understanding of the natural environment of the study area Waidhofen a.d. Ybbs was gathered based on a preliminary data analysis. However, for the aim of developing a hydrologic model to investigate land use change impacts on spring discharge, a

Objectives	Model development, implementation and application			Uncertainty quantification	
Chapter No.	Chapter 2	Chapter 3	Chapter 4	Chapter 5	Chapter 6
Hypotheses	Dolomite aquifers can display high temporal and spatial variability in hydrochemical signals on small spatial scales (i.e. 10 km²).	The recharge area of a given karst system can be subdivided into distinct units, defined as hydrotopes.	The FREEWAT plugin in QGIS offers a tailored framework to build a graphical user interface for the developed hydrotope-based karst aquifer model.	The ranges of most sensitive LuKARS parameters can be better constrained with active subspaces leading to a reduction in parameter and model result uncertainties.	The dimension and the feature of the active subspace can be related to underlying geometrical and hydrological properties of a chatchment.
Contents	- Hydrochemical analysis of long-term time series - Cluster analysis and grouping of springs - Conceptual model of the karst aquifer	- Lumped parameter model development (LuKARS) - Model application and validation - Land use change modeling	- Graphical user interface für LuKARS - Coupling with FREEWAT plugin in QGIS - Modular integration for pre- and post-processing	- Parameter uncertainty quantification - Analysis of active subspaces - Parameter dimension reduction	- Hydrological interpretation of active subspaces - Indentification of relevant catchment properties - Indentification of relevant hydrological properties
Article	Narany, Bittner et al. (2019). Environmental Earth Sciences.	Bittner et al. (2018a). Journal of Hydrology.	Bittner et al. (2019). Environmental Modelling & Software.	Teixeira Parente, Bittner et al. (2019). Water Resources Research.	Bittner et al. (2020). Advances in Water Resources.

Figure 1.2: Outline of this cumulative dissertation.

clear conceptual understanding of the recharge area and its connected aquifer system is essential. Mudarra and Andreo (2011) and Mudarra et al. (2012) highlighted the value of using time series of major ions to get an enhanced picture of the internal structure and the functionning of karst systems. They investigated limestone karst systems in southern Spain with pronounced karst features. Several similar investigations exist which also focus on limestone dominated karst systems (Perrin et al., 2003; Goldscheider, 2005; Mahler et al., 2008). In contrast, pure dolomite karst systems, such as that in Waidhofen a.d. Ybbs, are less investigated and controversely discussed in terms of karstification (Dossi et al., 2007; Hilberg and Schneider, 2011). Moreover, hydrochemical parameters are not frequently monitored (< 4 measurements per year) in the study area Waidhofen a.d. Ybbs and long term time series of major ions only exist from the obligatory drinking water monitoring. Although the temporal resolution of these time series is not satisfying, the spatial resolution is good thanks to the numerous springs (shown in Fig. 1.1a) on a small spatial scale (ca. 10 km^2). Hydrochemical data were obtained at these springs over the past 40 years. Hence, to get a better understanding of the hydrological functionning of the Waidhofen karst system, we hypothesized that *dolomite aquifers can display high temporal and spatial variability in their hydrochemical signals also on a small spatial scale.* The research questions we asked to validate the hypothesis are as follows.
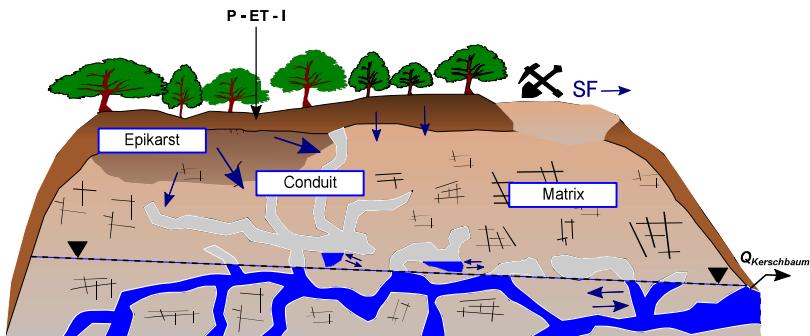
Figure 1.3: Conceptual model of the Kerschbaum spring recharge area as derived in the work of Narany et al. (2019). The meanings of the used symbols are as follows: P is precipitation, I means interception, ET represents evapotranspiration, SF is surface flow and Q$_{Kerschbaum}$ is the spring discharge at the Kerschbaum spring.

- 1) Can we derive the spatial and temporal variability of hydrochemical conditions in a dolomitic karst system on a small spatial scale?

- 2) Is it possible to infer relevant information about the heterogeneous nature of a small scale dolomite aquifer based on the spatio-temporal variability shown by long term hydrochemical time series with a low temporal resolution (i.e. up to four measurements per year)?

The research hypothesis and questions were addressed in the article of Narany et al. (2019)

presented in Chapter 2.

The objective in the study of Narany et al. (2019) was to get a conceptual hydrological understanding of the karst system in Waidhofen a.d. Ybbs (shown as an example for the Kerschbaum spring recharge area in Fig. 1.3. Therefore, long-term hydrochemical time series of major ions obtained from the five existing karst springs and one pumping well were evaluated by means of statistical analyses. Based on the temporal evolution and the hydrochemical characteristics determined for each spring, a cluster analysis was conducted to find similarities and differences in the behavior of the springs on a small spatial scale. Three different clusters were built based on that analysis, all of which showing different contributions from the unsaturated (epikarst) and saturated zone. Finally, a conceptual model of the entire karst system was derived based on the basic knowledge of the interpretation of the local geology and the hydrochemical signatures of each spring and the pumping well.

1.2.2 Hypothesis 2: A recharge area of a given karst system can be subdivided into distinct units of homogeneous soil and land use properties, defined as hydrotopes

Based on the conceptual understanding of the Waidhofen karst system generated in the work of Narany et al. (2019), a mathematical model should be developed that is able to simulate the hydrological effects of the land use change observed in the study area (Section 1.1). While modeling land use change impacts is not a new topic in the hydrological community (Nandakumar and Mein, 1997; Siriwardena et al., 2006; Breuer et al., 2009; Mango et al., 2011), it just became an emerging objective in the karst community (Sarrazin et al., 2018). As mentioned earlier, various kinds of mathematical models exist, e.g. black-box, lumped and physically-based models, that all differ in their degree of complexity and process representation (Labat et al., 1999; Reimann et al., 2011; Tritz et al., 2011; Mekonnen et al., 2018). Although physically-based models are generally preferred tools for modeling land use change impacts in hydrological research (Chu et al., 2010), their application in karst systems is limited due to a lack of data related to the internal structure of karst systems (Hartmann et al., 2014a). For this reason, most modeling studies in karst hydrology used lumped parameter approaches to assess and simulate karst water resources and hydrological processes (Fleury, 2005; Fleury et al., 2007; Hartmann et al., 2012b; Sivelle et al., 2019). Given this recent state in karst hydrological modeling, the model to be developed should be lumped and semi-distributed, thus, taking advantage of the conceptual character of lumped models and the fully distributed character of physically-based models. Out of this motivation, we hypothesized that *a recharge area of a given karst system can be subdivided into distinct units of homogeneous soil and land use properties, defined as hydrotopes*. The research questions we asked to validate the hypothesis are as follows.
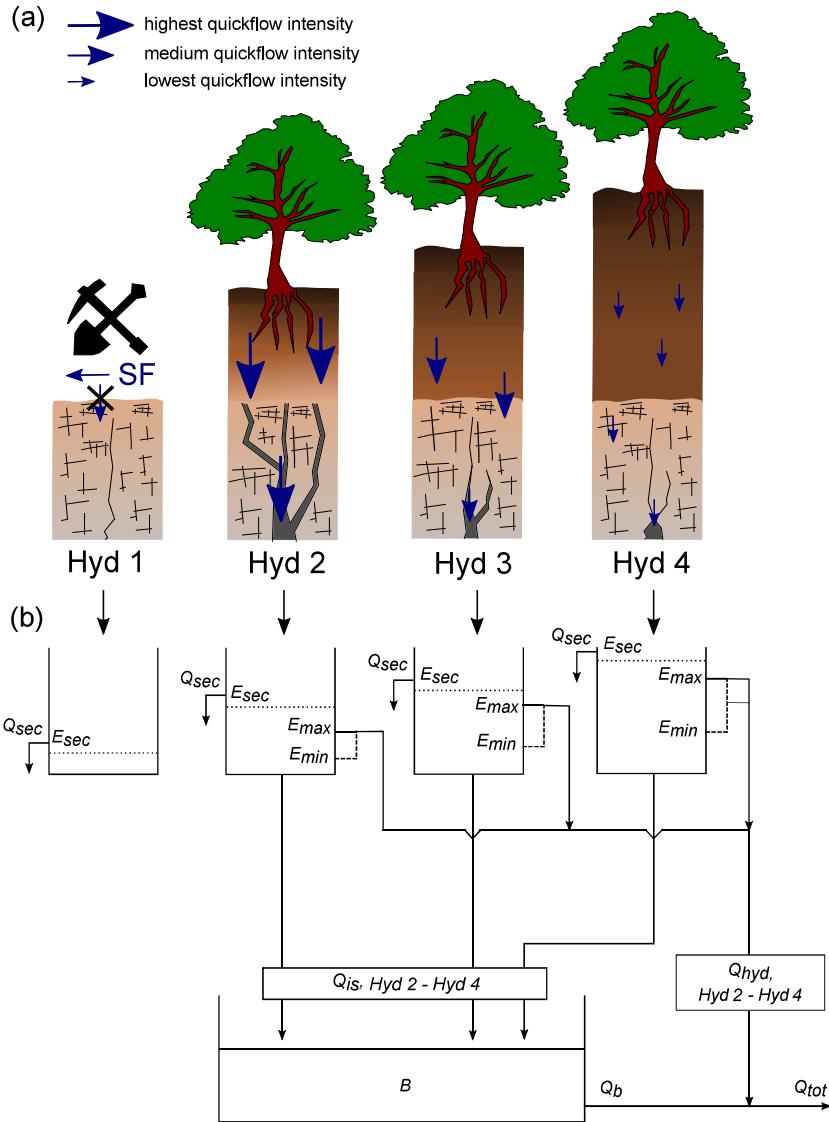
Figure 1.4: Hydrotopes model concept of LuKARS. The meanings of the used symbols are as follows: SF is surface flow, Hyd is the abbreviation for hydrotope, Q_{sec}, Q_{is} and Q_{hyd} are the hydrotope-specific flow components and Q_b and Q_{tot} represent the baseflow and the total spring discharge, respectively. E_{sec}, E_{min} and E_{max} are the hydrotope-specific storage thresholds. A more detailed explanation is given in Chapter 3.

- 1) Can we create a new semi-distributed modeling approach that lumps the predominant hydrotopes present in a catchment?

- 2) Is it possible to calibrate and validate the modeling approach for a reference karst system?

- 3) In order to proof the model concept, can we transfer the modeling approach to other karst systems and their related catchments while maintaining the calibrated hydrotope parameters?

- 4) Can the developed model reproduce the observed impacts of land use changes in the Kerschbaum spring discharge?

Ths research hypothesis and questions were addressed in the article of Bittner et al. (2018a) presented in Chapter 3.

The objective in the work of Bittner et al. (2018a) was to develop a lumped parameter model that can be used to simulate the land use change impacts by the increasing quarry areas on the Kerschbaum spring discharge. The idea was to build a framework that integrates landscape unit with homogeneous soil and land use properties, i.e. hydrotopes, as distinct parts in a lumped parameter model (Fig. 1.4). Fig. 1.4 shows this model structure and how each hydrotope (Fig. 1.4a) becomes conceptualized as a lumped bucket (Fig. 1.4b). This model was named LuKARS (Land use change modeling in KARSt systems). The study showed, that by changing the area of one of these hydrotopes, it is possible to simulate the hydrological impacts this land use change implies. Finally, the developed model was tested and validated for other recharge areas in order to ensure its transferability to other catchments.

1.2.3 Hypothesis 3: The FREEWAT plugin in QGIS offers a tailored framework to build a graphical user interface for the developed hydrotope-based karst aquifer model

Given that the idea of developing a hydrologic model to perform land use change impact studies emerged from the case study problem presented in Section 1.1, it was necessary that the tool is applicable by practioners who are not familiar with programming. Recent initiatives exist that try to overcome this very limitation by providing open source tools for water resource management in form of a graphical user interface (GUI), e.g. Winston (2009) and Olivera et al. (2006). In the particular case of semi- or distributed hydrologic models, such a GUI needs to be able to manage the spatial distribution of relevant model parameters, This fact leads to the idea of using a geographical information system (GIS) as user interface for this kind of hydrologic models. Recent efforts have been made to use the freely available QGIS environment (www.qgis.org) as a GUI for different hydrologic models, such as SWAT (Dile et al., 2016; Park et al., 2019). While these software couplings were oriented towards getting a GUI for one specific model, a more general framework would be helpful to integrate different tools for different purposes in water resource management (De Filippis et al., 2017). The FREEWAT plugin in QGIS (www.freewat.eu) is

such an initiative which has a modular structure consisting of pre-processing, simulation and post-processing tools (Rossetto et al., 2018). FREEWAT was a formerly funded EU project, finished in 2017, and the maintenance and development of the pulgin now depends on the voluntary contribution of researchers. So far, the plugin only comprises a physically-based hydrologic model, i.e. MODFLOW-OWHM (Hanson et al., 2014), and a rainfall-discharge model is still missing. Given the hydrotope-based framework of LuKARS that makes an integration in a GIS environment valuable, we argued that the FREEWAT plugin in QGIS offers a tailored framework to build a GUI for the LuKARS model. For this work, the following taks were formulated and addressed in the article of Bittner et al. (2020b) presented in Chapter 4.

- 1) Linking our modeling approach to the existing FREEWAT structure consisting of pre-processing, evaluation and post-processing modules.

- 2) Using the GIS system for coupling the process of hydrotope generation, model building and model evaluation in one interface.
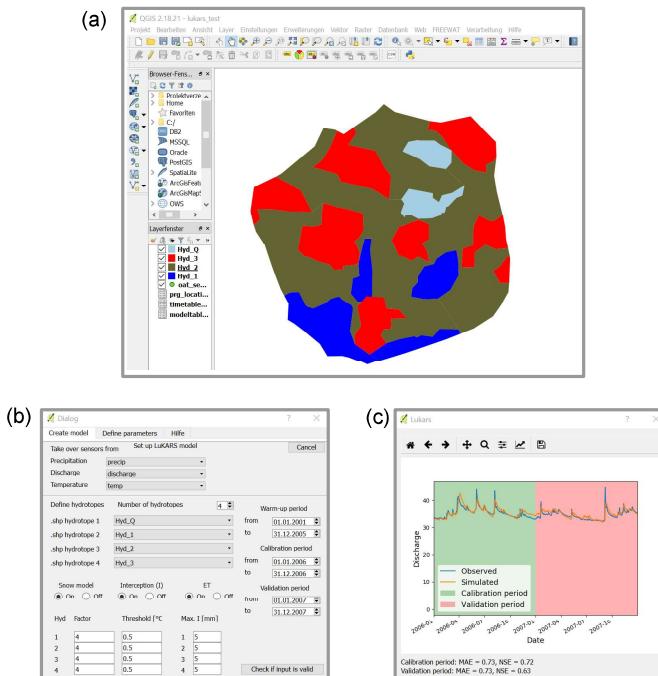
Figure 1.5: LuKARS interfaces as implemented in FREEWAT.

The objective in Bittner et al. (2020b) was to make the developed modeling approach LuKARS accessible and applicable also for non-researchers. Given that the research ideas of this PhD study evolved from a real world problem, it was a particular aim to make the model usable by the waterworks Waidhofen a.d. Ybbs and also by other interested stakeholders. Therefore, the developed karst aquifer model was implemented in the FREEWAT environment, which provides a QGIS framework for open-source tools for water resource management. LuKARS takes advantage of existing tools for model pre- and post-processing in FREEWAT. Moreover, it was shown that GIS environment provides a straightforward modeling framework for the hydrotope-based structure of LuKARS. Fig. 1.5 shows as an example three different interfaces from the LuKARS integration in FREEWAT, which are the QGIS interface including the hydrotopes (Fig. 1.5a), the model set-up interface (Fig. 1.5b) and the results window (Fig. 1.5c). All relevant model data objects can be stored and shared as time series and/or geospatial data. The software including an test application for the Kerschbaum spring in Waidhofen was made available for public use on GitHub (https://github.com/dbittner87/LuKARS).

1.2.4 Hypothesis 4: The dimensions of the parameter space in LuKARS can be reduced using the active subspace method while better constraining the parameter ranges of the most sensitive model parameters. This leads to a reduction in model parameter and output uncertainties

As pointed out in Section 1.2.2, the lack of spatially distributed data about the internal structure of karst systems makes conceptual rainfall-discharge models suitable tools to predict karst spring discharge. This is because these lumped models allow for a conceptual simplification of the karst system functioning (Hartmann et al., 2014a; Jourde et al., 2015). Nevertheless, it is not trivial to find an acceptable model representation since most of the parameter ranges cannot be determined or constrained by field observations. On the one hand, a severe simplification of a karst aquifer with a low-dimensional parameter space, i.e. 4 to 6 parameters, can lead to an underrepresentation of relevant hydrological processes. However, such a low-dimensional parameter space can reduce parameter uncertainties and model equifinality (Jakeman and Hornberger, 1993; Hartmann et al., 2017). On the other hand, considering the more complex nature of a karst system in a modeling framework can improve its conceptual representation (Hartmann, 2018). In most cases, such a complex lumped parameter model cannot be adequately calibrated since its parameters are not sufficiently constrained by the measured discharge data (Hartmann et al., 2014a). In the particular case of a lumped parameter model, which not only intends to simulate karst spring discharge but also the impacts of land use changes, a higher dimensional parameter space is needed. Therefore, identifying the parameters that are constrained by calibration data and their respective sensitivities is a recent effort of the karst modeling community (Mazzilli et al., 2012a; Hartmann et al., 2017; Mudarra et al., 2019). In this context, different approaches were recently proposed to reduce model structure and parameter uncertainties for karst hydrologic models. Most of these methods can be grouped into so-called multi-objective calibration approaches, using additional

data sources like hydrochemical data (Hartmann et al., 2017), the autocorrelation of the discharge (Moussu et al., 2011), ground-based gravity measurements (Mazzilli et al., 2013) and dye tracer concentrations (Mudarra et al., 2019). Despite all these efforts, dealing with the high dimensionality of the model parameter space remains a challenge and there is a need to quantify how and which model parameters are constrained by calibration data. A recently developed method, called the active subspace method (Constantine et al., 2014), identifies directions in the parameter space that are most constrained by the calibration data. These parameter directions provide information about the sensitivity of parameters as well as about the relation between specific parameters. This information about parameter relations is the main strength of the active subspace method which goes beyond the information derived from other global sensitivity analysis methods, e.g. Sobol (Sobol, 2001). Therefore, we hypothesized that *the dimensions of the parameter space in LuKARS can be reduced using the active subspace method while better constraining the parameter ranges of the most sensitive model parameters. This leads to a reduction in model parameter and model result uncertainties*. The research questions we asked to validate the hypothesis are as follows.

- 1) Which are the most sensitive parameters of the developed model?

- 2) Can we reduce the parameter uncertainties in a Bayesian framework by better constraining the prior parameter ranges?

- 3) To what extent is it possible to reduce the parameter dimensions of the model?

- 4) What are the uncertainties in the model output when using the model with reduced parameter dimensions?
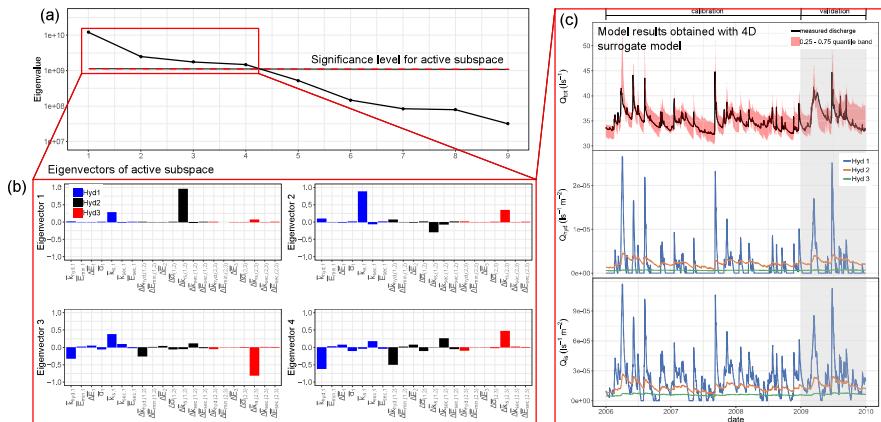
Figure 1.6: Concept of defining and active subspace. a) Identification of active subspace. b) Eigenvectors in active subspace. c) Modeling results obtained with lower-dimensional surrogate model defined in active subspace.

The research hypothesis and questions were addressed in the article of Teixeira Parente et al. (2019a) presented in Chapter 5.

The objective in the work of Teixeira Parente et al. (2019a) was to quantify the parameter uncertainties of LuKARS. Depending on the number of hydrotopes implemented in LuKARS, the model can have a large parameter space. For this reason, the chosen methodology for uncertainty quantification should also be usable for parameter dimension reduction. The active subspace method represents such a method and was recently proposed for exact these purposes. Thus, the main aim here was to apply this method for the developed modeling approach. In an active subspace, the contribution of the parameters related to groundwater recharge were recognized as most informed for the investigated Kerschbaum spring LuKARS model. For these, the prior ranges became most constrained in the posterior. It was shown that the original 21-dimensional parameter space of the Kerschbaum spring model could be reduced to a 4-dimensional surrogate model. Fig. 1.6 highlights this process of identifying the active subspace in the eigenvalue decay (Fig. 1.6a) and the relevant eigenvectors (Fig. 1.6b). The model output uncertainties when using the lower dimensional model were $< 10\%$ with respect to the mean spring discharge (Fig. 1.6c).

1.2.5 Hypothesis 5: The dimension and the feature of the active subspace can be related to underlying geometrical and hydrological model parameters, used to describe different hydrological properties of a chatchment

The active subspace method, was successfully applied in different hydrological investigations (Jefferson et al., 2015; Erdal and Cirpka, 2019), also including the study performed to validate the hypothesis formulated in Section 1.2.4 (Teixeira Parente et al., 2019a). In this study, the parameter and model output uncertainties of LuKARS were quantified. Moreover, the active subspace found in Teixeira Parente et al. (2019a) was used to effectively reduce the dimensions of the LuKARS parameter space. However, how the parameter combinations identified in the directions of an active subspace can be interpreted from a hydrological point of view is not clear. Given this research gap, we hypothesized that *the dimension and the feature of the active subspace can be related to underlying geometrical and hydrological properties of a chatchment.* The research questions we asked to validate the hypothesis are as follows.

- 1) Which geometrical properties of a hydrotope mostly affect the dimension and the feature of an identified active subspace?

- 2) Which hydrological properties do have an impact on the dimension and the feature of an identified active subspace?

The research hypothesis and questions were addressed in the article of Bittner et al. (2020a) presented in Chapter 6.
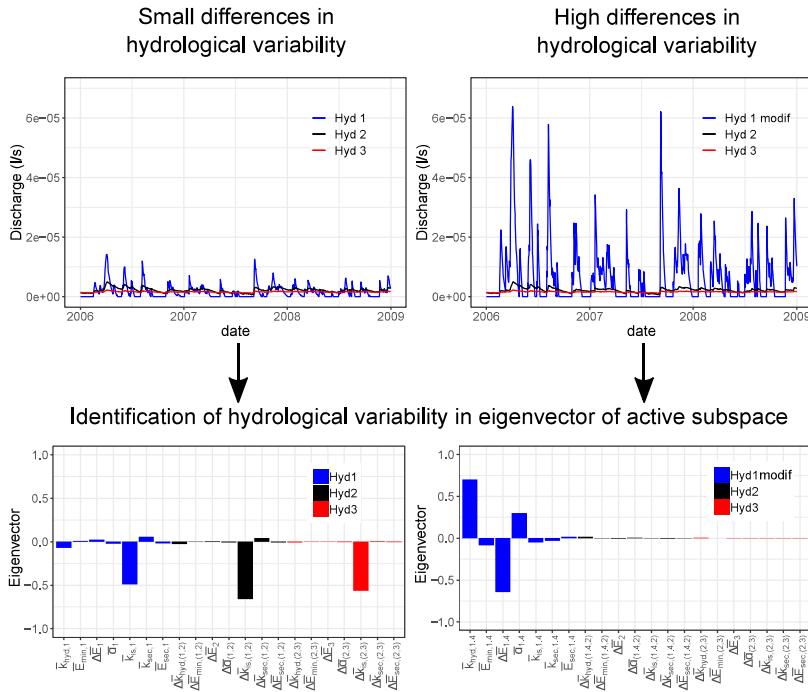
Figure 1.7: Concept of identifying hydrological properties in active subspace. The figure shows how the variability of the specific discharge from a hydrotope can be identified in the eigenvector of the relevant eigenvalues in an active subspace.

The objective of the study from Bittner et al. (2020a) was to perform a parametric study of the LuKARS model with the active subspace method. In the work of Teixeira Parente et al. (2019a), we identified dominant contributions from the parameters controlling groundwater recharge in active subspaces. Here, a framework was proposed how to hydrologically interpret these results of the active subspace method. A total of 21 scenarios were investigated in three test cases where the hydrotope areas and hydrological properties were modified in well-known ranges. The results highlight that it is possible to determine relevant hydrological and catchment properties from an identified active subspace. As an example, Fig. 1.7 shows how the hydrological variability can be identified in an eigenvector of the active subspace. Furthermore, it was proposed that the active subspace information could be used to plan tailored field campaigns in order to obtain relevant data for any modeling project.

Chapter 2

Hydrochemical data analyses and conceptualization of the Waidhofen karst system

Narany et al. (2019)[1]

Abstract

Dolomite karst systems are less common and less exploited than limestone systems, but still they can significantly contribute to drinking water supply in many countries. The knowledge about spatial and temporal variations of hydrochemical parameters of such systems is much more limited than for limestone karst aquifers. In the present research, 40-year long observations of hydrochemical parameters gathered from five springs and a pumping well in Waidhofen an der Ybbs (Austria) were used to show the variability of chemical water composition in a small scale ($\sim$ 10 km^2) dolomite karst system. Integration of classic geochemical methods and multivariate statistical analysis revealed that the hydrofacies correlate directly with the lithofacies (dolomite) in the study area. At the same time, measured concentrations of Ca^{2+}, Mg^{2+}, Na$^+$, Cl$^-$, and HCO$_3^-$ allow for a classification of the springs in three groups based on their ionic ratios. This classification highlights the spatial and temporal variability that can be encountered in dolomite karst systems, even on small spatial scales, that are relevant for water suppliers. Moreover, temporal observations of hydrochemical parameters show increasing trends of nitrate concentrations in all sampling points, though with different rates. The analysis of the stable isotopes δ^{15}N–NO$_3^-$ and δ^{18}O–NO$_3^-$ revealed that nitrification processes in forest floors and mineral soils are the main source of nitrate in most locations investigated. The findings of the present study highlight the necessity of a detailed temporal and spatial distributed monitoring to support water resources management in dolomitic karst aquifers.

---

[1]Narany, T.S., **Bittner, D.**, Disse, M., Chiogna, G., 2019. Spatial and temporal variability in hydrochemistry of a small scale dolomite karst environment. Environmental Earth Sciences 78, 273.

2.1 Introduction

Karst aquifers constitute an important source for drinking water supply for about 25% of the world's population (Hillebrand et al., 2015). In Europe, karst systems occupy nearly 35% of the land surface (Goldscheider, 2005) and in some countries, such as Austria, more than 50% of the drinking water supply originates from karst springs (Hartmann et al., 2014a). Generally, karst aquifers are considered as rapid flow and transport systems, which store large volumes of water due to their geological properties (Jebreen et al., 2018; Benson and Yuhr, 2015). However, the rapid and often unfiltered water exchange between the land surface and the karst aquifer makes karst systems highly vulnerable. While the heterogeneous hydrological and hydrochemical dynamics are well documented for limestone aquifers (Musgrove et al., 2016; Mudarra et al., 2012; Mahler et al., 2008; Perrin et al., 2003), this spatio-temporal variability is poorly investigated for dolomite-dominated karst systems (Dossi et al., 2007; Goldscheider, 2005). According to Hilberg and Schneider (2011), dolomite aquifers could be considered as more reliable drinking water sources when compared to limestone aquifers due to the steadier discharge conditions and minimal impacts of precipitation or seasonal effects they exhibit. Thus, a better understanding of these systems would lead to improved water resources management strategies.

Insightful information about the hydrological functioning of karst systems is generally provided through the monitoring of physical and chemical parameters (Bicalho et al., 2017; Mudarra et al., 2012) and can be used as indirect indicators to characterise karst systems (Mudarra and Andreo, 2011). Physical parameters, such as rainfall data, spring discharge, temperature and electrical conductivity (EC) can be easily monitored and used to obtain information on the hydrodynamic behaviour of karst systems (Bicalho et al., 2017; Hartmann et al., 2014a). On the contrary, the lack of continuous and significant hydrochemical data causes a poor understanding of the processes controlling water quality, particularly how natural processes and human activities influence karst (Hartmann et al., 2014a; Charizopoulos et al., 2018). While the analysis of long-term discharge time series of karst springs is not new (Fiorillo and Guadagno, 2010), only a limited number of research studies focused on the hydrochemistry of dolomite karst systems over an extended period of time (Schmidt et al., 2013; Miorandi et al., 2010).

Although dolomite aquifers are mostly considered not to be as heterogeneous as limestone aquifers (Hilberg and Schneider, 2011; Krawczyk and Ford, 2006; Wang et al., 2004), we hypothesize that they can display high temporal and spatial variability in their hydrochemical signals also on a small spatial scale. To test this hypothesis, the present study investigates long-term hydrochemical time series (40 years of data) from 5 springs and a pumping well located in a small-scale recharge area in the Triassic dolomite sequence of the Northern Calcareous Alps (NCA) close to Waidhofen a.d. Ybbs (Austria). The specific aims of this work are i) to present a rare novel dataset for water quality parameters, something which is uncommon as it describes the chemical composition of a dolomite karst system over 40 years, ii) to derive the spatial and temporal variability of hydrochemical conditions in the dolomitic karst system of Waidhofen an der Ybbs on a small scale (10.86 km^2), which is of interest for water supply purposes, and iii) to infer relevant information

about the heterogeneous nature of the dolomite aquifer based on the spatio-temporal variability shown by the hydrochemical time series. We apply multidimensional data analysis methods based on hydrochemical data sets from long-term observations to investigate the hydrochemical time series. These include classic geochemical methods coupled with multivariate statistical analysis. Although the temporal resolution of the present time series is low (about 4 measurements per year, typical for mandatory water quality analysis of water suppliers), the availability of long-term hydrochemical time series provides valuable information to characterize the spatio-temporal variability of this small-scale karst system. If our hypothesis is not rejected, then this variability should be acknowledged for both practical as well as for scientific research purposes. In the first case, the spatial distribution and the frequency of the monitoring campaigns should be adequate to ensure water quality standards. In the second case, the analysis performed on a single time series in such a system cannot be considered representative for the ongoing hydrochemical processes even at a small spatial scale (~ 10 km^2).

2.2 Materials and Methodologies

2.2.1 General characteristics of the study area

Waidhofen an der Ybbs is situated in the alpine foreland in the state of Lower Austria (Niederöster-reich) (Figure 2.1a). The study area is located 10 km south of the city of Waidhofen a.d. Ybbs and covers an area of approximately 10.86 km^2. The area is part of the foothills of the NCA, with minimum and maximum altitudes from 415 to 969 m asl, respectively. The regional climate is categorized as 'Central European humid temperate', with a mean annual temperature of 8 °C, and mean annual precipitation of 1379 mm. The rainfall rate shows a characteristic summer-maximum, with the peak during the month of July (Bittner et al., 2018a). According to Markart et al. (2012), the substrata of the mountainous landscape are dominated by dolostones. The karst springs originating from the dolomitic bedrock, namely Mitterlug, Hinterlug, Hiselwirt, Glashütten and Kerschbaum, are the main sources of drinking water supply for more than 25,000 inhabitants (Leaders, 2012). Moreover, the water supplier operates a pumping well (Forster well, No. 5 in Figure 2.1c) located in the Waidhofenbach valley, which is filtered in the dolomitic basement rock and used once the water demand cannot be met by the water supplying springs.

Kerschbaum is the most important spring for the water supply system with a mean daily discharge rate of 2,932 m^3/d, followed by Hinterlug and Mitterlug with mean daily discharge rates of 957 m^3/d and 329 m^3/d, respectively. Hieslwirt spring and Glashütten spring are ungauged. The dominant land covers are deciduous and mixed coniferous-deciduous forests and cultivated grassland (Promper et al., 2014). Stone quarries cover approximately 1.7 % of the entire study area (Koeck, 2017).

2.2.2 Geology and hydrogeology

The study area of Waidhofen a.d. Ybbs, as part of the NCA, is dominated by a lithologic sequence of dolomitic basement rocks (Figure 2.1c). The complex stratigraphy of the NCA has a significant influence on the hydrogeological characteristics of the region (Hilberg, 2016). Main dolomite (Hauptdolomit) is the dominant strata along the northern part of the NCA, which was formed in the course of marine sedimentation phases during the Triassic era and partially reaches vertical thicknesses of up to 1000 m (Hilberg, 2016). Despite the dominance of carbonatic bedrocks, characteristic karst features like dolines, caves or sinkholes are only partly present in the study area, since dolomitic rocks do not show tendencies to develop karstic features like limestones (Leaders, 2012).
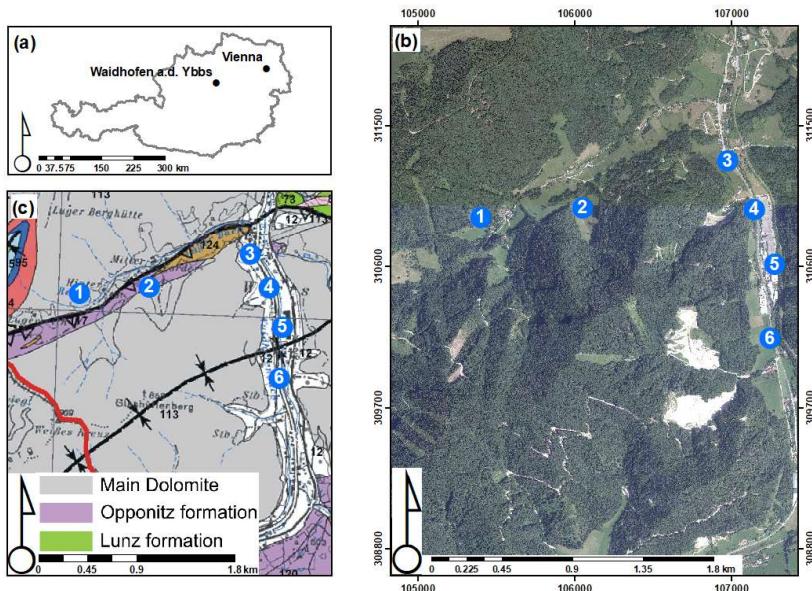
Figure 2.1: (a) Location of Waidhofen a.d. Ybbs in Austria; (b) Orthophoto showing the main land cover in the study area and the locations of the investigated springs and well, which are 1 = Hinterlug, 2 = Mitterlug, 3 = Hieslwirt, 4 = Glashütten, 5 = Forster well, 6 = Kerschbaum; (c) The geological map highlighting the dominance of dolomitic basement rocks, the striking fault separating the Glashütten- and Schnabelberg massifs as well as the outcrop of the Opponitz formation at Mitterlug spring, representing the aquitard for the Mitterlug spring aquifer.

The two mountain massifs in the study area, namely Schnabelberg (Hinterlug spring in northern part) and Glashüttenberg (Mitterlug, Hieslwirt, Glashütten and Kerschbaum spring in southern

part) are tectonically separated by a strike-slip fault (Figure 2.1c). This fault is documented by the outcrop of the Opponitz formation (underlying the Main Dolomite sequence, also Triassic, mainly calcareous schists, travertine and marl, mostly impermeable) at Mitterlug spring (Opponitz layer), representing the aquitard for the aquifer feeding Mitterlug spring (Hacker, 2003). The syncline fault striking through Glashüttenberg massif is considered as an underground basin and water storage system, which drains the Glashüttenberg massif in the north-east direction. Although the Mitterlug, Hieslwirt, Glashütten and Kerschbaum springs are fed by the same mountain massif, Hacker (2003) showed that they do not all share the same recharge areas, indicating a high degree of hydrogeological heterogeneity on a small spatial scale. Moreover, Hacker (2003) provided evidence for a deep karstified aquifer system in the Glashüttenberg mountain massif and further highlights the complexity of this small scale karst aquifer system. Generally, karst aquifers are characterised by short mean residence times of the fast flow component ranging between a few hours or days.

2.2.3   Groundwater sampling and analysis

2.2.3.1   Continuous monitoring and sampling

Water samples were collected from five springs, namely Hinterlug, Mitterlug, Hieslwirt, Glashütten, and Kerschbaum and one pumping well (Forster well) in Waidhofen for physicochemical analysis, following the framework of the statutory water quality monitoring established in Austria. Sampling intervals and the parameters to be monitored are prescribed by law in the Austrian Drinking Water Ordinance (Chovanec 1994). The available water quality data from the waterworks Waidhofen a.d. Ybbs have a temporal resolution of one to four measurements per year in the time from 1977 to 2017. Data gaps are present in the long-term data set because of discontinuous monitoring, and some parameters being excluded due to changes in monitoring plans, priority, or other logistic reason at different times during the more than 40 year of monitoring of the study area. Therefore, only twelve water quality parameters, namely Temperature (Temp), pH, EC, calcium (Ca^{2+}), magnesium (Mg^{2+}), sodium (Na^+), potassium (K^+), sulphate (SO_4^{2-}), chloride (Cl^-), carbonate (CO_3^{2-}), bicarbonate (HCO_3^-), nitrate (NO_3^-) were chosen for this study. Additional spring water samples were collected for NO_3^- isotope analysis in September 2017, as well in May and September 2018.

2.2.3.2   Analytical methods

Temp, pH, and EC were measured in the field using a pH meter WTW pH 540 GLP and conductivity meter (WTW 330 i). Only accredited laboratories are permitted to perform water quality analysis for drinking water supply. According to the information from the water works owner, the applied sampling analysis methods and detection limits changed over the investigated time period. However, since 2005, Ca^{2+}, Mg^{2+}, Na^+, and K^+ were analysed based on the ionic chromatography method (ISO 14911:1998), with a minimum detection limit of 0.5 mg/L for calcium and magnesium, and 0.1 mg/L for sodium and potassium. Also, NO_3^-, SO_4^{2-}, and Cl^- were analysed

via dissolved anions by liquid ion chromatography (ISO 10304-1:2007), with a minimum detection limit of 0.1 mg/L. Samples with ion balance error larger than $\pm$ 10% were eliminated from the dataset.

For the isotope analysis of the nitrate species in the water samples, the ratio of stable Oxygen isotopes ($\delta^{18}O$–NO_3^-) and the ratio of stable N isotopes ($\delta^{15}N$–NO_3^-) of NO_3^- were analysed using the stable isotope ratio mass spectrometry (IRMS) method with an analytical precision of $\pm$ 0,8 ‰ and $\pm$ 0,3 ‰, respectively.

2.2.4 Multivariate statistical analysis

2.2.4.1 Trend analysis

Natural and anthropogenic changes can introduce trends and shifts in hydrologic time series data, which could be identified and quantified by applying parametric and non-parametric time series analysis methods (Narany et al., 2017). For consistently increasing or decreasing trends ("monotonic trends") the nonparametric test such as the Mann-Kendall Test (Mann, 1945; Kendall, 1975) is commonly applied to assess the statistical significance of trends (Yue and Wang, 2004). The Mann-Kendall and modified Mann-Kendall tests (Yue and Wang, 2004; Hamed and Rao, 1998) were applied on EC, Ca^{2+}, Mg^{2+}, SO_4^{2-}, CO_3^{2-} and NO_3^- samples, which were collected for all springs throughout different time periods, starting from July 1977 for EC, July 1989 for Ca^{2+}, July 1989 for Mg^{2+}, July 1992 for SO_4^{2-}, July 1990 for NO_3^- and July 1980 for CO_3^{2-}. All the mentioned water quality parameters were collected in the Forster well since July 2004. Sampling was not scheduled regularly during the 40-years monitoring period, therefore only samples belonging to the winter season (December, January and February) and summer season (June, July, and August) were considered for trend analysis. The results of the non-parametric Mann-Kendall test may give wrong results if the time series is autocorrelated (Yue and Wang 2004). To address this issue, a modified version of the Mann Kendall test based on a variance correction approach (Yue and Wang 2004) was applied for the time series data of EC, Ca^{2+}, Mg^{2+}, SO_4^{2-}, and NO_3^- of the sampling stations that showed serial correlation in the trend analysis (Ca^{2+} in Kerschbaum spring; EC in Hieslwirt, Kerschbaum, and Glashütten springs, NO_3^- in Hieslwirt, Hinterlug, and Glashütten springs; SO_4^{2-} in Hieslwirt, Hinterlug, and Kerschbaum springs, Mg^{2+} Hieslwirt, Kerschbaum, and Glashütten springs). Moreover, Sen's slope estimator (Sen, 1968) was used to determine increasing or decreasing trends in the time series data with positive or negative values of Sen's slope respectively.

2.2.4.2 Hierarchical cluster analysis (HCA)

The HCA is a data classification technique which is widely applied in Earth sciences for classification of hydrochemical data (Cloutier et al., 2008) using predetermined selection criterions to classify objects in clusters that show high internal homogeneity (within cluster) and high external heterogeneity (between clusters) (Nosrati and Van Den Eeckhaut, 2012). In this study, HCA was performed on the normalized data of groundwater samples from all five springs and the Forster

well, using six main parameters including Ca^{2+}, Mg^{2+}, Na^+, HCO_3^-, Cl^- and SO_4^{2-}. Euclidean distance (straight line distance between two points in a c-dimensional space defined by c number of variables) measures were applied to measure similarity/dissimilarity among the variables while the Ward's linkage method (Ward Jr, 1963) was chosen to link initial clusters produced during initial clustering steps. The Kruskal-Wallis test (Kruskal and Wallis, 1952) was applied to check the statistical significance of the results from the cluster analysis.

2.3 Results

2.3.1 General Hydrochemistry

Results of the descriptive statistics for the chemical composition of the five dolomite karst springs (Hieslwirt, Kerschbaum, Glashütten, Hinterlug, and Mitterlug) and the pumping well (Forster well) are reported in Table 2.1. According to Hilberg and Schneider (2011), calcium (Ca^{2+}), magnesium (Mg^{2+}), sodium (Na^+), potassium (K^+), sulphate (SO_4^{2-}), chloride (Cl^-), and hydrocarbonate (HCO_3^-) could be considered as the main hydrochemical parameters in the formations of the NCA.

Table 2.1: Descriptive statistics of water physiochemical parameters in Waidhofen.

Sampling points	Statistic	Temp °C	pH	CO_3^{2-} mg/L	Ca^{2+} mg/L	Mg^{2+} mg/L	Na^+ mg/L	K^- mg/L	NO_3^- mg/L	HCO_3^- mg/L	Cl^- mg/L	SO_4^{2-} mg/L	EC µS/cm	$\delta^{15}N–NO_3$	$\delta^{18}O–NO_3$
Hieslwirt	Minimum	8.0	7.1	10.1	40.0	13.0	1.0	0.1	3.0	220.0	0.5	3.0	341.0	-0.4	-3.1
	Maximum	10.1	8.3	12.7	60.0	27.0	1.5	3.5	9.5	287.7	5.2	9.0	460.0	7.7	2.9
	Mean	8.4	7.7	10.9	44.8	24.2	1.1	0.7	6.7	238.6	1.2	6.3	401.1	2.4	0.4
	Variance (n)	0.1	0.1	0.3	9.9	4.6	0.1	0.9	1.5	150.1	0.6	2.5	739.1	20.6	9.8
Kerschbaum	Minimum	8.0	7.2	10.6	49.0	24.0	1.9	0.0	2.0	231.0	1.0	3.2	430.0	2	2.2
	Maximum	9.6	8.3	14.8	74.0	33.0	9.5	7.8	11.4	322.5	23.3	12.0	570.0	2.1	4.3
	Mean	9.0	7.6	13.3	57.5	26.9	3.5	0.8	5.2	287.6	5.2	8.6	486.8	2.0	3
	Variance (n)	0.1	0.0	0.4	13.4	2.2	1.6	0.9	0.7	151.0	11.2	2.3	680.3	0.003	1.3
Glashütten	Minimum	8.6	7.4	10.6	42.0	15.0	0.6	0.0	1.0	231.0	0.1	2.0	349.0	1.1	1.2
	Maximum	10.8	8.3	12.6	56.0	29.0	3.4	9.5	6.0	274.6	8.7	9.0	510.0	2.6	4.9
	Mean	9.3	7.7	11.8	47.1	25.7	2.0	0.9	3.8	256.7	1.5	4.9	433.0	1.9	2.5
	Variance (n)	0.2	0.0	0.1	7.9	3.9	1.3	4.0	0.8	46.5	1.5	1.0	953.6	0.6	4.1
Hinterlug	Minimum	7.1	7.0	11.8	48.0	21.0	1.0	0.0	4.0	257.1	0.2	6.2	396.0	-0.7	3.1
	Maximum	9.8	8.3	14.2	75.0	33.0	4.4	18.8	10.0	309.4	16.6	11.9	554.4	0.4	3.9
	Mean	8.6	7.7	13.1	56.6	26.8	2.2	4.2	7.5	284.5	1.7	8.1	465.6	0.0	3.4
	Variance (n)	0.2	0.0	0.2	16.1	3.2	2.5	27.3	1.2	106.9	5.1	1.5	922.0		0.19
Mitterlug	Minimum	6.5	7.1	7.8	36.0	18.0	1.1	1.6	6.9	170.0	0.2	3.9	333.3	-0.1	1.1
	Maximum	9.9	8.3	11.6	58.0	28.0	4.4	6.4	10.3	253.3	9.0	10.0	450.0	-0.1	4.8
	Mean	8.0	7.7	10.1	42.8	23.4	2.5	3.2	8.7	219.3	1.4	6.9	389.3	-0.1	3.1
	Variance (n)	0.4	0.1	0.4	13.2	2.6	1.9	3.6	0.7	196.5	2.1	2.5	675.3	0	3.5
Forster well	Minimum	7.4	8.4	12.8	28.2	20.0	1.9	0.2	3.7	272.3	0.2	3.4	362.0	–	–
	Maximum	8.0	9.7	13.6	86.6	28.7	11.4	2.7	5.5	292.0	23.9	24.4	432.0	–	–
	Mean	7.6	8.8	13.2	52.5	27.1	3.5	0.5	4.5	285.0	1.7	5.1	390.6	–	–
	Variance (n)	0.1	0.1	0.1	41.5	1.6	10.5	0.1	0.2	15.4	12.0	9.1	104.1	–	–

Generally, EC (this work is referred to specific EC at Temp = 25 °C) is used as an indicator for various aquifer lithologies, because it is mainly controlled by the dissolution processes within the aquifer. In the study area, the mean EC ranged from a minimum 389 µS/cm for the Mitterlug spring to a maximum 486 µS/cm for the Kerschbaum spring.

Weathering of carbonate rocks in Alpine karst systems significantly contributes to the concentrations of major cations (i.e. Ca^{2+} and Mg^{2+}), and major anions (i.e. HCO_3^-) (Pfleiderer et al.,

2006). Long term (1989 to 2017) mean values of Ca^{2+} varied between 42.8 mg/L in the Mitterlug spring and 57.5 mg/L in the Kerschbaum spring. In addition, observed HCO_3^- values ranged between 287.6 mg/L in the Kerschbaum spring and 219.3 mg/L in the Mitterlug spring.

The typical dolomite and limestone systems include low concentrations of Na^+ and Cl^- (Kanduč et al., 2012). According to the results (Table 2.1), low concentrations of Na^+ and Cl^- were measured, specifically Na^+ values varied from maximum 11.4 mg/L in Forster well to 0.6 mg/L in Glashütten. Moreover, Cl^- concentrations varied from 23.9 mg/L in Forster well to 0.1 mg/L in Glashütten. Sulphate concentrations also varied from a maximum mean value of 8.6 mg/L in the Kerschbaum spring to a minimum mean value of 4.9 mg/L in Glashütten. NO_3^- concentrations also varied between a minimum of 1 mg/L in Glashütten spring and a maximum of 11.4 mg/L in the Kerschbaum spring. According to the EU legislation, the upper permissible limit of NO_3^- for tap water is 50 mg/L, therefore, all samples have values below these limits.

2.3.2 Spatial characterization of the karst aquifer and groundwater origin

2.3.2.1 Hydrochemical characterization of the karst springs
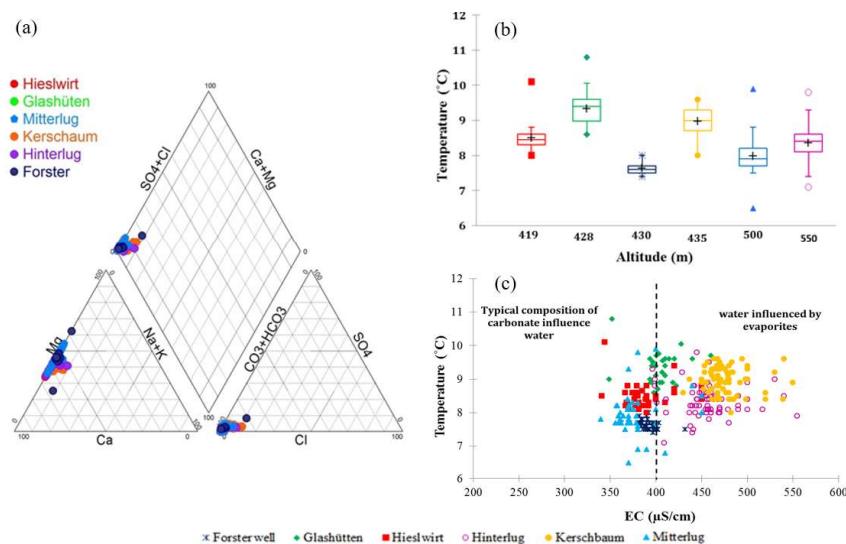
Figure 2.2: Piper diagram (a), temperature variations based on spring's altitude (b), and scatter diagram of EC vs temperature (c) of the five springs and pumping well

The collected water sample chemical compositions from the six sampling points during 1989 to 2017 were summarized using the diagram according to Piper (1944) (Figure 2.2). The groundwater type showed that all sampling points have a similar anionic composition, dominated by HCO_3^- with

an abundance order of $HCO_3^- > SO_4^{2-} > Cl^-$ (meq/L) and cationic composition, dominated by Ca^{2+} and Mg^{2+}, respectively, with an abundance order of $Ca^{2+} \cong Mg^{2+} > Na^+$ (meq/L). Only water samples collected from the Kerschbaum spring showed an abundance order of $HCO_3^- > SO_4^{2-} \cong Cl^-$ (meq/L).
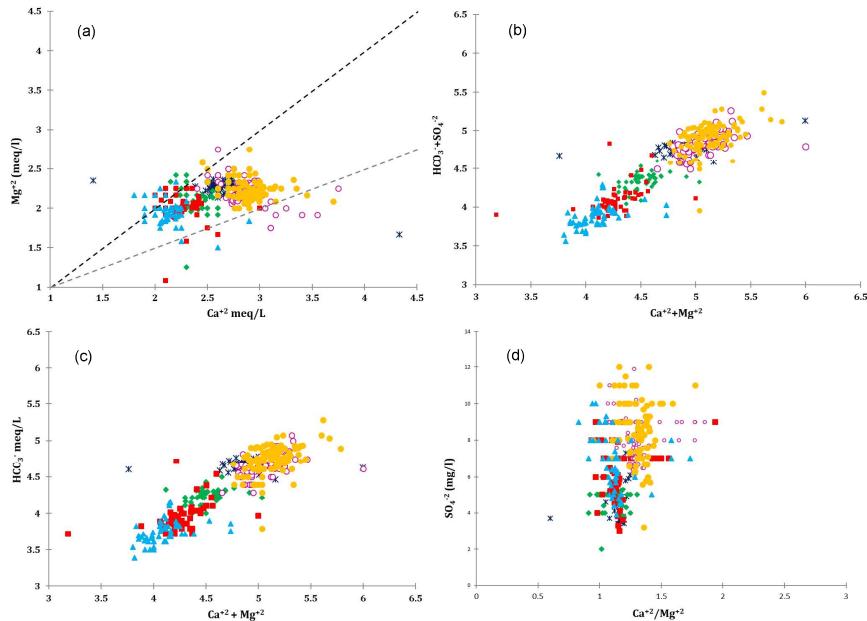
Figure 2.3: Distribution of ionic ratios for major groundwater ions in the study area

In Waidhofen, the spring's water temperature decreased with increasing altitudes from 9.3 °C at 428 m in Glashütten, to 8 °C at 500 m in Mitterlug (Figure 2.2b). However, Hieslwirt and Hinterlug did not show the same pattern as the rest of the study area. Moreover, with decreasing altitude, EC increased from 350 µS/cm in Mitterlug to > 400 µS/cm in Glashütten (Figure 2.2b). Concerning EC and temperature, sampling points were classified in two main groups (Figure 2.2c). The first group consists of Mitterlug, Hieslwirt, Glashütten springs and the Forster well where EC varied between a minimum of 330 µS/cm to maximum about of 450 µS/cm, which can indicate that the chemical compositions of water from the first group is mainly controlled by carbonate rocks (Hilberg and Schneider, 2011). In the second group, Kerschbaum and Hinterlug springs showed EC values ranging from 450 µS/cm to above 500 µS/cm with a mean temperature around 9 °C and different altitudes, which can indicate the impact of evaporates on groundwater chemistry.

The hydrochemistry of karst systems can be characterized by considering the ratio between calcium and magnesium. The average of Ca^{2+}/Mg^{2+} ratios in the Forster well, Glashütten, Hieslwirt,

Kerschbaum, Hinterlug and Mitterlug spring are 1.17, 1.10, 1.12, 1.28, 1.27, and 1.10, respectively. According to Figure 2.3a, the majority of the samples indicated the dissolution of dolomite with Ca^{2+}/Mg^{2+} was close to one ($\pm$ 0.2).

In general, a Ca^{2+}/Mg^{2+} molar ratio that is equal to one indicates dissolution of dolomite rocks (Mayo and Loucks, 1995). While Ca^{2+}/Mg^{2+} ratios in the range of 1.5 to 2 represent groundwater has been influenced by both dolomitic and limestone units, a Ca^{2+}/Mg^{2+} ratio > 2.0 signifies a higher influence of limestone in a regarded karst system (Pfleiderer et al., 2006). Dissolved Ca^{2+} and Mg^{2+} are largely supplied by weathering of carbonates in karst regions as examplified by the relatively high HCO_3^- concentration. Typically, the dissolution of dolomite should release equal amounts of $Ca^{2+} + Mg^{2+}$ and HCO_3^-. Therefore, the equivalent charge ratio of $Ca^{2+} + Mg^{2+}$ and HCO_3^- (close to 1:1 line) confirms the impact of dolomite dissolution. Figure 2.3b clearly revealed that almost all samples were plotted along the 1:1 line, which can suggest that calcium and magnesium were originated from dissolution of dolomite in this area. Significant positive correlation also exists between $[HCO_3^- + SO_4^{2-}]$ and $[Ca^{2+} + Mg^{2+}]$ in the spring and well samples, with the average $Ca^{2+} + Mg^{2+}/HCO_3^- + SO_4^{2-}$ ratios of 1.02 (Forster well), 1.07 (Glashütten), 1.04 (Hieslwirt), 1.04 (Kerschbaum), 1.04 (Hinterlug) and 1.05 (Mitterlug) (Figure 2.3c). The correlation between SO_4^{2-} and Ca^{2+}/Mg^{2+} was not significant (Figure 2.3d).

2.3.2.2 Classification the geochemical distribution of sampling points

In this study, cluster analysis was used to classify the groundwater samples collected from the sampling points into groups with similar groundwater quality properties. Three groups were selected based on cluster analysis results, each having different groundwater hydrochemical concentrations as the class centroids (Table 2.2). Class 1 includes 100 % of groundwater samples from the Mitterlug spring, and 76 % and 4 % of groundwater samples from the Hieslwirt and Glashütten springs, respectively. They represent groundwater types with lower concentrations of Ca^{2+}, Mg^{2+}, Na^+, Cl^-, and HCO_3^- (Table 2.2) as compared to groundwater samples from other sampling points. Class 2 includes 95 % of groundwater samples from Glashütten spring, and also 24 %, 13 % and 10 % of groundwater samples from the Hieslwirt, Hinterlug, and Kerschbaum spring, respectively. Apart from sulphate, the concentrations of the main hydrochemical parameters show slightly increased values in this class as compared to class 1. In class 3, 90 % of groundwater samples from the Kerschbaum spring, 87 % of samples from the Hinterlug spring and all samples from the Forster well show higher concentrations of Ca^{2+}, Mg^{2+}, Na^+, Cl^-, and HCO_3^- as compared to class 1 and 2. Therefore, concentrations of major ions follow the order: class 1 < class 2 < class 3 (Table 2.2).

The results of Kruskal-Wallis test (Table 2.3) showed significant differences (p value ≤ 0.05) between the springs that were classified as a class one (Mitterlug and Hieslwirt springs) and class three (and Kerschbaumer, Hinterlug springs and Forster well) considering Ca^{2+} concentrations. However, groundwater samples belonging to Mitterlug and Hieslwirt springs (Class one) did not show significant differences (p value = 0.125). Significant differences were also observed between Ca^{2+} concentrations in Glashütten spring (class two) and other sampling points, except Hieslwirt

spring. Hieslwirt and Glashütten are almost significantly different (p value = 0.051), explaining the results of the cluster analysis where 95 % of the Glashütten samples and 24 % of the Hieslwirt samples were jointly classified in class 2.

Table 2.2: Mean parameter values of the three principal water groups.

Class	Groundwater samples percentage	Class centroids (mg/L)					
		Ca^{2+}	Mg^{2+}	Na^+	HCO_3^-	Cl^-	SO_4^{2-}
C1	100 % Mitterlug + 76 % Hieslwirt + 4 % Glashütten	44.26	23.88	1.12	223.91	1.48	6.05
C2	95% Glashütten + 24 % Hieslwirt + 13 % Hinterlug + 10 % Kerschbaum	48.54	25.85	1.38	258.46	1.49	5.81
C3	90 % Kerschbaumer + 87 % Hinterlug + 100 % Forster well + 1 % Glashütten	56.42	26.86	3.08	288.06	3.06	7.49

Considering the Kruskal-Wallis test results for Mg^{2+} and HCO_3^- in Table 2.3, groundwater samples that were classified as class one (Mitterlug and Hieslwirt springs), class two (Glashütten + 24 % Hieslwirt) and class three (Kerschbaumer, Hinterlug springs and Forster well) showed significant differences (p value $\leq$ 0.05). However, significant differences were not observed between sampling points (Kerschbaumer, Hinterlug springs and Forster well) in class three (p value $>$ 0.05). Moreover, Hieslwirt and Mitterlug (class one) showed a p-value slightly smaller that 0.05 (p value = 0.047 and 0.042 regard to HCO_3^- and Mg^{2+}, respectively).

The same patterns in Kruskal-Wallis test were also observed for SO_4^{2-} (Table 2.3): Springs from class one (Table 2.2) showed significance differences (p value $\leq$ 0.05) with the springs and well in class two and three. Also considering SO_4^{2-}, Hieslwirt and Mitterlug (class one) with a p-value equal to 0.241 and Kerschbaum and Hinterlug (class three) with a p-value equal to 0.08 did not show a significant difference.

2.3.2.3 Temporal variations of spring and well water chemistry

The long-temporal extension of the hydrochemical time series provides a unique opportunity to study the processes and factors controlling groundwater chemistry in the study area. In this regard, trend analysis is applied to quantify the temporal variations of water chemistry over a defined interval.

The temporal evolution of EC (at 25 °C) showed a decreasing trend (p-value $<$ 0.05 and negative Sen's slope) over almost 40 years of monitoring (from 1977 to 2017) at all monitoring points, except of Mitterlug spring and Forster well (Figure 2.4a and Table 2.4). The water samples from the Mitterlug spring did not show any significant variation (p value = 0.14). In contrast, EC in the Forster well showed a different temporal pattern characterized by a slight increase (p-value $<$ 0.05 and positive Sen's slope) starting in 2004.

The Ca^{2+} time series clearly indicated an increasing trend (p-value $<$ 0.05 and positive Sen's slope) in the springs from 1989 to 2017 (Figure 2.4b and Table 2.4), which can indicate enhanced dissolution processes of Ca^{2+} minerals in the studied karst system. However, Ca^{2+} concentrations in the Forster well did not show any significant trend (p value = 0.123) between 2004 and 2017.

Ca^{2+} concentrations were consistently lower in Mitterlug, Hieslwirt and Glashütten than in Kerschbaum and Hinterlug during the entire monitoring period, similar to the observed patterns of EC.

Table 2.3: Result of Kruskal-Wallis test to check the statistical significance of the cluster analysis. Bold numbers indicate significant differences (p value $\leq$ 0.05).

	Ca^{2+} | Hieslwirt	Ca^{2+} | Kerschbaum	Ca^{2+} | Glashütten	Ca^{2+} | Hinterlug	Ca^{2+} | Mitterlug	Ca^{2+} | Forster
Ca^{2+} | Hieslwirt	1	**< 0.0001**	0.051	**< 0.0001**	0.125	**< 0.0001**
Ca^{2+} | Kerschbaum	**< 0.0001**	1	**< 0.0001**	0.238	**< 0.0001**	**< 0.0001**
Ca^2 | Glashütten	0.051	**< 0.0001**	1	**< 0.0001**	**0.000**	**0.000**
Ca^2 | Hinterlug	**< 0.0001**	0.238	**< 0.0001**	1	**< 0.0001**	**< 0.0001**
Ca^{2-} | Mitterlug	0.125	**< 0.0001**	**0.000**	**< 0.0001**	1	**< 0.0001**
Ca^{2-} | Forster	**< 0.0001**	**< 0.0001**	**0.000**	**< 0.0001**	**< 0.0001**	1

	Mg^{2+} | Hieslwirt	Mg^{2+} | Kerschbaum	Mg^{2+} | Glashütten	Mg^{2+} | Hinterlug	Mg^{2+} | Mitterlug	Mg^{2+} | Forster
Mg^{2+} | Hieslwirt	1	**< 0.0001**	**< 0.0001**	**< 0.0001**	0.042	**< 0.0001**
Mg^{2+} | Kerschbaum	**< 0.0001**	1	**0.000**	0.842	**< 0.0001**	0.099
Mg^{2+} | Glashütten	**< 0.0001**	**0.000**	1	**0.001**	**< 0.0001**	**< 0.0001**
Mg^{2+} | Hinterlug	**< 0.0001**	0.842	**0.001**	1	**< 0.0001**	0.078
Mg^{2+} | Mitterlug	0.042	**< 0.0001**	**< 0.0001**	**< 0.0001**	1	**< 0.0001**
Mg^{2+} | Forster	**< 0.0001**	0.099	**< 0.0001**	0.078	**< 0.0001**	1

	HCO_3^- | Hieslwirt	HCO_3^- | Kerschbaum	HCO_3^- | Glashütten	HCO_3^- | Hinterlug	HCO_3^- | Mitterlug	HCO_3^- | Forster
HCO_3^- | Hieslwirt	1	**< 0.0001**	**0.003**	**< 0.0001**	0.047	**< 0.0001**
HCO_3^- | Kerschbaum	**< 0.0001**	1	**< 0.0001**	0.180	**< 0.0001**	0.215
HCO_3^- | Glashütten	**0.003**	**< 0.0001**	1	**< 0.0001**	**< 0.0001**	**< 0.0001**
HCO_3^- | Hinterlug	**< 0.0001**	0.180	**< 0.0001**	1	**< 0.0001**	0.869
HCO_3^- | Mitterlug	0.047	**< 0.0001**	**< 0.0001**	**< 0.0001**	1	**< 0.0001**
HCO_3^- | Forster	**< 0.0001**	0.215	**< 0.0001**	0.869	**< 0.0001**	1

	Cl^- | Hieslwirt	Cl^- | Kerschbaum	Cl^- | Glashütten	Cl^- | Hinterlug	Cl^- | Mitterlug	Cl^- | Forster
Cl^- | Hieslwirt	1	**< 0.0001**	0.249	0.075	0.395	0.412
Cl^- | Kerschbaum	**< 0.0001**	1	**< 0.0001**	**< 0.0001**	**< 0.0001**	**< 0.0001**
Cl^- | Glashütten	0.249	**< 0.0001**	1	0.531	0.040	0.055
Cl^- | Hinterlug	0.075	**< 0.0001**	0.531	1	0.007	0.012
Cl^- | Mitterlug	0.395	**< 0.0001**	0.040	0.007	1	0.970
Cl^- | Forster	0.412	**< 0.0001**	0.055	0.012	0.970	1

	SO_4^{2-} | Hieslwirt	SO_4^{2-} | Kerschbaum	SO_4^{2-} | Glashütten	SO_4^{2-} | Hinterlug	SO_4^{2-} | Mitterlug	SO_4^{2-} | Forster
SO_4^2 | Hieslwirt	1	**< 0.0001**	**0.000**	**< 0.0001**	0.241	**< 0.0001**
SO_4^{2-} | Kerschbaum	**< 0.0001**	1	**< 0.0001**	0.080	**< 0.0001**	**< 0.0001**
SO_4^{2-} | Glashütten	**0.000**	**< 0.0001**	1	**< 0.0001**	**< 0.0001**	0.038
SO_4^{2-} | Hinterlug	**< 0.0001**	0.080	**< 0.0001**	1	**0.000**	**< 0.0001**
SO_4^{2-} | Mitterlug	0.241	**< 0.0001**	**< 0.0001**	**0.000**	1	**< 0.0001**
SO_4^{2-} | Forster	**< 0.0001**	**< 0.0001**	0.038	**< 0.0001**	**< 0.0001**	1

The Mg^{2+} time series showed different trend patterns for different sampling points. No trend (p-value $\geq$ 0.05) was detected in Hieslwirt, Hinterlug springs (from 1989 to 2017) and Forster well (from 2004 to 2017). While, Mitterlug, Glashütten, and Kerschbaum springs showed decreasing trends (p-value < 0.05 and negative Sen's slope) of Mg^{2+} concentrations over 28 years (Figure 2.4c and Table 2.4).

The SO_4^{2-} time series showed decreasing trends (p-value < 0.05 and negative Sen's slope) in Mitterlug, Hieslwirt, and Kerschbaum springs from 1991 and in the Forster well from 2004 to 2017. Glashütten and Hinterlug springs did not display any significant trend (p-value $\geq$ 0.05) of SO_4^{2-} concentrations in 26 years of water monitoring (Figure 2.4d and Table 2.4). Similar to the patterns observed for EC, Ca^{2+}, and Mg^{2+}, the most pronounced SO_4^{2-} trends were observed in Hinterlug and Kerschbaum. While, the lowest SO_4^{2-} concentrations trend was observed in Forster well.
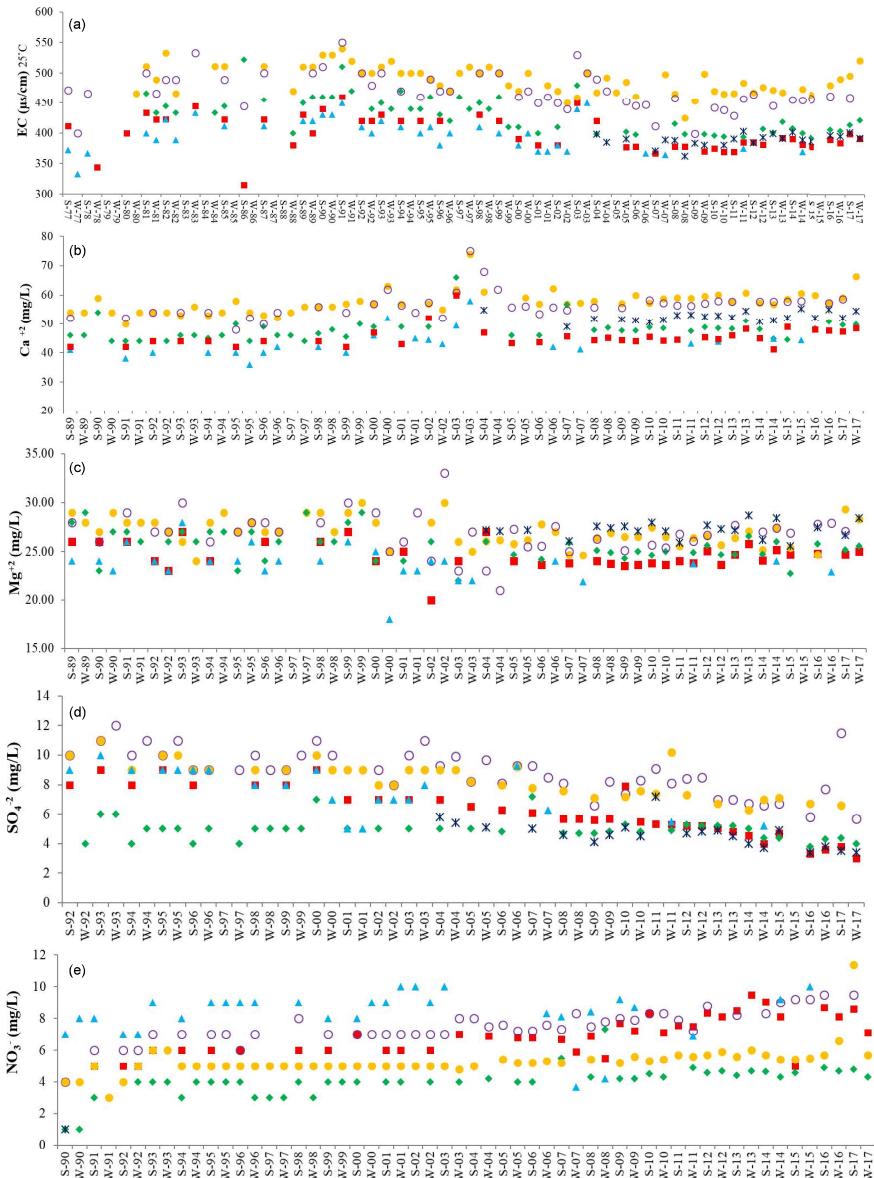
Figure 2.4: Temporal trend of groundwater physico-chemical parameters

NO_3^- concentrations are available for more than 27 years (from 1990 to 2017); however, the application of Pettitt's test (Pettitt, 1979) revealed a significant change (p value < 0.0001, $\alpha = 0.05$) in the time series in Kerschbaum, Hinterlug, Glas-hütten, and Hieslwirt springs in 2004, 1998, 2000, and 1995, respectively. To overcome the influence of these break points on time series analysis, the Mann-Kendall test was performed for nitrate concentrations in the period from 2004 to 2017. An increasing trend (p-value < 0.05 and positive Sen's slope) was observed at all sampling points (Figure 2.4e and Table 2.4).

In contrast to EC, Ca^{2+}, Mg^{2+}, and SO_4^{2-}, the highest concentrations of NO_3^- were observed in Mitterlug, Hieslwirt, and Hinterlug, while the lowest concentration patterns of NO_3^- were observed in Glashütten and the Forster well. The increasing trend of NO_3^- concentrations in all sampling stations has raised concerns about the possible source of nitrate in Waidhofen.

In the presented study, the stable isotope values of $\delta^{15}N$ and $\delta^{18}O$ were applied to identify nitrate sources in the study area, since nitrate sources can show different isotopic "fingerprints" of nitrogen (15N/14N) and oxygen (18O/16O) isotope ratios. Hence, the determination of $\delta^{15}N-NO_3^-$ and $\delta^{18}O-NO_3^-$ in water samples can provide meaningful insights for the identification of nitrate sources in the study area (Matiatos, 2016). According to Einsiedl et al. (2005), the values of $\delta^{15}N$ and $\delta^{18}O$ in the nitrate species are strongly different depending on the respective nitrate source.

Table 2.4: Results of Mann-Kendall test in the springs and pumping well.

		Mitterlug	Hieslwirt	Glashütten	Hinterlug	Kerschbaum	Forster well
EC	Kendall's tau	-0.172	-0.290	-0.477	-0.318	-0.367	0.315
	P-value	0.140	< 0.0001	< 0.0001	0.001	< 0.0001	0.039
	Sen's slope	-0.307	-0.529	-0.857	-0.556	-0.569	0.522
	Trend	No trend	Decreasing	Decreasing	Decreasing	Decreasing	slightly increasing
Ca^{2+}	Kendall's tau	0.429	0.425	0.305	0.447	0.507	0.249
	P-value	0	< 0.0001	0.003	< 0.0001	< 0.0001	0.123
	Sen's slope	0.003	0.073	0.066	0.105	0.115	0.119
	trend	Increasing	Increasing	Increasing	Increasing	Increasing	No trend
Mg^{2+}	Kendall's tau	-0.292	-0.048	-0.278	-0.025	-0.257	0.097
	P-value	0.048	0.252	0.000	0.731	< 0.0001	0.564
	Sen's slope	-0.011	0.000	-0.011	0.000	-0.033	0.012
	trend	Slightly decreasing	No trend	Decreasing	No trend	Decreasing	No trend
SO_4^{2-}	Kendall's tau	-0.542	-0.886	-0.170	-0.565	-0.682	-0.574
	P-value	0.001	< 0.0001	0.148	< 0.0001	< 0.0001	< 0.0001
	Sen's slope	-0.100	-0.105	0.004	-0.078	-0.070	-0.071
	trend	Decreasing	Decreasing	No trend	No trend	Decreasing	Decreasing
NO_3^-	Kendall's tau	0.219	0.626	0.689	0.764	0.644	0.566
	P-value	0.019	< 0.0001	< 0.0001	< 0.0001	< 0.0001	< 0.0001
	Sen's slope	0.008	0.064	0.024	0.056	0.018	0.005
	trend	Increasing	Increasing	Increasing	Increasing	Increasing	Increasing

The $\delta^{15}N-NO_3^-$ ranged from a maximum value of 7.7 ‰ in Hieslwirt (September 2017) to a minimum value of -0.7‰ in Hinterlug (September 2018). $\delta^{18}O-NO_3^-$ also varied from a maximum of 4.8 ‰ in Mitterlug (May 2018) to a minimum value of -3.1‰ in Hieslwirt (May 2018) (Table 2.1). The combined determination of $\delta^{15}N$ and $\delta^{18}O$ values (Figure 2.5) distinguished two major nitrate sources in Waidhofen. In Mitterlug, Hieslwirt, and Hinterlug springs with slightly

lower δ^{15}N–NO$_3^-$, it can be reasoned the nitrate was produced from nitrification in forest soils (Figure 2.5). While, in Kerschbaum and Glashütten springs nitrate originated from nitrification process in mineral soils.
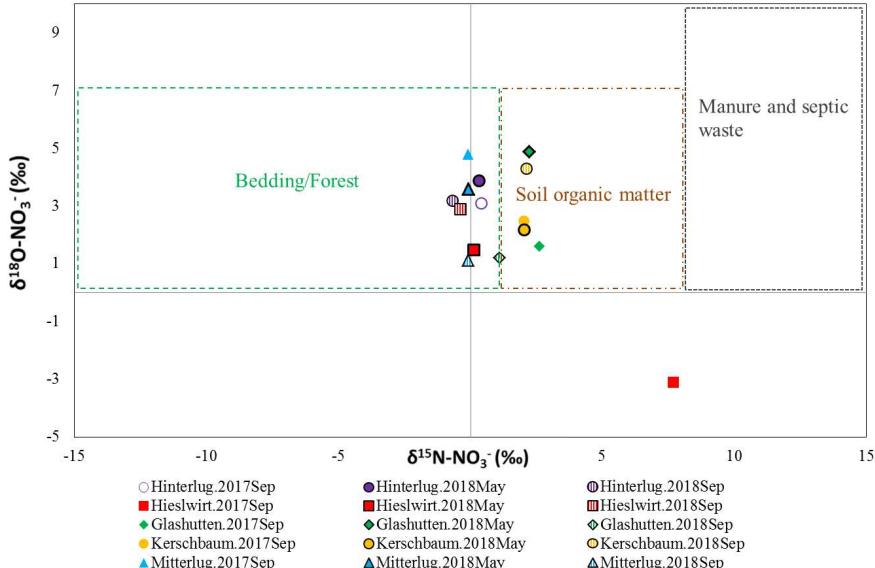
Figure 2.5: Schematic diagram of the isotopic composition of groundwater nitrate from various sources and nitrogen and oxygen isotope composition of karst groundwater.

2.4 Discussion

2.4.1 Spatial and temporal variations in carbonate dissolution

The waters in most of the karst area have been found to primarily contain calcium and bicarbonate ions, along with different quantities of magnesium ions, deriving from dissolution of dolomite or limestone as weathering reactions in carbonate rocks (Krawczyk and Ford, 2006). In Waidhofen, the Ca^{2+}-Mg^{2+}-HCO_3^- groundwater type in all sampling stations (Figure 2), along with almost equal Ca^{2+} and Mg^{2+} concentrations and low Na^+, K^+, and Cl^- content indicated that the hydrofacies correlate directly with the presence of dolomite as the dominant lithofacies in the study area. Dolomite weathering causes the higher concentrations of Mg^{2+} and HCO_3^- compared to SO_4^{2-}, Na^+, Cl^- in groundwater (Szramek et al., 2007). According to the Piper diagram (Figure 2.2) groundwater was found to be dominated by Ca^{2+}, Mg^{2+}, and HCO_3^-, and was characterized as a Ca^{2+}-Mg^{2+}-HCO_3^- (alkaline-earths-carbonatic) type, in all the sampling points. In the present

study, EC, temperature, and major ions were used as indirect indicators to characterize the karst system, because they reflect karstification and mineralization processes and show variation in response to different residence times and rainfall events in the study area (Mudarra and Andreo, 2011). According to Hilberg and Schneider (2011), mean EC in limestone or dolomitic aquifers should range between 300 and 350 µS/cm, while a higher total mineralization due to the participation of other components, such as gypsum or halite, indicates an influence of evaporitic units and cause higher EC values (Andreo et al., 2016).

Three conditions should be checked to identify a pure dolomite aquifer (Hilberg and Schneider, 2011); i) the concentrations of sulphate, sodium and chloride should not make up a majority of the groundwater composition, ii) the Ca^{2+}/Mg^{2+}-ratio should be close to 1 ($\pm$ 0.2) with a solution saturated in terms of calcite and dolomite and iii) the total amount of dissolved solids, expressed in terms of EC, should vary in the range from 300 to 350 µS/cm.

The presented results satisfy the first condition as very low Na^+, Cl^- and $SO_4{}^{2-}$ concentrations were observed (maximum concentrations are 11.4, 23.9, and 24.0 mg/L, respectively), indicating that the area is not affected by evaporitic deposits. Moreover, $Ca^{2+} + Mg^{2+}/HCO_3^- + SO_4{}^{2-}$ ratios equal to one and $(Ca^{2+} + Mg^{2+})/HCO_3^-$ molar ratio higher than one, along with the absence of a positive relation between $SO_4{}^{2-}$ and Ca^{2+}/Mg^{2+} ratio (Figure 2.3d) showed that the springs and the well are not influenced by high sulfate concentrations in this region.

The second condition was satisfied for the dataset because 64 % of the water samples showed Ca^{2+}/Mg^{2+} ratios $\leq$ 1.2 (section 2.3.2.1). The carbonatic nature of the aquifer system and the superordinate control of the dolomitic basement rock in the catchment area were reflected in the calcium to magnesium ratio (Figure 2.3a).

With respect to the third condition, variations of EC were classified in two groups (Figure 2.2c). The first group included the Mitterlug, Hieslwirt, and Glas-hütten spring and the Forster well with EC $\leq$ 400 µS/cm, considered as typical EC values for karst systems. The second group showed EC values > 400 µS/cm (up to 570 µS/cm) in Kerschbaum and Hinterlug springs. Higher EC values in these two springs could not be related with the dissolution of gypsum, because the results from the descriptive analysis (Table 2.1) and the ionic ratios (Figure 2.3c and d) did not indicate high values of $SO_4{}^{2-}$ in any sampling stations. Therefore, the reasons for such anomalously high values in EC are still a matter of research.

Besides the spatial differences in EC values between Kerschbaum and Hinterlug springs and other springs (Mitterlug, Hieslwirt, and Glashütten), the ionic ratios' plots (($Ca^{2+} + Mg^{2+}$) and ($Ca^{2+} + Mg^{2+}/HCO_3^- + SO_4{}^{2-}$)) (Figure 2.3) showed clear shifts from the low ionic ratios in Mitterlug spring to higher ionic ratios in Kerschbaum and Hinterlug springs, and Forster well, depicting different levels of water mineralization in a small-scale karst system. As shown in Figure 2.1, the Hinterlug spring is separated from the four others by a fault striking between the Mitterlug and Hinterlug springs (Bittner et al., 2018a). This may explain the identified spatial variability of the investigated hydrochemical parameters between Hinterlug and the other sampling points, in particular Mitterlug, Hieslwirt, and Glashütten. However, Kerschbaum, Mitterlug, Hieslwirt and Glashütten springs rise from the same mountain massif and therefore, the spatial variations in geo-

chemical compositions can be related to the residence time within the carbonate aquifer systems. Moreover, another possible explanation for this spatial variability is different water mineralization kinetics (Hartmann et al., 2014a) due to the differences in water temperature. Since the sampling points are located between a maximum elevation of around 500 m a.s.l (Mitterlug) and a minimum elevation of around 419 m a.s.l (Hieslwirt), the different residence times and the variations of the hydrochemical compositions within the less than 80 m of elevation difference points towards a high degree of spatial variability even in a small-scale karst system.
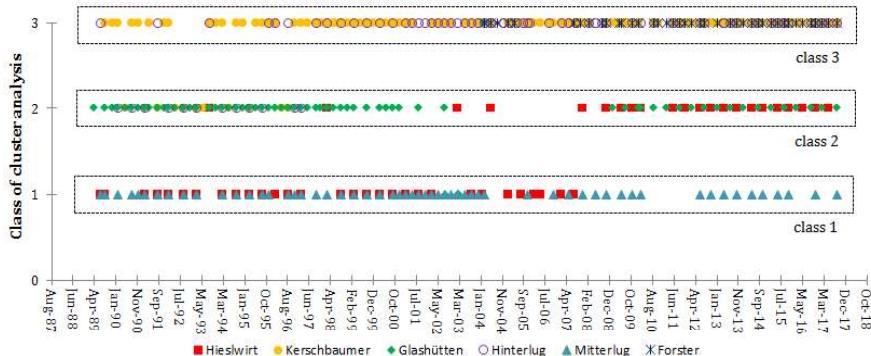
Figure 2.6: Classification of sampling point based on spatial and temporal variations.

Spatial and temporal variations of hydrochemical parameters obtained from the sampling points were also detected by plotting the results of the cluster analysis over time (from 1989 to 2017) (Figure 2.6). These findings further highlight the changing patterns in Ca^{2+}, Mg^{2+}, Na^+, Cl^-, and HCO_3^- concentrations in the Hieslwirt spring, from class one (low ionic concentrations) to class two (medium ionic concentrations) between 2004 to 2006 (Figure 2.6). This time period fits well with the beginning of water extraction from the Forster well, however, a detailed study is required to investigate this possible relationship and to justify the increase of Ca^{2+}, Mg^{2+}, Na^+, Cl^-, and HCO_3^- in the Hieslwirt spring since 2008. Moreover, Hinterlug, Kerschbaum, and the Foster well were classified as class three (high ionic concentrations), and did not show temporal variations, except between years 1990 to 1995. It is also important to note that, some mixing could be observed with class two. As discussed earlier, Hinterlug spring is tectonically separated from the other springs. However, the cluster analysis findings and ionic ratios revealed similar patterns of major ions between Hinterlug and Kerschbaum springs and Forster well. Since Forster well is filtered between -50 m and -100 m in the deep dolomitic bedrock, these correlations can be indicative that these two springs are fed by a deep karstified aquifer system. Therefore, the Schnabelberg mountain (where Hinterlug spring crops out), possibly has a similar deep aquifer system that feeds Hinterlug spring. However, detailed investigations should be conducted to understand these spatial variations between Hinterlug, Kerschbaum and other springs, which is a matter of our following

research activities.

2.4.2   Anthropogenic inputs to the groundwater system

Increasing nitrate trends in all sampling points during 27 years of groundwater monitoring have raised the concern about possible sources of nitrate in Waidhofen, where 78 % of the catchment area is covered by forests. According to Di Lorenzo et al. (2012), in natural grassland in temperate regions, the baseline concentrations of nitrate are typically below 2 mg/L. In the present study, all five observed springs drain a catchment that is predominantly covered by forests, with nitrate concentrations ranging from a minimum of 1 mg/L in Glashütten in 1990 to more than 11 mg/L in the Kerschbaum spring in 2017. Generally, additional information of possible nitrate sources can be obtained using dual isotope analysis of δ^{15}N–NO$_3^-$ and δ^{18}O–NO$_3^-$ (Albertin et al., 2012). This is done to overcome the problem of overlapping source signatures. In Mitterlug and Hinterlug springs with the average nitrate values of 8.7 and 7.5 mg/L, respectively, δ^{15}N–NO$_3^-$ showed values less than 2 ‰ and δ^{18}O–NO$_3^-$ showed values less than 4.8 ‰indicating nitrification processes in forest and grassland soil to be the primary source of nitrate in these two springs (Einsiedl and Mayer, 2006) (Figure 2.5). The same nitrate sources were identified for the Hieslwirt spring samples collected in May and September 2018, with δ^{15}N–NO$_3^-$ around 0.1 ‰ and - 0.4 ‰ and δ^{18}O–NO$_3^-$ around 1.5 ‰ and 2.9 ‰, respectively. Generally, the nitrification in the forest bedding produce nitrates that are significantly depleted in δ^{15}N–NO$_3^-$, compared to soil organic nitrogen (Spoelstra et al., 2007). The Hieslwirt samples collected in September 2017 show a higher δ^{15}N–NO$_3^-$ value of 7.7 ‰, which points towards manure and septic waste as a possible source of nitrate in this spring. However, since this value does not follow the same pattern as the other samples taken at this spring, we carefully considered this data point as an outlier. The average value of δ^{15}N–NO$_3^-$ in the collected samples from the Kerschbaum and Glashütten springs (average nitrate values of 5.2 and 3.8 mg/L, respectively) is above 2 ‰, indicating nitrate was derived from mineral soil. Our findings revealed higher concentrations and an increasing trend of nitrate derived from forest soil (Mitterlug, Hinterlug, and Hieslwirt springs) compared with nitrate concentrations derived from mineral soil in Kerschbaum and Glashütten springs. Moreover, the isotope results did not provide evidence of an impact of chemical fertilizers and manure, since δ^{15}N–NO$_3^-$ values of chemical fertilizers should vary between -8.0 ‰and +6.2 ‰. δ^{15}N–NO$_3^-$ values of manure should range from +10.0 ‰ and +20.9 ‰ for composted manure and from +8 ‰ and 16 ‰ (poultry manure) (Wassenaar, 1995). Therefore, in Waidhofen, δ^{15}N–NO$_3^-$ and δ^{18}O–NO$_3^-$ data conclusively indicate that nitrification process related to the soil organic matter is the primary source of nitrate in this forested area. By considering the Hieslwirt sample collected in September 2017 as an outlier, there is not any significant evidence of fertilizer applications, septic swages or manure as primary sources of nitrate in the study area. However, the reason for increasing trends of nitrate in this area remains a question which requires more frequent sampling of isotopic composition of groundwater nitrate in this karst system.

2.4.3   Conceptual model

Based on the results of our hydrogeochemical analysis of all time series, it is possible to infer a conceptual model of the aquifer system of the Glashüttenberg massif. Since the Hinterlug spring is the only spring originating from the Schnabelberg massif, it is not possible to create a comprehensive conceptual model of the entire mountain massif due to a lack of data.

As highlighted by the ionic ratios (Figure 2.3), the Kerschbaum spring shows a higher degree of mineralization as compared to the Mitterlug, Glashütten and Hieslwirt spring. Given that the degree of mineralization is comparable to the samples analyzed from the Forster well, which is filtered in the deep aquifer system, we can conclude that the Kerschbaum spring is partly fed by the deep aquifer system of the Glashüttenberg massif. The fact that the highest mean concentrations of Cl^- was obtained from the Kerschbaum spring also highlight a strong influence of the deep saturated parts of the aquifer system. Further, this conceptual model finds a physical explanation if we observe that the Kerschbaum spring can be fed by the saturated part of the subsurface groundwater basin as it is in the proximity of the syncline striking through the Glashüttenberg massif (Figure 2.1). These conclusions are also reflected by the results of the cluster analysis (Figure 2.6). The more variable and generally higher temperatures (Figure 2.2c) measured in the Kerschbaum spring as compared to the Forster well indicate the influence of the unsaturated zone on the total spring discharge. The high range of measured NO_3^- concentrations in the Kerschbaum spring, considered as an indicator for the contribution of the unsaturated zone to spring discharge, can also be related to the existence of preferential flow paths in the unsaturated zone of the Kerschbaum recharge area delivering infiltrated water directly to the spring. Summarizing, the Kerschbaum spring is affected by a rather constant supply of water coming from the saturated zone of the deep aquifer system and by preferential flow paths (e.g. conduits) through the unsaturated zone, highlighting a well-connected and karstified aquifer system in the southern to the central parts of the Glashüttenberg massif.

The analysis of the ionic ratios indicates also a transition of the degree of mineralization from the Glashütten to the Hieslwirt spring. Geographically, the closer the spring is located to the outcrop of the Opponitz and Lunz layers (both impermeable, see Figure 2.1c), the lesser the degree of mineralization. This relation is also reflected by the EC values obtained from the Glashütten and the Hieslwirt spring, with a lower mean EC in Hieslwirt (401.1 µS/cm) as compared to Glashütten (433.0 µS/cm). These results are indicative of the impact of the saturated zone of the deep aquifer system on spring discharge. This system is hosted in the syncline of the Glashüttenberg massif and its contribution to spring discharge decreases the closer a spring is located to the pinch-out of the dolomite reservoir and the outcrop of the impermeable Lunz layer. On the contrary, the Glashütten and the Hieslwirt spring differ from each other in NO_3^- concentrations in the period from 1990 to 2017. Considering that the land use in this part of the study area is rather homogeneous (beech forests), we argue that the impact of the unsaturated zone on the spring discharge is higher in the Hieslwirt than in the Glashüttenberg. This conclusion is further supported by the lower mean temperatures measured in the Hieslwirt spring as compared to the Glashütten spring, pointing towards a stronger influence of infiltration paths located in higher parts of the catchment

and less mixing with water from the saturated zone (also given the proximity to the pinch-out of the dolomite aquifer).

The described relations also explain why, most of the time, the cluster analysis shows that the Hieslwirt and the Mitterlug spring fall within one cluster (Figure 2.6). The Mitterlug spring is located at the highest elevation of all springs originating from the Glashüttenberg massif and consequently is least affected by the saturated zone of the deep karst system. This conclusion is based on the results from the hydrochemical analysis, where the Mitterlug spring has lowest mean values related to EC, Ca^{2+} and HCO_3^-, as well as by the low degree of mineralization (Figure 2.3). Moreover, the low temperatures measured in the Mitterlug spring also point towards a primary impact of infiltration and preferential flow paths located in the unsaturated zone of the higher parts of the Glashüttenberg massif. This dominant impact of the unsaturated zone on the Mitterlug spring discharge is further highlighted by the fact that the Mitterlug spring has the highest concentrations of NO_3^- as compared to all other springs.

In conclusion, the results of our analysis show that the influence of the saturated zone of the aquifer system in the central to northern parts of the Glashütten-berg massif is strongly affected by the proximity to the outcrop of the impermeable Opponitz and Lunz layers. Although the Glashütten and the Hieslwirt are close to each other, the identified differences in contributions from different parts of the aquifer system between both springs highlight a high degree of subsurface heterogeneity in the dolomitic basement rock in this part of the Glashüttenberg massif.

2.5 Conclusion

The present study gives indications to the origin of spring waters by consideration of dolomite karst hydrochemistry in Waidhofen a.d. Ybbs. Hydrochemical analysis revealed similar groundwater types (Ca^{2+}-Mg^{2+}-HCO_3^-) as a result of dolomite dissolution for all sampling points. However, the results of ionic ratios and cluster analysis indicated statistically significant spatial geochemical variations between the sampling points. In this regard, Mitterlug and Hieslwirt springs (class one), Glashütten (class two) and Kerschbaum and Hinterlug spring and Forster well (class 3) are classified based on the increasing concentrations of major ions (Ca^{2+}, Mg^{2+}, Na^+, HCO_3^-, Cl^-, and SO_4^{2-}). Moreover, long-term groundwater observations showed that Hieslwirt's hydrochemistry shifted from low ionic concentrations (class one) to medium ionic concentrations (class two). Generally, the finding of this study suggests that the dissolution of dolomite as a natural process controls the groundwater chemistry in the aquifer system of Waidhofen. Spatial and temporal variations in geochemical concentrations and EC between the sampling points are considered as an effect of different residence times and water mineralization in the dolomite aquifer system. Based on the hydrochemical and cluster analysis, we were able to develop a conceptual model of the Glashüttenberg massif, highlighting that also dolomite-dominated karst systems can exhibit a high spatio-temporal variability even on a small spatial scale mainly due to the heterogeneous response of the unsaturated zone. Increasing nitrate trends raised concerns about the impact of human activities on the karst system, however $\delta^{15}N$–NO_3^- and $\delta^{18}O$–NO_3^- data revealed the nitrification

processes in forest floor and mineral soil matters as the main source of nitrate in the study area. The increasing nitrate concentrations and the heterogeneity in the geochemical and hydrological (Bittner et al., 2018a) behavior of the system encouraged the local water authorities to strengthen the monitoring program and carefully monitor potential nitrate sources to sustainably protect the groundwater quality of the karst system. The conclusion that we can derive by the interpretation of the results specific for the study area under investigation have a broader impact. In fact, the general assumption that dolomite karst systems can be considered (approximately) homogenous units cannot be confirmed by our dataset. On the contrary, our study has shown that dolomite karst aquifers display a significant degree of spatio-temporal, hydrochemical variability which on the one hand highlights the importance of a tailored monitoring strategy to safely manage the water resources and on the other hand shows the necessity for further studies on dolomite karst system as they represent frequently used aquifer systems for water supply.

Chapter 3

Development of a lumped karst aquifer model for land use change impact studies - LuKARS

Bittner et al. (2018a)[1]

Abstract

Hydrological models represent valuable tools to investigate the impacts of land use changes on water resources. Most commonly, distributed, physically-based models are applied for land use change impact studies in hydrology. However, providing a physically-based and detailed description of subsurface flows in karst systems is challenging. Lumped models, in contrast, are easy to implement and widely used in karst hydrological research, albeit not applicable for land use change impact studies. To overcome these limitations, we developed a new semi-distributed model LuKARS (Land use change modeling in KARSt systems) that lumps the predominant hydrotopes (i.e. distinct landscape units characterized by homogeneous hydrological properties as a result of similar land use and soil types) present in a catchment as independent, non-linear units. Flows from each hydrotope represent a specific response of the vadose zone (soil-epikart-infiltration zone) in a defined recharge area. The saturated zone consists of a single linear storage unit recharged by each hydrotope independently. The main goal of this approach was to investigate land use change impacts in a dolomite karst system exploited for the water supply of the city of Waidhofen a.d. Ybbs (Austria) by changing the area covered by each hydrotope. Here, land use changes occured in the form of increasing spaces used for dolomite mining and at the expense of existing forest sites. With our parametrized model, we were able to reproduce the measured discharge in the largest spring of the Waidhofen karst system (Kerschbaum spring). Moreover, we succeeded in transferring the parametrized hydrotopes to other recharge areas (Hinterlug and Mitterlug) and validated the trans-

ferability of the modeling approach. Finally, we successfully showed the model's applicability for land use change impacts studies by validating the calibrated model in a period in which the space of the dolomite quarries in the Kerschbaum recharge area almost doubled. The results of our study show that an increase of the dolomite quarries negatively affects the water supply of the city of Waidhofen a.d. Ybbs.

3.1   Introduction

Karst aquifers constitute a major worldwide source of freshwater supply (Delbart et al., 2016; Hosseini et al., 2017), thus, special importance is paid to carbonate rock aquifers in hydrological research and water resource management (Hartmann et al., 2014a; Jin et al., 2015; Chang et al., 2017; Filippini et al., 2018). A detailed knowledge of hydrological processes, i.e. groundwater recharge, storage and discharge, as well as of the land use impacts on water quality and availability are of primary interest for sustainable exploitation of any karst aquifer. Hydrological models therefore serve as important tools to investigate the hydrological functioning of karst systems (Jourde et al., 2015). However, Hartmann et al. (2014a) outlined that land use change impact studies have rarely been conducted explicitly for karst catchment areas and they highlighted the necessity of such studies for sustainable water resource management in karstic areas. Therefore, the aim of this work is to present a new conceptual modeling approach that allows for the simulation of land use change impacts on the drinking water supply from karst aquifers.

"Black-box" models (Labat et al., 1999, 2000; Hu et al., 2008; Jukić and Denić-Jukić, 2008) and lumped conceptual models (Mangin, 1975; Arikan, 1988; Fleury, 2005; Fleury et al., 2007; Tritz et al., 2011; Hartmann et al., 2012a; Chang et al., 2017; Mazzilli et al., 2017) are the most commonly applied modeling approaches in karst hydrological research. However, "black-box" models can only be considered reliable for the conditions specific to their calibration period (Hartmann et al., 2014a) and lumped models assume one single water input time series for the considered system (Scanlon et al., 2002; Hartmann et al., 2012b). These two features make these modeling approaches inappropriate for land use change impact studies (Hartmann et al., 2014a). Distributed, process-based models are often used to assess potential impacts of land use changes on hydrological systems (Chen et al., 2017b). They aim to consider the spatial variability of hydrological parameters as well as the heterogeneous effects of land use and soil properties in a catchment. Although Reimann et al. (2011) and Kordilla et al. (2012) introduced promising modeling approaches for the distributed simulation of hydrological processes in karst aquifers, their application is usually hampered by the high complexity of subsurface systems and a general limitation in data availability (Jukić and Denić-Jukić, 2009; Hartmann et al., 2014a; Ladouche et al., 2014).

To overcome these limitations, we hypothesize that the recharge area of a given karst system can be subdivided into distinct units, defined as hydrotopes (Koeck and Hochbichler, 2012). We define hydrotopes as independent model units described by homogeneous hydrological characteristics, in particular infiltration properties, resulting from similar land use and soil types. Therefore,

we assume homogeneous infiltration properties for a given soil type with the same bedrock due to similar formation conditions of the saprolite, i.e. chemically weathered rock (Williams, 1983). The concept of hydrotopes was successfully applied in former hydrological and ecohydrological studies (Gurtz et al., 1999; Krysanova et al., 2005), however, it was not yet applied in the framework of land use change impact studies in karstic systems. Therefore, our research objectives are i) to create a new semi-distributed modeling approach that lumps the predominant hydrotopes present in a catchment, ii) to calibrate and validate the modeling approach for a reference karst system, iii) to proof our concept by transferring the modeling approach to other karst systems and their related catchments while maintaining the calibrated hydrotope parameters and iv) to investigate land use change impacts by changing the area covered by each hydrotope.

In LuKARS, we apply a non-linear transfer function proposed by Tritz et al. (2011), which is able to simulate the hysteretic behavior of the soil and epikarst storage that results from different water retention potentials during wetting and drying cycles. Different from Tritz et al. (2011), we use that function for the implementation of individual hydrotopes constituting the catchment area of a karst spring. In this way, each hydrotope is characterized by a specific hydrological response, which contributes to the total spring discharge. The saturated zone consists of a single linear storage unit recharged by each hydrotope independently. Thus, the proposed modeling approach benefits from the advantages of lumped models (i.e. the easy implementation and the low computational power) as well as from the characteristics of distributed models (i.e. integration of spatial heterogeneities of soil hydraulic properties). To the best of our knowledge, such a conceptual modeling approach integrating hydrotopes as lumped non-linear storages has not been widely discussed in karst hydrological research (Sarrazin et al., 2018).

The paper is structured as follows. In Section 3.2, we introduce the main characteristics of our investigated karst region in Waidhofen a.d. Ybbs (Austria). In Section 3.3, we present the setup and the governing equations of the hydrotope-based modeling approach. In Section 3.4 and 3.5, we present and discuss the results of the model calibration, model validation as well as the land use change impacts on the hydrological system. Finally, we conclude our investigations in Section 3.6.

3.2   Study area

3.2.1   Catchment description

The study area is located 10 km south of the city of Waidhofen a.d. Ybbs in Lower Austria (Fig. 3.1). This pre-alpine region is part of the eastern foothills of the Northern Calcareous Alps, with altitudes ranging from 415 to 969 m a.s.l. In this warm-moderate regional climate, with an annual mean temperature of 8 °C, mean daily temperatures below freezing occur mainly from December to February. Annual mean precipitation of 1379 mm was recorded at the weather station Hinterlug (Fig. 3.1b) during the period from 1981 to 2014. The annual distribution of precipitation is bimodal with maxima during both the summer (June and July) and winter months (December and January), with snowfall dominating precipitation in the winter (Supplementary material B.1.1).

Two small fluvial systems constitute the study area's drainage: the Waidhofenbach and the Luger-bach. Close to the weather station Hinterlug, the Lugerbach flows into the Waidhofenbach, which drains most of the study area into the Ybbs river in Waidhofen.

The local geology is dominated by a lithologic sequence of dolomitic basement rocks (Main Dolomite, Triassic age, Fig. 3.1a) and thus, typical karst phenomena such as springs, dry valleys and caves are present in the study area. Significant sinkholes are not present in the study area, leading to the conclusion that point-infiltration plays a minor role for recharge. Moreover, prior investigations revealed that a deep karstified groundwater system exists, also below the elevation level of the Waidhofenbach valley (Hacker, 2003). Considering the specific hydrogeological set-ting of the area, we can assume a well-connected network of fractures and conduits. The largest springs originating from those karstificable rocks are exploited for the municipal drinking water supply of Waidhofen a.d. Ybbs.
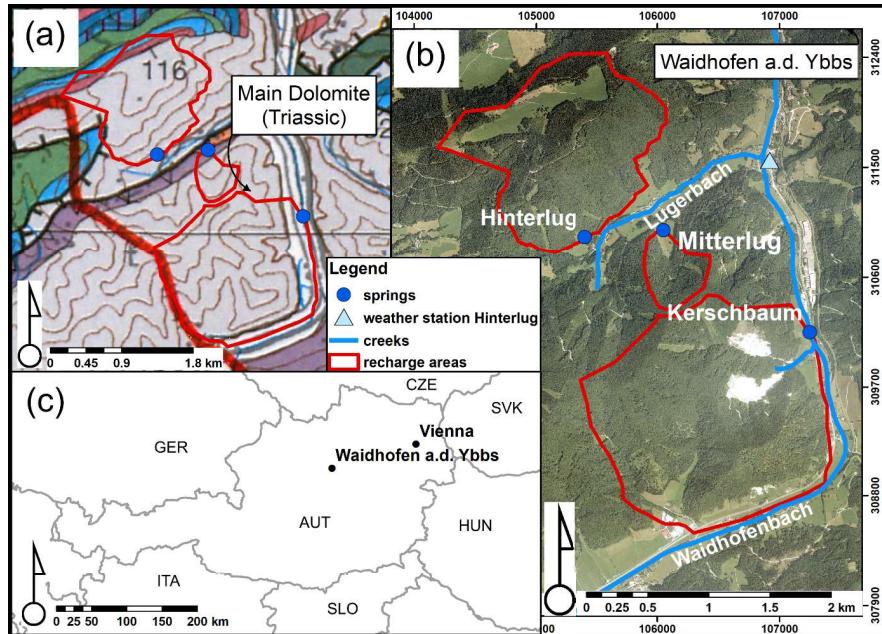
Figure 3.1: Overview of the study area, including (a) the geological map (GBA, 2018), (b) the orthophoto of the whole study area including the location of the three recharge areas with their corresponding karst springs and the draining fluvial systems (Gauss-Krüger coordinate system) and (c) the location of the city Waidhofen a.d. Ybbs in Austria.

In this work, we focus on three distinct springs and their recharge areas, namely the Ker-schbaum (2.5 km^2), Mitterlug (0.25 km^2) and Hinterlug (1.8 km^2) springs (Fig. 3.1b). The de-

lineation of the respective recharge areas was performed based on tracer tests by Hacker (2003). Each of these springs is fed by karst aquifers of the Main Dolomite, where the karst system of the Hinterlug spring is separated tectonically from the two others by a pronounced strike-slip fault that separates the two mountain massifs Schnabelberg (Hinterlug spring in northern part) and Glashüttenberg (Kerschbaum and Mitterlug spring in southern part). Even if the Kerschbaum and Mitterlug springs rise from the same mountain massif, prior investigations for the designation of protection areas revealed that the feeding karst aquifers can be considered independent (Hacker, 2003).

3.2.2 Hydrotopes

In the following, we shortly describe the hydrotopes that are dominant in the recharge areas of the three considered springs. Note that hydrotopes covering less than 1% of the respective recharge areas were not considered, assuming that their contribution to the spring discharges is negligible, as often done in other hydrological models (Neitsch et al., 2011), and they are merged with the dominant hydrotopes to fill the whole recharge areas.

Table 3.1: Relative spatial share (in %) of each hydrotope in the three recharge areas. No number means that the respective hydrotope is not present in the regarded recharge area. The description of the forest hydrotopes (Hyd B1 - Hyd B4) indicates the dominant over- and understorey vegetation.

Hydrotope (Hyd)	Covered catchment area (%)			Description
	Kerschbaum	Hinterlug	Mitterlug	
Hyd Q	4	–	–	Dolomite quarries
Hyd B1	13	–	2	Bluegrass-Beech Forest
Hyd B2	56	6	36	White Sedge-Beech Forest
Hyd B3	27	–	53	Christmas Rose-Beech Forest
Hyd B4	–	79	–	Wood Barley-Beech Forest
Hyd P	–	15	9	Pasture

A detailed field mapping campaign was carried out yielding the Forest Hydrotope Model data base and report. All subsequently mentioned hydrotope categories are part of this database (Koeck and Hochbichler, 2012). The result of those field investigations is a detailed classification of the predominant hydrotopes in the study area (Fig. 3.2). Hydrotopes were mapped and classified according to i) the overstorey trees as indicators for interception capacities and preferential flow paths in the soil (rooting), ii) the understorey vegetation as an indicator for the hydrological site conditions (dry to wet) and iii) the dominant soil types and respective thicknesses (shallow to deep) as qualitative parameters for the hydrophysical site properties. The soil depths in the study area range from 20 cm to 60 cm (Markart et al., 2012). The spatial share of each hydrotope in all defined recharge areas is shown in Table 3.1.
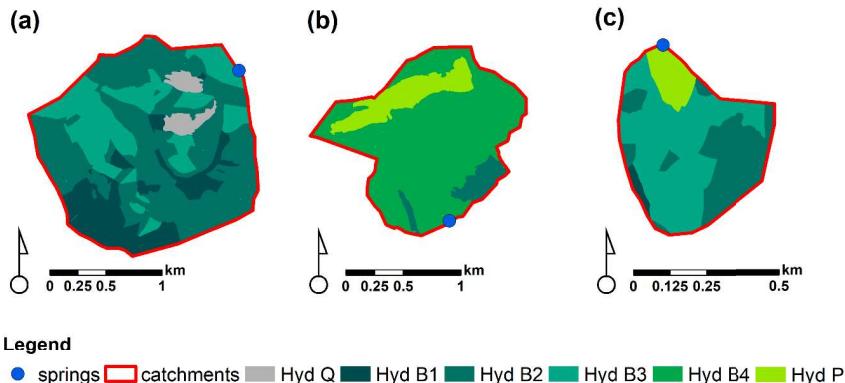
Figure 3.2: Spatial distribution of the dominant hydrotopes in the three recharge areas as characterized by Koeck and Hochbichler (2012). (a) Kerschbaum recharge area, (b) Hinterlug recharge area and (c) Mitterlug recharge area.

Hyd Q represents dolomite quarries located in the Kerschbaum spring recharge area. In 2007, when the orthophoto illustrated in Fig. 3.1b was taken, the quarries covered 4% of the Kerschbaum spring recharge area. Due to the removal of local vegetation and soil cover, the dolomitic basement rocks remained bare in these areas. The catchment classifications and the runoff modeling performed according to Markart (2004) and Kohl (2011) revealed that the dolomite quarry surfaces have discharge coefficients of almost 1 and do not contribute to a considerable amount of the recharge in the subsurface karst system. Instead, the quarries are drained by a small creek that flows into the Waidhofenbach and thus do not feed the Kerschbaum spring (Fig. 3.1b).

Hyd P indicates pastures, located in the Mitterlug and Hinterlug spring recharge areas. Hydrotopes B1, B2, B3 and B4 represent the forest type hydrotopes, all having beeches (*Fagus sylvatica*) as the dominant tree species.

Hyd B1 is the "Bluegrass-Beech Forest" hydrotope and is present in the recharge areas of the Kerschbaum and Mitterlug spring. Shallow soils with high proportions of coarse fragments and a minor occurrence of fine-grained textures are characteristic for that hydrotope. The dominance of bluegrass (*Sesleria albicans*) in the understorey vegetation indicates mostly dry site conditions as a result of low water storage capacities and locations on sun-exposed slopes.

Hyd B2 represents the "White Sedge-Beech Forest" type and is the only hydrotope that can be found in every investigated recharge area. Here, the characteristic soil types show more fined grained textures as well as moderate thicknesses, thus having an elevated storage capacity and a lower permeability than soils on the Hyd B1 sites. White sedges (*Carex alba*) were mapped as the dominant understorey vegetation and indicate moderately fresh site conditions.

Hyd B3 is the "Christmas Rose-Beech Forest" type and occurs in the Kerschbaum and Mitter-

lug recharge areas. Moderate to great solum thicknesses of predominantly loam textured soils are characteristic for these sites. The incidence of Christmas roses (*Helleborus niger*) points towards fresh site conditions.

Hyd B4 is the "Wood Barley-Beech Forest" type and exclusively occurs in the Hinterlug recharge area. As compared to the former Beech-Forest type hydrotopes, Hyd B4 soils have the highest loam contents as well as the greatest soil depths. Permanently moist site conditions are characteristic for Hyd B4 and evidenced by the presence of wood barley (*Hordelymus europaeus*) and woodruff (*Galium odoratum*).

3.3 Methods

3.3.1 Modeling concept

LuKARS aims to simulate the hydrological processes that take place in each hydrotope, to simulate their respective interaction with the saturated groundwater system and, finally, to reproduce the observed discharge behavior of a spring. Similar to Tritz et al. (2011), we consider the hydrotopes to conceptually represent the vadose zone (soil-epikarst-infiltration zone) and to be directly connected to the saturated zone. In the model, all hydrotopes receive an effective precipitation input that depends on the hydrotopes' canopy interception, evapotranspiration and snow melt/retention in winter. Moreover, each hydrotope is characterized by a specific retention capacity. Therefore, the same input signal leads to different reactions of the hydrotopes both under dry (E_{min}) and wet conditions (E_{max}). The conceptual model considers that the activation of conduits is faster if infiltration happens faster, which is less retained in a thin hydrotope (low soil storage) than in a thick one (high soil storage). The basic idea of implementing a series of hydrotopes in a single modeling framework is based on the assumption of a hydrophysical uniqueness of each hydrotope. In particular, the model aims to reproduce hydrotope-specific hysteresis cycles and the hydrological effects of long dry and wet cycles on each hydrotope. The temporal state of the catchment storage system, i.e. dry or wet conditions, therefore plays an important role for the initialization of different discharge processes (Tritz et al., 2011; McNamara et al., 2011). Fig. 3.3 illustrates the structure of LuKARS and the possible flow processes that are described in the following:

1) Part of the water is moved out of the catchment once a hydrotope-specific threshold (E_{sec}) is exceeded. E_{sec} [L] is defined as an activation level for flow processes leading to water losses, i.e. overland flow processes and secondary spring activation (Mazzilli et al., 2017). From a conceptual perspective, the flow component Q_{sec} [L^{3}T^{-1}] integrates the flows that do not arrive at a regarded karst spring and that are transferred outside the investigated recharge area.

2) Another part of the water stored in a hydrotope is discharged to the outlet of the catchment ($Q_{hyd,1}$ to $Q_{hyd,4}$ [L^{3}T^{-1}]) if the hydrotope-specific maximum storage capacity E_{max} [L] is exceeded. This flow is considered a quickflow component occurring in preferential flow paths, such as subsurface conduits, and is responsible for the fast reaction of a spring discharge to rainfall and snowmelt events (Blume and Van Meerveld, 2015). The conceptual idea is that the hydrotopes

with shallow and coarse-grained soils have the highest connectivity to karst conduits (e.g. Hyd 2 in Fig. 3.3). The quickflow stops once the storage volume drops below the hydrotope-specific minimum storage capacity E_{min} [L].
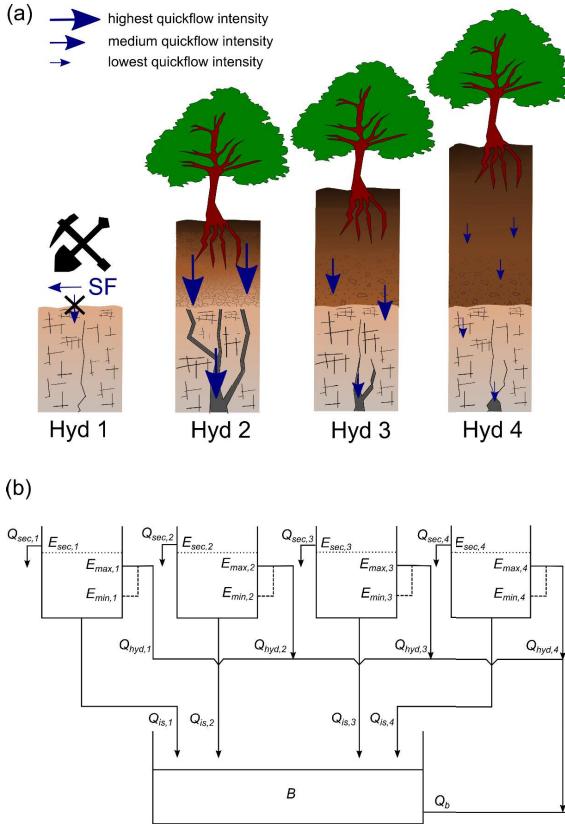
Figure 3.3: Example of the conceptualization of the hydrotopes and the model implementation as performed for the Kerschbaum recharge area. (a) The conceptual representation of the present hydrotopes. Hyd 1 indicates the dolomite quarries with no groundwater recharge and the dominance of surface runoff (SF). The connectivity to the karst system is largest in Hyd 2 with shallow and coarse-textured soils and lowest in Hyd 4. (b) Model implementation of the four hydrotopes in the Kerschbaum recharge area.

3) A next part of the water stored in a hydrotope leaks into a lower reservoir B as inter-storage flow Q_{is} [L^{3}T^{-1}]. This flow represents the process of groundwater recharge. Deep and fine-textured soils provide a more stable groundwater recharge (e.g. Hyd 4 in Fig. 3.3) than shallow

and coarse-textured soils (e.g. Hyd 2 in Fig. 3.3).

4) The last flow component Q_b [L^3T^{-1}] represents water transferred from the storage B to the spring. This flow to the spring outlet simulates a baseflow contribution from the phreatic aquifer system to the spring discharge.

3.3.2   Governing equations

The modeling approach we propose to use is based on the application of a non-linear storage threshold function, similar to what is suggested in Tritz et al. (2011). In the following, the subscript notation indicates that the respective terms are hydrotope specific.

LuKARS solves the following balance equation for each hydrotope:

$$\frac{dE_x}{dt} = \begin{cases} S_x - \frac{Q_{sec,x}+Q_{is,x}+Q_{hyd,x}}{a_x} & \text{if } E_x > 0 \\ 0 & \text{if } E_x = 0 \end{cases} \tag{3.1}$$

where E_x indicates the water level [L] in hydrotope x, t [T] is the time, whereas S_x represents the hydrotope-specific sink and source term as a mass balance of precipitation, snow melt, evapotranspiration and interception [LT^{-1}], as detailed in the next section. a_x [L^2] is the absolute area covered by the respective hydrotope.

For the baseflow storage, the following balance equation is implemented in the model:

$$\frac{dE_b}{dt} = \begin{cases} \frac{\Sigma(Q_{is,x})-Q_b}{A} & \text{if } E_b > 0 \\ 0 & \text{if } E_b = 0 \end{cases} \tag{3.2}$$

where E_b is the water level [L] in the baseflow storage and Q_{is} [L^3T^{-1}] stands for the total flow from all hydrotopes to the baseflow storage. The variable A [L^2] represents the whole catchment area. Eq. 3.1 and 3.2 are solved for each time step n using their discretized forms, as given in Eq. 3.3 and 3.4, respectively:

$$E_{x,n+1} = \max[0, E_{x,n} + (S_{x,n} - \frac{Q_{sec,x,n}+Q_{is,x,n}+Q_{hyd,x,n}}{a_x})\Delta t] \tag{3.3}$$

$$E_{b,n+1} = \max[0, E_{b,n} + (\frac{\Sigma(Q_{is,x,n})-Q_{b,n}}{A})\Delta t] \tag{3.4}$$

The discharge terms are computed as follows:

$$Q_{hyd,x,n} = \varepsilon_n[\frac{\max(0, E_{x,n}-E_{min,x})}{E_{max,x}-E_{min,x}}]\alpha_x \frac{k_{hyd,x}}{l_{hyd,x}}a_x \tag{3.5}$$

$$Q_{is,x,n} = E_{x,n}k_{is,x}a_x \tag{3.6}$$

$$Q_{sec,x,n} = \max(0, E_{x,n}-E_{sec,x})k_{sec,x}a_x \tag{3.7}$$

$$Q_{b,n} = E_{b,n} k_b A \tag{3.8}$$

$E_{max,x}$ [L] and $E_{min,x}$ [L] are the upper and lower storage thresholds of the hydrotope and $E_{sec,x}$ [L] is the hydrotope-specific activation level for a secondary spring discharge. Following the notation of Tritz et al. (2011), $k_{is,x}$ [LT^{-1}] and $k_{sec,x}$ [LT^{-1}] are the discharge coefficients for $Q_{is,x}$ [L^{3}T^{-1}] and $Q_{sec,x}$ [L^{3}T^{-1}], respectively. The discharge coefficient for the quickflow of a hydrotope is represented by $k_{hyd,x}$ [L^{2}T^{-1}]. Notice that all three discharge coefficients are hydrotope-specific. In contrast with Tritz et al. (2011), we consider the term $l_{hyd,x}$ [L], which is the hydrotopes' mean distance to the adjacent spring and accounts for the relative location of the same hydrotope types in a specific catchment. The ratio between k_{hyd} and l_{hyd}, represents the discharge coefficient. The dimensionless connectivity/activation indicator ε specifies whether or not the quickflow component from a hydrotope is active during time step n and is defined as follows:

$$\varepsilon_{n+1} = 0 \text{ if } \begin{cases} \varepsilon_n = 0 \ \& \ E_{x,n+1} < E_{max,x} \text{ or} \\ \varepsilon_n = 1 \ \& \ E_{x,n+1} \leq E_{min,x} \end{cases} \tag{3.9}$$

$$\varepsilon_{n+1} = 1 \text{ if } \begin{cases} \varepsilon_n = 0 \ \& \ E_{x,n+1} \geq E_{max,x} \text{ or} \\ \varepsilon_n = 1 \ \& \ E_{x,n+1} > E_{min,x} \end{cases} \tag{3.10}$$

For each time step, the total inter-storage discharge (Q_{is} [L^{3}T^{-1}]), computed as the sum of the inter-storage discharge of each hydroptope, is added to the underlying linear storage. Finally, the spring discharge (Q_{tot} [L^{3}T^{-1}]) is computed as the sum of the quickflow provided by each hydrotope and the baseflow component from the linear storage:

$$Q_{tot,n} = Q_{b,n} + \sum_x Q_{hyd,x,n} \tag{3.11}$$

3.3.3 Sink and source terms

Interception of solid and liquid precipitation and evapotranspiration losses are computed separately by the model, since interception is high in forested sites while evapotranspiration is high from non-forest surfaces (in our case quarries and pastures). Moreover, we applied a degree-day model (Martinec, 1960) to describe snow melt and accumulation in the study area. The model first estimates daily losses from interception, then it computes snow accumulation and snowmelt. Finally, the removal of evapotranspiration losses is calculated. The input term S_x [LT^{-1}] in Eq. 3.1 is calculated as follows:

$$\begin{aligned} S_x &= M_d - Et_d & \text{if } P = 0 \quad \text{and} \\ S_x &= P - I_d + M_d - Et_d & \text{if } P > 0 \end{aligned} \tag{3.12}$$

where P represents the daily precipitation [LT^{-1}], M_d [LT^{-1}] is the amount of snowmelt in

the case of the presence of a snow layer and I_d [LT^{-1}] and Et_d [LT^{-1}] are the daily losses of interception and evapotranspiration.

As indicated in the DVWK (1996), interception in beech-dominated forests increases from 11 % in the winter season (21st December) to 17 % in the summer season (21st June) and then decreases again to the winter value. The daily I_d time series was generated via linear interpolation between these two values. To avoid unrealistic interception losses during heavy rainfall events, percentage losses were limited to a maximum of 5 mmd^{-1} (Markart et al., 2006). In the non-forested hydrotopes, I_d is set to 0 since no interception can occur. Considering the data availability, we used the method proposed by Thornthwaite (1948) to calculate potential evapotranspiration (Et_{pot}) based on monthly mean temperatures as follows:

$$Et_{pot} = 16 \, (10\frac{T}{H})^r \tag{3.13}$$

where Et_{pot} [LT^{-1}] is the monthly potential evapotranspiration, T [°C] is the mean monthly temperature, and H is the heat index defined as

$$H = (\frac{T}{5})^{1.514} \tag{3.14}$$

with exponent r given by

$$r = 6.75e^{-7}H^3 + 7.71e^{-5}H^2 + 1.792e^{-2}H + 0.49239 \tag{3.15}$$

The computed sum of monthly Et_{pot} represents an estimate for months with a length of 30 days and 12 hours of possible sunshine per day. For simplicity reasons, we considered Et_{pot} to be representative estimates for each month and did not further adjust the monthly time series regarding differences in the sum of the days of a month and the latitudinal variability of possible sunshine hours per day. Thus, we divided Et_{pot} by the number of days and assumed the resulting Et_d [LT^{-1}] to be representative for the 15th day of a month. The selection of Thornthwaite's method is based on the fact that the results obtained with this method are close to the annual ET values calculated by Markart et al. (2006) for our study area. Similar to our interception calculations, we interpolated linearly between these values to obtain a characteristic time series of Et_d.

The degree-day method we applied in LuKARS is given by:

$$M_{pot} = F \max(0, T - T_f) \tag{3.16}$$

where M_{pot} stands for the potential melt rate in the form of a snow water equivalent [LT^{-1}], T is the daily mean temperature [°C], T_f represents a threshold temperature [°C] controlling either snow accumulations or melts and F is defined as the degree-day factor [LT^{-1}°C^{-1}]. We assumed the following conditions for snow accumulation (S_{snow} [L]) and actual snowmelt (M_d [LT^{-1}]):

$$
\begin{aligned}
S_{snow,n} &= S_{x,n} & &\text{if } T_n < T_f & &\text{and} \\
S_{snow,n+1} &= S_{x,n} + S_{x,n+1} & &\text{if } T_n < T_f \, \& \, T_{n+1} < T_f & &\text{and} \\
S_{snow,n+1} &= \max(0, S_{snow,n} - M_d) & &\text{if } T_{n+1} \geq T_f & &
\end{aligned}
\tag{3.17}
$$

and

$$
\begin{array}{lll}
M_d = 0 & \text{if } T < T_f & \text{and} \\
M_d = M_{pot} & \text{if } T \geq T_f \,\&\, S_{snow} \geq M & \text{and} \\
M_d = S_{snow} & \text{if } T \geq T_f \,\&\, S_{snow} < M &
\end{array}
\tag{3.18}
$$

A table summarizing the notations used in LuKARS is further provided in Supplementary material B.1.2.

3.3.4 Estimation of the hydrotope storage thresholds

Differences in physical soil properties are the most important criteria to differentiate the hydrotopes. Namely, soil texture and soil thickness are the most relevant factors for the internal hydrological behavior of a hydrotope. To estimate the storage thresholds E_{min} and E_{max} for each of the considered hydrotopes, we used a new hydropedological fieldguide (DWA, 2018) that was developed to characterize a site of interest in terms of hydrological aspects (Kohl et al., 2016). Site mapping with this tool is performed analogous to the German soil classification system (Ad-hoc-Arbeitsgruppe Boden, 2005). The tool derives the dominant hydrological processes as well as the storage capacities under the dry and wet conditions of a selected site, based on the physical soil, catchment and land use information (Supplementary material B.1.3).

To translate qualitative information about the soil properties of the hydrotopes in our study area into quantitative values, i.e. soil thickness and texture, we used the available data for similar sites presented by Leitgeb et al. (2013). Finally, we took the storage capacities for dry and wet conditions as indicated by the hydropedological fieldguide to set Emin and Emax threshold values for each hydrotope.

3.3.5 Calibration and validation process

To calibrate the snow module of the model, we converted the measured snow depth time series at Hinterlug weather station (BMNT, 2018) in snow water equivalent (SWE) time series, using the approach of Jonas et al. (2009). The temperature thresholds for the three spring catchment areas were chosen according to the main exposition of each recharge area.

The natural hydrological behavior of the hydrotopes, i.e. groundwater recharge, quickflow and storage, is predetermined by their physical properties. Hence, the parameters describing the behavior of a hydrotope should be calibrated accordingly and should be consistent with the expected hydrological response of the system. This means, for example, that the hydrotope with the most coarse-grained and shallowest soils should have the highest discharge parameter khyd and the lowest range of storage volume ($E_{max} - E_{min}$). Once calibrated, k_{hyd} remains constant while transferring the hydrotopes to other catchments. The discharge coefficient will vary among different catchments according to the spatial distribution of the hydrotopes in the catchment since it depends on the mean distance between the area covered by a hydrotope and the outlet (l_{hyd}). Hence, each hydrotope should be transferable to other catchment areas by solely modifying the

exponent α, E_{sec} and k_{sec}. In this way, different catchment characteristics, such as the steepness of the slopes, can be included. Since k_{sec} is the most unknown parameter in our modeling approach, we carefully calibrated it so that k_{sec} has a maximum range of two orders of magnitude with regard to all hydrotopes. The parameter sets for Hyd B1, B2 and B3 were calibrated for the Kerschbaum recharge area, and Hyd P and B4 were calibrated in the Hinterlug catchment. Since we did not have any information about the soil characteristics of Hyd P, we calibrated this particular hydrotope based on the known pasture properties derived from comparable study areas and determined the storage thresholds with the hydropedological fieldguide (DWA, 2018). The parameters of Hyd B2 were transferred from the Kerschbaum to the Hinterlug catchment.

Note that the Mitterlug spring discharge is not measured directly at the spring itself, but at a storage system located behind an overflow basin. This leads to the fact that this time series is unusable to quantitatively assess the correctness of the hydrotopes' parametrization at Mitterlug spring on a daily scale. Thus, we calculated monthly mean values from the daily discharge time series measured at the storage system. Since neither water leaves nor additional water enters the system before the monitoring point, we used the monthly mean discharge for validation. We treat this catchment as an ungauged one for which we validate the parameter sets of the hydrotopes as determined for the Kerschbaum and Hinterlug recharge areas.

The models were calibrated and validated for the years 2006 and 2007 when the dolomite quarries covered 4% of the Kerschbaum recharge area. For further model validation as well as to proof its applicability for land use change impact studies, we also run LuKARS for the Kerschbaum catchment for the years 2010 – 2013, when the area covered by the dolomite quarries almost doubled (Fig. 3.7) at the expense of the area covered by Hyd B2. Due to the presence of large data gaps in the observed discharge time series from 2010 to 2013, we focused our model validation on three distinct timeframes in 2010, 2012 and 2013, for which we have reliable measurements. These three validation periods comprise high and low flow conditions to ensure a meaningful evaluation of the model results for different hydrological states of the system.

More information about the input data used for the model simulations is presented in Supplementary material B.1.4.

3.4 Results

3.4.1 Calibration and validation periods

The chosen parameter sets of all hydrotopes, the baseflow storages of the three recharge areas as well as the snow model parameters are presented in Table 3.2. The results of the calibration and validation periods of the snow model as well as the simulated and observed hydrographs of the Kerschbaum and Hinterlug springs are presented in Fig. 3.4. We can observe that the snow model overestimates the SWE from January 2006 to April 2006, whereas the Kerschbaum snow model produces higher SWE compared to the Hinterlug snow model. However, the timing of snow retention and the snowmelt of both models fits reasonably well. Similarly, the snow models

accurately match the timing of retention and melt during the validation phase.

The comparison between observed and simulated hydrographs (Q_{tot}) indicates that LuKARS is able to simulate the observed discharge behavior in the Kerschbaum and Hinterlug springs accurately. A Nash-Sutcliffe Efficiency (NSE) (Nash and Sutcliffe, 1970) of 0.64 for the Kerschbaum spring and a NSE of 0.76 for the Hinterlug spring highlight an accurate reproduction of the observed discharge (**Table 3**). Moreover, a MAE of 0.76 [ls^{-1}] for the Kerschbaum spring and a MAE of 1.72 [ls^{-1}] for the Hinterlug spring also indicate that there is an acceptable reproduction of the simulated discharge.

Table 3.2: Overview of all model parameters for each hydrotope and all recharge areas.

Hydrotope-specific parameters parameter		Hyd Q	Hyd B1	Hyd B2	Hyd B3	Hyd B4	Hyd P
E_{min} [mm]		0	23	60	90	110	110
E_{max} [mm]		1	31	120	200	250	145
E_{sec} [mm]		0	35	180	380	220	210
k_{hyd} [m^{2}d^{-1}]		0	90	85	77	70	85
k_{is} [m mm^{-1}d^{-1}]		0	0.02	0.0055	0.0025	0.0006	0.002
α [-]		0	0.9	0.8	0.55	2.3	0.9
Catchment-specific, hydrotope parameters							
	Kerschb.	550	1600	900	960	–	–
l_{hyd} [m]	Hinterlug	–	–	370	–	800	1160
	Mitterlug	–	520	430	390	–	130
	Kerschb.	0.9	0.095	0.026	0.022	–	–
k_{sec} [m mm^{-1}d^{-1}]	Hinterlug	–	–	0.016	–	0.025	0.008
	Mitterlug	–	0.095	0.006	0.004	–	0.008
Catchment-specific parameters							
		Kerschbaum		Hinterlug		Mitterlug	
k_b [m mm^{-1}d^{-1}]		0.00043		0.0011		0.02	
F [mm d^{-1}°C^{-1}]		4		4		4	
T_f [°C]		0.5		0		2	

When focusing on the calibration period of the Kerschbaum spring, the model mostly matches the observed peaks as well as the recession limbs of peak discharges. Here, the model overestimates the peak at the beginning of April 2006 and slightly undershoots the summer peak discharges. A similar behavior can be observed for the Hinterlug discharge: the model is able to reproduce the measured discharge time series but it also fits the peak in April 2006. In contrast, the model underestimates the pronounced peak discharge recorded in the Hinterlug hydrograph in February 2006. The simulated peak discharges in summer 2006 match the recorded time series reasonably well.

With respect to the validation period, the calibrated Kerschbaum model fits the measured hydrograph in 2007. A NSE of 0.54 and a MAE of 0.77 [ls^{-1}] underline a good match between the observed discharge behavior and our simulations. Similar to the validation of the Kerschbaum

spring, the results for Hinterlug show an acceptable match between observed and simulated discharge time series.
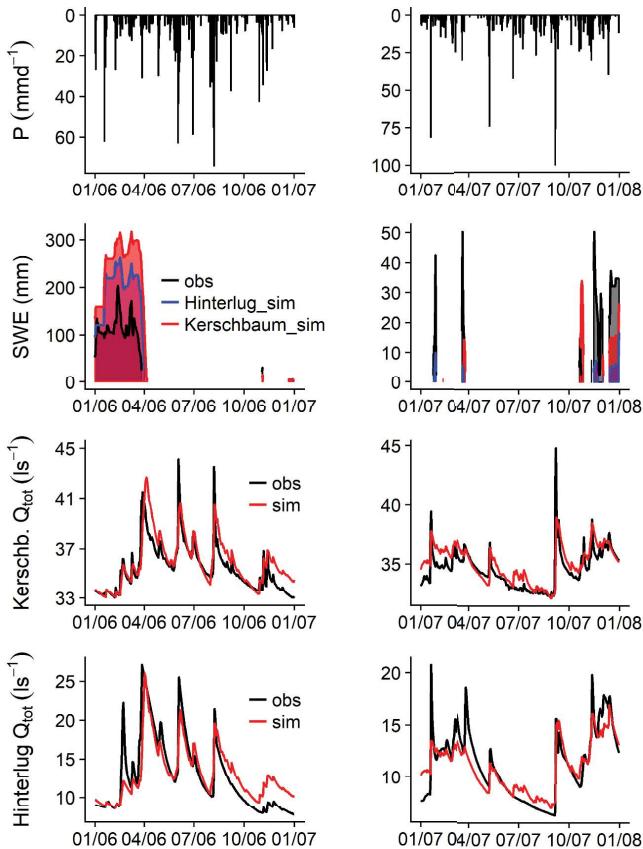
Figure 3.4: Modeling results for the Kerschbaum and Hinterlug springs during the calibration phase 2006 (left column) and the validation period 2007 (right column). The graphic shows the precipitation (P) time series, the transformed snow water equivalent (SWE) from the snow depth measurements and the snow model results and the observed (obs) and simulated (sim) discharge time series (Q_{tot}) for the Kerschbaum and the Hinterlug spring.

In contrast to the Kerschbaum model, the Hinterlug model underestimates the peak discharges in January, April and December 2007. However, a NSE of 0.77 and a MAE of 1.09 $[ls^{-1}]$ indicate the ability of the model to reproduce the total discharge and the discharge dynamics recorded in the Hinterlug spring (Table 3.3).

Table 3.3: Results of the objective functions for the model performances during the calibration period (2006) and the validation period (2007).

| Recharge area | Calibration period (2006) | | Validation period (2007) | |
	NSE	MAE [ls^{-1}]	NSE	MAE [ls^{-1}]
Kerschbaum	0.64	0.76	0.54	0.77
Hinterlug	0.76	1.72	0.77	1.09

The highest specific quickflow (Q_{hyd}) in the Kerschbaum recharge area originates from Hyd B1 in response to rainfall or snowmelt events, whereas Hyd B2 and B3 show weaker quickflow responses (Fig. 3.5). The variability of Q_{hyd} is highest in Hyd B1 and lowest in Hyd B3. In the recharge area of the Hinterlug spring, Q_{hyd} is highest in Hyd P and B2, whereof the later shows the highest variance of the specific discharge. However, Hyd B4 generates the highest Q_{hyd} in response to the snowmelt event in April 2006. Moreover, Q_{hyd} of Hyd B4 appears to be the most dynamic hydrotope for what concerns the steepness of the recession limbs in the hydrograph. Q_{hyd} originating from Hyd P is less variable as compared to Hyd B2 and B4 throughout the calibration and validation period. Q_{hyd} from Hyd Q is constantly 0.

Considering the specific recharge (Q_{is}), the highest flow contributions in the Kerschbaum recharge area originate from Hyd B2, followed by Hyd B1 and B3 (Fig. 3.5). Similar to the quickflow, the variability of Q_{is} is highest in Hyd B1 and lowest in Hyd B3. In the Hinterlug catchment, the most specific Q_{is} also originates from Hyd B2, followed by Hyd P. The specific Q_{is} from Hyd B4 can be considered of minor importance compared to the recharge from both other hydrotopes. Q_{is} from Hyd Q is constantly 0.

3.4.2 Validation of hydrotopes concept in ungauged spring catchments

As pointed out in Section 3.3.5, we calculated the monthly means of the Mitterlug spring discharge to enable a quantitative comparison between model and measurements. This monthly time series and the simulated hydrograph of the Mitterlug model are visualized in Fig. 3.6.

The simulated time series was obtained by carefully calibrating the k_{sec} parameters in the same range in which k_{sec} of the hydrotopes in the other recharge areas are located. Regarding the north exposition of the whole recharge area, we increased T_f of the applied snow model to account for the natural delay of spring discharge onset in response to longer snow retention phases. An overall fit between the monthly Q_{sim} and the monthly Q_{obs} can be observed throughout the two simulated years (2006-2007). In 2006, both the modeled annual trend and the total discharge adequately reproduce the observed values. In 2007, the simulation results still reproduce the behavior of the aggregated monthly time series; however, the simulated discharge slightly overshoots the observed time series. Finally, a NSE of 0.83 and a MAE of 0.49 [ls^{-1}] highlight a good match between the monthly means of observed and simulated discharges.
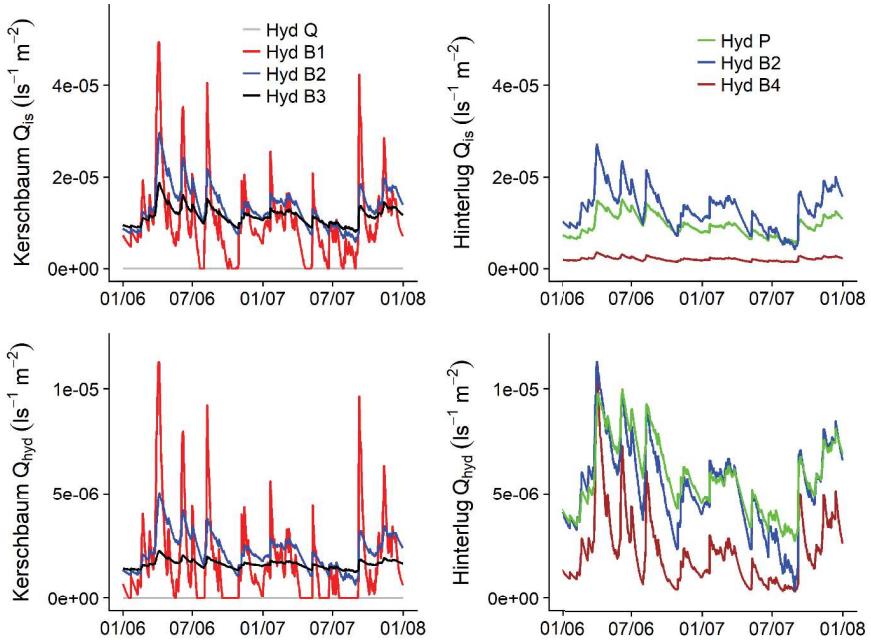
Figure 3.5: Specific discharge contributions to the groundwater recharge (Q_{is}) and the quickflow (Q_{hyd}) from each hydrotope in the Kerschbaum and the Hinterlug recharge area. A higher resolved version of this figure is presented in the Supplementary material B.1.5.

3.4.3 Application of LuKARS for land use change

A comparison between the model performances under changed land use conditions is visualized in Fig. 3.7. We can observe that the model considering 4% of area covered by quarries leads to higher discharge compared to the model in which we correctly reproduce the increase in the area covered by quarries. Particularly the simulated low flow discharges deviate most in the two modeled hydrographs. When focusing on the three distinct validation periods (Fig. 3.7a-c), we see that the simulation results considering a larger share of Hyd Q better match the observed discharge. In contrast, the model run with 4% quarries systematically overestimates the measured records. The results from the updated model are in good agreement, in particular, considering the recorded peak flow events during the validation phases in 2010 and 2012 (Fig. 3.7a and b).

Although the model results obtained considering the occurred land use change underestimate the peak flows during the low flow period in 2013 (Fig. 3.7c), the modeled low flow discharge fits the measured time series reasonably well. We can also observe, in all validation periods, a consistent increase of the NSE and a decrease in the MAE for the model considering land use

change in comparison to the model neglecting the effect of the quarry (Table 3.4).
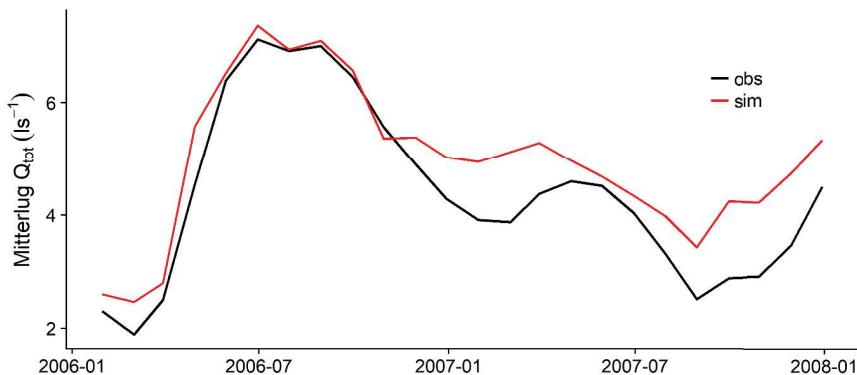
Figure 3.6: Validation of LuKARS in the Mitterlug recharge area. The red and black graphs indicate the simulated and observed time series of mean monthly discharge, respectively.

3.5 Discussion

3.5.1 Evaluation of the hydrotope-based modeling approach LuKARS

Regarding the error statistics determined for the simulation runs of the calibration and validation period for the Kerschbaum and Hinterlug spring, we can state that, according to the NSE and MAE (Table 3.3), the results of both models accurately match the observed discharges. In particular, when focusing on the peak discharges in 2006 and 2007 (Fig. 3.4), the hydrotopes modeling approach fits the temporal dynamics and the total amounts of the karst-typical sharp peak discharges in response to both snowmelt and rainfall. Furthermore, the model captures peak discharges in response to rainfall events after precedent wet, e.g. 06/2006, and precedent dry, e.g. 05/2007, periods, thus showing its ability to simulate the hydrological response of the soil-epikarst system following different antecedent conditions. The overall match of the hydrograph recession limbs, as a physical indicator for karst conduit depletion and transition from conduit to matrix flow, underlines the model's capability to reproduce the temporal internal dynamics of the karst storage system. In addition, the good agreement of simulated and measured low flow periods highlight that the baseflow can be expressed as the sum of a continuous water supply from the hydrotopes (Q_{hyd}) to the spring and the flow from a collective reservoir (Q_b).

The largest deviations between Q_{obs} and Q_{sim} occur when snow processes affect spring discharges, in particular, the underestimation of Qsim at Hinterlug in February 2006 and from March to April 2007 and the overestimation during the snow retention phase in winter 2006/2007 at Ker-

schbaum and Hinterlug springs. In particular, for the Hinterlug spring, these deviations explain the relatively high MAE of 1.72 [ls^{-1}] during the calibration year 2006. We argue that these discrepancies result from SWE over- and underestimation, since the modeled discharge peaks in response to rainfall events coincide with the monitored discharge. Although we introduced different T_f to account for the different main expositions of each recharge area, these inconsistencies of model simulations, i.e. either over- or underestimation of snowmelt and retention, suggest that the simplicity of the degree-day method is insufficient to adequately model snow processes in this pre-alpine catchment.

Table 3.4: Results of the objective evaluation functions for the Kerschbaum model performance for land use change during three validation phases in the period from 2010-2013.

Objective function	1st validation (2010)		2nd validation (2012)		3rd validation (2013)	
	4%	7%	4%	7%	4%	7%
NSE	-0.98	0.65	-0.33	0.71	-0.77	0.58
MAE	0.98	0.38	1.16	0.45	1.08	0.39

Regarding the Q_{hyd} hydrographs of each hydrotope (Fig. 3.5), the shallowest and most coarse-grained hydrotope soils, in particular Hyd B1, show the fastest and most intense reactions to the rainfall or snowmelt inputs. Q_{is} behaves similarly due to the low storage capacity and high discharge coefficient k_{is}. The low storage capacity further causes Q_{hyd} and Q_{is} to become 0 during long dry periods, e.g. in July 2006. This behavior complies with the conceptual idea that the connectivity to fast draining conduits to the spring and flow paths feeding the saturated aquifer is highest if the hydrotope soils are shallow with mainly coarse-grained sediments. The same relation between soil thickness, soil texture and discharge behavior also applies for Hyd B2, Hyd B3 and Hyd P and thus meets our hydrotope modeling concept; Hyd B2 has a lower storage capacity, higher discharge parameters k_{is} and k_{hyd} and, consequently, has a more variable specific discharge than Hyd B3 in terms of Q_{hyd} and Q_{is}.

When comparing the Q_{hyd} and Q_{is} of Hyd B2 in the Kerschbaum and Hinterlug recharge areas (Fig. 3.5), both specific discharge time series are more dynamic in the Hinterlug recharge area than in the Kerschbaum one. These differences in the specific discharge behavior are the result of different mean distances from the Hyd B2 to the respective spring (l_{hyd}) and justify the use of l_{hyd} as a location parameter for any hydrotope in a defined recharge area. Despite the high storage capacity and the low k_{hyd} of Hyd B4 in the Hinterlug recharge area, Q_{hyd} originating from Hyd B4 is strongly dynamic with partially high specific discharge (Fig. 3.5). Since Hyd B4 covers 79% of the Hinterlug recharge area and with regard to the pronounced peak discharges in Q_{obs} at Hinterlug spring (Fig. 3.4), this dynamic contribution of Q_{hyd} is of major importance to adequately reproduce Q_{obs} by Q_{sim}. We argue that the quickflow in the Hinterlug recharge area is the result of pushing old water from the hydrotope's high storage volume towards the spring once new water enters the system during a rainfall or snowmelt event; a process similar to the return flow occurring on steep slopes with layered soil structures. This further explains the constantly low specific Q_{is} originating

from Hyd B4.
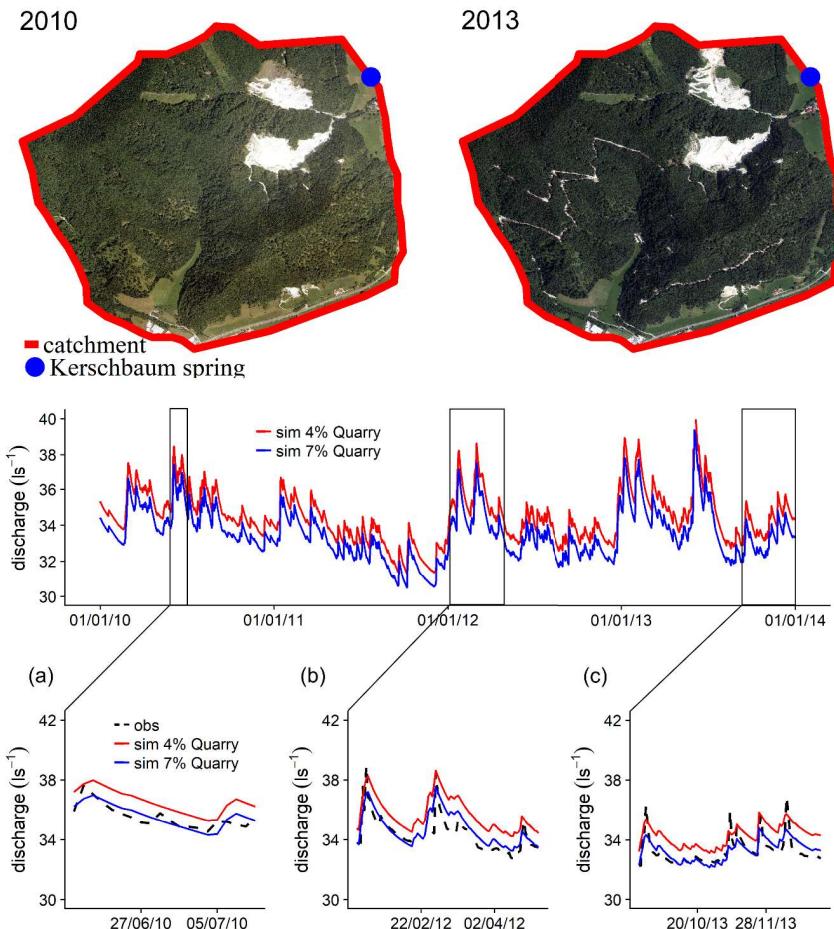
Figure 3.7: Validation of the Kerschbaum model for the years 2010 − 2013 affected by land use change. Top: orthophotos taken in 2010 and 2013. Middle: Simulated spring discharge without land use change (red) and simulated discharge with land use change (blue). Bottom: comparison of both model runs with the measured time series (obs) for three distinct periods, (a) from 20/06/2010 to 09/07/2010, (b) from 18/01/2012 to 26/04/2012 and (c) from 16/09/2013 to 31/12/2013.

With the chosen hydrotope parameter sets, we were able to simulate the assumed variability of

Q_{hyd} and Q_{is} for each hydrotope (Fig. 3.5), i.e. higher variability with shallow soils composed of a mainly coarse-grained soil texture (e.g., Hyd B1) and lower variability with thick and mainly fine-textured soils (e.g., Hyd B3). Hence, our calibration approach to decrease k_{hyd} and to increase the range between E_{min} and E_{max} in parallel with more fine-textured and thicker hydrotope soils leads to plausible hydrological behaviors of each hydrotope. Moreover, the thresholds E_{min} and E_{max}, as determined with DWA (2018), constrain the storage capacities of the hydrotopes reasonably well.

3.5.2   Model validation in the ungauged Mitterlug spring recharge area

Given the results of the application example for the Mitterlug spring, we consider the good fit between the monthly Q_{obs} and Q_{sim} (Fig. 3.6) as a proof of the concept of LuKARS, since we obtained the results by simply transferring the parameter sets of the present hydrotopes as determined in two distinct recharge areas. Apart from the parametrization of the hydrotopes, the good match between the monthly time series furthermore corroborates the applicability of the distance parameter l_{hyd} as denominator in the discharge coefficient. The increased T_f and the corresponding delayed onset of snowmelt at Mitterlug spring is justified by the north exposition of the whole recharge area. However, a measured time series of daily discharge would be needed to quantitatively validate the hydrotopes' transferability with regard to the peak discharges and recession parts of the daily time series.

3.5.3   Model validation for land use change impacts

With respect to the model application for the years 2010-2013 to validate its applicability for land use change impact studies, a significant improvement of the model results was achieved when increasing Hyd Q to 7%. The systematic overestimation of the model simulations including 4% Hyd Q results from an overestimated share of area that contributes to the total discharge in the Kerschbaum spring. When increasing the area of Hyd Q at the expense of Hyd B2, we reduced the total discharge contribution from Hyd B2 in the recharge area. Due to the fact that Q_{is} is higher than Q_{hyd} in Hyd B2 (Fig. 3.5), this surface reduction primarily leads to a reduction of the baseflow (Q_b). The lower baseflow explains why the discharge time series of both model simulations (Fig. 3.7) deviate most during low flow periods. The good fit between the simulated discharge of the updated model and the measured hydrograph during both high flow (Fig. 3.7a and b) and low flow periods (Fig. 3.7c) indicates that the improvements of the model results are not only related to one specific condition of the natural hydrograph. The undershot peak discharges during the low flow period in 2013 (Fig. 3.7c) are related to underestimated responses to moderate precipitation events (< 15 mmd^{-1}) followed by dry periods. Although the model does not match these peak discharges in 2013, the low flow discharge is properly described by the model results. In addition, these peak discharge underestimations are the result of a non-exceedance of E_{max} in Hyd B1 and the related non-appearance of Q_{hyd} from this hydrotope (not shown) and thus are not related to the land use change adaptation in the model. Transferred to our understanding of the

karst system, this land use change leads to a reduction of groundwater recharge. Less recharge subsequently causes a reduction of the low flow discharge in the Kerschbaum spring.

3.5.4 Model uncertainties

The proposed model LuKARS requires as fundamental input data a reliable size for the catchment area and a detailed soil classification for the definition of the hydrotopes. Both information can be gathered by tailored field campaigns and an inaccurate description of the catchment size or of the hydrotope classification leads to major errors in model output (Mazzilli et al., 2012a).

For what concerns meteorological input data, at the moment the model uses a single time series as input. This makes the model suitable for small size catchments, typical for water supply systems in alpine regions. The extension to larger catchments will require a proper management of meteorological input data. In future versions of the model, this aspect will be included considering approaches commonly used for semi-distributed hydrological models (Bieger et al., 2017).

Finally, although the model aims to be as parsimonious as possible, we have a large amount of fitting parameters (24 for the Kerschbaum spring, 16 for the Hinterlug spring and 4 for the Mitterlug recharge area) and most of them cannot be explicitly derived from independent field observations. In this context, we point out the importance of performing a rigorous parameter uncertainty analysis and we warmly recommend, whenever possible, to perform a multi-objective model calibration (Moussu et al., 2011; Mazzilli et al., 2013; Tuo et al., 2018) to reduce model equifinality. The purpose of this work is to show that it is possible to include land use change in a hydrological karst model using hydrotopes as fundamental units. Therefore, we applied a very simple calibration approach based on trial and error and on our expert knowledge about the study area. In Bittner et al. (2018b), we illustrate how the model parameters are informed by the spring discharge data. An automatic calibration toolbox for LuKARS is currently under development and will be released for free.

3.6 Conclusion

In this study, we developed a semi-distributed conceptual modeling approach LuKARS that lumps the different hydrotopes as stand-alone units in a catchment. We were able to proof the applicability and transferability of our modeling concept by applying the calibrated hydrotopes to other recharge areas in which those hydrotopes were mapped. Furthermore, we showed that the presented approach provides a valuable tool for land use change impact studies in karstic systems by validating the calibrated Kerschbaum model for a period in which the recharge area suffered from increasing dolomite mining.

Generally, the calibrated hydrotopes should be tested in other karst catchments in order to validate their parametrization as well as to investigate the relevance of the calibration parameters for an accurate process representation considering different catchment characteristics. An example is Hyd B4, which has the highest storage capacity solely regarding its physical properties, but only

occurs in the Hinterlug recharge area with the steepest slopes of all catchments; making a further validation of the parametrization indispensable for catchments with less steep slopes. Since the applicability of LuKARS in ungauged catchments and for land use change investigations is limited to calibrated hydrotopes that were validated for specific site conditions, more investigations are required to parametrize and test more hydrotopes with different soil and land use properties.

Chapter 4

A graphical user interface for LuKARS

Bittner et al. (2020b)[1]

Abstract

Simulating karst spring discharge and land use change impacts in a recharge area is strategic for water resource management in many countries worldwide. For this task, we introduce a user-friendly modeling environment by integrating the recently proposed LuKARS (Land use change modeling in KARSt systems) model into the FREEWAT (FREE and Open Source Software Tools for WATer Resource Management) framework. LuKARS is a rainfall-discharge model for karst systems that simulates the impact of land use changes by changing the area of the dominant hydrotopes, i.e. landscape units with homogeneous soil and land use properties, in a catchment. FREEWAT is a free and open source toolkit for water resource management implemented in QGIS desktop application. The integration of LuKARS into FREEWAT takes advantage of the GIS capabilities to map, visualize and change the relevant hydrotope shapefiles. Then, FREEWAT provides a modular framework for pre- and post-processing tools that facilitate the setup, calibration, analysis, storage and sharing of a LuKARS model.

4.1 Introduction

Mathematical models are tools which are commonly applied to simulate different processes of the hydrologic cycle (Casper et al., 2019; Chiogna et al., 2018; Hartmann et al., 2014b; Tuo et al., 2018). Typically, these models are based on sophisticated mathematical frameworks developed and applied by researchers and water experts. In recent years, more and more open source codes are available to model various processes of the hydrologic cycle (Arnold et al., 1998; Borsi et al., 2013; Winston, 2009). Their complex nature makes them not intuitive for what relates to their

---

[1] **Bittner, D.**, Rychlik, A., Klöffel, T., Leuteritz, A., Disse, M., Chiogna, G., 2020. A GIS-based model for simulating the hydrological effects of land use changes on karst systems – The integration of the LuKARS model into FREEWAT. Environmental Modelling and Software, 104682.

applicability. In particular, those people who need to apply these tools, e.g. water resource managers, are not necessarily familiar with programming languages and are, thus, often not able to apply these models (De Filippis et al., 2017).

In the years 2015 to 2017, the European Union funded a coordinated initiative to overcome this limitation within the HORIZON 2020 program: the FREEWAT project (www.freewat.eu) project. In FREEWAT, researchers from various European countries developed a free and open-source plugin including tools for water resource management, such as a hydrologic model and time series analysis methods, in the QGIS environment (Rossetto et al., 2018). The aim of this plugin is to use QGIS as a convenient and intuitive graphical user interface (GUI) that enables practitioners to deal with sophisticated software generics (Rossetto et al., 2019). Although FREEWAT can be considered as new, its broad applicability was already highlighted in multiple case studies, such as the management of coastal aquifers, modeling groundwater - surface water interactions and the assessment of climate change impacts on groundwater resources (De Filippis et al., 2020). FREEWAT comprises three main modules in which different tools are provided: the pre-processing module, the simulation codes module and the post-processing module. So far, the simulation codes module contains various packages of the MODFLOW-2005 family Harbaugh (2005) and MODFLOW-OWHM (Hanson et al., 2014), all of them being coded for physically-based flow and transport modeling, primarily in groundwater systems. The MODFLOW family of codes is only applicable for groundwater dominated systems but not e.g. for rainfall-runoff modeling.

In the particular case of karst hydrology, rainfall-runoff models are commonly applied for spring discharge predictions (Mazzilli et al., 2012b; Ollivier et al., 2019) and to enhance the understanding of hydrological processes in karst aquifers (Duran et al., 2020; Sivelle et al., 2019).Karst aquifers are widely used as drinking water supply both in Europe and worldwide and hence require appropriate model-based management (Chen et al., 2017a; Stevanović, 2019). Although promising physically-based model codes for the distributed simulation of karst aquifer processes exist (Chen et al., 2017b; Giese et al., 2018; Henson et al., 2018; Reimann and Hill, 2009; Reimann et al., 2011), and initiatives started to improve their applicability Berthelin et al. (2020); Berthelin and Hartmann (2020), a reasonable implementation of these models still is often restricted by data limitations (Jukić and Denić-Jukić, 2009; Ladouche et al., 2014).

Various types of rainfall-runoff karst models exist with different conceptual approaches. One common approach is to consider different combinations of the dominant flow compartments, i.e. conduits and matrix, as distinct buckets (Chang et al., 2017; Fleury et al., 2007; Jourde et al., 2015). For this conceptual idea of representing karst systems, Mazzilli et al. (2019) proposed an open-source GUI that is intuitively applicable also by practioners. Another way to conceptualize the behavior of karst systems in lumped models is to consider the complexity of recharge processes and the infiltration to slow and quickflow paths (Bittner et al., 2018a; Hartmann et al., 2012b; Ollivier et al., 2019). Given that no GUI for this type of conceptual approach exists, the implementation of such karst aquifer model in FREEWAT makes this framework more comprehensive and applicable for a broader range of water resource management issues.

We want to contribute to the FREEWAT modeling framework by implementing the recently

proposed LuKARS model (Bittner et al., 2018a,0; Teixeira Parente et al., 2019a) into the QGIS-integrated FREEWAT environment. LuKARS is a rainfall-runoff model that can be used to predict spring discharge in karst systems and was developed to perform land use change impact studies in karstic environments. This bucket-type model is based on the integration of dominant hydrotopes in a recharge area, which are distinct spatial entities defined by homogeneous soil and land use properties (Arnold et al., 1998). Each hydrotope shows a specific hydrological response to recharge events depending on its specific properties. Since spatially distributed properties need to be defined for each hydrotope when setting up a LuKARS model, integrating LuKARS in a GIS environment can make the visualization, application and evaluation of the model more intuitive. Moreover, LuKARS is one of the few karst hydrologic models that takes into consideration the possibility of modeling land use change impacts on karst spring discharge. This feature offers a solution to a timely challenge of the karst modeler community (Hartmann et al., 2014a). Therefore, we consider the GIS integration of LuKARS into FREEWAT as a valuable contribution to provide applicable and open source tools for water resources management.

In Section 4.2, we describe the concept of LuKARS and how the technical integration of the model into the QGIS-FREEWAT environment was performed. In Section 4.3, we show how LuKARS fits into the existing modular structure of FREEWAT. For a better reproducibility, we showcase the LuKARS tool in FREEWAT with a case study application. Finally, we discuss and conclude our efforts in Section 4.4 and 4.5.

4.2 Materials and methods

In this section, we provide a short description about the conceptual idea of LuKARS (Fig. 4.1a and b), the related assumptions and the flow components that are simulated by the model. Moreover, we provide a technical summary how the integration of LuKARS into FREEWAT was achieved.

4.2.1 Concept of LuKARS

The concept of LuKARS assumes that the dominant flow components in a karst system, i.e. the quickflow through conduits and fractures and a slow flow through the matrix, are controlled by the physical properties of the shallow subsurface, i.e. the soil-epikarst system. If the soil properties of a hydrotope are characterized by shallow soils with a coarse-grained texture (e.g. Hyd 2 in Fig. 4.1a), the quickflow paths are better connected and the hydrotope shows a fast and intense response to a given input signal, e.g. precipitation. In a hydrotope dominated by deep and more fine-textured soils (e.g. Hyd 4 in Fig. 4.1a), the quickflow is less intense and matrix infiltration is more constant.

In LuKARS, each hydrotope is represented by a distinct bucket that has three different flow components (Fig. 4.1b), i.e. the quickflow (Q_{hyd}), the infiltration into the rock matrix (Q_{is}) feeding the baseflow storage (B) and a secondary spring discharge (Q_{sec}). Q_{hyd} is activated once a hydrotope specific storage value (E_{max}) was exceeded and stops after the hydrotope storage reaches a

lower threshold (E_{min}). By that, a hysteretic behavior of the soil-epikarst system is simulated. Q_{is} and Q_{sec} are both implemented based on linear transfer functions. In contrast to Q_{is}, Q_{sec} is only active if the hydrotope storage is higher than a defined threshold for secondary spring discharge (E_{sec}). For more information about the mathematical details, the interested reader is referred to the works of Bittner et al. (2018a), Teixeira Parente et al. (2019a) and Bittner et al. (2020a), where LuKARS was applied for the case study of Waidhofen an der Ybbs (Fig. 4.1c).
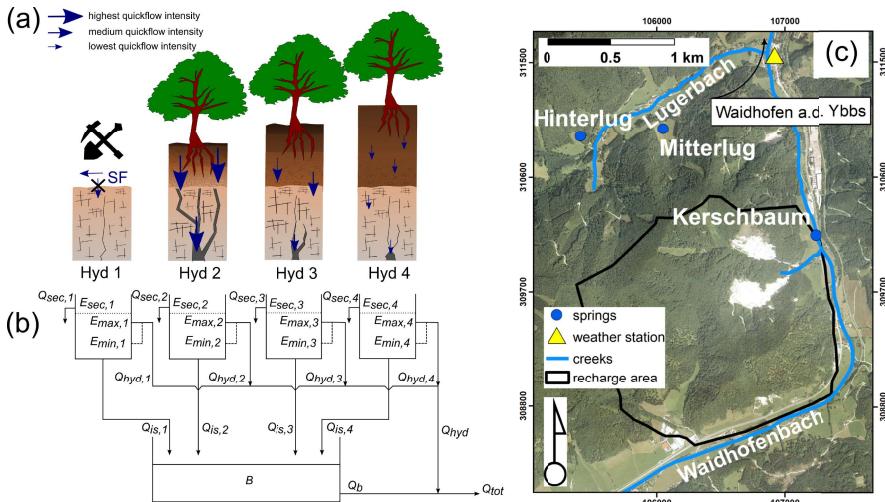
Figure 4.1: Overview of the LuKARS model concept and the study area. (a) Physical concept of the hydrotopes implemented in LuKARS. (b) Model representation of the LuKARS hydrotopes. (c) The Kerschbaum spring recharge area close to Waidhofen a.d. Ybbs (Austria).

4.2.2 LuKARS integration in FREEWAT

The goal of the LuKARS integration was to take advantage of the modular framework of FREE-WAT and using the provided pre- and post-processing tools. This concept is shown in Fig. 4.2, which highlights the use of the GIS to create and visualize the hydrotope shapefiles as well as the FREEWAT input data management in the pre-processing step. In the post-processing, the integration of LuKARS benefits from the existing time series analysis tools in FREEWAT and the GIS functionalities to store the hydrotope parameters in shapefiles.

The integration of all FREEWAT tools into the QGIS environment is performed with the Python programming language. Although most of QGIS is written in C++, it allows for connecting Python scripts as standalone tools and plugins via PyQGIS (Bhatt et al., 2014). During the installation process of QGIS, a folder directory is created in which additional plugins, such as FREEWAT, can be pasted. In this way, QGIS knows what has to be loaded when starting. Following the

guidelines provided on the project webpage, a FREEWAT folder containing all relevant python scripts should be dropped in this directory. This directory establishes the connection between QGIS, FREEWAT and LuKARS. LuKARS is stored in a single folder containing all necessary Python scripts to be added to the mentioned FREEWAT folder. Most of the LuKARS code was programmed object-oriented with Python classes. This folder is connected to the plugin by calling it in the overall plugin operating code Freewat.py. Then, when starting QGIS, LuKARS appears in the FREEWAT drop-down menu in the QGIS toolbar. It is planned that the LuKARS model comes with one of the next official releases of FREEWAT. However, interested persons can also download the required LuKARS python scripts from GitHub (https://github.com/dbittner87/LuKARS). A detailed description where these utilities need to be added in the QGIS-FREEWAT folder structure is also provided there.
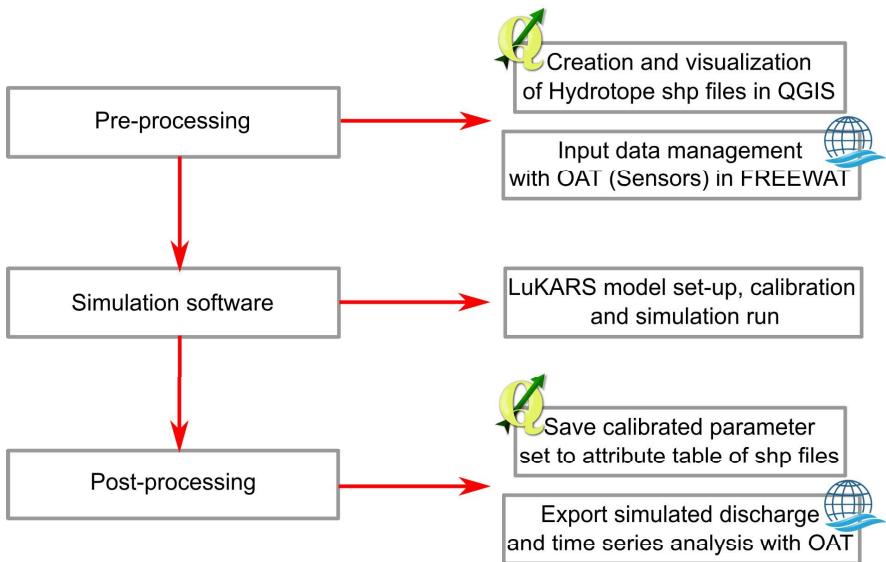
Figure 4.2: A concept of the modular framework of FREEWAT in QGIS consisting of Pre-processing, Simulation software and Post-processing tools and how this framework is used for LuKARS.

4.3 Using LuKARS in FREEWAT

In order to make the use of LuKARS user-friendly, general steps that need to be taken to perform modeling tasks with FREEWAT should be similar for all models integrated in this framework. In the following, we explain the relevant steps during the pre-processing, modeling and post-processing phases. We showcase this application for the Kerschbaum spring case study used

in Bittner et al. (2018a). The Kerschbaum springshed is a small-scale, pre-alpine and dolomite dominated aquifer system close to Waidhofen a.d. Ybbs (Austria) (Fig. 4.1c). The recharge area is affected by anthropogenic impacts in form of increasing mining activities. In order to investigate the hydrological impacts of this land use change, Bittner et al. (2018a) developed the LuKARS model. For more information about this area we refer to the work of Narany et al. (2019). The required data files to perform this simulation can be downloaded from GitHub.

4.3.1 Pre-processing

In order to run LuKARS, time series data with a daily temporal resolution (at least precipitation and spring discharge) and hydrotope shapefiles (vector data) are needed. Similar to the use of MODFLOW in FREEWAT, the first step to be done is to go to Model Setup → Create Model. This step is required in order to define the length and time units, set the working directory and to define the coordinate reference system (CRS). After finishing this initial step, FREEWAT creates different model tables as data objects in which the defined information is stored.

In the next step we need to load all relevant input time series in the Observation analysis tool (OAT) (Cannata and Neumann, 2017; Cannata et al., 2018). The OAT library includes two classes: the OAT Sensor and the OAT Method class. We use the OAT Sensor class to load and store the time series needed for LuKARS. The advantage of using OAT at this pre-processing step is that the time series can be stored in a SQLite database. If we save the QGIS project after loading the time series with OAT, we do not have to load them again once we resume our LuKARS project in FREEWAT. As time series input, LuKARS requires at least a precipitation and a discharge time series with daily temporal resolution. Optionally, it is possible to load a temperature time series that is used to run a temperature-based evapotranspiration model (Thornthwaite, 1948) and a snow model (degree-day method, Martinec (1960)). In order to get a daily evapotranspiration time series from the monthly values obtained with the Thornthwaite method, the monthly evapotranspiration is divided by the number of days in a month. The resulting daily evapotranspiration value is assumed to be representative for the 15th day of a month. Then, a daily evapotranspiration time series is obtained through linear interpolation between each month. The selection of these modeling approaches is based on the fact that they provide reliable results for the Kerschbaum spring recharge area as shown in the work of Bittner et al. (2018a). It is planned that further different approaches will be integrated in future versions. For our case study example, we loaded daily time series of spring discharge, precipitation and temperature.

In the next step, we can either load or generate hydrotope shapefiles. For the Kerschbaum case study, the hydrotope shapefiles already include the relevant model parameters introduced in Table 4.1. If these shapefiles have to be generated, there are different methods to create them, e.g. by Koeck and Hochbichler (2012) or the German Association for Water, Wastewater and Waste (Deutsche Vereinigung für Wasserwirtschaft, Abwasser und Abfall, DWA) (DWA, 2018). In Bittner et al. (2018a), we used a modified hydrotope map of the one created by Koeck and Hochbichler (2012). The map we use here (see Fig. 4.3a) was created using a recently proposed hydropedological fieldguide by DWA (2018). The DWA (2018) method has the advantage that it

can also be used to derive ranges for some of the lumped parameters required in LuKARS (Bittner et al., 2020a). So far, there is no automatic routine to generate the hydrotope shapefiles. It has to be noted that for using LuKARS in FREEWAT, each hydrotope needs to be stored in a separate shapefile. We decided to store them in different shapefiles in order to simplify their individual manipulation, their distinct manual calibration as well as the process of loading the hydrotopes in the LuKARS FREEWAT interface. These shapefiles need to be projected in the same CRS as previously defined in the model tables since the CRS is needed to automatically calculate the exact area each LuKARS hydrotope covers in a regarded recharge area.
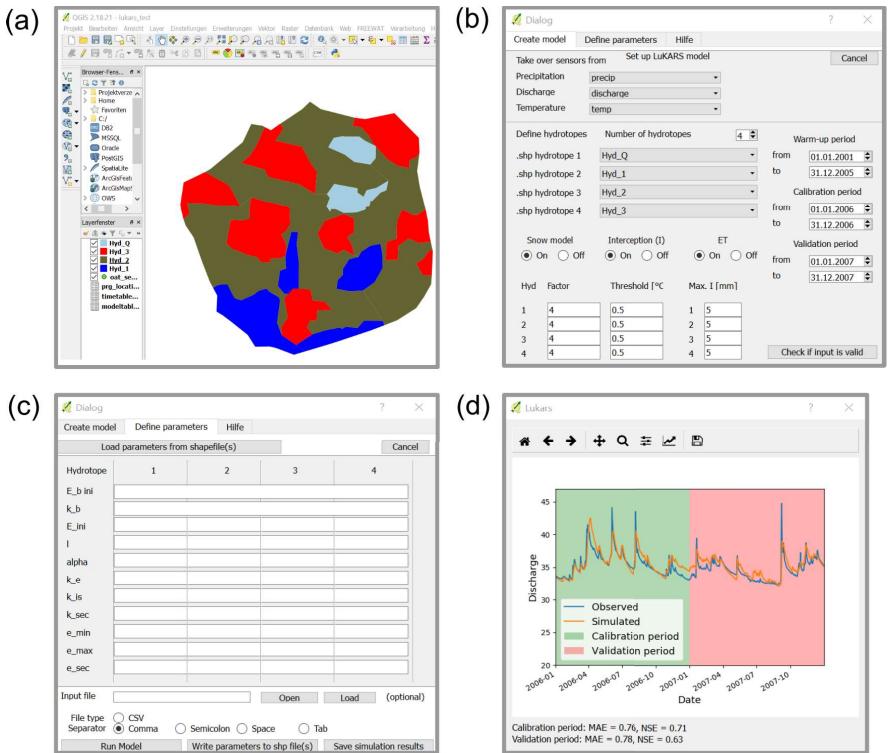
Figure 4.3: Overview of the GUI's used in LuKARS in FREEWAT. a) The QGIS interface showing the hydrotope map of the Kerschbaum spring recharge area as an example. b) Setting up the LuKARS model by loading the relevant time series saved as OAT sensors (precipitation and discharge are required, temperature is optional) and hydrotope shapefiles, selecting which additional module(s) to be used and defining all modeling periods. c) Definition of all model parameters. d) Plotting window showing the modeling results.

4.3.2 Model application

After the hydrotope shapefiles and the required time series have been loaded, we can start using the LuKARS model in FREEWAT. The first interface that is loaded is shown in Fig. 4.3b. Since the time series are stored as OAT sensors, the interface recognizes them and we just need to select the right one for each input.

Then, we have to define the total number of hydrotopes which will be loaded in LuKARS. Note that in the current version, the maximum number of possible hydrotopes is limited to four. This is due to the fact that each hydrotope has seven calibration parameters. In Teixeira Parente et al. (2019a) it was shown that the parameter uncertainties when having four hydrotopes can still be handled, but so far we do not know how this changes when more than four hydrotopes need to be calibrated. For the Kerschbaum spring case study, we have four hydrotopes that have to be loaded. These are Hyd Q, Hyd 1, Hyd 2 and Hyd 3. The order in which we load the hydrotopes is not crucial. For more information about the hydrotopes, we refer to Bittner et al. (2020a).

In the right part of the interface (Fig. 4.3b), we define the warm-up, calibration and validation period. If the chosen periods overlap, an error message occurs to warn the user and the starting dates of each period will adapted automatically. For example, if the calibration period overlaps with the warm-up period, the starting date of the calibration period is set to the end date of the warm-up period. For our case study, the following periods are defined as in Bittner et al. (2018a): warm-up period from 01/01/2001 to 12/31/2005, calibration period from 01/01/2006 to 31/12/2006 and validation period from 01/01/2007 to 31/12/2007 (Fig. 4.3).

In the lower part of the interface, the optional snow, evapotranspiration and interception modules can be activated. The snow module makes use of the degree-day method (Martinec, 1960) and requires setting a melt factor F [mm d^{-1}°C^{-1}] as well as a temperature threshold T_f [°C] for melt for each hydrotope. The interception module requires setting a maximum interception value I_{max} [mm] that depends on the respective land cover of the hydrotope. For a given event, the effective rainfall is calculated by subtracting Imax from the measured precipitation value. The evapotranspiration module does not require the definition of any further parameters.

After everything was defined, it is possible to advance to the Define parameters interface after proving the validity of all input (*Check if input is valid*). The function to check the validity of the input helps the users recognizing errors before starting the model calibration.

The *Define parameters* interface is shown in Fig. 4.3c. Three different ways for setting the hydrotope parameters are integrated in LuKARS. If no parameter set exists for a recharge area to be modeled, the first choice would be to manually define the parameters. Another option is to load a parameter set from a csv-file. A template how this file should be constructed is provided on GitHub. The third option is to load the parameters from the hydrotope shapefiles. For the Kerschbaum spring example, we provide the parameters in Table 4.1. Once all parameters were defined, the *Run model* button initiates a LuKARS simulation with the given parameter set and a new window opens that shows the simulated and the observed hydrograph of a regarded karst spring.

Table 4.1: Overview of all model parameters for each hydrotope and all recharge areas. A detailed description of the model can be found in Bittner et al. (2018a) Bittner et al. (2018) and in the material provided on GitHub.

Hydrotope-specific parameters					
Parameter	Hyd Q	Hyd 1	Hyd 2	Hyd 3	Parameter description
E_{ini} [mm]	0	1	1	1	Initial value of hydrotope storage
E_{min} [mm]	0	23	60	90	Hydrotope storage under dry cond.
E_{max} [mm]	1	31	120	200	Hydrotope storage under sat. cond.
E_{sec} [mm]	0	35	180	380	Activat. level for secondary springs
k_{hyd} [m^{2}d^{-1}]	0	90	85	77	Discharge parameter for quickflow
k_{is} [m mm^{-1}d^{-1}]	0	0.02	0.0055	0.0025	Discharge coeff. for recharge
k_{sec} [m mm^{-1}d^{-1}]	0.9	0.095	0.026	0.022	Secondary spring discharge coeff.
α [-]	0	0.9	0.8	0.55	Quickflow exponent
l_{hyd} [m]	550	1600	900	960	Mean hydrotope distance to spring
F [mm d^{-1}°C^{-1}]	4	4	4	4	Melt factor in degree-day method
T_f [°C]	0.5	0.5	0.5	0.5	Temp. threshold for snow melt
I_{max} [mm]	0	5	5	5	Max. interception of land use
Baseflow storage parameters					
k_b [m mm^{-1}d^{-1}]	0.00043				Baseflow discharge coefficient
$E_{b,ini}$ [mm]	2900				Initial value of baseflow storage

4.3.3   Post-processing

The newly opened window allows to visually compare the simulated and the observed time series (Fig. 4.3d). Moreover, the window is split into two frames, one for the calibration and one for the validation period. For both periods, two objective evaluation criteria are calculated, namely the mean absolute error (MAE) and the Nash-Sutcliffe Efficeny (Nash and Sutcliffe, 1970). In case those criteria do not show an acceptable goodness of fit for the calibration period, we can go back to the *Define parameters* interface and change the parameters. During this trial-and-error calibration, the modeler should only focus on the goodness of fit in the calibration window of course. In order to better focus on parts of the simulation period, we can zoom into a period of interest, e.g. a high flow event, to see which properties of the measured time series are matched by our simulated time series and which are not. This calibration procedure can be continued until an acceptable parameter set was found. Once such a parameter set was identified, we can save the graph as an image file which can then be shared with stakeholders or included in a report. Also, the simulated time series can be exported as a txt or csv file using the *Save simulation results* function in the *Define parameters* interface. Finally, we can save the hydrotope parameters to the attribute table of the respective hydrotope shapefiles by applying the *Write parameters to shp file(s)* function in the *Define parameters* interface. This allows to easily share the relevant model files with stakeholders and to apply the model on other computers without the need to define the parameters from scratch. Once having written the parameters to the shapefiles, they can directly be loaded to the *Define*

parameters interface by clicking *Load parameters from shapefile(s)*. It is important to note that no automatic calibration procedure is coupled to LuKARS in FREEWAT so far but will be included in future releases.

Additional post-processing tools are provided in the FREEWAT environment, in particular in OAT. The OAT Method integrates several statistical analysis tools that can be used to compare the simulated and observed time series. For more details about these tools, the interested reader is referred to Rossetto et al. (2018).

4.3.4 Land use change impact modeling

Once a reliable parameter set was identified, we can use this parameter set to simulate the hydrological impacts of a land use change on karst spring discharge. To do so, modified hydrotope shapefiles are needed that include the respective land use change compared to the original set of hydrotopes. Several ways exist how land use change scenarios and modified hydrotope shapefiles can be generated, e.g. participatory approaches (Mehdi et al., 2018) or repetitive field mapping campaigns (DWA, 2018). Another possibility, which was chosen by Bittner et al. (2018a), is to derive land use changes from change detection analysis with orthophotos. In order to copy the parameter set found during calibration to the modified hydrotope shapefiles, we can use the *Copy from vector layer tool* in FREEWAT. This function copies the attribute tables from the original hydrotopes to the new ones. By that, we can avoid to manually enter the parameters in LuKARS again. Using the modified hydrotopes, a LuKARS run can be performed and the effects of the respective land use change on spring discharge can be evaluated. As an example, we provide such a set of hydrotope shapefiles including the land use change modeled in Bittner et al. (2018a) on GitHub.

4.4 Discussion

Given that the FREEWAT project ended in 2017, the maintenance of the initiative now depends on joint efforts by the developers group and those who like to contribute to it. In our study, we highlight that previous research studies and related outcomes can act as a platform for further developments and enhancements. The LuKARS integration in FREEWAT provides a GUI for a lumped karst aquifer model, making its application more intuitive for stakeholders dealing with water management issues in karst systems. Possible stakeholders who may use LuKARS in the future are researchers, water resources managers, public authorities, engineers and non-governmental organizations. They can be reached by the broad number of persons who already apply FREEWAT and are informed about new releases, by social media and stakeholders workshops.

LuKARS represents a complementary GUI for karst hydrologic modeling since the way how it conceptualizes karst aquifers is different as compared to the KarstMod platform introduced by Mazzilli et al. (2019). The integration approach was chosen following the state of the art of software development, i.e. object-oriented. Thus, the Python model classes and the implemented

functions can easily be accessed, applied and adapted by interested persons who are familiar with programming. Nevertheless, some improvements are envisaged for future releases in order to enhance the applicability of LuKARS in FREEWAT. So far, the generation of hydrotope shapefiles is based on field mapping campaigns using different mapping approaches. However, a map-based generation of hydrotope shapefiles should be made possible if detailed information about soil physical properties and land use is available in form of raster and/or vector data. We plan to create an automated procedure that can process available soil and land use data in order to generate hydrotope shapefiles within a GIS environment.

A limitation of the current LuKARS version in FREEWAT is that it requires manual calibration. However, lumped karst aquifer models are typically calibrated with automatic calibration routines (Hartmann et al., 2017; Teixeira Parente et al., 2019a). It is foreseen to implement an automatic calibration framework in the modular structure of FREEWAT, such that it will be usable also for other models available in the platform. For example, we believe that implementing the SAFE toolbox by Pianosi et al. (2015) into the FREEWAT framework would be very welcome by the user community.

Finally, the current version of LuKARS allows for the definition of up to four hydrotopes. Larger scale studies may require a larger number of hydrotopes. However, this would lead to a rapid increase of fitting parameters and the risk of overfitting. The opportunity of increasing the number of hydrotopes should be tested for different case studies, e.g. using the World Karst Spring hydrograph (WoKaS) database presented by Olarinoye et al. (2020), and made available along with an automatic sensitivity and parametric uncertainty toolbox.

4.5   Conclusions

In this paper we introduce a user-friendly environment for modeling the impacts of land use changes on the spring discharge of a karst system. We integrated the LuKARS model into the FREEWAT environment, which is a water resources management toolkit implemented as a plugin in QGIS. The advantages of the ÖuKARS integration following the tight-coupled FREEWAT approach are, that

1. QGIS serves as a GUI and provides a useful platform to map, store and change the dominant hydrotopes in a recharge area of interest,

2. FREEWAT's modular framework for hydrological modeling, i.e. pre-pro-cessing, simulation codes and post-processing represents a tailored framework to bring in new model codes that make the FREEWAT environment more comprehensive,

3. Stakeholders can use the measured and simulated time series obtained with the LuKARS model and apply all analysis tools present in FREEWAT.

We want to emphasize that FREEWAT provides a valuable environment with open source modeling and analysis tools that can easily be applied by stakeholders. The continuous discussions in

this group of researchers and practitioners guarantees that the framework improves while remaining applicable. Moreover, this close cooperation also makes sure that only tools will be integrated which are considered beneficial for FREEWAT and its end-users.

Chapter 5

Uncertainty quantification of LuKARS and parameter dimension reduction using active subspaces

Teixeira Parente et al. (2019a)[1]

Abstract

In this article, we perform a parameter study for a recently developed karst hydrological model. The study consists of a high-dimensional Bayesian inverse problem and a global sensitivity analysis. For the first time in karst hydrology, we use the active subspace method to find directions in the parameter space that dominate the Bayesian update from the prior to the posterior distribution in order to effectively reduce the dimension of the problem and for computational efficiency. Additionally, the calculated active subspace can be exploited to construct sensitivity metrics on each of the individual parameters and be used to construct a natural model surrogate. The model consists of 21 parameters to reproduce the hydrological behavior of spring discharge in a karst aquifer located in the Kerschbaum spring recharge area at Waidhofen a.d. Ybbs in Austria. The experimental spatial and time series data for the inference process were collected by the water works in Waidhofen. We show that this case study has implicit low-dimensionality, and we run an adjusted Markov chain Monte Carlo algorithm in a low-dimensional subspace to construct samples of the posterior distribution. The results are visualized and verified by plots of the posterior's push-forward distribution displaying the uncertainty in predicting discharge values due to the experimental noise in the data. Finally, a discussion provides hydrological interpretation of these results for the Kerschbaum area.

5.1 Introduction

Models are commonly used in karst systems to investigate the dominant hydrological processes and the quantity and quality of water resources in well-defined surface or subsurface catchments. Various karst modeling approaches exist, ranging from black-box models (Labat et al., 2000, 1999; Jukić and Denić-Jukić, 2008), i.e., transferring an input signal to a desired output signal, over lumped parameter models (grey-box) (Fleury et al., 2009; Mazzilli et al., 2017; Sivelle et al., 2019) to distributed process-based models (Reimann and Hill, 2009; Giese et al., 2018; Henson et al., 2018; Sauter et al., 2006). Given their ability to represent the physical characteristics of a catchment in detail, distributed process-based models are usually the first choice in water resources research. In the particular case of karst aquifers, however, acquiring the relevant data for these models is challenging due to the heterogeneous nature of karstic systems and their mostly unknown subsurface drainage systems (Xu et al., 2018). Also, past studies have shown that even if physical parameters may be obtained from field observations, the fact that they mostly represent point measurements can lead to a severe mismatch when using these parameters in distributed hydrological models (Hogue et al., 2006; Rosero et al., 2010). For these reasons, lumped process-based models are commonly accepted modeling approaches in karst water resources research (Jukić and Denić-Jukić, 2009; Jourde et al., 2015; Hartmann et al., 2013b). The parameters of such lumped modeling approaches are typically not directly measurable in the field and need to be estimated in the framework of model calibration (Hartmann et al., 2017). This leads to a decisive trade-off: on the one hand, lumped models based on a low number of calibration parameters, e.g., 4 to 6, are less prone to non-uniqueness in parameter identification (Jakeman and Hornberger, 1993; Beven, 2006), i.e., different parameter combinations lead to the same result. However, the representation of the dominant hydrological processes in karst systems may be too simple and not sufficiently represented by this low number of parameters (Hartmann et al., 2013a). In contrast, by including more calibration parameters to better represent relevant processes in the model structure, such as the effect of land use changes on spring discharges, the parameters may become unidentifiable, which can reduce the prediction accuracy of the model (Hartmann et al., 2014a). To tackle the challenge of applying lumped parameter models with a high-dimensional parameter space for karst hydrological research studies, there is a need to perform comprehensive parameter studies to avoid model overparametrization and to reduce model parameter and output uncertainties.

With the rise of computational power in the last two decades, Bayesian inverse problems have become a popular part of comprehensive parameter studies for hydrological models (Engeland and Gottschalk, 2002; Kavetski et al., 2006; Kitanidis and Lee, 2014; Thiemann et al., 2001). In contrast to classical inverse problems, whose formulation is often ill-posed, a Bayesian problem formulation introduces regularizing prior information which gives a different formulation that is mathematically well behaved. Bayesian inversion aims at finding a posterior distribution on the model parameters incorporating the information of measured, noisy data, e.g., spring discharge. The posterior, which is also used to quantify uncertainty in the inferred parameters, is proportional to the product of the likelihood function and the prior, a distribution that is assumed to be known

for the model parameters based on prior knowledge, e. g., resulting from field campaigns or manual model calibration.

The most common strategy used for approximating a posterior is to construct samples from the distribution with desired properties. *Markov chain Monte Carlo* (MCMC) and its derivatives are popular sample-based techniques (Vrugt et al., 2008; Martín-Arias et al., 2020); however, they present computational challenges. These algorithms generally require a very large number of evaluations of the model to provide an acceptable result. In the hydrological community, where a single model evaluation is often quite computationally expensive, naive implementations of these methods may not be viable, and having too few samples causes the solution to be polluted with sampling error. One way to reduce this effect is to construct a surrogate model that has a much lower computational cost. Common approaches for global surrogate models include stochastic finite element approaches for forming polynomial approximations (Xiu and Karniadakis, 2002; Wan and Karniadakis, 2006; Le Maître et al., 2004a,0) and using tensor grid or sparse grid stochastic collocation methods (Almeida and Oden, 2010; Nobile et al., 2008). Another strategy is to use adaptive sampling methods to reduce sample-based error as shown in e. g., Haario et al. (2006); Vrugt et al. (2009); Mattis and Wohlmuth (2018). Another attribute that affects the computational expense of sample-based approximation methods is high-dimensionality in the space of uncertain parameters because it may slow the identification of areas of high probability and has the tendency to produce highly correlated samples. There has been much effort in developing algorithms that are more efficient and reduce computational expense due to high-dimensional parameter spaces by effectively reducing the dimension (Boyce and Yeh, 2014; Bui-Thanh and Girolami, 2014; Constantine et al., 2016; Cui et al., 2016).

A relatively new technique for dimension reduction is the *active subspace method* presented in Constantine et al. (2014), Constantine (2015), and Russi (2010), which seeks orthogonal directions in the space of parameters that dominate the Bayesian update from the prior to the posterior distribution. These dominant directions span the subspace and define a new coordinate system a low-dimensional Markov chain can move in. Chains in lower dimensions have preferable properties concerning autocorrelation times which makes them more efficient when producing posterior samples of hydrological model parameters. As a bonus, the active subspace can be exploited also to calculate global sensitivity metrics for individual parameters as shown in Constantine and Diaz (2017). The active subspace method has previously been successful in reducing the effective dimension of parameter spaces, e. g., for efficient Bayesian inversion of a complex subsurface process (Teixeira Parente et al., 2019b), or to study sensitivities in a hydrological model (Jefferson et al., 2015). An added benefit of the active subspace method is that there is a natural cheap global surrogate model embedded in the method via global polynomial regression in the low-dimensional active subspace. Thus the advantage of the active subspace method is threefold: it effectively reduces the dimension of the Bayesian inverse problem, it easily produces global sensitivity metrics, and it naturally allows for the construction of a cheap global surrogate model. All of these are gained from the same moderate number of forward model evaluations.

While several hydrological studies address the issue of model parameter sensitivities for infer-

ence (e. g. Cuntz et al. (2016); Mockler et al. (2016); Vanuytrecht et al. (2014)), there has been little effort in karst hydrological research to investigate the low-dimensionality of a corresponding parameter estimation problem (e. g., Sarrazin et al. (2018)). Our approach is different to these studies in the sense that we study dominant *directions* in parameter spaces and do not focus on sensitivities of coordinate-aligned, i. e., individual parameters. In this regard, the objective of this manuscript is the introduction of the active subspace method to the field of karst hydrology as a technique for dimension reduction and sensitivity analysis in parameter studies. We demonstrate this method and its mentioned advantages by investigating parameter relationships in the LuKARS model, a lumped karst aquifer model with a high-dimensional parameter space that was recently developed by Bittner et al. (2018a) to perform land use change impact studies in karstic environments. We hypothesize that it is possible to reduce the dimensions of the parameter space in LuKARS, thus saving computational cost, and to better constrain the parameter ranges of the most sensitive model parameters leading to a reduction in model parameter and model result uncertainties.

This article is organized as follows. Section 5.2 provides a brief introduction into the study area and the structure of the LuKARS model. In Section 5.3, we explain Bayesian inversion, how we exploit active subspaces for it, the construction of global sensitivity values and the concrete setting for our application. The computational results are presented in Section 5.4, followed by a comprehensive discussion in Section 5.5 in which we also comment on limits and transferability of the proposed method. Finally, we conclude with a summary in Section 5.6.

5.2 Case study

5.2.1 Kerschbaum spring recharge area

The karst spring that we investigate in the present study is the Kerschbaum spring located about 10km south of the city of Waidhofen a.d. Ybbs (Austria) (Fig S1 a and b). Its recharge area was delimited in a former study by Hacker (2003) and comprises about $2.5 \, \text{km}^2$. This pre-alpine catchment is part of the eastern-most foothills of the Northern Calcareous Alps with the lowest elevation of 435 m at the Kerschbaum spring and a maximum elevation of 868 m on the summit of the mountain Glashüttenberg. The climate of the study area can be described as warm-moderate, with an annual mean temperature of $8°\text{C}$ and an annual mean precipitation of 1379 mm, both determined from daily measuring data recorded at the Hinterlug weather station between 1981 and 2014. Forests represent the dominant land cover in the study area with beeches as primary tree species. Moreover, parts of the recharge area are used for dolomite mining.

From a geological point of view, the entire recharge area of the Kerschbaum spring is dominated by a lithologic sequence of Triassic dolostones (Fig. S1 c). Apart from the absence of significant sinkholes in the regarded recharge area, leading to the fact that diffuse infiltration plays a key role for groundwater recharge, Hacker (2003) also provided evidence for a deep karstified aquifer system with a well-connected drainage system through fractures and conduits in the Kerschbaum spring aquifer. It is important to note that the Kerschbaum spring represents the most

important source for the freshwater supply of the city and the surroundings of Waidhofen and is thus of particular interest for water resources research studies (Bittner et al., 2018a).

5.2.2   The LuKARS model

The LuKARS model was recently proposed by Bittner et al. (2018a) with the aim to investigate the hydrological effects of land use changes in karst systems. LuKARS therefore considers the dominant hydrotopes in a defined recharge area, i. e., areas characterized by homogeneous soil and land cover properties, as distinct spatial units. The sum of the individual hydrotope responses to a given input signal (e. g., precipitation) plus the contribution of a shared linear baseflow storage is then the total spring discharge that should be modeled at a catchment's outlet. As input data, the model itself needs a precipitation time series as well as the hydrotope soil information to run. If further processes affecting the effective precipitation are considered, such as interception and evapotranspiration, further input data is required. In our case, we also take into account snow melt and accumulation, interception and evapotranspiration, for which we further need a temperature time series with a daily resolution. Moreover, a measured discharge time series is needed from the spring of interest to calibrate and validate the model. In the particular case of the Kerschbaum spring, the discharge is measured with a flowmeter directly in the spring. The discharge, precipitation, and temperature time series with a daily resolution for our model period from 2006 to 2008 were kindly provided by the water works Waidhofen a.d. Ybbs. The input time series are shown in Fig. S3. The LuKARS model for the Kerschbaum spring in Waidhofen a.d. Ybbs was set up in Bittner et al. (2018a) and includes four spatially lumped dominant hydrotopes in the considered recharge area, shown in Fig. S2. Hydrotopes 1-3 have beeches as dominant tree species; however, they differ in terms of their individual soil characteristics and spatial shares. While the first hydrotope (denoted by Hyd 1) covers 13% of the recharge area and is characterized by shallow soils with mostly coarse-grained soil particles, hydrotope 3 (denoted by Hyd 3), in contrast, covers 27% of the catchment and is defined by deeper and fine textured soils. Hydrotope 2 (denoted by Hyd 2) has the largest spatial share in the Kerschbaum spring recharge area (56%) and represents a transition hydrotope between Hyd 1 and Hyd 3 with moderate soil thicknesses and coarse to fine-textured soils. Hydrotope Q (denoted by Hyd Q) characterizes the dolomite quarries, which covered about 4% of space in the recharge area during the model period (2006-2008) in this study.

From a hydrological point of view, the areas of the dolomite quarries are drained by surface runoff and do not contribute to the Kerschbaum spring discharge. As an obligation to avoid a possible contamination of the aquifer from the quarry areas, a protective layer consisting of fine material prevents infiltration into the groundwater system. Thus, Hyd Q is excluded from model calibration and will not be mentioned hereafter. Also, Bittner et al. (2018a) derived the baseflow coefficient k_b to match the relatively constant baseflow discharge of the Kerschbaum spring with its low temporal variability. For this reason, as well as to put the focus on calibrating the hydrotope parameters, k_b was chosen as calibrated by Bittner et al. (2018a). More details about the LuKARS model, i. e., a description of the equations used in LuKARS and the relevant parameters, are provided in A.1. In the following, we use an index $i \in \{1, 2, 3\}$ to denote specifications for Hyd i.

Each hydrotope is modeled as an independent bucket that has three different discharge components. The first, representing quickflow ($Q_{\mathrm{hyd},i}$) occurring via preferential flow paths (e. g., conduits), is described by a non-linear hysteresis function that is activated once a defined storage threshold ($e_{\mathrm{max},i}$) is reached and stops after the storage value falling below a predefined minimum storage value ($e_{\mathrm{min},i}$). The second and third discharge components are both implemented by a linear discharge function and represent the discharge to a shared baseflow storage ($Q_{\mathrm{is},i}$) as well as secondary spring discharge ($Q_{\mathrm{sec},i}$), i. e., a discharge component that transfers water out of the catchment and does not contribute to the spring discharge. All together, seven parameters need to be calibrated for the implementation of each single hydrotope. These are the discharge parameter $k_{\mathrm{hyd},i}$ and the dimensionless exponent α_i for $Q_{\mathrm{hyd},i}$, the storage thresholds for the quickflow activation ($e_{\mathrm{min},i}$) and ($e_{\mathrm{max},i}$), parameter $k_{\mathrm{is},i}$ as the discharge coefficient of $Q_{\mathrm{is},i}$ and, finally, $k_{\mathrm{sec},i}$ and $e_{\mathrm{sec},i}$ as the discharge coefficient and the activation level for $Q_{\mathrm{sec},i}$, respectively. Given the different physical characteristics of all defined hydrotopes, the parameters of one hydrotope need to follow some constraints with respect to the parameters used for the implementation of other hydrotopes. From a practical point of view, this means that a hydrotope with shallow and coarse-grained soils (e. g., Hyd 1) needs to have a lower storage capacity and higher discharge coefficient as compared to a hydrotope with deep and fine-textured soils (e. g., Hyd 3). For the particular case of the three hydrotopes in the Kerschbaum spring recharge area, the parameter constraints are given as follows:

$$
\begin{aligned}
k_{\mathrm{hyd},1} &\geq k_{\mathrm{hyd},2} \geq k_{\mathrm{hyd},3} \\
e_{\mathrm{min},1} &\leq e_{\mathrm{min},2} \leq e_{\mathrm{min}.3} \\
e_{\mathrm{max},1} &\leq e_{\mathrm{max},2} \leq e_{\mathrm{max},3} \\
\alpha_1 &\geq \alpha_2 \geq \alpha_3 \\
k_{\mathrm{is}.1} &\geq k_{\mathrm{is},2} \geq k_{\mathrm{is},3} \\
k_{\mathrm{sec},1} &\geq k_{\mathrm{sec},2} \geq k_{\mathrm{sec}.3} \\
e_{\mathrm{sec},1} &\leq e_{\mathrm{sec},2} \leq e_{\mathrm{sec}.3}
\end{aligned}
\tag{5.1}
$$

Although the introduced condition for the α values is not strictly necessary, we implemented it to further enhance the quick response of hydrotopes with a low difference between $e_{\mathrm{min},i}$ and $e_{\mathrm{max},i}$ and a generally low value of $e_{\mathrm{max},i}$ during high precipitation events. (Bittner et al., 2018a) manually calibrated the LuKARS model for the Kerschbaum spring recharge area. Based on this trial-and-error calibration, it was possible to reliably determine possible ranges of all model parameters. These are shown in Table 5.1 and will be used as prior parameter intervals for the presented study in a Bayesian setting.

5.3 Parameter inference

In this section we present our approach for solving the Bayesian inverse problem of inferring parameter information for the LuKARS model. Since high-dimensional parameter spaces complicate Bayesian inference, we utilize the active subspace method, a recent emerging set of tools for

dimension reduction. We focus the inference process only with a few linear combinations of parameters that are dominantly driving the update from the prior to the posterior distribution. After the method is explained formally, but with links to the actual hydrological problem, we explain Bayesian inversion and its application in detail.

Table 5.1: Prior intervals for physical parameters

No.	Parameter	Lower bound	Upper bound	Unit	Description
1	$k_{\mathrm{hyd},1}$	9	900	$\mathrm{m^2 d^{-1}}$	discharge parameter for $Q_{\mathrm{hyd},1}$
2	$e_{\mathrm{min},1}$	10	50	mm	min. storage capacity Hyd 1
3	$e_{\mathrm{max},1}$	15	75	mm	max. storage capacity Hyd 1
4	α_1	0.7	1.6	–	quickflow exponent of Hyd 1
5	$k_{\mathrm{is},1}$	0.002	0.2	$\mathrm{m\,mm^{-1}d^{-1}}$	discharge parameter for $Q_{\mathrm{is},1}$
6	$k_{\mathrm{sec},1}$	0.0095	0.95	$\mathrm{m\,mm^{-1}d^{-1}}$	discharge parameter for $Q_{\mathrm{sec},1}$
7	$e_{\mathrm{sec},1}$	25	70	mm	activation level for $Q_{\mathrm{sec},1}$
8	$k_{\mathrm{hyd},2}$	8.5	850	$\mathrm{m^2 d^{-1}}$	discharge parameter for $Q_{\mathrm{hyd},2}$
9	$e_{\mathrm{min},2}$	40	80	mm	min. storage capacity Hyd 2
10	$e_{\mathrm{max},2}$	80	160	mm	max. storage capacity Hyd 2
11	α_2	0.5	1.3	–	quickflow exponent of Hyd 2
12	$k_{\mathrm{is},2}$	0.00055	0.055	$\mathrm{m\,mm^{-1}d^{-1}}$	discharge parameter for $Q_{\mathrm{is},2}$
13	$k_{\mathrm{sec},2}$	0.0023	0.23	$\mathrm{m\,mm^{-1}d^{-1}}$	discharge parameter for $Q_{\mathrm{sec},2}$
14	$e_{\mathrm{sec},2}$	130	220	mm	activation level for $Q_{\mathrm{sec},2}$
15	$k_{\mathrm{hyd},3}$	7.7	770	$\mathrm{m^2 d^{-1}}$	discharge parameter for $Q_{\mathrm{hyd},3}$
16	$e_{\mathrm{min},3}$	75	120	mm	min. storage capacity Hyd 3
17	$e_{\mathrm{max},3}$	160	255	mm	max. storage capacity Hyd 3
18	α_3	0.2	0.7	–	quickflow exponent of Hyd 3
19	$k_{\mathrm{is},3}$	0.00025	0.025	$\mathrm{m\,mm^{-1}d^{-1}}$	discharge parameter for $Q_{\mathrm{is},3}$
20	$k_{\mathrm{sec},3}$	0.0015	0.15	$\mathrm{m\,mm^{-1}d^{-1}}$	discharge parameter for $Q_{\mathrm{sec},3}$
21	$e_{\mathrm{sec},3}$	320	450	mm	activation level for $Q_{\mathrm{sec},3}$

5.3.1 Active subspaces

The active subspace method, introduced in Constantine et al. (2014), Constantine (2015), and Russi (2010), identifies dominant directions in the domain of a multivariate, scalar-valued function $f : \mathbf{R}^n \to \mathbf{R}$. In our context, f is a data misfit function (details in Section 5.3.3) which quantifies the mismatch between observed and simulated spring discharge and is defined on the space of parameters to be calibrated. In other words, we seek directions on which f varies more than on other directions, on average. Consider a function f of the form $f(\mathbf{x}) = g(\mathbf{A}^\top \mathbf{x})$ for each $\mathbf{x} \in \mathbf{R}^n$, where $\mathbf{A} \in \mathbf{R}^{n \times k}$, $0 < k < n$, is a rectangular matrix. Such functions are called *ridge functions*; see Pinkus (2015). Take a vector $\mathbf{v} \in \mathbf{R}^n$ from the null space of $\mathbf{A}^\top$, i.e., $\mathbf{A}^\top \mathbf{v} = 0$, and compute

$$f(\mathbf{x} + \mathbf{v}) = g(\mathbf{A}^\top (\mathbf{x} + \mathbf{v})) = g(\mathbf{A}^\top \mathbf{x}) = f(\mathbf{x}). \tag{5.2}$$

This equation shows that f is constant along the null space of $\mathbf{A}^\top$ meaning that the n-dimensional function is actually intrinsically k-dimensional. In practice, the goal is relaxed to finding approximations g and $\mathbf{A}$ such that it holds that $f(\mathbf{x}) \approx g(\mathbf{A}^\top \mathbf{x})$. For the hydrological problem of interest, it means that we try to find a few directions in the parameter space that are significantly informed by the discharge data. We will see that some, but not all, directions change from the prior to the posterior distribution. This fact is exploited to save a considerable amount of computational expense.

Note that this is a different approach compared to other sensitivity analysis methods like *total sensitivity indices* (or *Sobol indices*) (Sobol, 2001) and *Factor Priorisation* (Saltelli et al., 2008). These methods investigate coordinate-aligned sensitivities, i. e., associated with a particular parameter (factor) of a hydrological model. Active subspaces can be viewed as a generalization in the sense that we study dominant "directions" within a parameter space, or, more precisely, we look for linear combinations of parameters that dominate the model output (here, spring discharge) on average.

In the following, we assume that f is continuously differentiable and has partial derivatives that are square-integrable with respect to a given probability density function ρ. We study a matrix which is the ρ-averaged outer product of the gradient of f with itself, i. e.,

$$\mathbf{C} := \mathbf{E}[\nabla f(\mathbf{X}) \nabla f(\mathbf{X})^\top] = \int_{\mathbf{R}^n} \nabla f(\mathbf{x}) \nabla f(\mathbf{x})^\top \rho(\mathbf{x}) \, d\mathbf{x}. \tag{5.3}$$

In the parameter estimation problem, the weighting probability density ρ is the prior density, defined for every model parameter, from the Bayesian inversion context (Section 5.3.3). Note that $\mathbf{C} \in \mathbf{R}^{n \times n}$ is symmetric and positive semi-definite. For some vector $\mathbf{v} \in \mathbf{R}^n$, compute

$$\mathbf{v}^\top \mathbf{C} \mathbf{v} = \mathbf{E}[(\mathbf{v}^\top \nabla f(\mathbf{X}))^2]. \tag{5.4}$$

Thus, $\mathbf{v}^\top \mathbf{C} \mathbf{v}$ displays the averaged variation of our objective function f along $\mathbf{v}$. This quantity is maximized (in the set of unit vectors) by the normalized eigenvector $\mathbf{v}_1$ of $\mathbf{C}$ corresponding to the largest eigenvalue λ_1 and gives

$$\mathbf{E}[(\mathbf{v}_1^\top \nabla f(\mathbf{X}))^2] = \lambda_1. \tag{5.5}$$

For example, if $\mathbf{v}_1 = \mathbf{e}_1 := (1, 0, \ldots, 0)^\top$, it means that f is most sensitive (on average) w.r.t. changes of the first parameter. Since small eigenvalues mean a small variation in the direction of corresponding eigenvectors, this observation suggests to compute an orthogonal eigendecomposition $\mathbf{C} = \mathbf{W} \Lambda \mathbf{W}^\top$, where $\mathbf{W} = [\mathbf{w}_1, \ldots, \mathbf{w}_n]$ contains the eigenvectors and $\Lambda = \mathrm{diag}(\lambda_1, \ldots, \lambda_n)$ contains corresponding eigenvalues in decreasing order. The symmetry of $\mathbf{C}$ allows us to choose $\mathbf{w}_i$ giving an orthonormal basis of $\mathbf{R}^n$. The eigenvalues and eigenvectors can be exploited to span a lower-dimensional space along which f is dominantly varying. We can decide to split $\mathbf{W}$ after the k-th column and to neglect the space spanned by $\mathbf{w}_{k+1}, \ldots, \mathbf{w}_n$, i. e.,

$$\mathbf{W} = [\mathbf{W}_1 \ \ \mathbf{W}_2] \tag{5.6}$$

such that $\mathbf{W}_1 \in \mathbf{R}^{n \times k}$ and $\mathbf{W}_2 \in \mathbf{R}^{n \times (n-k)}$. We write

$$\mathbf{x} = \mathbf{W}\mathbf{W}^\top \mathbf{x} = \mathbf{W}_1 \mathbf{y} + \mathbf{W}_2 \mathbf{z}, \tag{5.7}$$

where $\mathbf{y} := \mathbf{W}_1^\top \mathbf{x}$ is called the *active variable* and $\mathbf{z} := \mathbf{W}_2^\top \mathbf{x}$ the *inactive variable*. The span of $\mathbf{W}_1$, i.e., $\mathscr{R}(\mathbf{W}_1) := \{\mathbf{W}_1 \mathbf{v} \mid \mathbf{v} \in \mathbf{R}^k\}$, is called the *active subspace* (of f). In other words, the coordinate system is transformed to a new orthogonal basis given by the eigenvectors. The new axes corresponding to the eigenvector with the largest eigenvalue is aligned to the direction of maximum averaged variation of f in the original coordinate system.

The matrix $\mathbf{C}$ is generally not available exactly in practice and must be approximated. Constantine and Gleich (2014), Holodnak et al. (2018) and Lam et al. (2018) proposed and analyzed a Monte Carlo approximation, i.e.,

$$\mathbf{C} \approx \tilde{\mathbf{C}} := \frac{1}{N} \sum_{j=1}^{N} \nabla f(\mathbf{X}_j) \nabla f(\mathbf{X}_j)^\top, \tag{5.8}$$

where $\mathbf{X}_j \sim \rho$, $j = 1, \ldots, N > 0$. The recommended number of samples N required to get a sufficiently accurate estimate of eigenvalues and eigenvectors is heuristically given by

$$N \approx \beta \, m \log(n) \tag{5.9}$$

for a so-called *sampling factor* $\beta \in [2, 10]$. The factor $m \in \mathbf{N}$ denotes the number of eigenvalues/eigenvectors to be estimated accurately. The heuristic is motivated in Constantine and Gleich (2014) by results from random matrix theory in Tropp (2012). We utilize *bootstrapping* (Constantine and Gleich, 2014; Efron and Tibshirani, 1994) to ensure that the number of gradient samples N provides a sufficiently good approximation of the eigenvalues of $\tilde{\mathbf{C}}$. Since $\tilde{\mathbf{C}}$ is only an approximation/perturbation of the exact matrix $\mathbf{C}$, eigenvalues and eigenvectors are also only available in perturbed versions, i.e.,

$$\tilde{\mathbf{C}} = \tilde{\mathbf{W}} \tilde{\Lambda} \tilde{\mathbf{W}}^\top. \tag{5.10}$$

Perturbed active and inactive variables are denoted by $\tilde{\mathbf{y}} := \tilde{\mathbf{W}}_1^\top \mathbf{x}$ and $\tilde{\mathbf{z}} := \tilde{\mathbf{W}}_2^\top \mathbf{x}$, respectively.

We additionally need a function $\tilde{g}$ defined on the low-dimensional (perturbed) active subspace approximating f as a ridge function, i.e.,

$$f(\mathbf{x}) \approx \tilde{g}(\tilde{\mathbf{W}}_1^\top \mathbf{x}) \tag{5.11}$$

for each $\mathbf{x} \in \mathbf{R}^n$. It is known that the best approximation in an L^2 sense is the conditional expectation conditioned on the active variable $\tilde{\mathbf{y}}$, i.e.,

$$\tilde{g}(\tilde{\mathbf{y}}) = \int_{\mathbf{R}^{n-k}} f(\tilde{\mathbf{W}}_1 \tilde{\mathbf{y}} + \tilde{\mathbf{W}}_2 \tilde{\mathbf{z}}) \, \rho_{\tilde{\mathbf{Z}}|\tilde{\mathbf{Y}}}(\tilde{\mathbf{z}}|\tilde{\mathbf{y}}) \, d\tilde{\mathbf{z}}. \tag{5.12}$$

The conditional probability density function $\rho_{\tilde{\mathbf{Z}}|\tilde{\mathbf{Y}}}$ is defined in the usual way, see e.g., Billingsley

(1995, Section 20 and 33).

In Section 5.4, we make use of a cheap response surface to $\tilde{g}$ gained by a polynomial regression approach since evaluating $\tilde{g}$, or even a Monte Carlo approximation of it, can get costly due to additional evaluations of f required. This surrogate is constructed according to instructions described in Algorithm 1. There are several examples in the literature that show that a polynomial approximation can be useful in the context of active subspaces, e.g., (Cortesi et al., 2017; Teixeira Parente et al., 2019b). The accuracy of a regression fit is measured by the r^2 value, or *coefficient of determination* (see, for example, Glantz and Slinker (1990)).

Algorithm 1 Response surface construction

Assume $M > 0$ samples $\mathbf{x}_i$, $i = 1, \ldots, M$, according to ρ and corresponding function values f_i, $i = 1, \ldots, M$, are given.

1. Compute samples $\tilde{\mathbf{y}}_i$ in the active subspace by

$$\tilde{\mathbf{y}}_i = \tilde{\mathbf{W}}_1^\top \mathbf{x}_i, \quad i = 1, \ldots, M. \tag{5.13}$$

2. Find a regression surface $\tilde{G}$ for pairs $(\tilde{\mathbf{y}}_i, f_i)$ such that

$$\tilde{G}(\tilde{\mathbf{y}}_i) \approx f_i, \quad i = 1, \ldots, M. \tag{5.14}$$

3. Get a low-dimensional approximation of f at $\mathbf{x}$ by computing

$$f(\mathbf{x}) \approx \tilde{G}(\tilde{\mathbf{W}}_1^\top \mathbf{x}). \tag{5.15}$$

5.3.2 Global sensitivity analysis with active subspace

Constantine and Diaz (2017) show that it is possible to get global sensitivity values from the active subspace that are comparable, in practical situations, with more familiar metrics like *variance-based sensitivities*, also known as *total sensitivity indices* or *Sobol indices* (Saltelli et al., 2008; Sobol, 2001).

Since the expensive computations for building the matrix $\tilde{\mathbf{C}}$ are already done, no further huge computational costs are needed. By "global" we mean that the sensitivities, assigned to each parameter individually, are averaged quantities. In particular, the matrix $\mathbf{C}$ from Eq. (5.3), which will be exploited to compute global sensitivities, is constructed with gradients of the function of interest f at different locations weighted with a given probability density ρ. For our application of the LuKARS model, the function f and the density ρ are taken to be data misfit function and the prior density of the model parameters from the Bayesian context described in Section 5.3.3.

The vector of sensitivities $\mathbf{s} \in \mathbf{R}^n$, in which the i-th component displays the (global) sensitivity

of f w.r.t. parameter $\mathbf{x}_i$, is in Constantine and Diaz (2017) computed via

$$s_i := s_i(m) := \sum_{j=1}^{m} \lambda_j w_{i,j}^2, \quad i = 1, \ldots, m, \ 0 < m \le n. \tag{5.16}$$

Here, we will set $m = n$. Thus, we can write more compactly

$$\mathbf{s}(n) = (\mathbf{W} \circ \mathbf{W})\boldsymbol{\lambda}, \tag{5.17}$$

where $\boldsymbol{\lambda} = (\lambda_1, \ldots, \lambda_n)^\top \in \mathbf{R}^n$ is the vector of eigenvalues and $\circ$ denotes elementwise multiplication.

Similarly to the estimated quantities in previous sections, we will only have an estimate $\tilde{\mathbf{s}}$ available due to the finite approximation of $\mathbf{C}$. In general, it is hard to give strict bounds for the number of samples N required to get a sufficiently accurate approximation to $\mathbf{s}$. Hence, we use as many samples as were shown to be sufficient in (Constantine and Diaz, 2017).

5.3.3 Bayesian inversion

The aim of Bayesian inversion is to approximate a *posterior* probability distribution on the space of parameters $\mathbf{x} \in \mathbf{R}^n$, $n \in \mathbf{N}$, that incorporates uncertainty in the estimated parameters due to noise in the measured discharge data. Stuart (2010) gives a rigorous mathematical framework for Bayesian inverse problems, even in infinite-dimensional parameter spaces. The starting point in Bayesian inversion is a *prior* probability distribution ρ_{prior} that serves as a first guess on the distribution of the model parameters *without* any incorporation of measured hydrological data. The prior also serves to regularize the inverse problem. This choice is often driven by intuition or expert knowledge. Mathematically speaking, we seek a distribution on $\mathbf{x}$ conditioned on the observation of specific measured data. This leads directly to the well-known Bayes' theorem.

Data $\mathbf{d} \in \mathbf{R}^{n_{\mathbf{d}}}$, $n_{\mathbf{d}} \in \mathbf{N}$, are here modeled as

$$\mathbf{d} = \mathscr{G}(\mathbf{x}) + \boldsymbol{\eta}, \tag{5.18}$$

where $\boldsymbol{\eta} \sim \mathscr{N}(0, \Gamma)$ is additive Gaussian noise, modeling measurement errors, with mean zero and covariance matrix $\Gamma \in \mathbf{R}^{n_{\mathbf{d}} \times n_{\mathbf{d}}}$ and $\mathscr{G} : \mathbf{R}^n \to \mathbf{R}^{n_{\mathbf{d}}}$ is called the *parameter-to-observation map*. This map is composed of a *forward operator* $G : \mathbf{R}^n \to V$, displaying, e.g., the solution to a partial differential equation (PDE), and an *observation operator* $\mathscr{O} : V \to \mathbf{R}^{n_{\mathbf{d}}}$, being, e.g., a linear functional on the PDE solution space V. For the LuKARS model, $\mathscr{G}$ is the mapping from the calibration parameters $\mathbf{x}$ (related to parameters in Table 5.1 and described in Section 5.3.5) to the discharge values. By Bayes' theorem, we can define the posterior density as

$$\rho_{\text{post}}(\mathbf{x}) := \rho_{\text{post}}(\mathbf{x}|\mathbf{d}) = \frac{\rho_{\text{like}}(\mathbf{x})\,\rho_{\text{prior}}(\mathbf{x})}{Z}, \tag{5.19}$$

where $Z := \int_{\mathbf{R}^n} \rho_{\text{like}}(\mathbf{x}')\,\rho_{\text{prior}}(\mathbf{x}')\,d\mathbf{x}'$ is a normalizing constant to get a proper probability density

with unit mass. The *likelihood* ρ_{like} denotes the probability that a parameter $\mathbf{x}$ is explaining the discharge data $\mathbf{d}$ corrupted by noise. In this context, i.e., assuming additive Gaussian noise, the likelihood is given by

$$\rho_{\text{like}}(\mathbf{x}) \propto \exp(-f_{\mathbf{d}}(\mathbf{x})) \tag{5.20}$$

with the *data misfit function* $f_{\mathbf{d}}(\mathbf{x}) := \frac{1}{2}\|\mathbf{d} - \mathscr{G}(\mathbf{x})\|_{\Gamma}^2$ and $\|\cdot\|_{\Gamma} := \|\Gamma^{-1/2}\cdot\|_2$. Note that the data misfit function is not a typical squared error function, but involves weights by the noise covariance matrix Γ.

The posterior density is often intractable since its evaluation requires the solution of a potentially computationally intense problem hidden in the forward operator G. The situation becomes even worse if the inverse problem is stated in a high-dimensional parameter space. Whereas a single run of the LuKARS model is sufficiently cheap in our case study, the issue is the high-dimensionality of the problem. A common way to approximate an expensive posterior distribution is to construct samples distributed according to the posterior. However, many sampling techniques suffer from the curse of dimensionality. Well-known sampling approaches comprise, e.g., Markov chain Monte Carlo (MCMC), *Sequential Monte Carlo* (SMC), *Importance Sampling*, and combinations of them.

In this work, we use a *Metropolis-Hastings algorithm* from Hastings (1970) which belongs to the class of MCMC methods. The algorithm constructs a discrete Markov chain whose components are taken as samples and are stationarily distributed according to the desired distribution which is the posterior here. The samples are naturally correlated which is a drawback compared to other sampling techniques that produce independent samples. However, advantages of this algorithm are the absence of restricting assumptions and the fact that it does not suffer from the curse of dimensionality as badly as other samplers. Nevertheless, MCMC methods can have deteriorating behavior in higher dimensions because the number of steps needed to get a sufficiently small correlation between two samples can be rather large. Since the forward operator G is evaluated in every step in the Metropolis-Hastings algorithm, the standard usage of the algorithm can get computationally expensive, especially if G is costly.

In this manuscript, we run a standard Metropolis-Hastings algorithm in low dimensions. For finding low-dimensional structure in our problem, we apply the active subspace method, described in the previous subsection, which allows to find dominant directions in a parameter space that drive the update from the prior to the posterior distribution in Bayesian inverse problems. Additionally, it provides a cheap surrogate of the data misfit function in the low-dimensional space (see Section 5.3.1).

5.3.4 MCMC in the active subspace

For Bayesian inversion, the function of interest that we aim to approximate with a low-dimensional approximation is the data misfit function $f_{\mathbf{d}}$ from Eq. (5.20), i.e.,

$$f_{\mathbf{d}}(\mathbf{x}) := \frac{1}{2}\|\mathbf{d} - \mathscr{G}(\mathbf{x})\|_{\Gamma}^2. \tag{5.21}$$

The gradient of $f_{\mathbf{d}}$ needed for the computation of $\tilde{\mathbf{C}}$ is

$$\nabla f_{\mathbf{d}}(\mathbf{x}) = \nabla \mathscr{G}(\mathbf{x})^{\top} \Gamma^{-1}(\mathscr{G}(\mathbf{x}) - \mathbf{d}), \tag{5.22}$$

where $\nabla \mathscr{G}$ denotes the Jacobian matrix of the parameter-to-observation operator $\mathscr{G}$ which models the relationship between model parameters and discharge values in the LuKARS model.

Not only the perturbed active subspace, but also a cheap surrogate $\tilde{G}_{\mathbf{d}}$ for $\tilde{g}_{\mathbf{d}}$, given by

$$\tilde{g}_{\mathbf{d}}(\tilde{\mathbf{y}}) = \int_{\mathbf{R}^{n-k}} f_{\mathbf{d}}(\tilde{\mathbf{W}}_1 \tilde{\mathbf{y}} + \tilde{\mathbf{W}}_2 \tilde{\mathbf{z}}) \, \rho_{\tilde{\mathbf{Z}}|\tilde{\mathbf{Y}}}(\tilde{\mathbf{z}}|\tilde{\mathbf{y}}) \, d\tilde{\mathbf{z}}, \tag{5.23}$$

can be exploited for an accelerated MCMC algorithm in lower dimensions producing posterior samples for a Bayesian inverse problem as shown in Constantine et al. (2016). The construction of $\tilde{G}_{\mathbf{d}}$ as a polynomial approximation is described in Algorithm 1. Note that there are no additional full model evaluations necessary for this construction. The full model evaluations that we get as a byproduct of the gradient calculations (see Eq. (5.22)) can be reused. By acceleration, we mean that the mixing behavior of the resulting Markov chains constructed by a standard Metropolis-Hastings algorithm can improve in lower dimensions. As a consequence, the computational effort to produce a certain number of posterior samples is reduced.

In a first step, we compute samples of the posterior distribution defined on the low-dimensional subspace, called *active posterior samples*. In order to evaluate the (approximate) posterior density $\tilde{\rho}_{\text{post},\tilde{\mathbf{Y}}}$ in the active subspace given by

$$\rho_{\text{post},\tilde{\mathbf{Y}}}(\tilde{\mathbf{y}}) \approx \tilde{\rho}_{\text{post},\tilde{\mathbf{Y}}}(\tilde{\mathbf{y}}) \propto \exp(-\tilde{G}_{\mathbf{d}}(\tilde{\mathbf{y}})) \, \rho_{\text{prior},\tilde{\mathbf{Y}}}(\tilde{\mathbf{y}}), \tag{5.24}$$

where $\tilde{G}_{\mathbf{d}}$ is the response surface approximating $\tilde{g}_{\mathbf{d}}$, we need an approximation to $\rho_{\text{prior},\tilde{\mathbf{Y}}}$ denoting the marginal prior density on the perturbed active variable. The marginal prior density is in general not analytically available and has to be estimated, e. g., with kernel density estimation (KDE). Note that for the Metropolis-Hastings algorithm it is only important to know the density up to a constant. The algorithmic details are given in Algorithm 2.

The active posterior samples are naturally correlated. Nevertheless, the autocorrelation time is much lower compared to higher dimensional Markov chains. The so-called *effective sample size* (ESS) displaying estimation quality of a sequence of samples can be computed by a formula from Brooks et al. (2011),

$$N_{\tilde{\mathbf{y}}^{(\ell)},\text{ESS}} = \frac{N_{\tilde{\mathbf{y}}}}{1 + 2 \sum_{j=1}^{J_{\max}} r_j^{(\ell)}}. \tag{5.26}$$

The ℓ-th component of a sample $\tilde{\mathbf{y}}$ is denoted by $\tilde{\mathbf{y}}^{(\ell)}$ and the number of samples available by $N_{\tilde{\mathbf{y}}}$. The expression $r_j^{(\ell)}$ describes the autocorrelation between the ℓ-th component of samples $\tilde{\mathbf{y}}$ with lag j. The maximum lag regarded is given by $J_{\max}$. We determine the final effective sample size with

$$N_{\text{ESS}} = \min_{\ell=1,\dots,k} N_{\tilde{\mathbf{y}}^{(\ell)},\text{ESS}}. \tag{5.27}$$

Algorithm 2 MCMC in the active subspace

Assume a state $\tilde{\mathbf{y}}_i$ is given at step i. Let $\rho(\cdot \,|\, \tilde{\mathbf{y}}_i)$ be a symmetric proposal density function and denote the surrogate on $\tilde{g}_{\mathbf{d}}$ with $\tilde{G}_{\mathbf{d}}$. Furthermore, suppose a density $\hat{\rho}$ estimating $\rho_{\mathrm{prior},\tilde{\mathbf{Y}}}$ is given. Then, one step of the algorithm is:

1. Propose a candidate $\mathbf{y}' \sim \rho(\cdot \,|\, \tilde{\mathbf{y}}_i)$.

2. Compute the acceptance probability with
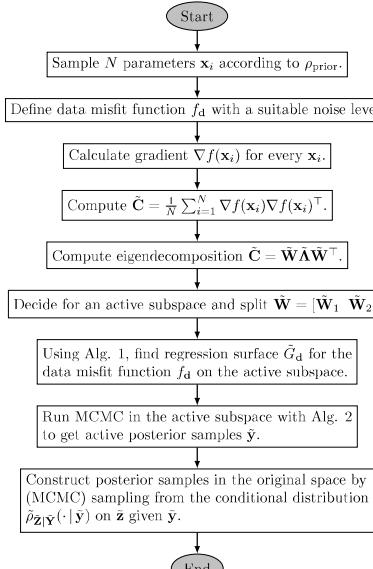
$$\gamma(\mathbf{y}', \tilde{\mathbf{y}}_i) := \min \left\{ 1, \frac{\exp(-\tilde{G}_{\mathbf{d}}(\mathbf{y}'))\,\hat{\rho}(\mathbf{y}')}{\exp(-\tilde{G}_{\mathbf{d}}(\tilde{\mathbf{y}}_i))\,\hat{\rho}(\tilde{\mathbf{y}}_i)} \right\}. \tag{5.25}$$

3. Draw a uniform sample $u \sim \mathscr{U}(0, 1]$.

4. Accept/reject $\mathbf{y}'$ according to $u \leq \gamma(\mathbf{y}', \tilde{\mathbf{y}}_i)$.
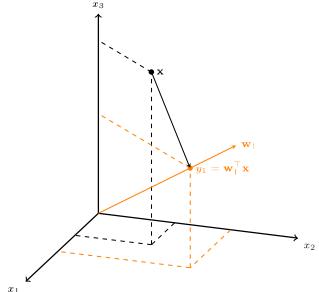
After completing Algorithm 2, the entire set of active posterior samples $\tilde{\mathbf{y}}$ is reduced to a set of size N_{ESS} by taking every p-th sample in the chain (where p is chosen such that we get a set of size N_{ESS}). The auto-correlation of the chosen samples is thus reduced. This technique is called *thinning* (see, e.g., (Link and Eaton, 2012)). The adequacy of the size of samples depends on their application in general. However, it is possible to check it, for example by bootstrapping or, if the surrogate is cheap enough, by construction and comparison of multiple Markov chains having different lengths.

Our final goal is to construct samples of the posterior distribution in the original n-dimensional space. Eq. (5.7) suggests to sample $\tilde{\mathbf{z}}$-components for each $\tilde{\mathbf{y}}$ from the reduced set of samples gained from Algorithm 2. Since it is generally not trivial to sample from the conditional distribution of $\tilde{\mathbf{z}}$ given $\tilde{\mathbf{y}}$, $\rho_{\tilde{\mathbf{Z}}|\tilde{\mathbf{Y}}}(\tilde{\mathbf{z}}|\tilde{\mathbf{y}})$, we have to run another Metropolis-Hastings algorithm. Note that for this sampling, we only need to sample from $\rho_{\mathrm{prior}}(\tilde{\mathbf{W}}_1\tilde{\mathbf{y}} + \tilde{\mathbf{W}}_2\tilde{\mathbf{z}})$ because $\rho_{\tilde{\mathbf{Z}}|\tilde{\mathbf{Y}}}$ is proportional to that distribution. We again compute (nearly uncorrelated) samples of $\tilde{\mathbf{z}}$ given a particular sample $\tilde{\mathbf{y}}$ to finally translate them to posterior samples $\mathbf{x} = \tilde{\mathbf{W}}_1\tilde{\mathbf{y}} + \tilde{\mathbf{W}}_2\tilde{\mathbf{z}}$ in the original full-dimensional parameter space.

A summarizing flowchart displaying the described steps of our approach is depicted in Fig. 5.1 a). We emphasize that full model evaluations are only necessary for the construction of the active subspace. The surrogate can be constructed with model evaluations $\mathscr{G}(\mathbf{x}_i)$ that we get as a byproduct from the calculation of gradients, see Eq. (5.22). However, if it is required to perform a check for the potential issue of overfitting in the regression fit, additional model evaluations are necessary. For example, we computed another 20,000 model simulations to prevent overfitting, although the original 1,000 evaluations would have been enough (see Section 5.4). Eventually, Fig. 5.1 b) visualizes the fact that the active subspace method is looking for dominant *directions* in a high-dimensional parameter spaces instead of studying sensitivities of coordinate-aligned, individual parameters.

Figure 5.1: a) Flowchart displaying the main steps in the present Bayesian inference process with active subspaces. b) Visualization of a one-dimensional active subspace in a three-dimensional parameter space. The parameter $\mathbf{x} \in \mathbf{R}^3$ is projected on the active subspace spanned by $\mathbf{w}_1$ giving the active variable $y_1 = \mathbf{w}_1^\top \mathbf{x}$.

5.3.5 Parameter setting

Before we describe the results of the parameter study in the next section, we discuss the calibrated parameters and their notation. As mentioned in Section 5.2, there are three hydrotopes with 7 variable parameters each. These parameters are called *physical parameters* in the following. All of the 7 parameters have the same physical meaning for each hydrotope.

There are two reasons that lead to the introduction of artificial parameters which we call *calibration parameters* in the following. One reason is that the k_* values are calibrated on a log scale. Therefore, we define

$$k_*^{\log} = \log(k_*) \tag{5.28}$$

for each $k_* \in \{k_{\mathrm{hyd},i}, k_{\mathrm{is},i}, k_{\mathrm{sec},i}\}$, $i = 1, 2, 3$. The second reason is the dependence of the physical parameters which needs to be circumvented since the application of active subspaces in Bayesian inverse problems prefers independently distributed and normalized parameters. There exist two types of dependencies, namely

1. cross-hydrotope dependencies caused by Eq. (5.1)

2. a dependence between parameters $e_{\min,i}$ and $e_{\max,i}$, since $e_{\min,i} \leq e_{\max,i}$.

The first point concerns only parameters in hydrotope 2 and 3. Hence, we write

$$p_i = p_{i,\text{lb}} + \triangle p_{(i-1,i)}(\min\{p_{i,\text{ub}}, p_{i-1}\} - p_{i,\text{lb}}) \tag{5.29}$$

or

$$p_i = \max\{p_{i-1}, p_{i,\text{lb}}\} + \triangle p_{(i-1,i)}(p_{i,\text{ub}} - \max\{p_{i-1}, p_{i,\text{lb}}\}), \quad i = 2, 3, \tag{5.30}$$

depending on whether the physical parameter $p_i \in \{k_{\text{hyd},i}^{\log}, e_{\min,i}, \alpha_i, k_{\text{is},i}^{\log}, k_{\text{sec},i}^{\log}, e_{\text{sec},i}\}$ follows a decreasing or, respectively, increasing behavior (see Eq. (5.1)). The fixed values $p_{i,\text{lb}}$ and $p_{i,\text{ub}}$ denote the lower and upper bound of respective physical parameters given in Table 5.1. The parameters $\triangle p_i \in [0, 1]$ are the newly introduced calibration parameters. They are independent of other calibration parameters. For the second point, we replace (for the purpose of calibration) the parameters $e_{\max,i}$ by $\triangle e_i$ and set

$$e_{\max,i} = e_{\min,i} + \triangle e_i, \quad i = 1, 2, 3. \tag{5.31}$$

The parameter $\triangle e_i$ is now independent of $e_{\min,i}$. Minimum and maximum values for $\triangle e_i$ are computed with respective intervals from Table 5.1, i.e., we have

$$e_{\max,i,\text{lb}} - e_{\min,i,\text{lb}} \leq \triangle e_i \leq e_{\max,i,\text{ub}} - e_{\min,i,\text{ub}}, \tag{5.32}$$

which is valid since it holds that $e_{\max,i,\text{lb}} - e_{\min,i,\text{lb}} \leq e_{\max,i,\text{ub}} - e_{\min,i,\text{ub}}$ for every $i = 1, 2, 3$.

Finally, all calibration parameters need to be normalized, i.e., they are mapped from their corresponding interval to $[-1, 1]$. Normalized parameters are denoted with a bar. Summarizing, the vector of all normalized independent calibration parameters is

$$\begin{aligned} \mathbf{x} = (&\bar{k}_{\text{hyd},1}^{\log}, \bar{e}_{\min,1}, \triangle \bar{e}_1, \bar{\alpha}_1, \bar{k}_{\text{is},1}^{\log}, \bar{k}_{\text{sec},1}^{\log}, \bar{e}_{\text{sec},1}, \\ &\triangle \bar{k}_{\text{hyd},(1,2)}^{\log}, \triangle \bar{e}_{\min,(1,2)}, \triangle \bar{e}_2, \triangle \bar{\alpha}_{(1,2)}, \triangle \bar{k}_{\text{is},(1,2)}^{\log}, \triangle \bar{k}_{\text{sec},(1,2)}^{\log}, \triangle \bar{e}_{\text{sec},(1,2)}, \\ &\triangle \bar{k}_{\text{hyd},(2,3)}^{\log}, \triangle \bar{e}_{\min,(2,3)}, \triangle \bar{e}_3, \triangle \bar{\alpha}_{(2,3)}, \triangle \bar{k}_{\text{is},(2,3)}^{\log}, \triangle \bar{k}_{\text{sec},(2,3)}^{\log}, \triangle \bar{e}_{\text{sec},(2,3)})^{\top} \in \mathbf{R}^{21}. \end{aligned} \tag{5.33}$$

5.4 Results

In the following, we assume a normally distributed measurement error (noise) at a level of 5% for the measured spring discharge as it was kindly provided by the water works owner Waidhofen a.d. Ybbs for the applied flowmeter. This translates to $\Gamma_{ij} = (0.05 \times d_i)^2 \delta_{ij}$, $i, j = 1, \ldots, n_{\mathbf{d}}$, where Γ is the covariance matrix. Additionally, we assume a uniform distribution on the calibration parameters from Eq. (5.33), i.e., $\mathbf{x} \sim \mathcal{U}[-1, 1]^{21}$. The prior intervals for the physical parameters are given in Table 5.1. Note that the prior distribution on the physical parameters is not uniform due to the transformation described in Section 5.3.5.

For the computation of $\tilde{\mathbf{C}}$ from Eq. (5.8), we use $N = 1,000$ gradient samples of $\nabla f_{\mathbf{d}}$, although only about 250 samples would be necessary to estimate the first $m = 8$ eigenvectors sufficiently accurately according to Eq. (5.9) with a pessimistic sampling factor $\beta = 10$. The reason for choosing this rather large number is to make sure that the global sensitivity values, for which such heuristics do not exist, are also estimated accurately. The gradient was approximated by central finite differences. Using seven cores of type Intel(R) Xeon(R) E5 at $3\,\mathrm{GHz}$ each, the required $1,000 \times (21 \times 2 + 1) = 43,000$ forward runs need about 4.3 hours since it required 2.5 seconds for a single run of the model.
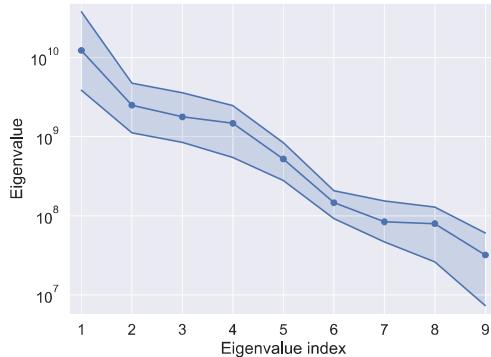

Figure 5.2: Spectrum of the matrix $\tilde{\mathbf{C}}$ for the data misfit function $f_{\mathbf{d}}$ with a 5% noise level. The light blue area around the eigenvalues indicates variability of the eigenvalues caused by the random nature of the approximation $\tilde{\mathbf{C}}$.

The resulting eigenvalues and first four eigenvectors are plotted in Fig. 5.2 and Fig. 5.3 a)-d), respectively. Fig. 5.2 shows the spectral decay on a logarithmic scale. The light blue area around the eigenvalues displays minimum and maximum eigenvalues gained from bootstrapping and indicates the variability of eigenvalues due to the random nature of the approximation $\tilde{\mathbf{C}}$ (see Eq. (5.8)). Gaps after the first and fourth eigenvalue suggest the existence of one- and four-dimensional active subspaces. Fig. 5.3 a)-d) shows eigenvectors with components colored according to the hydrotope they are supposed to model. It shows that parameters 5, 12, and 19, having large contributions in the first three eigenvectors, take a dominant role. All of these parameters involve the k_{is} value for each hydrotope. Moreover, we can observe a ranking between the corresponding hydrotopes of these parameters, with decreasing order of the k_{is} values from Hyd 2, Hyd 1 to Hyd 3 in the first eigenvector. A different pattern is observed for the contributions of parameters related to k_{hyd}, represented by parameters 1, 8, and 15 for Hyd 1, Hyd 2, and Hyd 3, respectively. These parameters appear in eigenvectors 2 to 4 and show a different ranking as compared to the k_{is} parameters, with a decreasing contribution from Hyd 1, Hyd 2 to Hyd 3. It is important to highlight that parameter 15 only shows a small contribution in eigenvector 3 and 4. A third important parameter group is

related to k_{sec}, here represented by parameters 6, 13, and 20. They appear in eigenvectors 2 to 4 and have comparable contributions in Hyd 1 and Hyd 2 (parameters 6 and 13) but only a minor contribution in Hyd 3 (see eigenvector 4). Interestingly, for hydrotope 1 and 2 the same parameters show up with a similar shape in eigenvector $\tilde{\mathbf{w}}_4$.
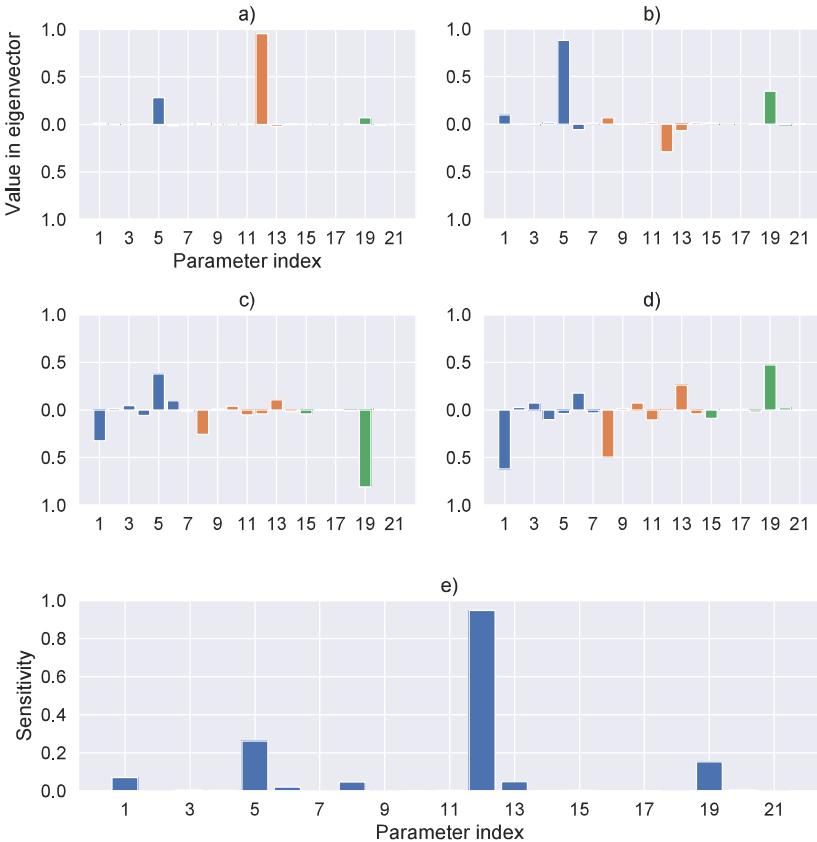
Figure 5.3: The subfigures show sensitivities with respect to the calibration parameters described in Section 5.3.5. First two rows: First four eigenvectors of the matrix $\tilde{\mathbf{C}}$ ($\tilde{\mathbf{w}}_i$, $i = 1, 2, 3, 4$) for the data misfit function $f_{\mathbf{d}}$ with a 5% noise level. Along these directions, the data misfit function changes much more, on average, than along other directions (eigenvectors). The colors distinguish the three hydrotopes (blue: Hyd 1, orange: Hyd 2, green: Hyd 3). Last row: Global sensitivity values of the data misfit function $f_{\mathbf{d}}$ with a 5% noise level. These values are computed using the eigenvalues and eigenvectors of $\tilde{\mathbf{C}}$ described in Section 5.3.2. The ratio of maximum and minimum sensitivities is 3.6×10^6.

It is important to emphasize that the resulting eigenvectors for the Bayesian data misfit can look different to ones gained from using the *Nash-Sutcliffe model efficiency coefficient* (NSE), which is a more common misfit function in hydrology, introduced in Nash and Sutcliffe (1970).

This can be explained by the fact that the NSE is focusing on high-flow conditions as it is a (non-weighting) squared error function (Gupta et al., 2009), whereas the Bayesian data misfit function is a weighting/relative squared error function (weights are given by entries in the noise covariance matrix Γ) and, thus, does not favor low- or high-flow conditions.

With the eigenvalue/-vector plot, we have already gained some insight in the parameter sensitivities. Fig. 5.3 e) shows the global sensitivities of the data misfit function $f_{\mathbf{d}}$ normalized to $[0, 1]$. The most sensitive parameter is $\triangle k_{\text{is},(1,2)}$, but also $\bar{k}_{\text{is},1}$ and $\triangle k_{\text{is},(2,3)}$ have their contributions since they show up in $\tilde{\mathbf{w}}_2$ and $\tilde{\mathbf{w}}_3$, respectively, with non-negligible corresponding eigenvalues. At the same time, parameters 6, 13, and 20, involving k_{sec} values in the hydrotopes, show sensitive in the first eigenvectors. Parameters displaying k_{hyd} values have small contributions but only in hydrotope 1 and 2. All other parameters do not show much sensitivity since their components contribute only to eigenvectors having eigenvalues that are orders of magnitudes smaller than the first four. As a consequence, we expect that the more sensitive parameters change their distribution (and also joint distributions) from the prior to the posterior during Bayesian inference.
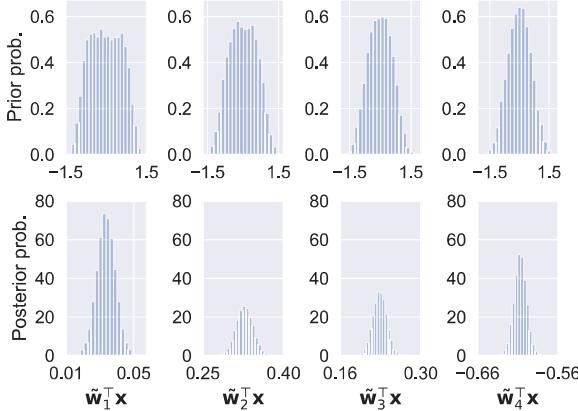
Figure 5.4: 1D marginal prior and posterior distributions in the 4D active subspace.

We decide for a 4D subspace and compute a 4th order polynomial to get the response surface $\tilde{G}_{\mathbf{d}}$ of $\tilde{g}_{\mathbf{d}}$ by Algorithm 1. Since polynomials of 4th order already have 70 degrees of freedom in four dimensions, we compute another 20,000 samples of $f_{\mathbf{d}}(\mathbf{x})$, with $\mathbf{x}$ following the prior, to preclude overfitting. Nevertheless, the 1,000 samples from the computation of $\tilde{\mathbf{C}}$ would have been enough to get the same r^2 score which is ≈ 0.77. This score, also called coefficient of determination, is

a statistical measure for the goodness of a fit and reflects the percent of variance explained. If predictions of a regression match perfectly well with the data points, the r^2 score becomes 1. In contrast, it can become less than zero, if the predicted values are worse than choosing the constant mean value of the data. In this regard, our r^2 score indicates that our surrogate is a sufficiently well behaved fit.

Table 5.2: Left: Posterior means and standard deviations of physical parameters. The informed parameters are highlighted in bold. Right: Highest 2D correlations for physical parameters.

No.	Phys. par.	Mean	Std.
1	$k_{hyd,1}$	3.07×10^2	2.34×10^2
2	$e_{min,1}$	29.86	11.57
3	$e_{max,1}$	44.49	12.90
4	α_1	1.17	0.26
5	$\mathbf{k_{is,1}}$	$\mathbf{5.18 \times 10^{-2}}$	$\mathbf{3.98 \times 10^{-3}}$
6	$k_{sec,1}$	0.17	0.22
7	$e_{sec,1}$	47.78	12.95
8	$k_{hyd,2}$	70.62	55.81
9	$e_{min,2}$	60.46	11.27
10	$e_{max,2}$	1.20×10^2	16.14
11	α_2	0.82	0.21
12	$\mathbf{k_{is,2}}$	$\mathbf{4.52 \times 10^{-3}}$	$\mathbf{1.61 \times 10^{-4}}$
13	$k_{sec,2}$	2.03×10^{-2}	3.23×10^{-2}
14	$e_{sec,2}$	1.76×10^2	25.99
15	$k_{hyd,3}$	25.94	21.75
16	$e_{min,3}$	95.71	14.18
17	$e_{max,3}$	2.06×10^2	20.23
18	α_3	0.43	0.14
19	$\mathbf{k_{is,3}}$	$\mathbf{6.35 \times 10^{-4}}$	$\mathbf{1.69 \times 10^{-5}}$
20	$k_{sec,3}$	6.21×10^{-3}	1.07×10^{-2}
21	$e_{sec,3}$	3.85×10^2	37.48

Phys. par.		Cor. coef.
$e_{min,1}$	$e_{max,1}$	0.89
$k_{is,1}$	$k_{is,2}$	0.77
$e_{min,3}$	$e_{max,3}$	0.70
$e_{min,2}$	$e_{max,2}$	0.70
$k_{hyd,2}$	$k_{sec,2}$	0.66
$k_{is,1}$	$k_{hyd,2}$	0.64
$k_{is,1}$	$k_{sec,2}$	0.63
$k_{hyd,2}$	$k_{is,2}$	0.59
$k_{sec,1}$	$k_{is,3}$	0.57
$k_{sec,2}$	$k_{sec,3}$	0.56
$k_{is,2}$	$k_{sec,2}$	0.52

The Metropolis-Hastings algorithm described in Algorithm 2 is used to construct a Markov chain giving (correlated) posterior samples in the active subspace. Its proposal variance was adjusted to 0.005 in order to give an acceptance rate of $\approx 35\%$. We compute 1,000,000 samples and regard the first 100,000 samples as part of the burn-in which are not considered as part of the final distribution. The remaining samples give an effective sample size of about 12,000 which is enough to sufficiently represent a distribution in four dimensions. The resulting distribution on the active variables, attained from the about 12,000 samples, is displayed in Fig. 5.4. Note that the x scales of the upper and lower row of plots are quite different. This due to the fact that if we did not change the lower x scale, the lower histograms would basically become thin lines displaying no information about the variance of the distribution. However, we see that the active variables are substantially informed which is exactly what we hoped to achieve. Also note that the first plot in the upper row, displaying the 1D marginal prior distribution of the first active variable $\tilde{y}_1 = \tilde{\mathbf{w}}_1^\top \mathbf{x}$,

is almost a classical (rectangular) uniform distribution. This is caused by the large contribution of only one parameter in $\tilde{\mathbf{w}}_1$ which is $\triangle k_{\mathrm{is},(1,2)}$ in this case. The more parameters contribute to an active variable, the more its marginal prior distribution differs from a rectangle, see $\tilde{y}_4 = \tilde{\mathbf{w}}_4^\top \mathbf{x}$ for example.

The samples in the inactive subspace $\tilde{\mathbf{z}}$ are computed as described in Subsection 5.3.4 and composed with active posterior samples to give posterior samples in the original space. Resulting 1D marginal statistics of the physical parameters are given in Table 5.2 (left). As expected, the physical parameters related to calibration parameters with significant components in the active subspace are highly informed. The first calibration parameter ($\bar{k}_{\mathrm{hyd},1}^{\log}$) having a small but not negligible contribution according to the sensitivity values in Fig. 5.3 e) is already only mildly informed. The other parameters do not change or only very little because of the choice of the active subspace.

Additionally, Table 5.2 (right) displays the highest resulting two-dimensional posterior correlation coefficients of the physical parameters in LuKARS. They are consistent with the components of corresponding calibration parameters that show up in the 4D active subspace. The largest correlation occurs between $e_{\mathrm{min},1}$ and $e_{\mathrm{max},1}$. A large correlation coefficient of 0.7 is also found between the respective storage values of Hyd 2 and Hyd 3, $e_{\mathrm{min},2}$ and $e_{\mathrm{max},2}$, as well as between $e_{\mathrm{min},3}$ and $e_{\mathrm{max},3}$.

As a verification for our choice of a 4D subspace, we show that the uncertainty in the approximated posterior distribution is dominated by the uncertainty in the data, and not by approximation errors caused by dimension reduction. We do this by approximating the posterior's *push-forward distribution*, i.e., the distribution gained by propagating the approximated posterior through the parameter-to-observation operator $\mathscr{G}$, which models the discharge values for a given input parameter. Hence, we computed 1,000 samples of the distribution $\mu_{\mathrm{post}}(\{\mathbf{x}\,|\,\mathscr{G}(\mathbf{x}) \in \cdot\})$, where μ_{post} denotes the posterior distribution with density ρ_{post}. Fig. 5.5 a) shows the 95% quantile band around the data with 5% additive Gaussian noise assumed together with a 75% quantile band around the median of the posterior's push-forward distribution. More loosely speaking, the plot shows that around 75% of discharges simulated with random parameters drawn from the posterior will lie within the inherent uncertainty of the observed discharge. The uncertainty in the dynamics around the measured discharges in the Kerschbaum spring is matched well by the uncertainty of the push-forward posterior distribution which confirms the choice of a 4D subspace. Since we started with an uninformed prior (a uniform distribution), we can not expect to end up with a push-forward posterior much more certain than the uncertainty in the experiments. At this point, we would like to emphasize that it is possible to get a reasonably good approximation of the posterior by considering only 4 directions in the space of 21 parameters. In this manner, particularly regarding the low flow conditions and the recession limbs of the peak discharges, we can observe a variation of only up to ± 5l/s which is roughly the variation due to experimental noise. Also, the mean and the median of the push-forward distribution give results agreeing with the data which, in addition, supports the decision for a 4D subspace.

Additionally, this type of plot shows that different decisions for the dimension of the active subspace lead to different posterior approximations. Fig. 5.5 b) shows the push-forward distribu-

tion of a posterior gained with a 1D subspace. However, interestingly, assuming a noise level of 10% and taking only a 1D subspace also leads to usable results in the sense that the corresponding approximation to the posterior's push-forward distribution matches the inherent uncertainty in the data well. However, note that the r^2 score of $\tilde{G}_\mathbf{d}$ was only about 0.23 in this case. Although we see that the assumptions are rather unrealistic and the approximation quality of $\tilde{G}_\mathbf{d}$ is too bad, it is worth noting that already the first eigenvector contains some information about the posterior meaning that the mean and median of the corresponding push-forward posterior give reasonable discharge values in comparison with the data as shown in Fig. 5.5 b).
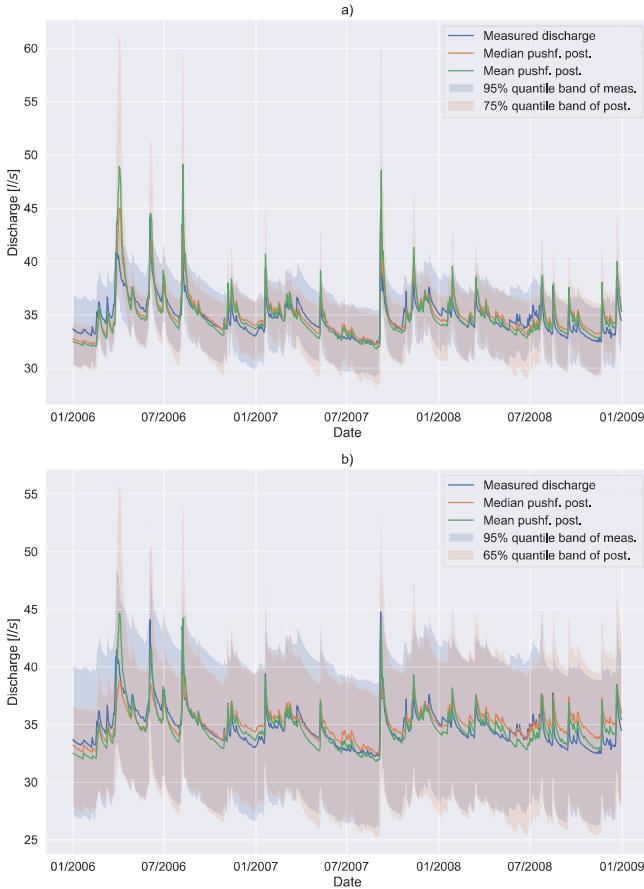

Figure 5.5: Push-forward distributions of the posteriors gained with a 4D (a) and 1D (b) subspace, assuming a 5% and 10% noise level, respectively, along with their mean and median.

5.5 Discussion

Besides the introduction of the active subspace method as a technique for dimension reduction in Bayesian inverse problems to the karst hydrology community, a major aim of our work, as mentioned in Section 5.1, was to perform a parameter inference in the Bayesian sense providing information about the behavior of our model and its uncertainties. For the LuKARS model of the Kerschbaum spring in Waidhofen a.d. Ybbs, we found a 4-dimensional subspace of the original 21-dimensional parameter space. This does, however, not mean that only 4 individual physical model parameters are informed by the discharge data since an active subspace represents a linear combination of sensitive parameters, represented by the parameters in the eigenvectors corresponding to dominant eigenvalues. In this regard, the relation between sensitive parameters in each dimension of the active subspace provides deeper insights into the model behavior than just the sensitivities of individual parameters. The results, from a broader perspective, show that 7 physical/model parameters are most sensitive. These parameters consist of coefficients for the baseflow storages ($k_{\mathrm{is},i}$, $i = 1, 2, 3$), for the quickflow storages ($k_{\mathrm{hyd},i}$, $i = 1, 2$), and for the secondary spring discharges ($k_{\mathrm{sec},i}$, $i = 1, 2$).

The remaining paragraphs in this section are devoted to give a detailed hydrological interpretation of the results showed in the previous section. These interpretations are based on the following information. The observed spring discharge is modeled as the sum of the relative contribution of each hydrotope. Moreover, the LuKARS model of the Kerschbaum spring has fast responding hydrotopes (i.e., hydrotopes that quickly deliver water to the karst spring after precipitation events, e.g., Hyd 1) and slow responding hydrotopes (i.e., hydrotopes, which slowly deliver water to the spring after precipitation events, e.g., Hyd 3).

Parameters 5, 12, and 19 show the largest contributions in the first 4 eigenvectors in Fig. 5.3 a)-d). These parameters correspond to the k_{is} physical parameters, which delimit the flow contributions from the hydrotopes to the linear baseflow storage. As derived in Bittner et al. (2018a), the baseflow storage exhibits a relatively constant discharge behavior with a small temporal variability and its discharge coefficient k_{b} was not changed within the presented research study. Since the outflow from the baseflow storage is controlled by its variable storage (e_{b}) and its constant discharge coefficient (k_{b}), the hydrotope discharge coefficients for the groundwater recharge (k_{is}) also affect the baseflow discharge and its temporal dynamics since they control e_{b}. Given that k_{b} was not included as a calibration parameter, the k_{is} parameters are responsible to maintain the baseflow contribution as derived by Bittner et al. (2018a) and are most informed in the first eigenvector when applying the active subspace method.

Although parameters 5, 12, and 19 have the same physical interpretation, we can observe that they display different sensitivities for the different hydrotopes. This is due to the fact that different hydrotopes cover areas which are different in extension (Hyd 1 - 13%, Hyd 2 - 56% and Hyd 3 - 27%). Therefore, the interpretation of the most important parameters occurring in an eigenvector, should both consider the physical meaning of the parameter and the relative contribution of each single hydrotope to the total spring discharge, which is highly affected by the relative area covered

by the hydrotope. In this specific case, parameter 12, associated with Hyd 2, displays the largest value since it covers the largest area in the Kerschbaum spring catchment and thus has a significant contribution to the total spring discharge. Parameter 5 has the second largest value although Hyd 1 ranks as third in terms of coverage area. This is explained by the fact that Hyd 1 provides the most dynamic and variable discharge behavior of all hydrotopes. Hence, the discharge contribution from Hyd 1 is essential to reproduce the discharge dynamics observed in the Kerschbaum spring. Hyd 3 has the smallest contribution in eigenvector 1, which can be explained by its more constant and less variable discharge behavior as compared to Hyd 1 and its smaller spatial share as compared to Hyd 2. Hence, although Hyd 3 has a larger area covered than Hyd 1, parameter 19 is less dominant than parameter 5.

Although parameters 1 and 8 (involving k_{hyd} values of Hyd 1 and Hyd 2) do not show up in eigenvector 1, their contribution to eigenvectors 2 to 4 is worth discussing. These parameters follow a different ranking as compared to the k_{is} parameters, suggesting a larger sensitivity of parameter 1 from Hyd 1 as compared to parameter 8 from Hyd 2. Since the k_{hyd} parameters constrain the quickflow dynamics originating from each hydrotope, we argue that this ranking is the result of the different hydrological behaviors each hydrotope is supposed to simulate. Considering that Hyd 1, which shows the most dynamic behavior in response to precipitation or melt events, has a large contribution to the temporal variability of the discharge in the Kerschbaum spring, the importance of adequately representing the quickflow dynamics from Hyd 1 can be regarded as more important than the relative space covered by each hydrotope.

It is interesting to observe that the posterior means of the informed physical model parameters ($k_{\mathrm{is},i}$, $i = 1, 2, 3$, see Table 5.2) are close to corresponding calibrated parameters found by Bittner et al. (2018a). Moreover, the standard deviations of the k_{is} parameters in the posterior distribution are smaller as compared to the standard deviations found for the posterior distributions of all other physical parameters. This provides evidence that we can use the components of the first eigenvectors derived from the active subspace method to show which parameters get individually updated from the prior to the posterior distribution. Moreover, in comparison to the parameters obtained by manual calibration, we additionally obtain an uncertainty specification related to any model parameter.

It is striking that the correlations between $e_{\mathrm{min},i}$ and $e_{\mathrm{max},i}$ (for each $i = 1, 2, 3$) are high although they are not very dominant according to the first four eigenvectors. The reason for this is that this correlation is already present in the prior distribution on the physical parameters (see Eq. (5.31)). However, we argue that the higher positive correlation coefficient between $e_{\mathrm{min},1}$ and $e_{\mathrm{max},1}$ results from the dependence of the overall model output on the quickflow dynamics of Hyd 1 (Bittner et al., 2018a). The dynamics of the quickflow depend strongly on the difference between $e_{\mathrm{min},i}$ and $e_{\mathrm{max},i}$ (see Eq. (A.5)) and thus results in a high correlation coefficient between both storage thresholds. The positive correlations between the discharge coefficients of Hyd 2, in particular between $k_{\mathrm{hyd},2}$ and $k_{\mathrm{sec},2}$, $k_{\mathrm{hyd},2}$ and $k_{\mathrm{is},2}$ as well as between $k_{\mathrm{is},2}$ and $k_{\mathrm{sec},2}$, highlight the strong interdependence of all discharge components that originate from Hyd 2. The strongest correlation (0.66) is between the discharge coefficient of the quickflow ($k_{\mathrm{hyd},2}$) and the discharge coefficient

of the secondary spring discharge ($k_{\text{sec},2}$). This means that, if we increase $k_{\text{hyd},2}$ and not $k_{\text{sec},2}$, the quickflow contribution increases disproportionately and the total simulated spring discharge would overestimate the observed peak discharges. The same relationship holds for the strong correlation (0.59) between the discharge coefficient of the quickflow ($k_{\text{hyd},2}$) and the discharge parameter of the groundwater recharge ($k_{\text{is},2}$) as well as between the $k_{\text{is},2}$ and $k_{\text{sec},2}$ (0.52). These correlations confirm the fact that if we increase the discharge coefficient of one discharge component in a certain hydrotope, we need to simultaneously increase all other discharge coefficients in the same hydrotope to get a similar model output. If the other coefficients were not changed accordingly, we would disproportionately increase one discharge component (e. g., quickflow from Hyd 2) relative to others (e. g., $k_{\text{is},2}$ or $k_{\text{sec},2}$); so, the hydrotope would show a different hydrological behavior. This highlights that the parameter dependencies within each hydrotope individually help to maintain the hydrological behavior that is typical for each hydrotope. The reason why only the discharge parameters of Hyd 2 show high correlation coefficients is that Hyd 2 covers more than 50% of the Kerschbaum spring recharge area and, thus, has the highest contributions to the total spring discharge. The correlations between various discharge coefficients of different hydrotopes, e. g., $k_{\text{is},1}$ and $k_{\text{is},2}$, are interpreted as a consequence of the parameter constraints introduced in Eq. (5.1), similar to the dependence between $e_{\text{min},i}$ and $e_{\text{max},i}$ values.

We conclude by commenting on the limits and transferability of the active subspace method. One of the major disadvantages of the method is the need for gradients in the identification of the active subspace. Computing gradient information can be computationally expensive, especially if there are no alternatives to using a finite difference approach as, e. g., adjoint formulations (Plessix, 2006). In the given case, the computational costs for using central finite differences are reasonable since the model is sufficiently cheap. However, for more expensive models such an approach can be intractable. There are recent advances for computing active subspaces in a derivative-free way (Tripathy et al., 2016), however, the computation of derivatives is replaced by a non-trivial non-convex optimization problem. Since the framework of active subspaces is quite general and formulated without too many restricting assumptions, we consider its application as highly transferable. This claim is supported by several applications of the method for complex physical models, e. g., Erdal and Cirpka (2019); Constantine et al. (2015); Constantine and Doostan (2017); Diaz et al. (2018); Jefferson et al. (2015). The proposed use of the active subspace method extends the available tools for parameter and uncertainty estimation in hydrology. A comparison among all available methods is out of the scope of this work and should be pursued in the future through a collaborative work in the community. We hence provide only a brief comparison with DREAM, described in Vrugt (2016) and used to accelerate MCMC in Vrugt et al. (2009), as it has found wide recognition in Bayesian analysis of hydrological models. The main differences of DREAM compared to the presented approach are two-fold. First, basic DREAM runs multiple Markov chains in parallel, exchanging chain elements in a way retaining favorable properties like ergodicity and the Markov property (memorylessness). Secondly, a randomized subspace sampling strategy is then used to avoid inefficient mixing of Markov chains in higher dimensions. Our proposed approach, however, does not need an additional sampling strategy, since the Markov chains are

moving in the dominant low-dimensional subspace, whereas for DREAM the chain is still evolving in the full-dimensional space.

5.6 Summary

This manuscript shows results from a parameter study of a karst aquifer model for the Kerschbaum spring recharge area. The model uses 21 parameters to simulate the discharge behavior of the Kerschbaum karst spring in Waidhofen a.d. Ybbs. The study consists of a parameter inference in the Bayesian sense and a (global) sensitivity analysis. Since these problems have a non-trivial dimension, we first check for low-dimensional structure, if present, hidden in the inference process and exploit the so-called *active subspace method* for this. Additionally, without further expensive computations, we are then able to derive global sensitivity metrics.

It seems that the inference process is indeed intrinsically low-dimensional. Although the LuKARS model for the Kerschbaum spring has 21 calibration parameters, given the parameter constraints in Eq. (5.1), we find its dominant parameters and obtain well-constrained values for them by means of Bayesian inversion in the identified active subspace. In particular, we decide to reduce the Bayesian inverse problem from a 21D to a 4D problem which is verified by showing that the push-forward distribution of the approximated posterior has a promising similarity with the uncertainty in the data. The 1D and 2D posterior statistics, which differ a lot from corresponding prior statistics for dominant parameters, are computed to quantify uncertainty in the inference caused by measurement errors in the data.

Eventually, the active subspace method shows again to be valuable for Bayesian inference and sensitivity analysis in complex high-dimensional problems. The results are, however, rather useful from a computational perspective. The in-depth validation of the model with further sensitivity analyses, more interesting from a hydrological perspective, and a discussion of the consequences for the community are out of scope and, hence, not part of this study, but will follow in future research. In particular, we want to investigate the hydrological features that lead to the present dimensional reduction.

Chapter 6

Hydrological interpretation of the meaning of active subspaces

Bittner et al. (2020a)[1]

Abstract

The use of the active subspace method was recently proposed to reduce the dimension of complex hydrological models, perform sensitivity analysis of model parameters and quantify the uncertainty affecting model parameters. Although this inversion method is highly promising in terms of computational performance, a clear hydrological interpretation of the meaning of the active subspace that it identifies is missing. In this work, we infer how the active subspace changes in dimension and feature depending on geometrical and hydrological properties of the karst aquifer model LuKARS. We find that both the hydrotope area coverage and model parameters describing the catchment characteristics (here: water storage and discharge properties of the hydrotopes) have major impacts on the active subspace. Our results show that the active subspace method can be used to investigate the relation between the model structure, the area of a hydrotope and the simulated spring discharge.

6.1   Introduction

Hydrologists typically apply mathematical models to address questions related to the quantity and quality of water resources (Srinivasan and Arnold, 1994; Arnold et al., 1998; Bronstert et al., 2002; Brath et al., 2006; Hanasaki et al., 2008; Guse et al., 2015). Distributed models can provide reasonable physical representations of hydrological processes in a catchment but require detailed information about surface and subsurface properties (Henson et al., 2018; Chen et al., 2018). In the

---

[1]**Bittner, D.**, Teixeira Parente, M., Mattis, S., Wohlmuth, B., Chiogna, G., 2020. Identifying relevant hydrological and catchment properties in active subspaces: An inference study of a lumped karst aquifer model. Advances in Water Resources 135, 103472.

particular case of karst aquifers, that information often cannot be obtained due to their highly complex and heterogeneous subsurface structure (Jukić and Denić-Jukić, 2009; Ladouche et al., 2014). This lack of spatially distributed data about subsurface flow makes conceptual rainfall-discharge models suitable tools to predict the discharge of a karst system. Conceptual models allow to drastically simplify the description of the functioning of the subsurface system (Mazzilli et al., 2013; Hosseini et al., 2017; Mudarra et al., 2019; Ollivier et al., 2019). However, finding an acceptable conceptual model representation for complex hydrological systems is difficult (Hollaway et al., 2018). Once a conceptual model is considered apprioriate for a catchment, the next step is to identify if its parameters can be reasonably estimated considering the available observations. The general trade-off is two-fold (Jehn et al., 2019). Quite often model complexity can be characterized by its number of parameters. A low-dimensional parameter space, i.e. 4 to 6 parameters (Jakeman and Hornberger, 1993), can help to reduce parameter uncertainty but does not necessarily avoid the occurence of equifinality (Hartmann et al., 2017). Also, a low-dimensional parameter space does not guarantee model adequacy. More precisely, dominant hydrological processes, such as matrix infiltration or conduit flow, may not be predicted in a proper way. In case of a high dimensional parameter space, it is much easier to represent these processes in a complex karst system than with a small number of parameters (Hartmann, 2018). However, models requiring a large number of calibration parameters can suffer from overparametrization and parameters can lose their identifiability (Hartmann et al., 2014a).

Constantine et al. (2014) proposed the active subspace method to reduce the dimensions of a model's parameter space, to perform global sensitivity analysis and to quantify the parameter uncertainties. In this work, we focus on the use of the active subspace method to perform a global sensitivity analyisis for a lumped karst parameter model. When we talk about sensitivity analysis performed in an active subspace framework, we do not talk about the sensitivity of single physical parameters. Instead, we investigate the most relevant linear combinations of physical parameters. In other words, working in the active subspace framework naturally leads to the definition of the sensitivity of single parameters in relation to the values of other parameters. We call these linear combinations of parameters informed if the objective function measuring deviation from observed data is sensitive to it.

So far, the active subspace method was used in different hydrological research studies (Jefferson et al., 2015; Erdal and Cirpka, 2019; Teixeira Parente et al., 2019a), including an application to a karst hydrologic model in which Teixeira Parente et al. (2019a) effectively reduced the dimensions of the model's parameter space and quantified the uncertainties affecting the model parameters. Although these works clearly showed the advantages of using the active supspace method for inverse modeling and uncertainty quantification in a Bayesian framework, a detailed hydrological interpretation of what an identified active subspace means is still lacking.

In this work, we exploit the active subspace method to infer which geometrical and hydrological model parameters influence the feature and dimension of the active subspace. We take as an illustrative example the recently proposed LuKARS (Land use change modeling in KARSt systems) model (Bittner et al., 2018a). The LuKARS model is based on the implementation of

hydrotopes, i.e. distinct landscape units characterized by homogeneous hydrological properties as a result of similar land use and soil types (Arnold et al., 1998), and was developed to simulate the hydrological impacts of land use changes in a karst aquifer. We investigate a total of 3 synthetic test cases (TC), each consisting of 7 scenarios, modified after the LuKARS model of the Kerschbaum spring recharge area in Waidhofen a.d. Ybbs (Austria). The LuKARS model of the Kerschbaum spring consists of 4 hydrotopes; 3 calibration hydrotopes (each having 7 calibration parameters) and 1 hydrotope representing a dolomite quarry.

Our research hypothesis is that we can identify a clear pattern that can relate the dimension and the feature of the active subspace with underlying geometrical and hydrological model parameters, used to describe different hydrological properties of a chatchment. This is of practical relevance, because it is beneficial for modelers to know if it is worth characterizing all catchment properties in each hydrotope or if there is the possibility for assigning a priority for field investigations. To test the hypothesis, our particular research objectives are (i) to investigate which geometrical properties and (ii) which hydrological properties of a hydrotope mostly affect the dimension and the feature of an identified active subspace.

In the following, we provide a description of the active subspace method in Section 6.2. Then, in Section 6.3 we describe how we intgrated the LuKARS model in the active subspace framework. The results and discussion will be shown in Section 6.4. Finally, we conclude our findings in Section 6.5.

6.2   Methodology

In this section, we provide an abstract framework for our dimension reduction technique. A step-by-step explanation of how we investigate dependencies between active subspaces and catchment properties and which relevant information can be derived for hydrological modeling is given.

6.2.1   Definition of parameter ranges

The first step is to define reliable parameter ranges for all parameters of a model to be investigated. In case of lumped conceptual models, these ranges should be chosen large enough to contain plausible parameter values.

6.2.2   Define independent model parameters and distributions

A basic property of hydrologic models is that their model parameters are not necessarily independent from a statistical point of view (Bárdossy, 2006). However, the active subspace framework prefers independent parameters. Thus, based on the real model parameters, now called *physical parameters*, new synthetic parameters, called *calibration parameters*, need to be introduced to get statistical independency. The parameter ranges defined for the physical parameters need to be translated into the admissible parameter ranges of the calibration parameters. For that, it is essential

that the relationships between the physical parameters, and thus, also the calibration parameters, are known. For the calibration parameters we need to assume a theoretical density distribution ρ, e.g. uniform or a truncated Gaussian. Eventually, the ranges of the calibration parameters are mapped to the range of [-1,1].

6.2.3 Parameter sampling and measuring uncertainties

The active subspace method identifies directions in the calibration parameter space in which a preselected objective evaluation function changes most, on average (Constantine et al., 2014). For a hydrologic model the objective is to simulate a discharge time series that matches an observation set $\boldsymbol{d}$. The chosen model with a given set of input parameters $\boldsymbol{x}$ is represented by the map $\mathscr{G}$. For each parameter in $\boldsymbol{x}$, we take n samples from ρ. Given that measured discharge time series are affected by measuring errors, we also need to consider these errors as uncertainties in the proposed methodology. Therefore, assuming that $\mathscr{G}$ is a perfect model, we take $\boldsymbol{\eta} \sim \mathscr{N}(0, \Gamma)$ as a zero-centered Gaussian noise with covariance matrix Γ, such that:

$$\boldsymbol{d} = \mathscr{G}(\boldsymbol{x}) + \boldsymbol{\eta}. \tag{6.1}$$

6.2.4 Select objective evaluation function and approximate gradient

To identify the quality of a fit between a modeled and observed discharge time series, an objective evaluation function needs to be selected. In the framework of the active subspace method, Teixeira Parente et al. (2019a) used the data misfit function for the application of a hydrologic model. Here, the data misfit function is denoted by $f_{\boldsymbol{d}}$:

$$f_{\boldsymbol{d}}(\boldsymbol{x}) := \frac{1}{2} \|\boldsymbol{d} - \mathscr{G}(\boldsymbol{x})\|_{\Gamma}^2 := \frac{1}{2} \|\Gamma^{-1/2}(\boldsymbol{d} - \mathscr{G}(\boldsymbol{x}))\|_2^2. \tag{6.2}$$

It is important to state that the results obtained with the data misfit function are different from results obtained with the Nash-Sutcliffe Efficency (NSE) (Nash and Sutcliffe, 1970). Since the NSE is a nonweighting squared error function it is focusing high-flow conditions (Gupta et al., 2009). The data misfit function, in contrast, is a weighting squared error function that gives a relative error between model results and observations and does not favor low- or high-flow conditions.

To identify important directions of $f = f_{\boldsymbol{d}}$, one looks at eigenpairs of the symmetric positive semi-definite $n \times n$ matrix

$$\boldsymbol{C} := \int \nabla f(\boldsymbol{x}) \nabla f(\boldsymbol{x})^\top \rho(\boldsymbol{x}) \, d\boldsymbol{x} = \boldsymbol{W} \Lambda \boldsymbol{W}^\top, \tag{6.3}$$

where ρ indicates the density of the distribution of the calibration parameters. Thus, we only have to assume that f has partial derivatives which are square-integrable with respect to ρ. We emphasize that this is a rather weak assumption since it is satisfied for almost all types of discontinuities. Only functions that are nowhere differentiable or have non-integrable singularities, which

are rare and degenerated cases, do not fit in this context. The matrix $W = [w_1, \ldots, w_n]$ contains the eigenvectors w_i of C, and the matrix $\Lambda = \text{diag}(\lambda_1, \ldots, \lambda_n)$ is a diagonal matrix with the eigenvalues on the diagonal. The eigenvalues of C, which contain all calibration parameters, provide information about the average sensitivity of f in the direction of the corresponding eigenvector, since it holds that

$$\lambda_i = w_i^\top C w_i = \int (w_i^\top \nabla f(x))^2 \rho(x) \, dx. \tag{6.4}$$

In practice, C can be approximated by a finite Monte Carlo sum, i. e.

$$C \approx \frac{1}{N} \sum_{j=1}^{N} \nabla f(x_j) \nabla f(x_j)^\top = \tilde{W} \tilde{\Lambda} \tilde{W}^\top \tag{6.5}$$

for $N \in \mathbf{N}$ and parameter samples x_j taken from the defined parameter distribution ρ. Given that we approximate the matrix C using a finite Monte Carlo sum, the matrices $\tilde{W} = [\tilde{w}_1, \ldots, \tilde{w}_n]$ and $\tilde{\Lambda} = \text{diag}(\tilde{\lambda}_1, \ldots, \tilde{\lambda}_n)$ denote perturbations to their exact counterpart from Eq. 6.3.

6.2.5 Active subspace identification and sensitivity analysis

If the eigenvalues decay quickly, there are directions in the parameter space where f varies much more, on average, than other directions, i.e. these directions are significantly more informed by the data d. An eigenvalue associated to an eigenvector in the parameter space depends on the entire set of calibration parameters. Therefore, the analysis of each eigenvector/eigenvalue inform us about the behavior of the entire set of calibration parameters and their interaction. We decide to choose a k-dimensional subspace, i.e., we truncate after k eigenvalues/-vectors such that the $k+1$-th eigenvalue is the first eigenvalue whose difference to the largest eigenvalue is bigger than one order of magnitude (Step 1 in Fig. 6.1). Another alternative would be to base the truncation on the ratio between the sum of the remaining $n - k$ eigenvalues and the total sum. The two strategies would differ if there was a spectral plateau after one or two eigenvalues, i.e., $n - 1$ or $n - 2$ eigenvalues of the same or similar size. However, since this is generally not the case in our results, both strategies give similar decisions and our results in Section 6.4 do not strongly depend on a particular strategy.

The span of the eigenvectors associated with significant eigenvalues is called the active subspace (Step 2 in Fig. 6.1). At this point of the proposed methodology, the active subspace is exploited to investigate the relation between a measured discharge and specific catchment properties. The particular objective is to see if a physical explanation for the parameter sensitivities can be found in active subspaces. Therefore, the approximated eigenpairs $(\tilde{w}_i, \tilde{\lambda}_i)$ are used to compute global sensitivity metrics (Step 3 in Fig. 6.1) (Constantine and Diaz, 2017). The components of the vector s consisting of the sensitivity values are defined as

$$s_i = \sum_{j=1}^{n} \lambda_j (w_j)_i^2, \quad i = 1, \ldots, n. \tag{6.6}$$

Based on the identified active subspace, the model's parameter space can effectively be reduced for inversion (Teixeira Parente et al., 2019a). However, this topic was already illustrated in other works (Erdal and Cirpka, 2019; Teixeira Parente et al., 2019a) and will not be further discussed.
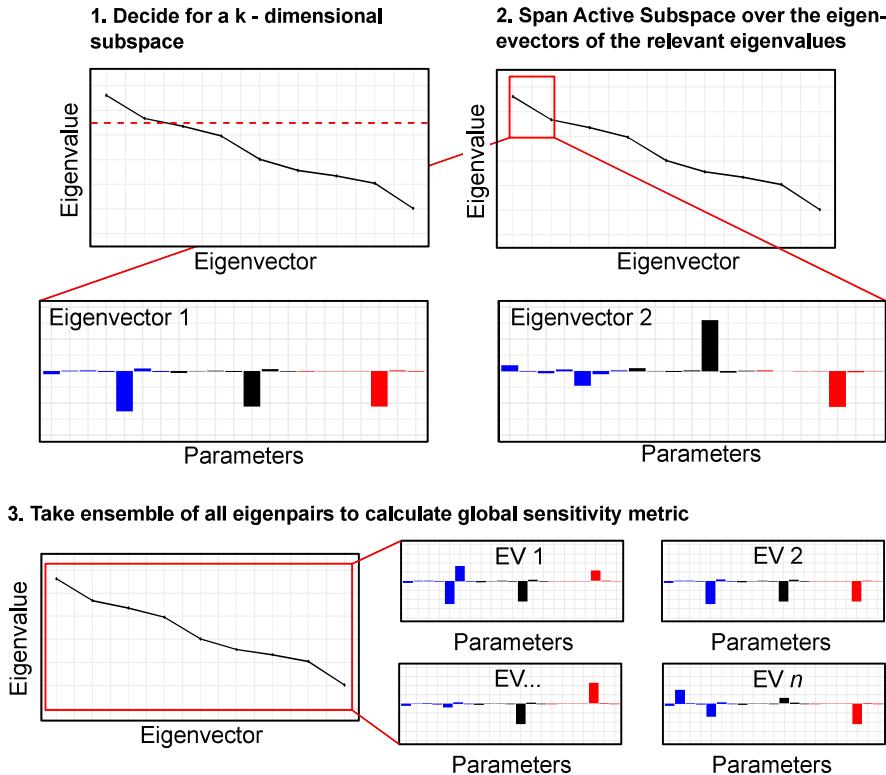

Figure 6.1: A conceptual sketch of the procedure for the active subspace identification and sensitivity analysis.

6.3 Application of the methodology to the LuKARS model

The proposed active subspace methodology is applied to the LuKARS model, which was developed by Bittner et al. (2018a). LuKARS is a semi-distributed lumped parameter model that was developed to simulate the hydrological impacts of land use changes in a karstic system. The model consists of different buckets that represent the dominant hydrotopes in a regarded recharge area (see Fig. 6.2a). LuKARS was set up for the Kerschbaum springshed (2.5 km^2) in Waidhofen a.d. Ybbs in Austria (Fig. 6.2b), which we use to create synthetic TC's. With a mean annual discharge

of 34 ls⁻¹, the Kerschbaum karst spring is part of the regional water supply system of Waidhofen a.d. Ybbs. The small-scale recharge area is predominantly covered by beech forests and parts of it are used for mining activities (Fig. 6.2b). A detailed description of the study area can be found in Narany et al. (2019). In the following, we provide a detailed explanation how we integrate the LuKARS model in the framework of the active subspace method. A detailed description of LuKARS and its equations is provided in A.1.

6.3.1 LuKARS implementation in the framework of the Active Subspace method

Based on our experiences from previous analyses, we derived a set of ranges for each parameter that is applied for the step described in Section 6.2.1. In the particular case of the minimum and maxium storage values of a hydrotope, i.e. $E_{\min}$ and $E_{\max}$, data driven ranges were obtained using the methodology of DWA (2018). The ranges of all other parameters were chosen large enough so that they contain reliable values. Table 6.1 lists these parameter ranges used in the active subspace method applied to LuKARS.
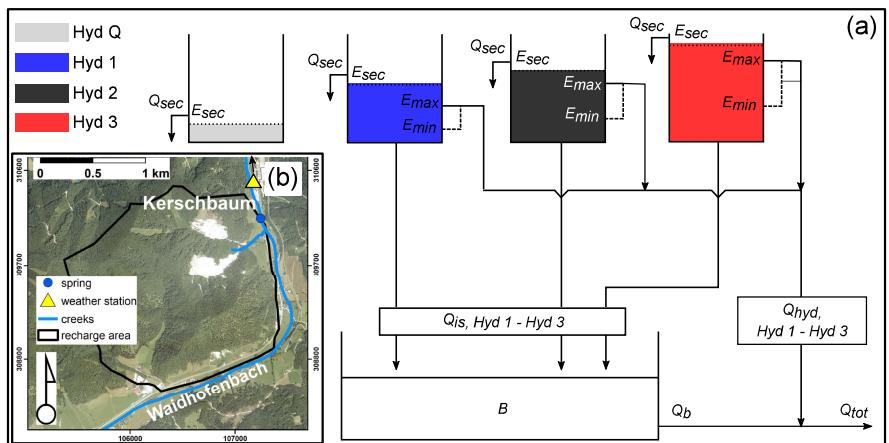

Figure 6.2: Conceptual model sketch and overview of the study area Waidhofen a.d. Ybbs (Austria). (a) Conceptual model of the recharge area as implemented in LuKARS, considering the four hydrotopes (Hyd Q, Hyd 1, Hyd 2 and Hyd 3) and the baseflow storage B. The different bucket sizes show the different storage capacities of the respective hydrotopes (not to scale). (b) The boundary of the Kerschbaum spring recharge area. The orthophoto, which was kindly provided by the water works Waidhofen a.d. Ybbs, shows that the predominant landcover is forest.

Each hydrotope in LuKARS has characteristic hydrological responses to precipitation events determined by its soil and land use properties. To what extent one particular hydrotope response

contributes to the total catchment response depends on both, the hydrotope's area and the parameters that control its discharge variability. On the one hand, hydrotopes having coarse-grained and shallow soils should have a high contribution to the quickflow and groundwater recharge. Moreover, the possibility that these hydrotopes become dry after a long period without any precipitation should be allowed. On the other hand, the parametrization of hydrotopes with more fine-textured and deep soils should allow to show slow and minor contributions to the quickflow and the groundwater recharge but be able to store a certain water volume. This means, that a given parameter set of a hydrotope with a small storage volume (e.g. a shallow, coarse-grained soil) needs to be interpreted in relation to the parameters applied to a second hydrotope with a higher storage volume (e.g. a thicker, more fine-grained soil). These physical constraints have to be met to accept a set of hydrotope parameters in LuKARS. For the Kerschbaum spring recharge area, the LuKARS model has 4 hydrotopes, each of them covering a defined percentage area. Hyd 1 has shallow and coarse-grained soils, Hyd 2 has more fine-grained soils with moderate thicknesses, Hyd 3 has mostly loam textured soils with more elevated thicknesses and Hyd Q represents the dolomite quarries. The dominant vegetation type for Hyd 1, Hyd 2 and Hyd 3 are beech forests. For this concrete example of the Kerschbaum spring model, Hyd Q is not included in the process of model calibration since, by law, the quarries drain all water on the surface outside the catchment (Bittner et al., 2018a). Thus, the Kerschbaum model has a total of 3 hydrotopes and a total of 21 model parameters that need to be calibrated. For these 21 model parameters the following physical constraints are met:

$$
\begin{aligned}
k_{\text{hyd},1} &\geq k_{\text{hyd},2} \geq k_{\text{hyd},3}, \\
E_{\text{min},1} &\leq E_{\text{min},2} \leq E_{\text{min},3}, \\
E_{\text{max},1} &\leq E_{\text{max},2} \leq E_{\text{max},3}, \\
\alpha_1 &\geq \alpha_2 \geq \alpha_3, \\
k_{\text{is},1} &\geq k_{\text{is},2} \geq k_{\text{is},3}, \\
k_{\text{sec},1} &\geq k_{\text{sec},2} \geq k_{\text{sec},3}, \\
E_{\text{sec},1} &\leq E_{\text{sec},2} \leq E_{\text{sec},3}.
\end{aligned}
\tag{6.7}
$$

As justified by (Teixeira Parente et al., 2019a), the condition introduced for α values is not strictly necessary, but was implemented to amplify the quick response of hydrotopes with low storage capacities, i.e. those displaying a small difference between $E_{\text{min},i}$ and $E_{\text{max},i}$ and a low value of $E_{\text{max},i}$. Since the model parameters for each hydrotope have to meet the constraints shown in Eq. (6.7), they are not independent from a statistical point of view. Following the second step in our methodology (Section 6.2.2), we need to introduce three types of non-normalized calibration parameters with a defined density ρ. We assumed a logarithmic distribution ρ of the parameter ranges of the hydrotope specific discharge parameters (k_{hyd}, k_{is} and k_{sec}, hereafter summarized as k_* parameters). All other calibration parameters have a uniform prior distribution.

1. Given the log distribution of the k_*, we define

$$k_*^{\log} = \log(k_*) \tag{6.8}$$

for each $k_* \in \{k_{\mathrm{hyd},i}, k_{\mathrm{is},i}, k_{\mathrm{sec},i}\}$, $i = 1, 2, 3$.

2. For $i = 1, 2, 3$, since $E_{\min,i} \leq E_{\max,i}$, parameter samples for $E_{\max,i}$ would be dependent on samples $E_{\min,i}$. Hence, we write $E_{\max,i} = E_{\min,i} + \Delta E_i$. We define therefore new (non-normalized) calibration parameters ΔE_i. This means that the parameter $E_{\max,i}$ is "replaced" by ΔE_i, which is independent of $E_{\min,i}$.

3. Similar to point 2), the physical constraints from Eq. (6.7) lead to the introduction of new (non-normalized) calibration parameters that mimic the difference between values of two successive hydrotopes.

4. The parameters with a Δ are new calibration parameters, taking values in [0,1] and replacing corresponding model parameters on the left hand side of the equal sign.

We make sure that these constraints are met and that values are chosen such that the corresponding model parameters lie in the respective specified intervals from Table 6.1. In particular, we write for $i = 2, 3$

$$
\begin{aligned}
k_{\mathrm{hyd},i}^{\log} &= k_{\mathrm{hyd},i,\mathrm{lb}}^{\log} + \Delta k_{\mathrm{hyd},(i-1,i)}^{\log} (\min\{k_{\mathrm{hyd},i,\mathrm{ub}}^{\log}, k_{\mathrm{hyd},i-1}^{\log}\} - k_{\mathrm{hyd},i,\mathrm{lb}}^{\log}), \\
E_{\min,i} &= \max\left\{E_{\min,i-1}, E_{\min,i,\mathrm{lb}}\right\} \\
&\quad + \Delta E_{\min,(i-1,i)} \left(E_{\min,i,\mathrm{ub}} - \max\left\{E_{\min,i-1}, E_{\min,i,\mathrm{lb}}\right\}\right), \\
\alpha_i &= \alpha_{i,\mathrm{lb}} + \Delta \alpha_{(i-1,i)} \left(\min\left\{\alpha_{i,\mathrm{ub}}, \alpha_{i-1}\right\} - \alpha_{i,\mathrm{lb}}\right), \\
k_{\mathrm{is},i}^{\log} &= k_{\mathrm{is},i,\mathrm{lb}}^{\log} + \Delta k_{\mathrm{is},(i-1,i)}^{\log} (\min\{k_{\mathrm{is},i,\mathrm{ub}}^{\log}, k_{\mathrm{is},i-1}^{\log}\} - k_{\mathrm{is},i,\mathrm{lb}}^{\log}), \\
k_{\mathrm{sec},i}^{\log} &= k_{\mathrm{sec},i,\mathrm{lb}}^{\log} + \Delta k_{\mathrm{sec},(i-1,i)}^{\log} (\min\{k_{\mathrm{sec},i,\mathrm{ub}}^{\log}, k_{\mathrm{sec},i-1}^{\log}\} - k_{\mathrm{sec},i,\mathrm{lb}}^{\log}), \\
E_{\mathrm{sec},i} &= \max\left\{E_{\mathrm{sec},i-1}, E_{\mathrm{sec},i,\mathrm{lb}}\right\} \\
&\quad + \Delta E_{\mathrm{sec},(i-1,i)} \left(E_{\mathrm{sec},i,\mathrm{ub}} - \max\left\{E_{\mathrm{sec},i-1}, E_{\mathrm{sec},i,\mathrm{lb}}\right\}\right),
\end{aligned} \tag{6.9}
$$

where lower ($_{\mathrm{lb}}$) and upper bounds ($_{\mathrm{ub}}$) of each interval for the model parameters are specified in Table 6.1. Given a reference hydrotope (e.g. Hyd 1 in Teixeira Parente et al. (2019a)), introducing new synthetic parameters is only necessary for the other hydrotopes (e.g., Hyd 2 and 3 in Teixeira Parente et al. (2019a)).

Eventually, all non-normalized calibration parameters are normalized, i. e., they are mapped to the interval [-1,1]. The normalized parameters are denoted with a bar above their name and form the final 21-dimensional vector x of calibration parameters, i. e.

$$\begin{aligned}
\boldsymbol{x} = (&\bar{k}_{\text{hyd},1}^{\log}, \bar{E}_{\text{min},1}, \Delta\bar{E}_1, \alpha_1, \bar{k}_{\text{is},1}, \bar{k}_{\text{sec},1}, \bar{E}_{\text{sec},1}, \\
&\Delta\bar{k}_{\text{hyd},(1,2)}^{\log}, \Delta\bar{E}_{\text{min},(1,2)}, \Delta\bar{E}_2, \Delta\bar{\alpha}_{(1,2)}, \\
&\quad \Delta\bar{k}_{\text{is},(1,2)}, \Delta\bar{k}_{\text{sec},(1,2)}, \Delta\bar{E}_{\text{sec},(1,2)}, \\
&\Delta\bar{k}_{\text{hyd},(2,3)}^{\log}, \Delta\bar{E}_{\text{min},(2,3)}, \Delta\bar{E}_3, \Delta\bar{\alpha}_{(2,3)}, \\
&\quad \Delta\bar{k}_{\text{is},(2,3)}, \Delta\bar{k}_{\text{sec},(2,3)}, \Delta\bar{E}_{\text{sec},(2,3)})^\top \in \mathbf{R}^{21}.
\end{aligned} \tag{6.10}$$

Table 6.1: Overview of the model parameter ranges defined for all hydrotopes used in the three test cases. The respective numbers indicate the lower bound and the upper bound of the parameter ranges which are used as prior intervals for the active subspace method. For the meaning of the parameters we refer to the explanation given in A.1

Test Case	Hydrotope	k_{hyd} [$m^2 d^{-1}$]	$E_{\min}$ [mm]	$E_{\max}$ [mm]	α [-]	k_{is} [m mm^{-1}d^{-1}]	k_{sec} [m mm^{-1}d^{-1}]	E_{sec} [mm]
	Hyd 2.1	8.5 - 850	40 - 80	80 - 160	0.5 - 1.3	0.00055 - 0.055	0.0023 - 0.23	130 - 220
TC 1	Hyd 2.2	8.5 - 850	40 - 80	80 - 160	0.5 - 1.3	0.00055 - 0.055	0.0023 - 0.23	130 - 220
	Hyd 2.3	8.5 - 850	40 - 80	80 - 160	0.5 - 1.3	0.00055 - 0.055	0.0023 - 0.23	130 - 220
	Hyd 1	9 - 900	10 - 50	15 - 75	0.7 - 1.6	0.002 - 0.2	0.0095 - 0.95	25 - 70
	Hyd 1.1	12 - 1200	10 - 50	15 - 75	0.7 - 1.6	0.002 - 0.2	0.0095 - 0.95	25 - 70
	Hyd 1.2	22 - 2200	10 - 50	15 - 75	0.7 - 1.6	0.002 - 0.2	0.0095 - 0.95	25 - 70
	Hyd 1.3	40 - 4000	10 - 50	15 - 75	0.7 - 1.6	0.002 - 0.2	0.0095 - 0.95	25 - 70
TC 2	Hyd 1.4	60 - 6000	10 - 50	15 - 75	0.7 - 1.6	0.002 - 0.2	0.0095 - 0.95	25 - 70
	Hyd 1.5	70 - 7000	10 - 50	15 - 75	0.7 - 1.6	0.002 - 0.2	0.0095 - 0.95	25 - 70
	Hyd 1.6	100 - 10000	10 - 50	15 - 75	0.7 - 1.6	0.002 - 0.2	0.0095 - 0.95	25 - 70
	Hyd 2	8.5 - 850	40 - 80	80 - 160	0.5 - 1.3	0.00055 - 0.055	0.0023 - 0.23	130 - 220
	Hyd 3	7.7 - 770	75 - 120	155 - 255	0.2 - 0.7	0.00025 - 0.025	0.0015 - 0.15	320 - 450
	Hyd 1	9 - 900	10 - 50	15 - 75	0.7 - 1.6	0.002 - 0.2	0.0095 - 0.95	25 - 70
TC 3	Hyd 2	8.5 - 850	40 - 80	80 - 160	0.5 - 1.3	0.00055 - 0.055	0.0023 - 0.23	130 - 220
	Hyd 3	7.7 - 770	75 - 120	155 - 255	0.2 - 0.7	0.00025 - 0.025	0.0015 - 0.15	320 - 450

6.3.2 Synthetic test cases of the Kerschbaum spring LuKARS model

Using the physical relations of the lumped hydrotope parameters (Eq. (6.7)), we want to investigate how much the spring discharge, generated using the LuKARS model for different TC's, depends on the model representation of specific catchment characteristics (here: hydrotope properties). Therefore, we aim to explore how changing hydrological conditions may affect the active subspaces and to see if this variability is reflected in the eigenvectors of the significant eigenvalues. In particular, under the assumption that the model properly represents the hydrology of the area, we want to see if we can identify a dependence of the spring discharge on different catchment properties, i.e. the discharge variability a hydrotope displays and the area it covers. For this purpose, we create three different synthetic TC's, each consiting of seven scenarios (summarized in Table 6.2).

TC 1: In TC 1, we assume that the recharge area of the Kerschbaum spring is homogeneous in terms of hydrotope properties. Therefore, we say that all hydrotopes, Hyd 2.1, Hyd 2.2 and

Hyd 2.3, have the same range of parameter values as indicated in Table 6.1. In the different scenarios, we vary the area covered by Hyd 2.1, Hyd 2.2 and Hyd 2.3 as shown in Fig. 6.3a. This TC reflects catchments with quite homogeneous properties. In TC 1 we investigate the dependence of spring discharge on the area covered by a hydrotope.

TC 2: In TC 2, we assume that all hydrotopes cover the same area in the catchment (Fig. 6.3b). We increase the discharge variability of the quickflow originating from Hyd 1 while maintaining constant properties of the other two hydrotopes (Table 6.1). With this TC, we represent catchments with different magnitudes of contrasting hydrological properties.

TC 3: Finally, in TC 3 we use three different hydrotopes, Hyd 1, Hyd 2 and Hyd 3, and assume different hydrotope areas following the distributions shown in Fig. 6.3c. In this TC, we simulate recharge areas with a complex set up of contrasting hydrological properties with changing impacts on the catchment response.

In order to better follow all different scenarios with varying hydrotope properties, the following naming scheme was applied: The scenario indices are composed of the number of the TC and the number of the scenario. E.g. Scenario 2 and 4 of TC 1 are named Scenario 1.2 and Scenario 1.4. In those cases, where the properties of one specific hydrotope were modified, we renamed the respective hydrotope by putting a number behind the hydrotope name. E.g., a modification of Hyd 1 is named Hyd 1.1, Hyd 1.2 and so forth. In all TC's, we maintain the 4 % dolomite quarries. The hydrotopes considered in the different TC's are also summarized in Table 6.1. Since all TC scenarios represent hypothetical cases, we had to create synthetic discharge time series as observations for the data misfit function (Eq. 6.2). Those time series were created with the LuKARS model using the parameter set reported in Table 6.3 and assuming a noise level of 5 % (as communicated by the water works Waidhofen a.d. Ybbs for the original, measured discharge time series of the Kerschbaum spring).

Table 6.2: Summary of all investigated test cases with their respective scenarios, hydrotopes and changes applied in each scenario.

| Test case	Scenarios	Hydrotopes	Changes in Scenarios
TC 1	1.1 - 1.7	Hyd 2.1, Hyd 2.2, Hyd 2.3	increasing area of Hyd 2.2, decreasing areas of Hyd 2.1 and Hyd 2.3
TC 2	2.1 - 2.7	Hyd 1.1 to Hyd 1.6, Hyd 1, Hyd 2, Hyd 3	increasing discharge parameter (k_{hyd}), ranging from Hyd 1.1 ($120\,\mathrm{m^2 d^{-1}}$) to Hyd 1.6 ($1000\,\mathrm{m^2 d^{-1}}$)
TC 3	3.1 - 3.7	Hyd 1, Hyd 2, Hyd 3	increasing area of Hyd 1, decreasing areas of Hyd 2 and Hyd 3
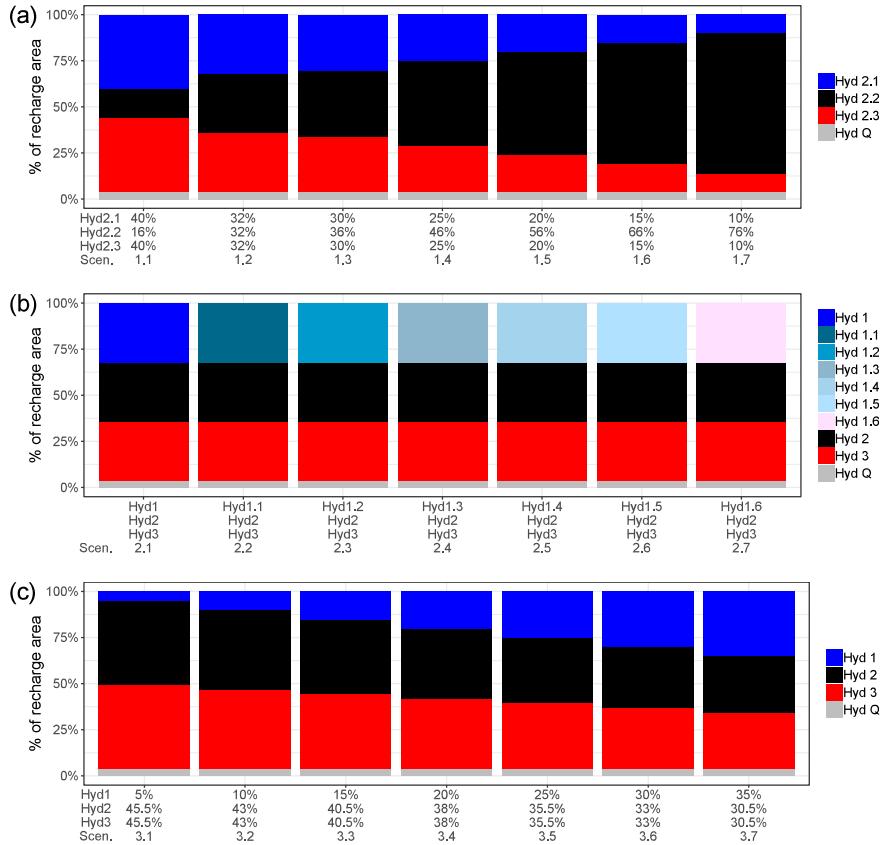
Figure 6.3: a) Investigated scenarios with same hydrotope properties and varying hydrotope areas for TC 1. b) Investigated scenarios of TC 2 having equal hydrotope areas, i.e. 32 %, and changing quickflow properties of Hyd 1. c) Investigated scenarios with changing areas of the real Kerschbaum spring hydrotopes for TC 3.

In a next step, we investigate how the mean sensitivities of each hydrotope change with varying hydrotope areas when considering homogeneous catchment conditions (TC 1), when changing hydrotope properties (TC 2) and when considering the real properties of the Kerschbaum spring hydrotopes with changing areas (TC 3). Mean hydrotope sensitivities represent the proportion of the sum of parameter sensitivities of one hydrotope to the sum of sensitivities of the entire parameter space. Then, we compare the global sensitivity metrices with the parameters showing up in the active subspaces of each scenario of the TC's. Here, we investigate if in the computed active

subspaces we can identify the catchment properties decisive for modeling the spring discharge. Finally, we use the active subspaces to identify the catchment properties of the Kerschbaum recharge area which are relevant for the spring discharge.

6.4 Results and Discussion

We want to emphasize that for the following results we consider a maximum of four significant eigenvalues. This means that if the eigenvalue decay over one order of magnitude contains more than four eigenvalues, the decay is not considered as significant enough to identify an active subspace. Further, we want to stress that the following results, comprising parameter sensitivities, are computed with respect to the normalized calibration parameters without any loss of generality for the interpretation of the results in the physical parameter space given the mapping through Eq. (6.7). To cut through the complexity of all scenarios of TC 1, 2 and 3, in the following we will show the eigendecomposition only for two scenarios in each TC. For the sake of completeness, however, we provide the illustrated results of all other simulations in the Supplementary Material.

Table 6.3: Overview of the model parameters used for each hydrotope to generate the synthetic discharge time series in each test case. For the meaning of the parameters we refer to the explanation given in A.1

Test Case	Hydrotope	k_{hyd} [m^{2}d^{-1}]	E_{min} [mm]	E_{max} [mm]	α [-]	k_{is} [m mm^{-1}d^{-1}]	k_{scc} [m mm^{-1}d^{-1}]	E_{scc} [mm]	l_{hyd} [m]
	Hyd 2.1	85	60	120	0.8	0.0055	0.023	180	900
TC 1	Hyd 2.2	85	60	120	0.8	0.0055	0.023	180	900
	Hyd 2.3	85	60	120	0.8	0.0055	0.023	180	900
	Hyd 1	90	23	31	0.9	0.02	0.095	35	1600
	Hyd 1.1	120	23	31	0.9	0.02	0.095	35	1600
	Hyd 1.2	220	23	31	0.9	0.02	0.095	35	1600
	Hyd 1.3	400	23	31	0.9	0.02	0.095	35	1600
TC 2	Hyd 1.4	600	23	31	0.9	0.02	0.095	35	1600
	Hyd 1.5	700	23	31	0.9	0.02	0.095	35	1600
	Hyd 1.6	1000	23	31	0.9	0.02	0.095	35	1600
	Hyd 2	85	60	120	0.8	0.0055	0.023	180	900
	Hyd 3	77	90	200	0.55	0.0025	0.035	380	960
	Hyd 1	90	23	31	0.9	0.02	0.095	35	1600
TC 3	Hyd 2	85	60	120	0.8	0.0055	0.023	180	900
	Hyd 3	77	90	200	0.55	0.0025	0.035	380	960

6.4.1 Test case 1

With TC 1, our specific objective was to investigate the dependence of a spring dicharge on the area coverage of the catchment's hydrotopes. In particular, we wanted to see if this dependence can be identified in the active subspace of an investigated scenario. Fig. 6.4a displays the average

sensitivity of each hydrotope for each scenario in TC 1 considering different hydrotope area distributions. The plot shows that with increasing area covered by Hyd 2.2 its sensitivity increases, too. Also, the sensitivities of Hyd 2.1 and Hyd 2.3 decrease with decreasing area.
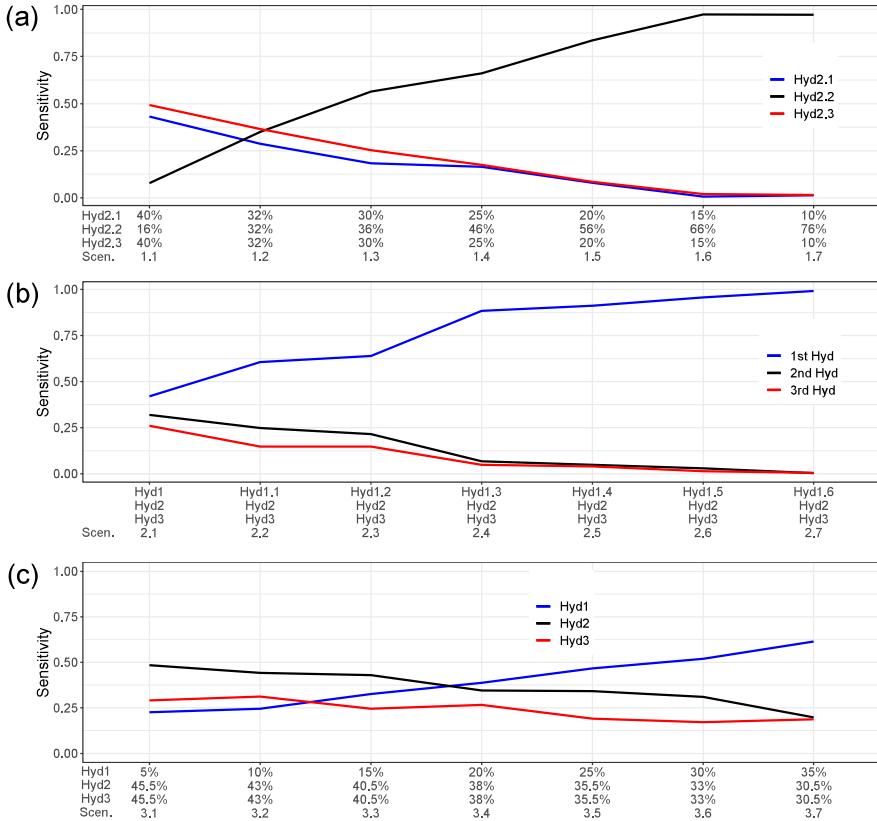

Figure 6.4: Average hydrotope sensitivities as obtained by the active subspace method for the investigated scenarios of a) TC 1, b) TC 2 and c) TC 3.

When Hyd 2.2 covers an area larger than 60 %, it practically becomes the only sensitive hydrotpe. We can further observe that all hydrotopes have almost the same sensitivity in Scenario 1.2 where all hydrotopes cover the same area. More precisely, Hyd 2.1 and Hyd 2.3 cover the same area in all scenarios of TC 1 with mostly the same sensitivities. Small differences between their sensitivities only occur in those scenarios where both hydrotopes together cover more than 50 % of the assumed recharge areas (Scenario 1.1, 1.2 and 1.3). This minor difference of sensitivities

can be related to the mean distance to the spring of both hydrotopes (l_{hyd}). Since Hyd 2.1 is farther away from the spring than Hyd 2.3 (Table 6.3), it is less sensitive than Hyd 2.3. Thus, we can identify a clear dependence of the mean sensitivity of a hydrotope on the area it covers. This finding is of particular relevance since the exact extent of karst recharge areas often is unknown.
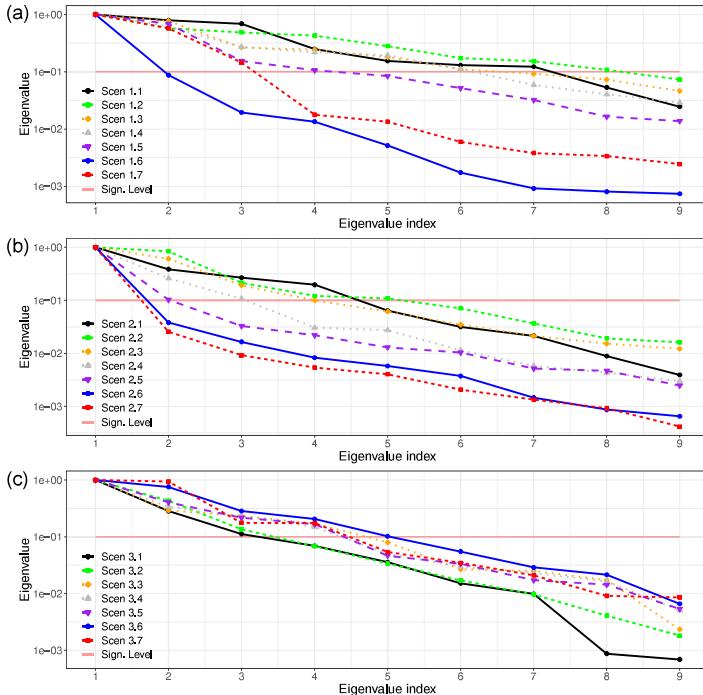

Figure 6.5: Eigenvalue decay for each investigated scenario in a) TC 1, b) TC 2 and c) TC 3 including the significance level in which we consider an active subspace. All eigenvalues are normalized to the respective maximum eigenvalue of each scenario. The red line indicates the level where we choose a k-dimensional active subspace (significance level)

The decay of the eigenvalues for each investigated scenario in TC 1, normalized to the maximum eigenvalue of the respective scenario, are shown in Fig. 6.5a. We can observe a correlation between the decrease in the active subspace dimension and the increase in the catchment area of Hyd 2.2. However, the relation is not always monotonic. Comparing the decays over the first 9 eigenvalues shown in Fig. 6.5a, we can observe the lowest decay for Scenario 1.2 and the highest decay for Scenario 1.6. The active subspace dimension ranges from 1 dimension (Scenario 1.6) to 8 dimensions (Scenario 1.2). The results suggest that the more the hydrotopes differ in terms of area coverage, the faster the decay of the eigenvalues. In other words, the more a catchment area

is dominated by one hydrotope, the lower the dimension of the active subspace.
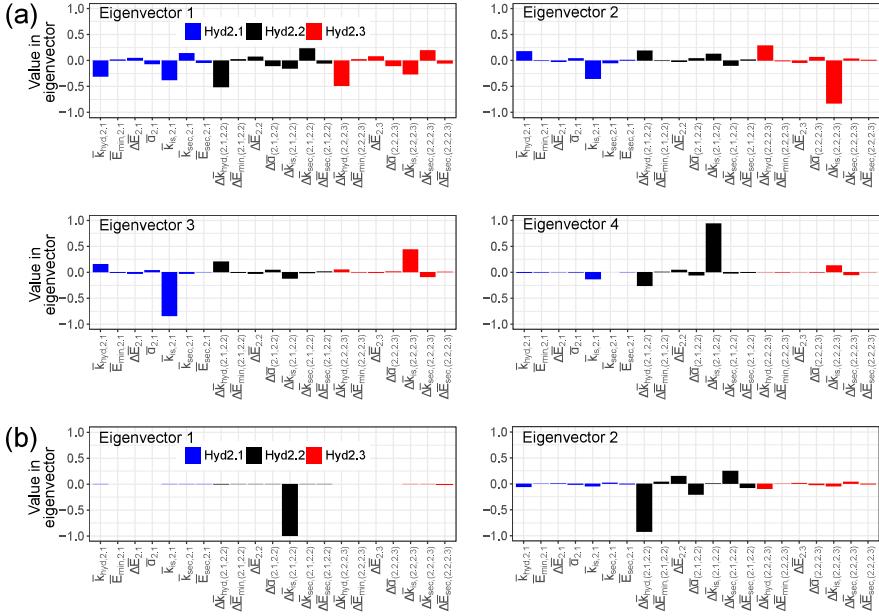
Figure 6.6: Results of the active subspace method applied to different scenarios of TC 1. a) Eigenvectors of the relevant eigenvalues of Scenario 1.2. b) Eigenvectors of the relevant eigenvalues of Scenario 1.6.

Comparable to the results of the global sensitivity analysis (Fig. 6.4a), we found that the dependence between spring discharge and the hydrotope area distribution is also reflected in the eigenvectors of the significant eigenvalues. We show this for Scenario 1.2 and 1.6. When looking at Eigenvector 1 of Scenario 1.2 (Fig. 6.6a), in which all hydrotopes cover the same area, we recognize that the contributions of all 7 hydrotope parameters are also similar between all hydrotopes. Further, the same parameters of each hydrotope have approximately equal contributions, in particular to the first eigenvector. These are the discharge parameters of the different flow components (k_{hyd}, k_{is} and k_{sec}) having similarly high loadings and the storage parameters (E_{min} and E_{max}) having similarly low loadings. From Eigenvalue 2 to 4, almost no decay happens (Fig. 6.5a), meaning that the eigenvectors of these eigenvalues have the same relevance. We argue that these similarities between the different hydrotope contributions are due to the fact that they all have similar properties in terms of their physical characteristics as well as their area coverage. Given this similarity, there are no hydrological reasons why the parameters of one hydrotope should be more informed than others. This feature is correctly captured by both, the active subspace behavior as

well as by the sensitivity analysis performed through the eigenvector decomposition of the active subspaces. Hence, the area covered by each hydrotope directly affects how discharge data informs the parameter space of LuKARS.

For Scenario 1.6, we can notice a considerable eigenvalue decay from the first to the second eigenvalue (Fig. 6.5a), pointing towards the existence of a 1-dimensional active subspace (Fig. 6.6b). Although the decay suggests the presence of a 1-dimensional subspace, we also show Eigenvector 2 to see by which parameters it is dominated. Looking at these two eigenvectors, the parameters of Hyd 2.2 clearly dominate these two dimensions, thus reflecting the results of the global sensitivity analysis shown as average hydrotope sensitivities in Fig. 6.4a. Here, the discharge parameter of the recharge (k_{is}) is most sensitive as it is the dominant parameter in the first eigenvector. Eigenvector 2 is also dominated by Hyd 2.2 parameters with a high contribution of the discharge parameters controlling the quickflow (k_{hyd}) and secondary spring discharge (k_{sec}). This shows that the model is mainly sensitive to the parameters constraining the amount as well as the variability of the three types of hydrotope discharges represented in the conceptual model (Q_{hyd}, Q_{is} and Q_{sec}, see also Fig. 6.2).

When further taking into account all other analyzed scenarios of TC 1 (Supplementary Material), we can state that the higher the relative area covered by Hyd 2.2, the more pronounced gets its contribution to the eigenvectors with significant eigenvalues. In all scenarios, the most sensitive parameters are the discharge parameters (k_{hyd}, k_{is} and k_{sec}). In summary, the results of TC 1 highlight that we can identify the impact of the area covered by a hydrotope on the spring discharge in an active subspace.

6.4.2 Test case 2

Our aim when creating TC 2 was to investigate if in an active subspace we can identify the relevance of the hydrological variability a hydrotope displays independently from its area. For this purpose, we created seven different scenarios considering equal areas of all hydrotopes, i.e. 32 % for Hyd 1, Hyd 2 and Hyd 3, and varying quickflow properties in one of the hydrotopes, displayed by Hyd 1, Hyd 1.1, Hyd 1.2, Hyd 1.3, Hyd 1.4, Hyd 1.5 and Hyd 1.6 (Scenarios 2.1 - 2.7, see Fig. 6.3b).

Fig. 6.4b shows the mean parameter sensitivities summed for all hydrotopes and for each of the investigated scenarios. It highlights that the parameter sensitivities of Hyd 1 increase when increasing the quickflow contribution. Considering the constant area covered by each hydrotope in all TC 2 scenarios (Fig. 6.3b), we show that the discharge variability displayed by a hydrotope, here Q_{hyd}, can fully explain the differences in the mean sensitivities of different hydrotopes.

When considering the eigenvalue decays in TC 2 (Fig. 6.5b), we can observe that the eigenvalue decay is highest in Scenario 2.7 and lowest in Scenario 2.2. Thus, the variations in hydrological variability of the hydrotopes lead to differences in active subspace dimensions, i.e. with increasing hydrological variability the eigenvalue decay increases. The active subspace dimension ranges from 1 dimension (Scenario 2.6 and 2.7) to 5 dimensions (Scenario 2.2). We can observe a correlation between the decrease in the active subspace dimension and the increase in k_{hyd} value.

However, also in this case the relation is not always monotonic and it depends on the cut off value that we chose for the eigenvalues to be considered relevant for the active subspace.

We show the results of the eigenvectors of the significant eigenvalues for two example scenarios in Fig.6.7, i.e. Scenario 2.2 and 2.7. To what extent the quickflow contribution increases between the scenarios is displayed in the empirical cumulative distribution function (ecdf) of Q_{hyd} shown in the Supplementary Material. As for TC 1, the results of all other scenarios from TC 2 are provided in the Supplementary Material.
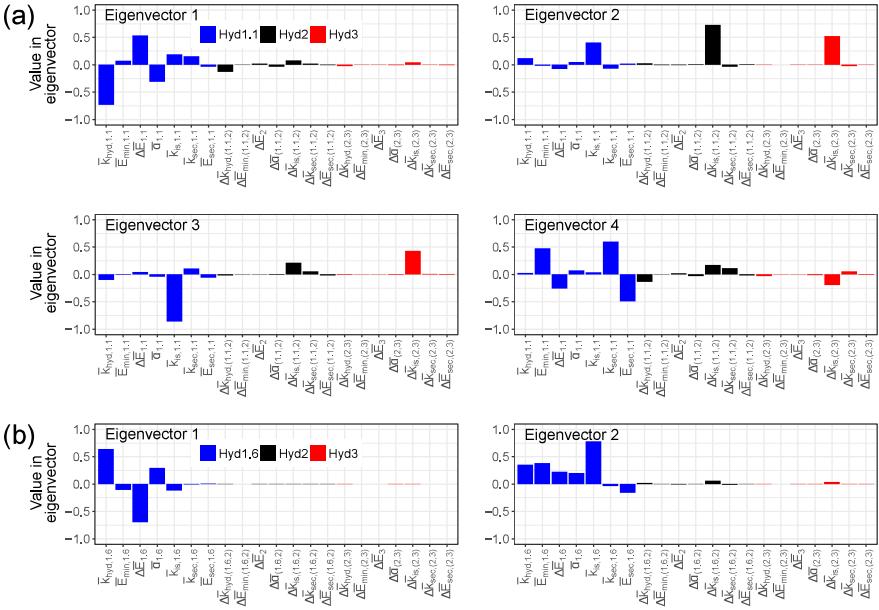

Figure 6.7: Results of the active subspace method applied to different scenarios of TC 2. a) Eigenvectors of the significant eigenvalues of Scenario 2.2. b) Eigenvectors of the significant eigenvalues of Scenario 2.7.

For Scenario 2.2, the decay of the eigenvalues shown in Fig. 6.5b is slow and without spectral gaps that span at least one order of magnitude. In the eigenvectors of the first four eigenvalues (Fig.6.7a), we recognize a dominant contribution of the first hydrotope's parameters (Hyd 1.1). It can be observed that all parameters of Hyd 1.1 are present with a noticable contribution in the shown eigenvectors, while the contributions from Hyd 2 and Hyd 3 are primarily related to their respective discharge parameter of the recharge (k_{is}). In Eigenvector 1, the dominant contributions are related to the parameters controlling the quickflow of Hyd 1.1 (k_{hyd}, E_{max} and α). In particular all discharge parameters of Hyd 1.1 have high scores in the shown eigenvectors. Eigenvector 2

is dominated by high loadings of the discharge parameters of the recharge (k_{is}), with decreasing order from Hyd 2 to Hyd 1.1 to Hyd 3. Eigenvector 3 behaves similarly to Eigenvector 2, while Eigenvector 4 is similar to Eigenvector 1.

In Scenario 2.7, the strong eigenvalue decay from Eigenvalue 1 to Eigenvalue 2 suggests the presence of a 1-dimensional active subspace (Fig. 6.5b). However, similar as we did for Scenario 1.6, we also show Eigenvector 2 to see by which parameters it is dominated. The eigenvectors, shown in Fig. 6.7b, again highlight a clear dominance of the parameters controlling the quickflow of Hyd 1.6 (k_{hyd}, E_{max} and α). Eigenvector 2 is dominated by the discharge parameter of the recharge (k_{is}) with still considerably high loadings of all other parameters of Hyd 1.6.

Looking at the ensemble of all TC 2 scenarios (Supplementary Material), the parameters which determine the variability of the quickflow component Q_{hyd}, have increasing contributions with increasing discharge variability (e.g. Fig. 6.7a and b). This shows that the active subspace method identifies the specific impact of the quickflow component of the first hydrotope on the spring discharge, which is increasing from Scenario 2.1 to 2.7. We further identify that the discharge parameters controlling the recharge (k_{is}) in Hyd 2 and Hyd 3 play a more significant role in the TC 2 scenarios than their respective quickflow discharge parameters (k_{hyd}). This highlights that, in contrast to the more pronounced quickflow contribution from the first hydrotope, the recharge Q_{is} originating from Hyd 2 and Hyd 3 is more important than the quickflow in these two hydrotopes. Thus, the results of TC 2 highlight that the active subspace method identifies the dominant discharge components in different hydrotopes.

6.4.3   Test case 3

TC 3 was created to investigate how the feature and dimension of the active subspace behave when both, the area and the hydrological properties of the hydrotopes vary in a catchment. In Fig. 6.4c, we show the mean parameter sensitivities summed for all hydrotopes and for each of the investigated scenarios. We can see that the parameter sensitivities of Hyd 1 increase when increasing its relative area coverage in the catchment. However, this occurs at a smaller rate than in TC 1. Simultaneously, when decreasing the areas of Hyd 2 and Hyd 3, their parameter sensitivities decrease, too. However, we can observe that the sensitivity of Hyd 1 parameters is not uniquely dependent on the hydrotope area. For instance, when focusing on the sensitivities in Scenario 3.4 (Fig. 6.4c), it can be seen that the parameters of Hyd 1 are most sensitive although Hyd 2 and Hyd 3 cover almost double the area of Hyd 1. Thus, we argue that the hydrotope's discharge variability and its area together lead to a more complex pattern of mean sensitivities as compared to TC 1 and TC 2. The question that arises is why the sensitivity of Hyd 1 is higher in Scenario 3.4, 3.5, 3.6 and 3.7, although in most of these scenarios its area is smaller than those of Hyd 2 and Hyd 3. The answer to this questions can be found when comparing the mean hydrotope sensitivities of TC 3 (Fig. 6.4c) with the variability of the two hydrotope discharge components, quickflow (Q_{hyd}) and groundwater recharge (Q_{is}). We show this as an example for Scenario 3.1 and 3.7 in the Supplementary Material. For Hyd 1, we can observe that the variability of Q_{hyd} and Q_{is} increases with increasing area coverage. The same relationship holds for Hyd 2, but in

reverse order, meaning that the variability of both flow components decreases with decreasing area covered by Hyd 2. Nevertheless, no pronounced change of discharge variability can be observed for Hyd 3, neither for Q_{hyd} nor Q_{is}. This shows that the impact of changing hydrotope areas on the discharge variability is higher in hydrotopes with low storage capacities than in those with high ones. Since the areas of Hyd 2 and Hyd 3 are similar in all scenarios but the magnitude of the discharge parameters is higher in Hyd 2, the discharge variability explains the difference in the mean hydrotope sensitivities. This finding can further be validated when comparing the hydrotope sensitivities (Fig. 6.4c) with the ecdf's of Scenarios 3.7 (Supplementary Material). It shows that in case the largest hydrotope also displays the highest discharge variability (here: Hyd 1), we can observe a high impact on the mean hydrotope sensitivities.
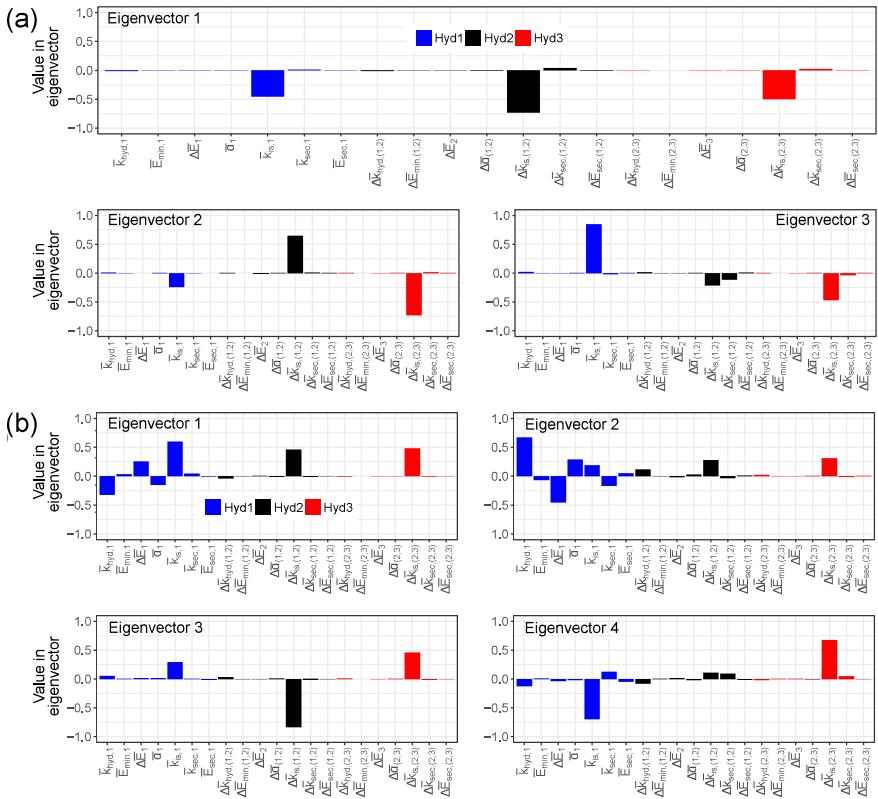

Figure 6.8: Results of the active subspace method applied to different scenarios of TC 3. a) Eigenvectors of the significant eigenvalues of Scenario 3.1. b) Eigenvectors of the significant eigenvalues of Scenario 3.7.

Further, we can observe that the eigenvalue decay over the first 9 eigenvalues is highest in Scenario 3.1 and lowest in Scenario 3.7 (Fig. 6.5c). However, the differences in the eigenvalue decays of all TC 3 scenarios are not as substantial as compared to those observed for TC 1 and 2. In fact, the active subspace dimension in TC 3 ranges from 3 dimensions (Scenario 3.1) to 5 dimensions (Scenario 3.6). Hence, we also learn that the complex interplay of changing areas and different hydrological variabilities of the hydrotopes do not lead to pronounced differences in active subspace dimensions. Therefore, the hydrological properties of a hydrotope may compensate for a smaller hydrotope area.

The discovered relationship between the hydrological variability of a hydrotope and the mean hydrotope sensitivity is also displayed in the eigenvectors of the significant eigenvalues, shown as examples for Scenario 3.1 and 3.7 in Fig. 6.8a and b, respectively. In Scenario 3.1 (Fig. 6.8a), where the area coverage of Hyd 1 is significantly smaller than Hyd 2 and Hyd 3, we can recognize a dominant contribution of Hyd 2 in Eigenvector 1, Hyd 3 in Eigenvector 2 and Hyd 1 in Eigenvector 3. In particular, we can observe a dominant contribution in all three hydrotopes of the discharge parameter controlling the recharge (k_{is}). Further, we can identify a similar eigenvector contribution of Hyd 1 and Hyd 3 parameters, also reflecting their similar mean sensitivities shown in Fig. 6.4c. This can be explained by the fact that the groundwater recharge is linear proportional to the baseflow (see Eq. A.16), making the discharge coefficients controlling the amount and variability of Q_{is} more sensitive than those of Q_{hyd}.

Looking at the eigenvectors of the four most significant eigenvalues of Scenario 3.7 (Fig. 6.8b), we can see that the discharge parameters of the recharge (k_{is}) again are the most important parameters of Hyd 1, Hyd 2 and Hyd 3, respectively. Different to Scenario 3.1, almost all parameters of Hyd 1 have a noteworthy contribution in the most important Eigenvectors 1 and 2. Interestingly, the contribution of the discharge parameter controlling the quickflow (k_{hyd}) appears to be similar, potentially even more dominant than the contribution of the discharge parameter of the recharge k_{is} in the first 2 eigenvectors. This can be related to the fact that Q_{hyd} has a much faster contribution to the spring discharge than Q_{is} passing through the groundwater storage and becoming baseflow. Hence, although Q_{hyd} is about 4 times lower than Q_{is} (see range of the discharge components in the ecdf's in Supplementary Material), in the active subspace we identify that their respective discharge coefficients are similarly informed.

6.5   Conclusion

In this work, we applied the active subspace method to the LuKARS rainfall-discharge model for three test cases to investigate how the active subspace changes in dimension and feature depending on geometrical properties, i.e. the area a hydrotope covers, and hydrological properties, i.e. the discharge variability a hydrotope displays. Therefore, we provided a framework in which we adapt the physical model parameters of LuKARS to make the active subspace method applicable for the model while maintaining the physical constraints between each hydrotope. Our aim was to investigate how much each parameter of the model is informed by the discharge data and how

different model setups affect the results of the active subspace analysis. Model parameters that are not sensitive to discharge observations should be then constrained using other data, although this may be non-trivial in karst systems. The main findings of each test case are the following:

TC 1: For catchments with rather homogeneous hydrological properties, we showed that we can identify the impact of varying hydrotope areas in an active subspace. We also show that if a hydrotope covers more than 60 % of the area, then discharge data are informative only for model parameters belonging to that hydrotope. This may guide tailored field investigation on a specific part of the catchment.

TC 2: For catchments with contrasting hydrological properties but similiar hydrotope areas, we highlighted that in an active subspace we can identify the impacts of individual hydrological processes on the catchment response. In particular, discharge data will inform model parameters belonging to the hydrotope mostly responsible for quickflow. To inform other model parameters, and in particular to better constrain model parameters representing the other hydrotopes, we suggest to integrate in model calibration measured time series of other hydrological variables (e.g. soil moisture).

TC 3: For catchments with heterogeneous hydrological properties and varying hydrotope areas we found that both features show a complex interplay in informing model parameters. The relationship between hydrological properties of a hydrotope and its area is strongly related to how much the spring discharge depends on the discharge variability. For those complex catchment setups we provide evidence that in an active subspace we can identify if the area covered by a hydrotope plays a more important role than its hydrological properties. In case the area is the most relevant feature, then its characterization using appropriate experimental methods (e.g. tracer tests) will be prioritiezed. In case other model parameters are more sensitive to discharge observations, it is worth measuring other hydrological variables to better constrain the model parameters which are not informed by discharge observations.

With our results, we highlight that the active subspace method can be used to guide modelers in obtaining field data relevant for their respective modeling purposes. This is possible because the eigenvectors of the relevant eigenvalues in an active subspace provide information about informed linear directions in the parameter space. Depending on how pronounced the parameters appear in those directions, we can learn about the importance of individual catchment features. Thus, we consider the information provided in these informed parameter directions as the main strength of the active subspace method which cannot be derived from other global sensitivity analysis methods typically applied in hydrology, e.g. Sobol (Sobol, 2001). In total, we highlight that the area a hydrotope covers has a more significant impact on the dimension of an active subspace than the discharge dynamics a hydrotope displays. We found that the discharge coefficients (k_* parameters) were the most sensitive parameters in all scenarios.

For future works, our methodology can be used to hydrologically interpret the results obtained from the active subspace method when applied to other hydrologic models. In our case, the information about the relevant catchment properties were constrained solely by discharge data. We

argue that the information about relevant properties of an investigated aquifer system can be better constrained when calibrating a model using more than one data source. Using hydrochemical and discharge data in a multi-objective calibration approach, similar to Hartmann et al. (2017), can be valuable to identify catchment properties which are relvant for both, hydrological and hydrochemical fluxes. Moreover, using the active subspace method in a framework of a multi-temporal scale calibration, e.g. (Schaefli and Zehe, 2009), can help to identify those model parameters which are sensitive for the high frequency components of a measured discharge.

Chapter 7

Conclusions

In this dissertation, a lumped parameter model was proposed that can be used to perform land use change impact studies in karst systems. This model, i.e. LuKARS, is based on the implementation of landscape units with similar soil and land use types, defined as hydrotopes. Moreover, a new methodology for uncertainty quantification and parameter dimension reduction, i.e. the active subspace method, was tested for LuKARS. It was shown that this method can help to effectively reduce the parameter dimensions as well as to quantify the model parameter and output uncertainties. Finally, a detailed framework for a hydrological interpretation of an active subspace was suggested.

7.1 Summary

At the beginning of this dissertation, the case study problem was defined (Section 1.1). In the pre-alpine and dolomite-dominated karst system in Waidhofen a.d. Ybbs, a continuous land use change was observed since the year 2007. Increasing areas were exploited for dolomite mining without knowing about related impacts on the springs which rise close to the quarries. Protecting these springs is, however, of great importance since they are used for the regional water supply of Waidhofen a.d. Ybbs. Thus, a detailed understanding of the aquifer system functionning, its dominant procesess and how it is linked to land surface operations was required to investigate the impacts of increasing dolomite quarries.

   In order to get a more profound knowledge how the karst system works, all existing data were collected and analyzed. A particular focus was given to long-term hydrochemical time series which were available for the five springs and the pumping well. Although these time series had an unsatisfying temporal resolution, i.e. ≤ 4 measurements per year, the small scale study area (ca. $10\,\mathrm{km}^2$) and the high number of springs provided a high spatial resolution of the dataset. In the study of Narany et al. (2019), it was shown that such a dataset can be used to get a detailed understanding of the internal functioning of a karst system. Primarily, the work highlighted that dolomite dissolution plays a major role in the hydrochemical signal obtained at all springs. However, a cluster analysis with that dataset helped to create a conceptual model of the mountain massif showing how the dif-

ferent springs are distinct or connected in the subsurface. It was further shown that these long-term hydrochemical time series were useful to determine the relative impact of the unsaturated and the saturated zone for each investigated spring. Generally, the closer a spring is located to a striking, impermeable layer (here: Opponitz layer), the higher the relative contribution of the unsaturated zone to the spring discharge. This particularly accounts for the Hieslwirt and Mitterlug springs. The closer a spring or well is located to the center of the syncline of the dolomitic basement, the more the hydrochemical patterns point towards a higher relative contribution of the saturated zone. This was especially observed for the Kerschbaum spring and the Forster well. The Glashütten spring was identified as an intermediate spring between these mentioned classes, which can be related to its geographical position between the Kerschbaum and the Hieslwirt spring. The Hinterlug spring showed a similar pattern as the Kerschbaum spring and the Forster well. However, given its clear tectonic separation from the springs of the Glashüttenberg massif, it was not considered in the conceptual model. Finally, the prior knowledge about the local geology (GBA, 2018) was used to justify the developed concept of the hydrological functioning of the Waidhofen karst system.

The higher the contribution of the unsaturated zone to a spring discharge, the more the spring is affected by land use actions. For the part of the catchment which is affected by increasing dolomite mining activities, i.e. the Kerschbaum spring recharge area, a clear pattern of contributions from the unsaturated and saturated zone was identified. This hydrological understanding of the Kerschbaum spring recharge area gathered from the work of Narany et al. (2019) provided the base for the development of a numerical model. The purpose of this model was to simulate and predict the impacts of the increasing mining activities in the area. Physical properties of the soil-epikarst system and land cover play an important role for the Kerschbaum spring discharge as shown by Narany et al. (2019). For this reason, building a modeling approach that is based on distinct landscape units with homogeneous soil and land use properties, i.e. hydrotopes, appeared promising. The specific hydrological response of a hydrotope should reflect the typical hysteretic behavior observed in soil-epikarst systems and allow for three discharge components, i.e. the quickflow, recharge and discharge drained outside the area (e.g. secondary spring discharge or surface runoff). In the work of Bittner et al. (2018a), this model, i.e. LuKARS, was developed for the Kerschbaum spring recharge area. It was calibrated for the year 2006 using a trial-and-error approach and then validated for the year 2007. Using the calibrated hydrotopes, the model was succesfully tested for the Hinterlug and Mitterlug spring recharge areas to ensure its transferability. In a next step, the calibrated Kerschbaum model was further applied for distinct time steps between 2010 to 2013. In this validation phase, the observed land use change was considered in the model structure. It was finally shown that the LuKARS model is able to simulate the hydrological impacts of the increasing dolomite quarries. The model results highlight that proceeding mining activities lead to a decrease in the discharge of the Kerschbaum spring and, thus, have a negative impact on the regional water supply.

The next step was to provide the model in an accesible and user-friendly way to make it applicable by practioners and decision-makers. In the particular case of Waidhofen a.d. Ybbs, this was the waterworks. However, the model should not only be provided to the responsibles of

the study area but to all interested persons dealing with land use change impact studies in karst systems. For that reason, a tailored framework was needed that provides a GUI for interested users. In the framework of the FREEWAT project, a QGIS plugin was developed that comprises various tools for water resource management. The plugin has a modular structure consisting of pre-processing, simulation and post-processing tools. Given that no rainfall-discharge model was included in the simulation module, the particular aim in the work of Bittner et al. (2020b) was to integrate LuKARS into FREEWAT. This software coupling was considered as beneficial for three reasons. First, the FREEWAT project ended in 2017 and its maintenance and development strongly depends on voluntary initiatives of researchers to support this developers group. Hence, the integration of LuKARS was considered as a valuable contribution to the overarching goal of making FREEWAT a comprehensive toolbox for water resource managers. Second, the present structure and the provided tools in the pre- and post-processing modules made FREEWAT a tailored framework for making LuKARS more accessible and applicable by non-researchers. Third, given its hydrotope-based structure, using a GIS system as GUI for LuKARS was a promising approach since all relevant model data objects could be stored either as time series or geospatial data. Finally, the developed software as well as the application example for the Kerschbaum spring recharge area were provided on GitHub.

Each hydrotope implemented in LuKARS has seven calibration parameters. Taking the example of the Kerschbaum spring LuKARS model, three hydrotopes need to be calibrated with a total of 21 calibration parameters. As discussed in the Introduction, in particular in Section 1.2.4, this high-dimensional parameter space makes the model prone to parametric and output uncertainties. Without knowing about these model uncertainties, using the LuKARS model to produce reliable predictions on the hydrological impacts of land use changes is challenging. For that reason, the purpose in the work of Teixeira Parente et al. (2019a) was to quantify the uncertainties related to model parameters and output of LuKARS and to investigate if the parameter space can be reduced and approximated by a surrogate model. The active subspace method was chosen as an appropriate tool since it can identify dominant directions in which the model parameters can be most constrained. Those directions further provide information about how different model parameters are related to each other, thus, going beyond a global sensitivity analysis. It was found that the parameters controlling groundwater recharge become most informed in the active subspace of the Kerschbaum LuKARS model. Moreover, the identified active subspace suggested that the initial 21-dimensional parameter space may be reduced to four dimensions. A Bayesian inversion was performed using a polynomial surrogate fitted to the four dimensional subspace. It was shown that the ranges of the parameters, which were most informed in the active subspace, became most constrained from the prior to the posterior. The model output uncertainties were quantified using 1000 random samples drawn from the original parameter space and including the updated information from the active subspace. The results highlight that when using the four dimensional surrogate model, the model output uncertainties are < 10 % with respect to the mean discharge of the Kerschbaum spring. Thus, it was concluded that using the active subspace method in a Bayesian inversion framework not only provides a tool to quantify model parameter and output uncertainties

but also to reduce the parameter dimensions in LuKARS. Given that the model output uncertainties were considerably low, using LuKARS in combination with the active subspace method can provide reliable predictions on land use change impacts in karst systems.

Although the application of the active subspace method to LuKARS provided good results for what relates to the quantification of model uncertainties, a clear hydrological intepretation of what an identified active subspace means is still missing. This research gap was addressed in the work of Bittner et al. (2020a). In particular, three different test cases, each consisting of seven scenarios were investigated in which either the area of a hydrotope, the properties of a hydrotope or both were changed. The first test case was defined to investigate the impact changing hydrotope areas have on the spring discharge when having homogeneous hydrological properties. It was shown that if a hydrotope covers more than 60 %, the spring discharge only informs model parameters that belong to this hydrotope. In the second test case, the area of the hydrotopes remained constant while the discharge variability of one hydrotope was increased from one to another scenario. The study showed that the higher the hydrological variability of the quickflow in one hydrotope, the more the spring discharge data informs the respective quickflow parameters of that hydrotope. Finally, in the thrid test case, the hydrotope area and the discharge variability varied were different in all scenarios. For these complex cases, it was shown that it is possible to identify in an active subspace if either geometrical or specific hydrological properties of a catchment play a more important role for the simulated spring discharge. How the hydrological properties and the area of a hydrotope are related strongly depends on how much the spring discharge is affected by the discharge variability of a hydrotope. In general, the application of the active subspace method can support a modeler to obtain relevant field data which are required for a particular modeling purpose. This study showed that relevant catchment and hydrological properties can be identified in an active subspace.

In summary, this dissertation provided a comprehensive study consisting of the two objectives: *Model development, implementation and application* and *Uncertainty quantification*. It was shown that a detailed conceptual understanding of a dolomite karst system can be gathered from long-term hydrochemical time series with a low temporal but a high spatial resolution. Based on this knowledge, a lumped parameter model, LuKARS, was developed which has been proven to be applicable for land use change impact studies in karstic areas. This model was made available as an open source GUI for water resource managers by implementing the model into the FREE-WAT plugin in QGIS. In order to ensure the reliability of the LuKARS model results, the active subspace method was applied to quantify model parameter and output uncertainties. The initial 21-dimensional parameter space of the Kerschbaum spring LuKARS model was succesfully reduced to a four dimensional surrogate model with considerably low output uncertainties. Finally, a clear hydrological interpretation of the meaning of an active subspace was given that supports a reliable and process-based dimension reduction of lumped parameter models like LuKARS.

7.2 Outlook

In this last section of the presented dissertation, an outlook is given for possible future research activities. Therefore, a specific outlook is given for possible developments of the LuKARS model and for the active subspace method.

7.2.1 Future enhancements of LuKARS

The LuKARS model was developed for a dolomite-dominated karst system. Dolomite aquifers, depending on the existing fracture system as well as on the geo- and hydrochemical boundary conditions of a catchment, generally show a lower degree of karstification than pure limestone aquifers. This fact is related to the higher solubility of Ca^{2+} as compared to Mg^{2+}. As a result, the discharge variability in limestone karst systems is generally higher than the hydrological dynamics observed at springs orginating from dolomite aquifers. Thus, LuKARS should be tested for a limestone-dominated aquifer in future research in order to ensure its general applicability for karst systems.

Moreover, a typical feature of karst systems is the duality of groundwater recharge, i.e. concentrated recharge through sinkholes or sinking streams and diffuse recharge in the catchment. In the particular case of the Waidhofen a.d. Ybbs study area, prior investigations of Hacker (2003) revealed that concentrated recharge does not play an important role for the aquifer system. This knowledge was adopted in the development of LuKARS, in which only diffuse recharge was considered. However, when transferring LuKARS to a limestone system, concentrated recharge may become a dominant factor and, thus, needs to be considered in the model structure. Hence, future works need to further advance the model code in order to account for the duality of the recharge processes in karst systems.
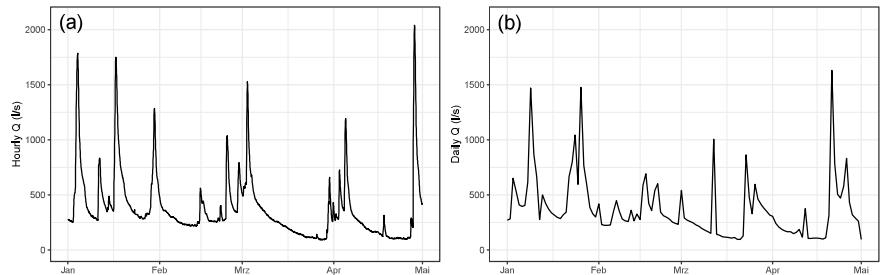

Figure 7.1: Comparison hourly vs. mean daily karst spring discharge. (a) Example for hourly discharge measured at a limestone karst spring. (b) Daily mean discharge obtained from the hourly time series shown in (a).

When applying LuKARS to a limestone karst system, the time steps on which the model is operated may become another challenge. As pointed out earlier, limestone-dominated karst systems

typically show a higher discharge variability than dolomite aquifers. Since LuKARS was developed to work with daily time steps, a further step should be to modify the model code such that it can be run on an hourly basis. In general, daily discharge values often miss information on relevant hydrological processes, such as conduit flow, and they sometimes do not show the typical characteristics of a karst spring hydrograph, i.e. the rising and recession limb of a peak discharge. As an illustrative example, Fig. 7.1 shows a comparison between hourly discharge values and daily means obtained from the hourly time series. Thus, operating LuKARS on an hourly basis can ensure that the relevant hydrological processes and characteristics observed discharge time series obtained from limestone-dominated karst springs can be captured.

Given that various discharge components are simulated by each hydrotope in LuKARS, specifically the quickflow and the recharge, it could be an interesting future work to perform a multi-objective calibration considering measured flow data from these different components. In particular, recharge areas in which not only the spring discharge but also conduit flow is monitored can provide great test sites for this recharge idea. Such a recharge area is e.g. the Milandre test site in the Swiss Jura mountains, which has been intensively investigated by the karst community (Perrin et al., 2007; Jeannin et al., 2016). The responsible persons of this test site were already contacted to initiate this joint research activity. It is assumed that this multi-objective calibration can provide an alternative way to reduce the model output uncertainties in LuKARS.
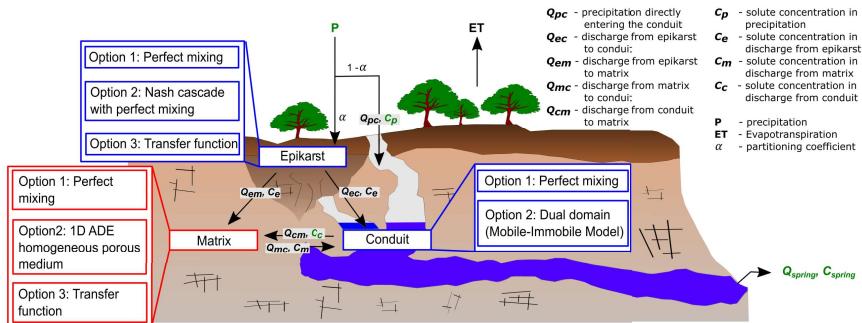

Figure 7.2: Possibilities for integrating and trying different solute transport routines in LuKARS. Different modeling approaches are presented for the three compartments in karst systems, i.e. the epikarst, matrix and conduits.

Besides the proposed enhancements for LuKARS as a rainfall-discharge model, the model could be further improved by the integration of solute transport routines. For different compartments of a karst aquifer, various solute transport approaches could be tested in order to figure out which of them works best in combination with a lumped parameter model. Some examples are given in Fig. 7.2. Having a coupled flow and transport model can further support to better constrain the ranges of calibration parameters, e.g. in the framework of a multi-objective calibration approach using discharge and hydrochemical time series.

7.2.2 Future works with Active Subspaces

The active subspace method was proven to be an efficient tool to quantify model parameter and output uncertainties, perform global sensitivity analysis, efficiently reduce the dimensions of a lumped parameter model and to provide relevant information about dominant hydrological and catchment properties. So far, the active subspace method uses the data misfit function to measure deviation between observed and simulated spring discharge. This can be further enhanced when coupling the active subspace method in a multi-objective calibration approach. It should be possible to include further time series, e.g. measured hydrochemical signals, in combination with discharge measurements. When applying this multi-objective approach in the existing Bayesian inversion context, it can be assumed that the parametric uncertainties can be more reduced than in a single-objective approach.
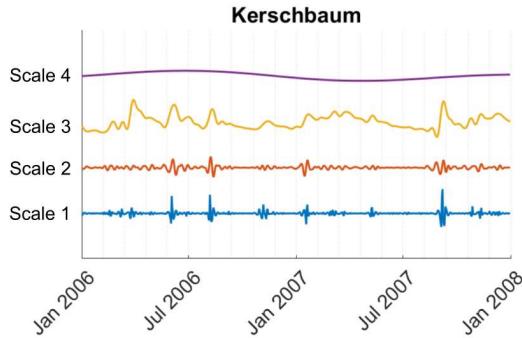

Figure 7.3: Example of different signals obtained from the discrete wavelet transform when applied to a spring discharge time series.

Similarly, the signals obtained from the discrete wavelet transform could act as a multi-temporal scale objective to which the data misfit function could be applied to. Such a decomposition is shown as an example in Fig. 7.3. By that, only one measured time series is needed but providing multiple calibration objectives to be coupled with the active subspace method. In order to validate the results, the weighted sum of eigenvalues and eigenvectors obtained for each signal should bring similar results as those obtained when using only the measured discharge time series.

As previous studies showed that the global sensitivity metrics obtained from the active subspaces is comparable to those gathered from Sobol's method (Sobol, 2001; Constantine and Diaz, 2017), it could be helpful to compare the active subspace results with those obtained from other global sensitivity analysis methods. It is assumed that this study can provide a detailed overview of advantages and disadvantages the active subspace method has as compared to others. Such a study can guide future modelers to select an appropriate sensitivity analysis tool for a predefined task (Bárdossy, 2006; Pianosi et al., 2015).

Bibliography

Ad-hoc-Arbeitsgruppe Boden, 2005. Bodenkundliche kartieranleitung (ka5). Auflage, Hannover .

Albertin, A.R., Sickman, J.O., Pinowska, A., Stevenson, R.J., 2012. Identification of nitrogen sources and transformations within karst springs using isotope tracers of nitrogen. Biogeochemistry 108, 219–232.

Almeida, R.C., Oden, J.T., 2010. Solution verification, goal-oriented adaptive methods for stochastic advection-diffusion problems. Comput. Methods Appl. Mech. Engrg. 199, 2472–2486.

Andreo, B., Gil-Márquez, J.M., Mudarra, M., Linares, L., Carrasco, F., 2016. Hypothesis on the hydrogeological context of wetland areas and springs related to evaporitic karst aquifers (málaga, córdoba and jaén provinces, southern spain). Environmental Earth Sciences 75, 759.

Arikan, A., 1988. Modalp: a deterministic rainfall-runoff model for large karstic areas. Hydrological sciences journal 33, 401–414.

Arnold, J.G., Srinivasan, R., Muttiah, R.S., Williams, J.R., 1998. Large area hydrologic modeling and assessment part i: model development 1. JAWRA Journal of the American Water Resources Association 34, 73–89.

Bakalowicz, M., 2005. Karst groundwater: a challenge for new resources. Hydrogeology journal 13, 148–160.

Bárdossy, A., 2006. Calibration of hydrological model parameters for ungauged catchments. Hydrol. Earth Syst. Sci. Discussions 3, 1105–1124.

Benson, R.C., Yuhr, L.B., 2015. Site Characterization in Karst and Pseudokarst Terraines: Practical Strategies and Technology for Practicing Engineers, Hydrologists and Geologists. Springer.

Berthelin, R., Hartmann, A., 2020. The shallow subsurface of karst systems: review and directions, in: Eurokarst 2018, Besançon. Springer, pp. 61–68.

Berthelin, R., Rinderer, M., Andreo, B., Baker, A., Kilian, D., Leonhardt, G., Lotz, A., Lichtenwoehrer, K., Mudarra, M., Padilla, I.Y., et al., 2020. A soil moisture monitoring network to characterize karstic recharge and evapotranspiration at five representative sites across the globe. Geoscientific Instrumentation, Methods and Data Systems 9, 11–23.

Beven, K., 2006. A manifesto for the equifinality thesis. Journal of Hydrology 320, 18–36.

Bhatt, G., Kumar, M., Duffy, C.J., 2014. A tightly coupled gis and distributed hydrologic modeling framework. Environmental Modelling and Software 62, 70–84.

Bicalho, C., Batiot-Guilhe, C., Taupin, J., Patris, N., Van Exter, S., Jourde, H., 2017. A conceptual model for groundwater circulation using isotopes and geochemical tracers coupled with hydrodynamics: A case study of the lez karst system, france. Chemical Geology .

Bieger, K., Arnold, J.G., Rathjens, H., White, M.J., Bosch, D.D., Allen, P.M., Volk, M., Srinivasan, R., 2017. Introduction to swat+, a completely restructured version of the soil and water assessment tool. JAWRA Journal of the American Water Resources Association 53, 115–130.

Billingsley, P., 1995. Probability and Measure. John Wiley & Sons.

Bittner, D., Narany, T.S., Kohl, B., Disse, M., Chiogna, G., 2018a. Modeling the hydrological impact of land use change in a dolomite-dominated karst system. Journal of Hydrology 567, 267–279.

Bittner, D., Parente, M.T., Mattis, S., Wohlmuth, B., Chiogna, G., 2018b. On the relationship between parameters and discharge data for a lumped karst aquifer model. arXiv preprint arXiv:1808.07009 .

Bittner, D., Parente, M.T., Mattis, S., Wohlmuth, B., Chiogna, G., 2020a. Identifying relevant hydrological and catchment properties in active subspaces: An inference study of a lumped karst aquifer model. Advances in Water Resources 135, 103472.

Bittner, D., Rychlik, A., Klöffel, T., Leuteritz, A., Disse, M., Chiogna, G., 2020b. A gis-based model for simulating the hydrological effects of land use changes on karst systems – the integration of the lukars model into freewat. Environmental Modelling and Software , 104682.

Blume, T., Van Meerveld, H., 2015. From hillslope to stream: methods to investigate subsurface connectivity. Wiley Interdisciplinary Reviews: Water 2, 177–198.

BMNT, 2018. ehyd, bundesministerium für nachhaltigkeit und tourismus, österreich. `ehyd.gv.at`. Accessed: 2018-04-18.

Borsi, I., Rossetto, R., Schifani, C., Hill, M.C., 2013. Modeling unsaturated zone flow and runoff processes by integrating modflow-lgr and vsf, and creating the new cfl package. Journal of hydrology 488, 33–47.

Boyce, S.E., Yeh, W.W.G., 2014. Parameter-independent model reduction of transient groundwater flow models: Application to inverse problems. Advances in water resources 69, 168–180.

Brath, A., Montanari, A., Moretti, G., 2006. Assessing the effect on flood frequency of land use change via hydrological simulation (with uncertainty). Journal of Hydrology 324, 141–153.

Breuer, L., Huisman, J., Willems, P., Bormann, H., Bronstert, A., Croke, B., Frede, H.G., Gräff, T., Hubrechts, L., Jakeman, A., et al., 2009. Assessing the impact of land use change on hydrology by ensemble modeling (luchem). i: Model intercomparison with current land use. Advances in Water Resources 32, 129–146.

Bronstert, A., Niehoff, D., Bürger, G., 2002. Effects of climate and land-use change on storm runoff generation: present knowledge and modelling capabilities. Hydrological processes 16, 509–529.

Brooks, S., Gelman, A., Jones, G., Meng, X.L., 2011. Handbook of Markov Chain Monte Carlo. CRC press.

Bui-Thanh, T., Girolami, M., 2014. Solving large-scale PDE-constrained Bayesian inverse problems with Riemann manifold Hamiltonian Monte Carlo. Inverse Problems 30, 114014, 23.

Cannata, M., Neumann, J., 2017. The observation analysis tool: A free and open source tool for time series analysis for groundwater modelling. Geoingeneria Ambientale e Nineria (GEAM - Geoengin. Environ. Min.) , 51–56.

Cannata, M., Neumann, J., Rossetto, R., 2018. Open source gis platform for water resource modelling: Freewat approach in the lugano lake. Spatial Information Research 26, 241–251.

Casper, M.C., Mohajerani, H., Hassler, S., Herdel, T., Blume, T., 2019. Finding behavioral parameterization for a 1-d water balance model by multi-criteria evaluation. Journal of Hydrology and Hydromechanics 67, 213–224.

Chang, Y., Wu, J., Jiang, G., Kang, Z., 2017. Identification of the dominant hydrological process and appropriate model structure of a karst catchment through stepwise simplification of a complex conceptual model. Journal of Hydrology 548, 75–87.

Charizopoulos, N., Zagana, E., Psilovikos, A., 2018. Assessment of natural and anthropogenic impacts in groundwater, utilizing multivariate statistical analysis and inverse distance weighted interpolation modeling: the case of a scopia basin (central greece). Environmental earth sciences 77, 380.

Chen, Z., Auler, A.S., Bakalowicz, M., Drew, D., Griger, F., Hartmann, J., Jiang, G., Moosdorf, N., Richts, A., Stevanovic, Z., et al., 2017a. The world karst aquifer mapping project: concept, mapping procedure and map of europe. Hydrogeology Journal 25, 771–785.

Chen, Z., Hartmann, A., Goldscheider, N., 2017b. A new approach to evaluate spatiotemporal dynamics of controlling parameters in distributed environmental models. Environmental Modelling and Software 87, 1–16.

Chen, Z., Hartmann, A., Wagener, T., Goldscheider, N., 2018. Dynamics of water fluxes and storages in an alpine karst catchment under current and potential future climate conditions. Hydrol. Earth Syst. Sci. 22, 3807–3823.

Chiogna, G., Marcolini, G., Liu, W., Ciria, T.P., Tuo, Y., 2018. Coupling hydrological modeling and support vector regression to model hydropeaking in alpine catchments. Science of The Total Environment 633, 220–229.

Chu, H.J., Lin, Y.P., Huang, C.W., Hsu, C.Y., Chen, H.Y., 2010. Modelling the hydrologic effects of dynamic land-use change using a distributed hydrologic model and a spatial land-use allocation model. Hydrological Processes 24, 2538–2554.

Cloutier, V., Lefebvre, R., Therrien, R., Savard, M.M., 2008. Multivariate statistical analysis of geochemical data as indicative of the hydrogeochemical evolution of groundwater in a sedimentary rock aquifer system. Journal of Hydrology 353, 294–313.

Constantine, P., Gleich, D., 2014. Computing active subspaces with Monte Carlo. arXiv preprint arXiv:1408.0545 .

Constantine, P.G., 2015. Active Subspaces. volume 2 of *SIAM Spotlights*. Society for Industrial and Applied Mathematics (SIAM), Philadelphia, PA. Emerging Ideas for Dimension Reduction in Parameter Studies.

Constantine, P.G., Diaz, P., 2017. Global sensitivity metrics from active subspaces. Reliability Engineering & System Safety 162, 1–13.

Constantine, P.G., Doostan, A., 2017. Time-dependent global sensitivity analysis with active subspaces for a lithium ion battery model. Statistical Analysis and Data Mining: The ASA Data Science Journal 10, 243–262.

Constantine, P.G., Dow, E., Wang, Q., 2014. Active subspace methods in theory and practice: applications to kriging surfaces. SIAM J. Sci. Comput. 36, A1500–A1524.

Constantine, P.G., Emory, M., Larsson, J., Iaccarino, G., 2015. Exploiting active subspaces to quantify uncertainty in the numerical simulation of the hyshot ii scramjet. Journal of Computational Physics 302, 1–20.

Constantine, P.G., Kent, C., Bui-Thanh, T., 2016. Accelerating Markov chain Monte Carlo with Active Subspaces. SIAM J. Sci. Comput. 38, A2779–A2805.

Cortesi, A., Constantine, P., Magin, T.E., Congedo, P.M., 2017. Forward and backward uncertainty quantification with active subspaces: application to hypersonic flows around a cylinder. Research Report RR-9097. INRIA Bordeaux, équipe Cardamom.

Cui, T., Law, K.J.H., Marzouk, Y.M., 2016. Dimension-independent likelihood-informed MCMC. J. Comput. Phys. 304, 109–137.

Cuntz, M., Mai, J., Samaniego, L., Clark, M., Wulfmeyer, V., Branch, O., Attinger, S., Thober, S., 2016. The impact of standard and hard-coded parameters on the hydrologic fluxes in the noah-mp land surface model. Journal of Geophysical Research: Atmospheres 121, 10,676–10,700.

De Filippis, G., Borsi, I., Foglia, L., Cannata, M., Mansilla, V.V., Vasquez-Suñe, E., Ghetta, M., Rossetto, R., 2017. Software tools for sustainable water resources management: the gis-integrated freewat platform. Rendiconti Online Società Geologica Italiana 42, 59–61.

De Filippis, G., Pouliaris, C., Kahuda, D., Vasile, T.A., Manea, V.A., Zaun, F., Panteleit, B., Dadaser-Celik, F., Positano, P., Nannucci, M.S., et al., 2020. Spatial data management and numerical modelling: Demonstrating the application of the qgis-integrated freewat platform at 13 case studies for tackling groundwater resource management. Water 12, 41.

Delbart, C., Valdes, D., Barbecot, F., Tognelli, A., Couchoux, L., 2016. Spatial organization of the impulse response in a karst aquifer. Journal of hydrology 537, 18–26.

Di Lorenzo, T., Brilli, M., Del Tosto, D., Galassi, D.M., Petitta, M., 2012. Nitrate source and fate at the catchment scale of the vibrata river and aquifer (central italy): an analysis by integrating component approaches and nitrogen isotopes. Environmental earth sciences 67, 2383–2398.

Diaz, P., Constantine, P., Kalmbach, K., Jones, E., Pankavich, S., 2018. A modified SEIR model for the spread of Ebola in Western Africa and metrics for resource allocation. Applied Mathematics and Computation 324, 141–155.

Dile, Y.T., Daggupati, P., George, C., Srinivasan, R., Arnold, J., 2016. Introducing a new open source gis user interface for the swat model. Environmental modelling & software 85, 129–138.

Dossi, C., Ciceri, E., Giussani, B., Pozzi, A., Galgaro, A., Viero, A., Viganò, A., 2007. Water and snow chemistry of main ions and trace elements in the karst system of monte pelmo massif (dolomites, eastern alps, italy). Marine and Freshwater Research 58, 649–656.

Duran, L., Massei, N., Lecoq, N., Fournier, M., Labat, D., 2020. Analyzing multi-scale hydrodynamic processes in karst with a coupled conceptual modeling and signal decomposition approach. Journal of Hydrology 583, 124625.

DVWK, H., 1996. Ermittlung der Verdunstung von Land-und Wasserflächen. DVWK-Merkblätter zur Wasserwirtschaft 238, 1–135.

DWA, 2018. Bodenhydrologische Kartierung und Modellierung. Deutsche Vereinigung für Wasserwirtschaft, Abwasser und Abfall e.V. DWA-M 922 Entwurf.

Dwarakish, G., Ganasri, B., 2015. Impact of land use change on hydrological systems: A review of current modeling approaches. Cogent Geoscience 1, 1115691.

Efron, B., Tibshirani, R.J., 1994. An introduction to the bootstrap. CRC press.

Einsiedl, F., Maloszewski, P., Stichler, W., 2005. Estimation of denitrification potential in a karst aquifer using the 15 n and 18 o isotopes of no 3-. Biogeochemistry 72, 67–86.

Einsiedl, F., Mayer, B., 2006. Hydrodynamic and microbial processes controlling nitrate in a fissured-porous karst aquifer of the franconian alb, southern germany. Environmental science & technology 40, 6697–6702.

Engeland, K., Gottschalk, L., 2002. Bayesian estimation of parameters in a regional hydrological model. Hydrol. Earth Syst. Sci. Discussions 6, 883–898.

Erdal, D., Cirpka, O.A., 2019. Global sensitivity analysis and adaptive stochastic sampling of a subsurface-flow model using active subspaces. Hydrol. Earth Syst. Sci. Discussions 2019, 1–25.

Filippini, M., Squarzoni, G., De Waele, J., Fiorucci, A., Vigna, B., Grillo, B., Riva, A., Rossetti, S., Zini, L., Casagrande, G., et al., 2018. Differentiated spring behavior under changing hydrological conditions in an alpine karst aquifer. Journal of hydrology 556, 572–584.

Fiorillo, F., Guadagno, F.M., 2010. Karst spring discharges analysis in relation to drought periods, using the spi. Water resources management 24, 1867–1884.

Fleury, P., 2005. Sources sous-marines et aquifères karstiques côtiers méditerranéens. Fonctionnement et caractérisation. Ph.D. thesis. University of Neuchatel.

Fleury, P., Ladouche, B., Conroux, Y., Jourde, H., Dörfliger, N., 2009. Modelling the hydrologic functions of a karst aquifer under active water management–the lez spring. Journal of Hydrology 365, 235–243.

Fleury, P., Plagnes, V., Bakalowicz, M., 2007. Modelling of the functioning of karst aquifers with a reservoir model: Application to Fontaine de Vaucluse (South of France). Journal of Hydrology 345, 38–49.

Ford, D., Williams, P.D., 2013. Karst hydrogeology and geomorphology. John Wiley & Sons.

GBA, 2018. Geologische Bundesländerkarten. geologische Bundesanstalt österreich. `https://gisgba.geologie.ac.at/arcgis/services/image/AT_GBA_GK100_200/ImageServer/WMSServer?request=GetCapabilities&`. Accessed: 2018-04-18.

Giese, M., Reimann, T., Bailly-Comte, V., Maréchal, J.C., Sauter, M., Geyer, T., 2018. Turbulent and laminar flow in karst conduits under unsteady flow conditions: Interpretation of pumping tests by discrete conduit-continuum modeling. Water Resources Research 54, 1918–1933.

Glantz, S.A., Slinker, B.K., 1990. Primer of applied regression and analysis of variance. McGraw-Hill.

Goldscheider, N., 2005. Karst groundwater vulnerability mapping: application of a new method in the swabian alb, germany. Hydrogeology Journal 13, 555–564.

Gupta, H.V., Kling, H., Yilmaz, K.K., Martinez, G.F., 2009. Decomposition of the mean squared error and nse performance criteria: Implications for improving hydrological modelling. Journal of Hydrology 377, 80–91.

Gurtz, J., Baltensweiler, A., Lang, H., 1999. Spatially distributed hydrotope-based modelling of evapotranspiration and runoff in mountainous basins. Hydrological Processes 13, 2751–2768.

Guse, B., Kail, J., Radinger, J., Schröder, M., Kiesel, J., Hering, D., Wolter, C., Fohrer, N., 2015. Eco-hydrologic model cascades: Simulating land use and climate change impacts on hydrology, hydraulics and habitats for fish and macroinvertebrates. Science of the Total Environment 533, 542–556.

Haario, H., Laine, M., Mira, A., Saksman, E., 2006. DRAM: Efficient adaptive MCMC. Stat. Comput. 16, 339–354.

Hacker, P., 2003. Hydrologisch-hydrogeologische Untersuchungen im Bereich des Glashütten-berges zur Frage des engeren Schutzgebietes für die Kerschbaumer-Quelle. ARC Seibersdorf research GmbH.

Hamed, K.H., Rao, A.R., 1998. A modified mann-kendall trend test for autocorrelated data. Journal of hydrology 204, 182–196.

Hanasaki, N., Kanae, S., Oki, T., Masuda, K., Motoya, K., Shirakawa, N., Shen, Y., Tanaka, K., 2008. An integrated model for the assessment of global water resources–part 1: Model description and input meteorological forcing. Hydrol. Earth Syst. Sci. 12, 1007–1025.

Hanson, R.T., Boyce, S.E., Schmid, W., Hughes, J.D., Mehl, S.W., Leake, S.A., Maddock III, T., Niswonger, R.G., 2014. One-water hydrologic flow model (MODFLOW-OWHM). Technical Report. US Geological Survey.

Harbaugh, A.W., 2005. MODFLOW-2005, the US Geological Survey modular ground-water model: the ground-water flow process. US Department of the Interior, US Geological Survey Reston, VA.

Hartmann, A., 2018. Experiences in calibrating and evaluating lumped karst hydrological models. Geological Society, London, Special Publications 466, 331–340.

Hartmann, A., Barberá, J.A., Andreo, B., 2017. On the value of water quality observations for karst model parameterization. Hydrol. Earth Syst. Sci. 21, 5971–5985.

Hartmann, A., Goldscheider, N., Wagener, T., Lange, J., Weiler, M., 2014a. Karst water resources in a changing world: Review of hydrological modeling approaches. Reviews of Geophysics 52, 218–242.

Hartmann, A., Kralik, M., Humer, F., Lange, J., Weiler, M., 2012a. Identification of a karst system's intrinsic hydrodynamic parameters: upscaling from single springs to the whole aquifer. Environmental earth sciences 65, 2377–2389.

Hartmann, A., Lange, J., Weiler, M., Arbel, Y., Greenbaum, N., 2012b. A new approach to model the spatial and temporal variability of recharge to karst aquifers. Hydrol. Earth Syst. Sci. 16, 2219–2231.

Hartmann, A., Mudarra, M., Andreo, B., Marin, A., Wagener, T., Lange, J., 2014b. Modeling spatiotemporal impacts of hydroclimatic extremes on groundwater recharge at a Mediterranean karst aquifer. Water Resources Research 50, 6507–6521.

Hartmann, A., Wagener, T., Rimmer, A., Lange, J., Brielmann, H., Weiler, M., 2013a. Testing the realism of model structures to identify karst system processes using water quality and quantity signatures. Water Resources Research 49, 3345–3358.

Hartmann, A., Weiler, M., Wagener, T., Lange, J., Kralik, M., Humer, F., Mizyed, N., Rimmer, A., Barberá, J., Andreo, B., et al., 2013b. Process-based karst modelling to relate hydrodynamic and hydrochemical characteristics to system properties. Hydrol. Earth Syst. Sci. 17, 3305–3321.

Hastings, W.K., 1970. Monte Carlo sampling methods using Markov chains and their applications. Biometrika 57, 97–109.

Henson, W.R., de Rooij, R., Graham, W., 2018. What makes a first-magnitude spring?: Global sensitivity analysis of a speleogenesis model to gain insight into karst network and spring genesis. Water Resources Research 54, 7417–7434.

Hilberg, S., 2016. Natural tracers in fractured hard-rock aquifers in the austrian part of the eastern alps—previous approaches and future perspectives for hydrogeology in mountain regions. Hydrogeology Journal 24, 1091–1105.

Hilberg, S., Schneider, J.F., 2011. The aquifer characteristics of the dolomite formation a new approach for providing drinking water in the northern calcareous alps region in germany and austria. Water resources management 25, 2705–2729.

Hillebrand, O., Nödler, K., Sauter, M., Licha, T., 2015. Multitracer experiment to evaluate the attenuation of selected organic micropollutants in a karst aquifer. Science of the Total Environment 506, 338–343.

Hogue, T.S., Bastidas, L.A., Gupta, H.V., Sorooshian, S., 2006. Evaluating model performance and parameter behavior for varying levels of land surface model complexity. Water resources research 42.

Hollaway, M.J., Beven, K.J., Benskin, C.M.H., Collins, A., Evans, R., Falloon, P., Forber, K.J., Hiscock, K.M., Kahana, R., Macleod, C.J., et al., 2018. The challenges of modelling phosphorus in a headwater catchment: Applying a 'limits of acceptability' uncertainty framework to a water quality model. Journal of Hydrology 558, 607–624.

Holodnak, J.T., Ipsen, I.C., Smith, R.C., 2018. A Probabilistic Subspace Bound with Application to Active Subspaces. arXiv preprint arXiv:1801.00682 .

Hosseini, S.M., Ataie-Ashtiani, B., Simmons, C.T., 2017. Spring hydrograph simulation of karstic aquifers: Impacts of variable recharge area, intermediate storage and memory effects. Journal of Hydrology 552, 225–240.

Hu, C., Hao, Y., Yeh, T.C.J., Pang, B., Wu, Z., 2008. Simulation of spring flows from a karst aquifer with an artificial neural network. Hydrological Processes: An International Journal 22, 596–604.

Jakeman, A., Hornberger, G., 1993. How much complexity is warranted in a rainfall-runoff model? Water Resources Research 29, 2637–2649.

Jeannin, P.Y., Hessenauer, M., Malard, A., Chapuis, V., 2016. Impact of global change on karst groundwater mineralization in the jura mountains. Science of the Total Environment 541, 1208–1221.

Jebreen, H., Wohnlich, S., Banning, A., Wisotzky, F., Niedermayr, A., Ghanem, M., 2018. Recharge, geochemical processes and water quality in karst aquifers: Central west bank, palestine. Environmental earth sciences 77, 261.

Jefferson, J.L., Gilbert, J.M., Constantine, P.G., Maxwell, R.M., 2015. Active subspaces for sensitivity analysis and dimension reduction of an integrated hydrologic model. Computers & geosciences 83, 127–138.

Jehn, F.U., Chamorro, A., Houska, T., Breuer, L., 2019. Trade-offs between parameter constraints and model realism: a case study. Scientific reports 9, 10729.

Jin, X., Zhang, L., Gu, J., Zhao, C., Tian, J., He, C., 2015. Modelling the impacts of spatial heterogeneity in soil hydraulic properties on hydrological process in the upper reach of the heihe river in the qilian mountains, northwest china. Hydrological Processes 29, 3318–3327.

Jonas, T., Marty, C., Magnusson, J., 2009. Estimating the snow water equivalent from snow depth measurements in the swiss alps. Journal of Hydrology 378, 161–167.

Jourde, H., Mazzilli, N., Lecoq, N., Arfib, B., Bertin, D., 2015. Karstmod: A generic modular reservoir model dedicated to spring discharge modeling and hydrodynamic analysis in karst, in: Hydrogeological and Environmental Investigations in Karst Systems. Springer, pp. 339–344.

Jukić, D., Denić-Jukić, V., 2008. Estimating parameters of groundwater recharge model in frequency domain: Karst springs jadro and žrnovnica. Hydrological Processes: An International Journal 22, 4532–4542.

Jukić, D., Denić-Jukić, V., 2009. Groundwater balance estimation in karst by using a conceptual rainfall–runoff model. Journal of Hydrology 373, 302–315.

Kanduč, T., Mori, N., Kocman, D., Stibilj, V., Grassa, F., 2012. Hydrogeochemistry of alpine springs from north slovenia: Insights from stable isotopes. Chemical geology 300, 40–54.

Karlsson, I.B., Sonnenborg, T.O., Refsgaard, J.C., Trolle, D., Børgesen, C.D., Olesen, J.E., Jeppesen, E., Jensen, K.H., 2016. Combined effects of climate models, hydrological model structures and land use scenarios on hydrological impacts of climate change. Journal of Hydrology 535, 301–317.

Kavetski, D., Kuczera, G., Franks, S.W., 2006. Bayesian analysis of input uncertainty in hydrological modeling: 1. theory. Water Resources Research 42.

Kendall, M., 1975. Rank correlation measures. Charles Griffin, London 202, 15.

Kitanidis, P.K., Lee, J., 2014. Principal component geostatistical approach for large-dimensional inverse problems. Water resources research 50, 5428–5443.

Koeck, R., 2017. PROLINE-CE, workpackage t2, activity t2.1. Pilot action 1.2: Waidhofen/YBBS. D.T2.1.4 descriptive documentation of pilot actions and related issues. Lead Institutions Municipality of Waidhofen/Ybbs.

Koeck, R., Hochbichler, E., 2012. Das Wald-Hydrotop-Modell als WSMS-Werkzeug im Quellenschongebiet der Stadt Waidhofen/Ybbs. Report in the course of the CC-WaterS project .

Kohl, B., 2011. Das Niederschlags-/Abflussmodell ZEMOKOST: Entwicklung eines praktikablen Modells zur Ermittlung von Hochwasserabflüssen in Wildbacheinzugsgebieten unter Einbeziehung verbesserter Felddaten. Ph.D. thesis. University of Innsbruck.

Kohl, B., Klebinder, K., Sotier, B., Markart, G., Meissl, G., 2016. Profilansprache, Kartierung, Regensimulation. Erkennen, Abbilden und Validieren der räumlichen Heterogenität von Abflussprozessen, in: Forum für Hydrologie und Wasserbewirtschaftung Hennef, pp. 9–20.

Kordilla, J., Sauter, M., Reimann, T., Geyer, T., 2012. Simulation of saturated and unsaturated flow in karst systems at catchment scale using a double continuum approach. Hydrol. Earth Syst. Sci. 16, 3909–3923.

Krawczyk, W.E., Ford, D.C., 2006. Correlating specific conductivity with total hardness in limestone and dolomite karst waters. Earth surface processes and landforms 31, 221–234.

Kruskal, W.H., Wallis, W.A., 1952. Use of ranks in one-criterion variance analysis. Journal of the American statistical Association 47, 583–621.

Krysanova, V., Hattermann, F., Wechsung, F., 2005. Development of the ecohydrological model swim for regional impact studies and vulnerability assessment. Hydrological Processes: An International Journal 19, 763–783.

Labat, D., Ababou, R., Mangin, A., 1999. Linear and nonlinear input/output models for karstic springflow and flood prediction at different time scales. Stochastic environmental research and risk assessment 13, 337–364.

Labat, D., Ababou, R., Mangin, A., 2000. Rainfall–runoff relations for karstic springs. part i: convolution and spectral analyses. Journal of Hydrology 238, 123–148.

Ladouche, B., Maréchal, J.C., Dorfliger, N., 2014. Semi-distributed lumped model of a karst system under active management. Journal of Hydrology 509, 215–230.

Lam, R., Zahm, O., Marzouk, Y., Willcox, K., 2018. Multifidelity Dimension Reduction via Active Subspaces. arXiv preprint arXiv:1809.05567 .

Le Maître, O.P., Knio, O.M., Najm, H.N., Ghanem, R.G., 2004a. Uncertainty propagation using wiener-haar expansions. J. Comput. Phys. 197, 28–57.

Le Maître, O.P., Najm, H.N., Ghanem, R.G., Knio, O.M., 2004b. Multi-resolution analysis of wiener-type uncertainty propagation schemes. J. Comput. Phys. 197, 502–531.

Leaders, A.W.P., 2012. Climate Change and Impacts on Water Supply. Technical Report. CC-WaterS.

Leitgeb, E., Reiter, R., Englisch, M., Lüscher, P., Schad, P., Feger, K.H., 2013. Waldböden: ein Bildatlas der wichtigsten Bodentypen aus Österreich, Deutschland und der Schweiz. John Wiley & Sons.

Link, W.A., Eaton, M.J., 2012. On thinning of chains in MCMC. Methods in ecology and evolution 3, 112–115.

Luo, K., Tao, F., Moiwo, J.P., Xiao, D., 2016. Attribution of hydrological change in heihe river basin to climate and land use change in the past three decades. Scientific reports 6, 33704.

Mahler, B., Valdes, D., Musgrove, M., Massei, N., 2008. Nutrient dynamics as indicators of karst processes: Comparison of the chalk aquifer (normandy, france) and the edwards aquifer (texas, usa). Journal of contaminant hydrology 98, 36–49.

Mangin, A., 1975. Contribution à l'étude hydrodynamique des aquifères karstiques. Ph.D. thesis. University of Dijon.

Mango, L.M., Melesse, A.M., McClain, M.E., Gann, D., Setegn, S., 2011. Land use and climate change impacts on the hydrology of the upper mara river basin, kenya: results of a modeling study to support better resource management. Hydrology and Earth System Sciences 15, 2245–2258.

Mann, H.B., 1945. Nonparametric tests against trend. Econometrica: Journal of the Econometric Society , 245–259.

Markart, G., 2004. Provisorische Geländeanleitung zur Abschätzung des Oberflächenabflussbeiwertes auf alpinen Boden-/Vegetationseinheiten bei konvektiven Starkregen (Version 1.0). Bundesamt und Forschungszentrum für Wald.

Markart, G., Kohl, B., Perzl, F., 2006. Der bergwald und seine hydrologische wirkung-eine unterschätzte größe? The mountain forest and its hydrological function—an underestimated factor , 34–43.

Markart, G., Perzl, F., Klebinder, K., Kohl, B., Adams, M., Sotier, B., Stary, U., Strasser, M., Suntinger, K., 2012. Evaluation and quantification of possible impacts of climate change on hydrological characteristics of forests in the waidhofen ad ybbs region. Final Report: CC-WaterS-Climate Change and Impacts on Water Supply. Bundesforschungszentrum für Wald, Vienna, Austria .

Martín-Arias, J., Hartmann, A., Mudarra, M., Martínez-Santos, P., Andreo, B., 2020. Simplified varkarst semi-distributed model applied to joint simulations of discharge and piezometric variations in villanueva del rosario karst system (malaga, southern spain), in: Eurokarst 2018, Besançon. Springer, pp. 145–150.

Martinec, J., 1960. The degree-day factor for snowmelt runoff forecasting. IUGG General Assembly of Helsinki, IAHS Commission of Surface Waters 51, 468–477.

Matiatos, I., 2016. Nitrate source identification in groundwater of multiple land-use areas by combining isotopes and multivariate statistical analysis: A case study of asopos basin (central greece). Science of the Total Environment 541, 802–814.

Mattis, S.A., Wohlmuth, B., 2018. Goal-oriented adaptive surrogate construction for stochastic inversion. Computer Methods in Applied Mechanics and Engineering 339, 36–60.

Mayo, A.L., Loucks, M.D., 1995. Solute and isotopic geochemistry and ground water flow in the central wasatch range, utah. Journal of Hydrology 172, 31–59.

Mazzilli, N., Guinot, V., Jourde, H., 2012a. Sensitivity analysis of conceptual model calibration to initialisation bias. Application to karst spring discharge models. Advances in Water Resources 42, 1–16.

Mazzilli, N., Guinot, V., Jourde, H., 2012b. Sensitivity analysis of conceptual model calibration to initialisation bias. application to karst spring discharge models. Advances in water resources 42, 1–16.

Mazzilli, N., Guinot, V., Jourde, H., Lecoq, N., Labat, D., Arfib, B., Baudement, C., Danquigny, C., Dal Soglio, L., Bertin, D., 2017. Karstmod: a modelling platform for rainfall-discharge analysis and modelling dedicated to karst systems. Environmental Modelling and Software .

Mazzilli, N., Guinot, V., Jourde, H., Lecoq, N., Labat, D., Arfib, B., Baudement, C., Danquigny, C., Dal Soglio, L., Bertin, D., 2019. Karstmod: a modelling platform for rainfall-discharge analysis and modelling dedicated to karst systems. Environmental Modelling & Software 122, 103927.

Mazzilli, N., Jourde, H., Jacob, T., Guinot, V., Le Moigne, N., Boucher, M., Chalikakis, K., Guyard, H., Legtchenko, A., 2013. On the inclusion of ground-based gravity measurements to the calibration process of a global rainfall-discharge reservoir model: case of the Durzon karst system (Larzac, southern France). Environmental Earth Sciences 68, 1631–1646.

McNamara, J.P., Tetzlaff, D., Bishop, K., Soulsby, C., Seyfried, M., Peters, N.E., Aulenbach, B.T., Hooper, R., 2011. Storage as a metric of catchment comparison. Hydrological Processes 25, 3364–3371.

Mehdi, B., Lehner, B., Ludwig, R., 2018. Modelling crop land use change derived from influencing factors selected and ranked by farmers in north temperate agricultural regions. Science of The Total Environment 631, 407–420.

Mekonnen, D.F., Duan, Z., Rientjes, T., Disse, M., 2018. Analysis of combined and isolated effects of land-use and land-cover changes and climate change on the upper blue nile river basin's streamflow. Hydrology and earth system sciences 22, 6187–6207.

Menció, A., Mas-Pla, J., Otero, N., Regàs, O., Boy-Roura, M., Puig, R., Bach, J., Domènech, C., Zamorano, M., Brusi, D., et al., 2016. Nitrate pollution of groundwater; all right..., but nothing else? Science of the total environment 539, 241–251.

Miorandi, R., Borsato, A., Frisia, S., Fairchild, I.J., Richter, D.K., 2010. Epikarst hydrology and implications for stalagmite capture of climate changes at grotta di ernesto (ne italy): results from long-term monitoring. Hydrological Processes 24, 3101–3114.

Mockler, E.M., O'Loughlin, F.E., Bruen, M., 2016. Understanding hydrological flow paths in conceptual catchment models using uncertainty and sensitivity analysis. Computers & Geosciences 90, 66–77.

Moussu, F., Oudin, L., Plagnes, V., Mangin, A., Bendjoudi, H., 2011. A multi-objective calibration framework for rainfall–discharge models applied to karst systems. Journal of Hydrology 400, 364–376.

Mudarra, M., Andreo, B., 2011. Relative importance of the saturated and the unsaturated zones in the hydrogeological functioning of karst aquifers: The case of alta cadena (southern spain). Journal of hydrology 397, 263–280.

Mudarra, M., Andreo, B., Mudry, J., 2012. Monitoring groundwater in the discharge area of a complex karst aquifer to assess the role of the saturated and unsaturated zones. Environmental earth sciences 65, 2321–2336.

Mudarra, M., Hartmann, A., Andreo, B., 2019. Combining experimental methods and modeling to quantify the complex recharge behavior of karst aquifers. Water Resources Research 55, 1384–1404.

Musgrove, M., Opsahl, S.P., Mahler, B.J., Herrington, C., Sample, T., Banta, J., 2016. Source, variability, and transformation of nitrate in a regional karst aquifer: Edwards aquifer, central texas. Science of the Total Environment 568, 457–469.

Nandakumar, N., Mein, R.G., 1997. Uncertainty in rainfall—runoff model simulations and the implications for predicting the hydrologic effects of land-use change. Journal of Hydrology 192, 211–232.

Narany, T.S., Aris, A.Z., Sefie, A., Keesstra, S., 2017. Detecting and predicting the impact of land use changes on groundwater quality, a case study in northern kelantan, malaysia. Science of the Total Environment 599, 844–853.

Narany, T.S., Bittner, D., Disse, M., Chiogna, G., 2019. Spatial and temporal variability in hydrochemistry of a small-scale dolomite karst environment. Environmental Earth Sciences 78, 273.

Nash, J.E., Sutcliffe, J.V., 1970. River flow forecasting through conceptual models part i—a discussion of principles. Journal of Hydrology 10, 282–290.

Neitsch, S.L., Arnold, J.G., Kiniry, J.R., Williams, J.R., 2011. Soil and water assessment tool theoretical documentation version 2009. Technical Report. Texas Water Resources Institute.

Nobile, F., Tempone, R., Webster, C.G., 2008. A sparse grid stochastic collocation method for partial differential equations with random input data. SIAM J. Num. Anal. 46, 2309–2345.

Nosrati, K., Van Den Eeckhaut, M., 2012. Assessment of groundwater quality using multivariate statistical techniques in hashtgerd plain, iran. Environmental Earth Sciences 65, 331–344.

Olarinoye, T., Gleeson, T., Marx, V., Seeger, S., Adinehvand, R., Allocca, V., Andreo, B., Apaéstegui, J., Apolit, C., Arfib, B., Bittner, D., et al., 2020. Global karst springs hydrograph dataset for research and management of the world's fastest-flowing groundwater. Scientific Data 7, 1–9.

Olivera, F., Valenzuela, M., Srinivasan, R., Choi, J., Cho, H., Koka, S., Agrawal, A., 2006. Arcgis-swat: A geodata model and gis interface for swat 1. JAWRA Journal of the American Water Resources Association 42, 295–309.

Ollivier, C., Mazzilli, N., Olioso, A., Chalikakis, K., Carrière, S.D., Danquigny, C., Emblanch, C., 2019. Karst recharge-discharge semi distributed model to assess spatial variability of flows. Science of The Total Environment , accepted article.

Park, S., Nielsen, A., Bailey, R.T., Trolle, D., Bieger, K., 2019. A qgis-based graphical user interface for application and evaluation of swat-modflow models. Environmental modelling & software 111, 493–497.

Perrin, J., Jeannin, P.Y., Cornaton, F., 2007. The role of tributary mixing in chemical variations at a karst spring, milandre, switzerland. Journal of Hydrology 332, 158–173.

Perrin, J., Jeannin, P.Y., Zwahlen, F., 2003. Epikarst storage in a karst aquifer: a conceptual model based on isotopic data, milandre test site, switzerland. Journal of hydrology 279, 106–124.

Pettitt, A., 1979. A non-parametric approach to the change-point problem. Journal of the Royal Statistical Society: Series C (Applied Statistics) 28, 126–135.

Pfleiderer, S., Klein, P., Reitner, H., Heinrich, M., 2006. The hydrogeology of the northern calcareous alps be-tween the rivers enns and ybbs_. Austrian Journal of .

Pianosi, F., Sarrazin, F., Wagener, T., 2015. A matlab toolbox for global sensitivity analysis. Environmental Modelling & Software 70, 80–85.

Pinkus, A., 2015. Ridge functions. volume 205. Cambridge University Press.

Plessix, R.E., 2006. A review of the adjoint-state method for computing the gradient of a functional with geophysical applications. Geophysical Journal International 167, 495–503.

Promper, C., Puissant, A., Malet, J.P., Glade, T., 2014. Analysis of land cover changes in the past and the future as contribution to landslide risk scenarios. Applied Geography 53, 11–19.

Reimann, T., Hill, M.E., 2009. Modflow-cfp: A new conduit flow process for modflow–2005. Groundwater 47, 321–325.

Reimann, T., Rehrl, C., Shoemaker, W.B., Geyer, T., Birk, S., 2011. The significance of turbulent flow representation in single-continuum models. Water Resources Research 47.

Rosero, E., Yang, Z.L., Wagener, T., Gulden, L.E., Yatheendradas, S., Niu, G.Y., 2010. Quantifying parameter sensitivity, interaction, and transferability in hydrologically enhanced versions of the noah land surface model over transition zones during the warm season. Journal of Geophysical Research: Atmospheres 115.

Rossetto, R., De Filippis, G., Borsi, I., Foglia, L., Cannata, M., Criollo, R., Vázquez-Suñé, E., 2018. Integrating free and open source tools and distributed modelling codes in gis environment for data-based groundwater management. Environmental Modelling and Software 107, 210–230.

Rossetto, R., De Filippis, G., Triana, F., Ghetta, M., Borsi, I., Schmid, W., 2019. Software tools for management of conjunctive use of surface-and ground-water in the rural environment: integration of the farm process and the crop growth module in the freewat platform. Agricultural Water Management 223, 105717.

Russi, T.M., 2010. Uncertainty Quantification with Experimental Data and Complex System Models. Ph.D. thesis. University of California, Berkeley.

Saltelli, A., Ratto, M., Andres, T., Campolongo, F., Cariboni, J., Gatelli, D., Saisana, M., Tarantola, S., 2008. Global sensitivity analysis: the primer. John Wiley & Sons.

Sarrazin, F., Hartmann, A., Pianosi, F., Rosolem, R., Wagener, T., 2018. V2Karst V1. 1: a parsimonious large-scale integrated vegetation–recharge model to simulate the impact of climate and land cover change in karst regions. Geoscientific Model Development 11, 4933–4964.

Sauter, M., Geyer, T., Kovács, A., Teutsch, G., 2006. Modellierung der Hydraulik von Karstgrundwasserleitern–eine Übersicht. Grundwasser 11, 143–156.

Scanlon, B.R., Healy, R.W., Cook, P.G., 2002. Choosing appropriate techniques for quantifying groundwater recharge. Hydrogeology journal 10, 18–39.

Schaefli, B., Zehe, E., 2009. Hydrological model performance and parameter estimation in the wavelet-domain. Hydrol. Earth Syst. Sci. 13, 1921–1936.

Schmidt, S., Geyer, T., Marei, A., Guttman, J., Sauter, M., 2013. Quantification of long-term wastewater impacts on karst groundwater resources in a semi-arid environment by chloride mass balance methods. Journal of hydrology 502, 177–190.

Sen, P.K., 1968. Estimates of the regression coefficient based on kendall's tau. Journal of the American statistical association 63, 1379–1389.

Siebert, S., Burke, J., Faures, J.M., Frenken, K., Hoogeveen, J., Döll, P., Portmann, F.T., 2010. Groundwater use for irrigation–a global inventory. Hydrology and earth system sciences 14, 1863–1880.

Siriwardena, L., Finlayson, B., McMahon, T., 2006. The impact of land use change on catchment hydrology in large catchments: The comet river, central queensland, australia. Journal of Hydrology 326, 199–214.

Sivelle, V., Labat, D., Mazzilli, N., Massei, N., Jourde, H., 2019. Dynamics of the flow exchanges between matrix and conduits in karstified watersheds at multiple temporal scales. Water 11, 569.

Smith, M., Cross, K., Paden, M., Laban, P., 2016. Spring–managing groundwater sustainably. IUCN, Gland, Switzerland .

Sobol, I.M., 2001. Global sensitivity indices for nonlinear mathematical models and their monte carlo estimates. Mathematics and computers in simulation 55, 271–280.

Spoelstra, J., Schiff, S., Hazlett, P., Jeffries, D., Semkin, R., 2007. The isotopic composition of nitrate produced from nitrification in a hardwood forest floor. Geochimica et Cosmochimica Acta 71, 3757–3771.

Srinivasan, R., Arnold, J.G., 1994. Integration of a basin-scale water quality model with gis 1. JAWRA Journal of the American Water Resources Association 30, 453–462.

Stevanović, Z., 2019. Karst waters in potable water supply: a global scale overview. Environmental Earth Sciences 78, 662.

Stuart, A.M., 2010. Inverse problems: A Bayesian perspective. Acta Numerica 19, 451–559.

Szramek, K., McIntosh, J.C., Williams, E.L., Kanduc, T., Ogrinc, N., Walter, L.M., 2007. Relative weathering intensity of calcite versus dolomite in carbonate-bearing temperate zone watersheds: Carbonate geochemistry and fluxes from catchments within the st. lawrence and danube river basins. Geochemistry, Geophysics, Geosystems 8.

Teixeira Parente, M., Bittner, D., Mattis, S., Chiogna, G., Wohlmuth, B., 2019a. Bayesian calibration and sensitivity analysis for a karst aquifer model using active subspaces. Water Resources Research 55, 7086–7107.

Teixeira Parente, M., Mattis, S., Gupta, S., Deusner, C., Wohlmuth, B., 2019b. Efficient parameter estimation for a methane hydrate model with active subspaces. Computational Geosciences 23, 355–372.

Thiemann, M., Trosset, M., Gupta, H., Sorooshian, S., 2001. Bayesian recursive parameter estimation for hydrologic models. Water Resources Research 37, 2521–2535.

Thornthwaite, C.W., 1948. An approach toward a rational classification of climate. volume 38.

Tripathy, R., Bilionis, I., Gonzalez, M., 2016. Gaussian processes with built-in dimensionality reduction: Applications to high-dimensional uncertainty propagation. Journal of Computational Physics 321, 191–223.

Tritz, S., Guinot, V., Jourde, H., 2011. Modelling the behaviour of a karst system catchment using non-linear hysteretic conceptual model. Journal of Hydrology 397, 250–262.

Tropp, J.A., 2012. User-friendly tail bounds for sums of random matrices. Foundations of computational mathematics 12, 389–434.

Tuo, Y., Marcolini, G., Disse, M., Chiogna, G., 2018. A multi-objective approach to improve swat model calibration in alpine catchments. Journal of hydrology 559, 347–360.

UN, 2018. Resolution 64/292: The human right to water and sanitation. united nations. `https://www.un.org/en/ga/search/view_doc.asp?symbol=A/RES/64/292`. Accessed: 2019-11-28.

Vanuytrecht, E., Raes, D., Willems, P., 2014. Global sensitivity analysis of yield output from the water productivity model. Environmental Modelling and Software 51, 323–332.

Vrugt, J.A., 2016. Markov chain monte carlo simulation using the dream software package: Theory, concepts, and matlab implementation. Environmental Modelling and Software 75, 273–316.

Vrugt, J.A., Ter Braak, C., Diks, C., Robinson, B.A., Hyman, J.M., Higdon, D., 2009. Accelerating Markov chain Monte Carlo simulation by differential evolution with self-adaptive randomized subspace sampling. International Journal of Nonlinear Sciences and Numerical Simulation 10, 273–290.

Vrugt, J.A., Ter Braak, C.J., Clark, M.P., Hyman, J.M., Robinson, B.A., 2008. Treatment of input uncertainty in hydrologic modeling: Doing hydrology backward with markov chain monte carlo simulation. Water Resources Research 44.

Wan, X., Karniadakis, G.E., 2006. Beyond wiener—askey expansions: Handling arbitrary pdfs. J. Sci. Comput. 27, 455–464.

Wang, S.J., Li, R.L., Sun, C.X., Zhang, D.F., Li, F.Q., Zhou, D.Q., Xiong, K.N., Zhou, Z.F., 2004. How types of carbonate rock assemblages constrain the distribution of karst rocky desertified land in guizhou province, pr china: phenomena and mechanisms. Land Degradation & Development 15, 123–131.

Ward Jr, J.H., 1963. Hierarchical grouping to optimize an objective function. Journal of the American statistical association 58, 236–244.

Wassenaar, L.I., 1995. Evaluation of the origin and fate of nitrate in the abbotsford aquifer using the isotopes of15n and18o in no3-. Applied geochemistry 10, 391–405.

WHO, 2017. Progress on drinking water, sanitation and hygiene: 2017 update and SDG baselines. World Health Organization.

Williams, P.W., 1983. The role of the subcutaneous zone in karst hydrology. Journal of hydrology 61, 45–67.

Winston, R.B., 2009. ModelMuse: a graphical user interface for MODFLOW-2005 and PHAST. US Geological Survey Reston, VA.

Xiu, D., Karniadakis, G.E., 2002. The wiener–askey polynomial chaos for stochastic differential equations. SIAM J. Sci. Comput. 24, 619–644.

Xu, Z., Massei, N., Padilla, I., Hartmann, A., Hu, B., 2018. Characterization, modeling, and remediation of karst in a changing environment. Environmental earth sciences 77, 476.

Yue, S., Wang, C., 2004. The mann-kendall test modified by effective sample size to detect trend in serially correlated hydrological series. Water resources management 18, 201–218.

Zipper, S.C., Keune, J., Kollet, S.J., 2019. Land use change impacts on european heat and drought: remote land-atmosphere feedbacks mitigated locally by shallow groundwater. Environmental Research Letters 14, 044012.

Appendix A

Article appendices

A.1   Appendix to Chapter 5

In LuKARS, the following balance equation is solved for each individual hydrotope:

$$\frac{de_i}{dt} = \begin{cases} S_i - \frac{Q_{\text{sec},i} + Q_{\text{is},i} + Q_{\text{hyd},i}}{a_i} & \text{if } e_i > 0 \\ 0 & \text{if } e_i = 0 \end{cases} \tag{A.1}$$

e_i is the water level [L] in hydrotope i, t [T] indicates the time and S_i is a hydrotope-specific sink and source term in form of a mass balance of precipitation, snow melt, evapotranspiration and interception. We used the temperature index approach from Martinec (1960) to calculate snow melt. Interception was estimated based on indications for beech forests in DVWK (1996). Then, evapotranspiration was calculated based on the method of Thornthwaite (1948). Q_{sec} [$L^3 T^{-1}$] summarizes all flow terms that do not contribute to the discharge at an investigated karst spring, i. e., secondary spring discharge and overland flow. $Q_{\text{is},i}$ [$L^3 T^{-1}$] represents the discharge from hydrotope i to a linear baseflow storage, considered as groundwater recharge. $Q_{\text{hyd},i}$ [$L^3 T^{-1}$] is a hydrotope-specific quickflow component through preferential flow paths (e. g., subsurface conduits) with a direct connection to the spring outlet. a_i [L^2] is the space covered by a respective hydrotope.

The following balance equation is solved for the baseflow storage:

$$\frac{de_{\text{b}}}{dt} = \begin{cases} \frac{\Sigma(Q_{\text{is},i}) - Q_{\text{b}}}{A} & \text{if } e_{\text{b}} > 0 \\ 0 & \text{if } e_{\text{b}} = 0, \end{cases} \tag{A.2}$$

e_{b} is the water level [L] in the baseflow storage and $\Sigma(Q_{\text{is},i})$ [$L^3 T^{-1}$] integrates the flows from all hydrotopes to the baseflow storage. Q_{b} [$L^3 T^{-1}$] indicates water flow from the storage B to the spring and simulates the matrix contribution from the saturated zone to the spring discharge. The variable A [L^2] is the space of the entire recharge area. The discretized forms of A.1 and A.2, as shown in A.3 and A.4, are solved for each time step n:

$$e_{i,n+1} = \max \left[0, e_{i,n} + \left(S_{i,n} - \frac{Q_{\text{sec},i,n} + Q_{\text{is},i,n} + Q_{\text{hyd},i,n}}{a_i} \right) * \Delta t \right] \tag{A.3}$$

$$e_{\text{b},n+1} = \max \left[0, e_{\text{b},n} + \left(\frac{\Sigma(Q_{\text{is},i,n}) - Q_{\text{b},n}}{A} \right) * \Delta t \right] \tag{A.4}$$

The discharge terms are computed as:

$$Q_{\text{hyd},i,n} = \varepsilon \left[\frac{\max(0, e_{i,n} - e_{\text{min},i})}{e_{\text{max},i} - e_{\text{min},i}} \right]^{\alpha_i} * \frac{k_{\text{hyd},i}}{l_{\text{hyd},i}} * a_i \tag{A.5}$$

$$Q_{\text{is},i,n} = k_{\text{is},i} * e_{i,n} * a_i \tag{A.6}$$

$$Q_{\text{sec},i,n} = k_{\text{sec},i} * \max(0, e_{i,n} - e_{\text{sec},i}) * a_i \tag{A.7}$$

$$Q_{\text{b},n} = k_{\text{b}} * e_{\text{b},n} * A \tag{A.8}$$

$e_{\text{max},i}$ [L] and $e_{\text{min},i}$ [L] are the upper and lower storage thresholds of hydrotope i. The exponent α_i controls the magnitude of the quickflow component from each hydrotope. $e_{\text{sec},i}$ [L] represents a hydrotope-specific activation level for Q_{sec}. $k_{\text{is},i}$ [LT^{-1}] and $k_{\text{sec},i}$ [LT^{-1}] are the specific discharge parameters for $Q_{\text{is},i}$ [L^{3}T^{-1}] and $Q_{\text{sec},i}$ [L^{3}T^{-1}]. $k_{\text{hyd},i}$ [L^{2}T^{-1}] indicates the specific discharge parameter for the quickflow and $l_{\text{hyd},i}$ [L] is the mean distance of hydrotope i to the adjacent spring, allowing to account for the relative location and distribution of hydrotope i in a specific recharge area. The ratio between $k_{\text{hyd},i}$ and $l_{\text{hyd},i}$ is the hydrotope discharge coefficient. Then, the dimensionless connectivity/activation indicator ε is defined as:

$$\varepsilon_{n+1} = 0 \quad \text{if} \begin{cases} \varepsilon_n = 0 \ \& \ e_{i,n+1} < e_{\text{max},i} \ \text{or} \\ \varepsilon_n = 1 \ \& \ e_{i,n+1} \le e_{\text{min},i} \end{cases} \tag{A.9}$$

$$\varepsilon_{n+1} = 1 \quad \text{if} \begin{cases} \varepsilon_n = 0 \ \& \ e_{i,n+1} \ge e_{\text{max},i} \ \text{or} \\ \varepsilon_n = 1 \ \& \ e_{i,n+1} > e_{\text{min},i}. \end{cases} \tag{A.10}$$

A.2   Appendix to Chapter 6

In a LuKARS model, areas with homogeneous infiltration conditions are implemented as distinct hydrological response units, called hydrotopes (Fig. 6.2a). Land use change impact studies can be performed by changing the hydrotope infiltration area. A hydrotope is analogous to a bucket that has three discharge components: the quickflow component (Q_{hyd} [L^3T^{-1}]), a secondary spring discharge (Q_{sec} [L^3T^{-1}]) and the recharge (Q_{is} [L^3T^{-1}]). Q_{hyd} is considered a hydrotope-specific quickflow occurring in preferential flow paths (e.g. subsurface conduits). The quickflow bypasses the baseflow storage B and is directly transferred to the spring outlet. The quickflow starts once a hydrotope-specific storage threshold (E_{max}) has been reached and stops after the hydrotope storage falls below a lower storage threshold (E_{min}). Q_{sec} integrates all flow components that do not arrive at the simulated karst spring and that are transferred outside the regarded recharge area, i.e. secondary spring discharge and overland flow (Tritz et al., 2011). Q_{is} is the discharge from one hydrotope to the underlying baseflow storage, B, that represents the process of groundwater recharge. Each hydrotope has 7 physical parameters, with length units L and time units T, that are as follows:

- k_{hyd} [L^2T^{-1}] is the discharge parameter for Q_{hyd},

- E_{min} [L] is the minimum storage capacity of a hydrotope,

- E_{max} [L] is the maximum storage capacity of a hydrotope,

- α [-] is the hydrotope-specific quickflow exponent,

- k_{is} [LT^{-1}] is the discharge parameter for Q_{is},

- k_{sec} [LT^{-1}] is the discharge parameter for Q_{sec},

- E_{sec} [L] is the activation level for Q_{sec}.

Following the conceptual sketch of LuKARS shown in Fig. 6.2a, the model solves the following discrete balance equations for each hydrotope i and for each time step n:

$$E_{i,n+1} = \max[0, E_{i,n} + (S_{i,n} - \frac{Q_{\text{hyd},i,n} + Q_{\text{sec},i,n} + Q_{\text{is},i,n}}{a_i}) \Delta t] \tag{A.11}$$

where E_i indicates the water level [L] in hydrotope i. S_i is the hydrotope-specific sink and source term as a mass balance of precipitation, snow melt, evapotranspiration and interception. Interception is calculated using estimates provided by DVWK (1996). A simple temperature index model (Martinec, 1960) is used to model snow melt and snow retention in the model. Then, evapotranspiration is considered using the method proposed by Thornthwaite (1948). $Q_{\text{hyd},i}$ [L^3T^{-1}] represents the quickflow component (e.g. conduit flow), $Q_{\text{sec},i}$ [L^3T^{-1}] is a secondary spring discharge and $Q_{\text{is},i}$ [L^3T^{-1}] is the groundwater recharge. The absolute area covered by a respective hydrotope is given by a_i [L^2].

$$E_{b,n+1} = \max[0, E_{b,n} + (\frac{\Sigma(Q_{is,i,n}) - Q_{b,n}}{A})\Delta t] \qquad (A.12)$$

is the balance equation for the baseflow storage B, where E_b indicates the water level [L] in the baseflow storage and $\Sigma(Q_{is,i})$ [L^3T^{-1}] are the cumulative flows from all hydrotopes to the baseflow storage. Q_b [L^3T^{-1}] represents water that is transferred from the storage B to the spring and simulates a baseflow contribution from the phreatic aquifer system to the spring discharge. The variable A [L^2] stands for the entire recharge area. The discharge terms are computed as follows:

$$Q_{hyd,i,n} = a_i \frac{k_{hyd,i}}{l_{hyd,i}} \varepsilon_n [\frac{\max(0, E_{i,n} - E_{min,i})}{E_{max,i} - E_{min,i}}]^{\alpha_i} \qquad (A.13)$$

$$Q_{sec,i,n} = a_i k_{sec,i} \max(0, E_{i,n} - E_{sec,i}) \qquad (A.14)$$

$$Q_{is,i,n} = a_i k_{is,i} E_{i,n} \qquad (A.15)$$

$$Q_{b,n} = A k_b E_{b,n} \qquad (A.16)$$

$E_{max,i}$ [L] and $E_{min,i}$ [L] represent the upper and lower storage thresholds of the hydrotope i. $E_{sec,i}$ [L] is the hydrotope-specific activation level for a secondary spring discharge. $k_{sec,i}$ [LT^{-1}], $k_{is,i}$ [LT^{-1}] and k_b [LT^{-1}] are the specific discharge parameters for $Q_{sec,i}$ [L^3T^{-1}], $Q_{is,i}$ [L^3T^{-1}] and Q_b [L^3T^{-1}], respectively. $k_{hyd,i}$ [L^2T^{-1}] represents the specific discharge parameter for the quickflow of a hydrotope and $l_{hyd,i}$ [L] is the mean distance of hydrotope i to the adjacent spring, thus accounting for the relative location of the same hydrotope types in a specific recharge area. The ratio between $k_{hyd,i}$ and $l_{hyd,i}$ represents the hydrotope discharge coefficient and α_i is a hydrotope-specific exponent of the quickflow. The dimensionless connectivity/activation indicator ε is defined as follows:

$$\varepsilon_{n+1} = 0 \text{ if } \begin{cases} \varepsilon_n = 0 \ \& \ E_{i,n+1} < E_{max,i} \text{ or} \\ \varepsilon_n = 1 \ \& \ E_{i,n+1} \leq E_{min,i} \end{cases} \qquad (A.17)$$

$$\varepsilon_{n+1} = 1 \text{ if } \begin{cases} \varepsilon_n = 0 \ \& \ E_{i,n+1} \geq E_{max,i} \text{ or} \\ \varepsilon_n = 1 \ \& \ E_{i,n+1} > E_{min,i} \end{cases} \qquad (A.18)$$

Appendix B

Article supplementary materials

B.1 Supplementary material to Chapter 3

### B.1.1 Climate of the study area
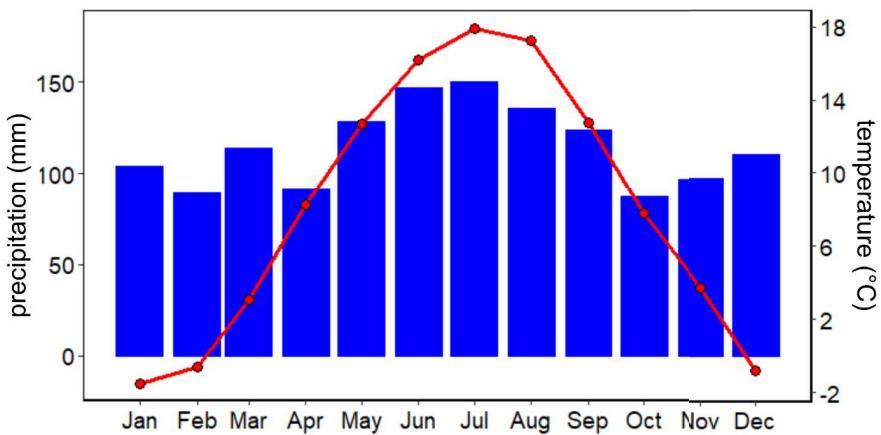
Figure B.1: Annual distribution of temperature and precipitation in the study area Waidhofen a.d. Ybbs. The monthly precipitation sums (blue bars) are averaged from 1981 – 2014 at the weather station Hinterlug (BMNT, 2018). Temperature was measured at the Mitterlug spring in the period from 2001 - 2016 and aggregated to monthly means (red line).

B.1.2   Model notation

Table B.1: Relevant model parameters of LuKARS. The x notations indicate that the respective parameter is hydrotope-specific.

Symbol	Description
$E_{min,x}$ [L]	hydrotope-specific minimum storage capacity
$E_{max,x}$ [L]	hydrotope-specific maximum storage capacity
$E_{sec,x}$ [L]	activation level for flow processes leading to water losses
$Q_{hyd,x}$ [L^{3}T^{-1}]	hydrotope quickflow component
$Q_{is,x}$ [L^{3}T^{-1}]	groundwater recharge from hydrotope x
$Q_{sec,x}$ [L^{3}T^{-1}]	flow component transferred outside the recharge area
Q_b [L^{3}T^{-1}]	baseflow
Q_{tot} [L^{3}T^{-1}]	total spring discharge
$k_{hyd,x}$ [L^{2}T^{-1}]	hydrotope-specific discharge parameter for Q_{hyd} [L^{3}T^{-1}]
$l_{hyd,x}$ [L]	mean distance of hydrotope x to the spring
$k_{is,x}$ [LT^{-1}]	hydrotope-specific discharge coefficient for Q_{is} [L^{3}T^{-1}]
$k_{sec,x}$ [LT^{-1}]	hydrotope-specific discharge coefficient for Q_{sec} [L^{3}T^{-1}]
α [-]	quickflow exponent of hydrotope x
ε [-]	connectivity/activation indicator for the quickflow
k_b [LT^{-1}]	discharge parameter for Q_b [L^{3}T^{-1}]
a_x [L]	area covered by haydrotope x
A [L]	recharge area
S_x [LT^{-1}]	sink and source term
E_x [L]	water level in hydrotope x
E_b [L]	water level in baseflow storage
M_d [LT^{-1}]	daily amount of snow melt
M_{pot} [LT^{-1}]	potential snow melt rate
I_d [LT^{-1}]	daily interception loss
Et_d [LT^{-1}]	daily evapotranspiration loss
T [°C]	mean monthly temperature
T_f [°C]	temperature threshold for snow melt
H [-]	heat index in Thornthwaite (1948) approach
r [-]	exponent in Thornthwaite (1948) approach
F [LT^{-1}°C^{-1}]	degree-day factor
S_{snow} [L]	accumulated snow water equivalent

B.1.3 DWA hydropedological fieldguide

The hydropedological fieldguide (DWA, 2018), developed by a DWA (German Association for Water, Wastewater and Waste) working group, represents a mapping tool for hydropedological processes. Generally, the tool comprises two parts: i) a general guideline for hydropedological mapping and ii) a MS-Excel evaluation scheme. To simplify the applicability as well as to increase the general acceptance of the tool, the mapping scheme (i.e. mapping sheet, included parameters and parameter classifications) is closely related to the German soil classification scheme (Ad-hoc-Arbeitsgruppe Boden, 2005). The tool works as follows: First, the user chooses a point in his/her area of interest that, from a hydrological point of view, is representative of the area he/she wants to investigate. Next, the user maps different soil parameters (such as soil type, bulk density, content of organic matter, hydromorphic properties and preferential flowpaths) for each soil layer at the given soil profile. Given the mapped parameters and assuming a defined rainfall event, the MS-Excel tool derives the dominant hydrological processes as well as the range of water storage volume for wet and dry conditions based on pedotransfer functions (Ad-hoc-Arbeitsgruppe Boden, 2005).

B.1.4 Model input data

Table B.2: Information about the temporal resolution, time intervals and measuring stations of the input data used for the model simulations.

Data	Measuring station	Temporal resolution	Time interval
Precipitation	Mitterlug spring	Daily	01/2006 - 12/2006 (calibration period)
			01/2007 - 12/2007 (validation period)
Snow depth	Hinterlug station (BMNT, 2018)	Daily	01/2006 - 12/2006 (calibration period)
			01/2007 - 12/2007 (validation period)
Temperature	Hinterlug station (BMNT, 2018)	Daily	01/2006 - 12/2006 (calibration period)
			01/2007 - 12/2007 (validation period)
$Q_{Kerschbaum}$	Kerschbaum spring tapping	Daily	01/2006 - 12/2006 (calibration period)
			01/2007 - 12/2007 (validation period)*
$Q_{Hinterlug}$	Hinterlug spring tapping	Daily	01/2006 - 12/2006 (calibration period)
			01/2007 - 12/2007 (validation period)
$Q_{Mitterlug}$	Overflow basin in water supplying system	Daily	01/2006 - 12/2007 (validation period)**

* Data gaps are present in the Kerschbaum spring discharge time series between 2010 and 2013

** We calculated monthly mean values from the daily discharge values due to high uncertainties in the daily time series resulting from improper monitoring (discharge not measured directly in spring tapping)

## B.1.5   Specific discharge contributions of the hydrotopes
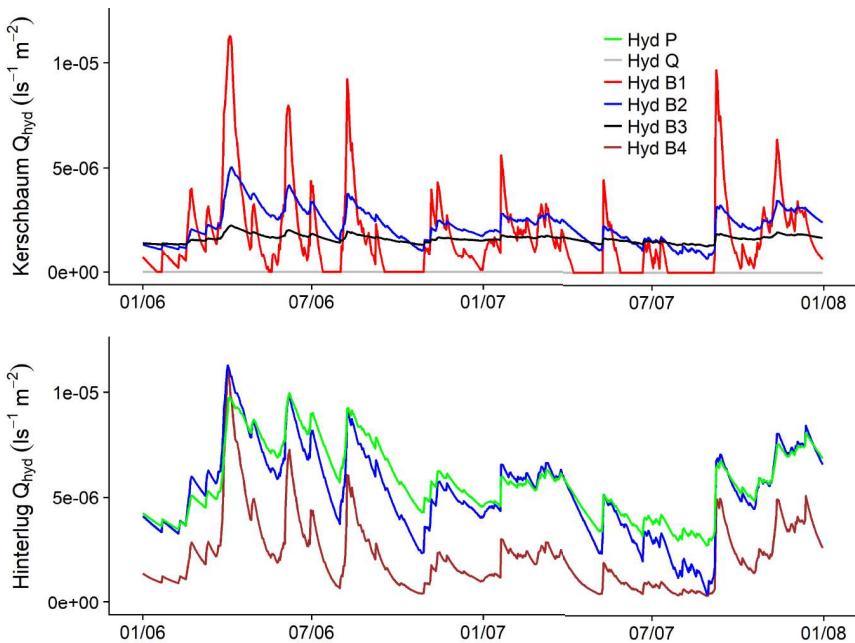
Figure B.2: Specific discharge contributions, here quickflow, of the hydrotopes in the Kerschbaum and Hinterlug recharge areas.
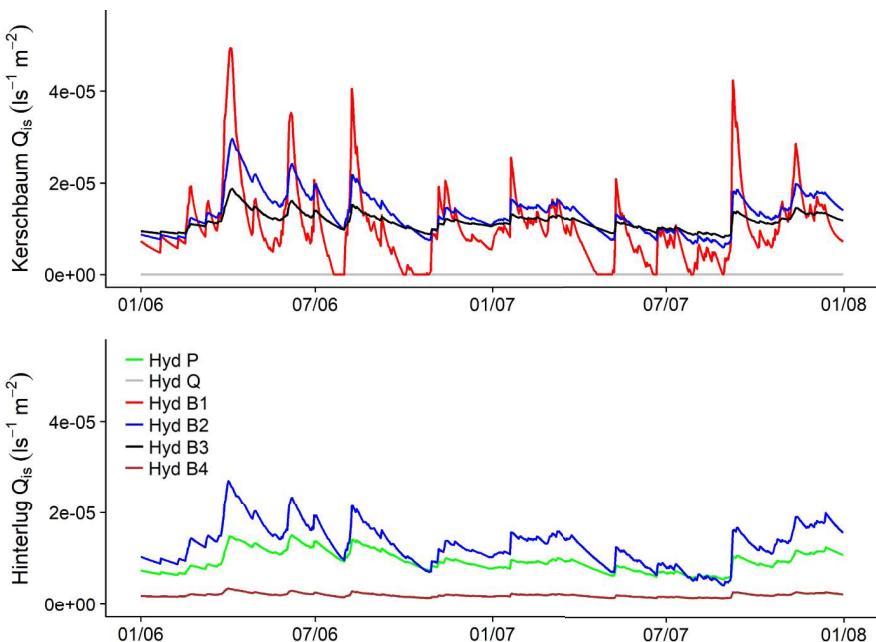
Figure B.3: Specific discharge contributions, here recharge, of the hydrotopes in the Kerschbaum and Hinterlug recharge areas.

B.2   Supplementary material to Chapter 5

The supporting information comprises three figures that are said to support the scientific content provided in the main text. Fig. B.4 gives an overview about the natural characteristics of the study area in Waidhofen a.d. Ybbs. The orthophoto in Fig. B.4a), taken in 2006, was kindly provided by the water works owner in Waidhofen. The shown recharge area of the Kerschbaum spring was mapped by Hacker (2003). Fig. B.5 is taken from Bittner et al. (2018a) to provide visual help for the LuKARS model and the interconnection of different hydrotopes. Fig. B.6 provides a visual overview of the input data processed to run the Kerschbaum LuKARS model. The daily temperature was used in the temperature index snow model (Martinec, 1960) as well as to calculate evapotranspiration (Thornthwaite, 1948). The precipitation time series was processed as an input for LuKARS and the discharge time series was used to calibrate the LuKARS model. All input data was kindly provided by the water works Waidhofen a.d. Ybbs.
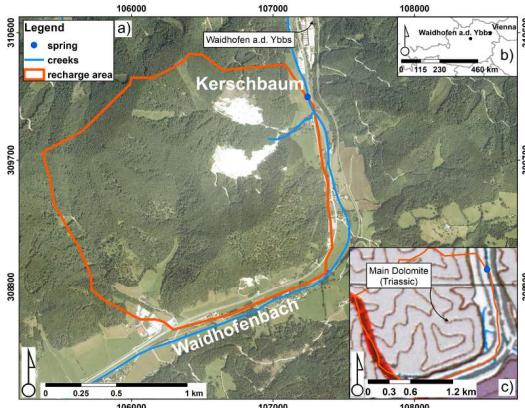
Figure B.4: Overview of the characteristics of the Kerschbaum spring recharge area and its geographical localization. a) an orthophoto and the boundary of the recharge area with the location of the Kerschbaum spring. b) the geographical position of Waidhofen a.d. Ybbs in Austria. c) the dominant presence of dolomitic basement rocks in the catchment (GBA, 2018). The isolines represent different elevation levels.
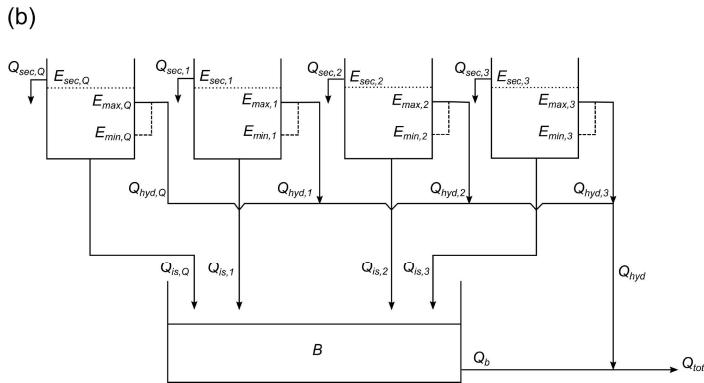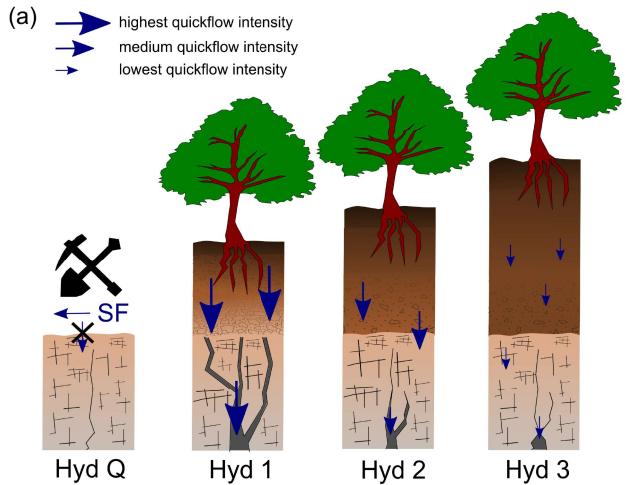
Figure B.5: Conceptual sketch of the LuKARS model structure as provided in Bittner et al. (2018a). Hyd Q represents the dolomite quarries, where no infiltration occurs due to a compacted protection layer and all water is drained by surface flow. The figure highlights the decreasing quickflow intensity from Hyd 1 to Hyd 3 due to the increasing soil depth and increasing content of fine-textured soil.
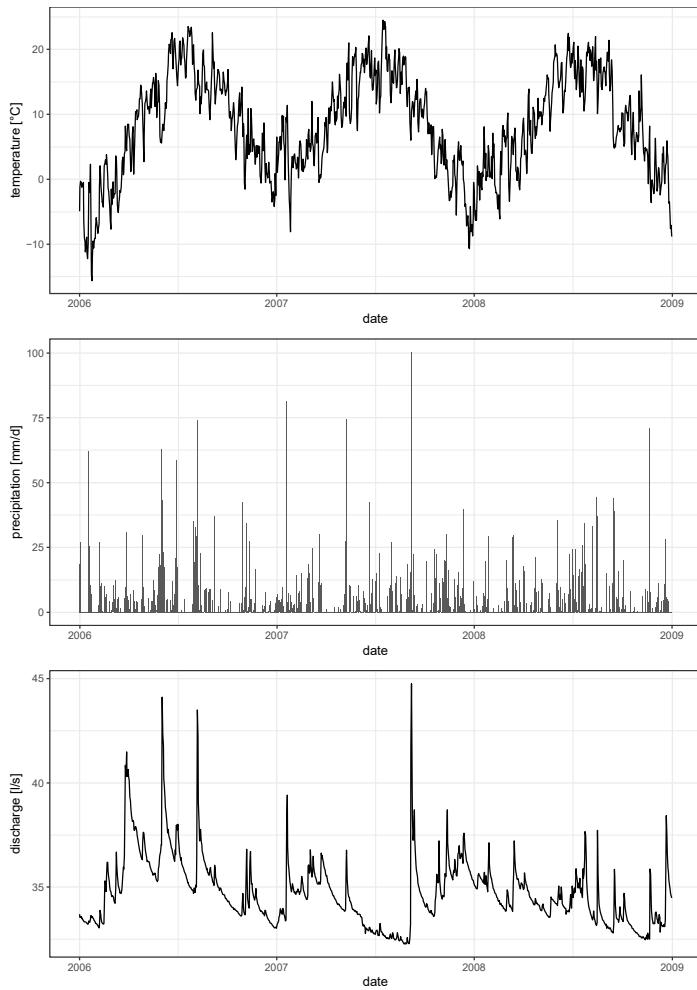
Figure B.6: Input data used to run the LuKARS model, including daily temperature (top), daily precipitation (middle), and daily discharge values of the Kerschbaum spring (bottom).

B.3   Supplementary material to Chapter 6
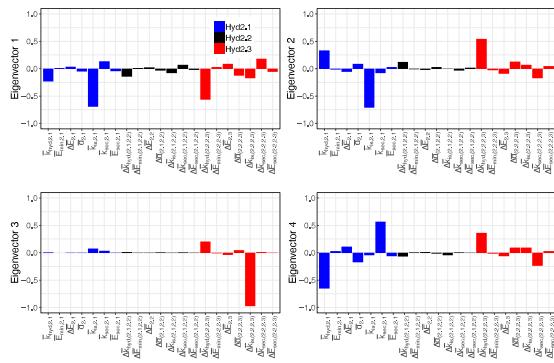
Figure B.7: Results of Scenario 1.1. Figure shows the eigenvectors of the first four eigenvalues.
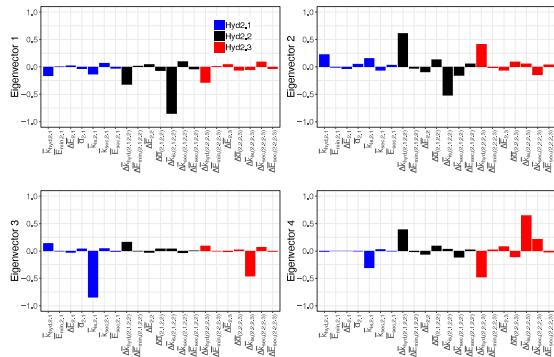
Figure B.8: Results of Scenario 1.3. Figure shows the eigenvectors of the first four eigenvalues.
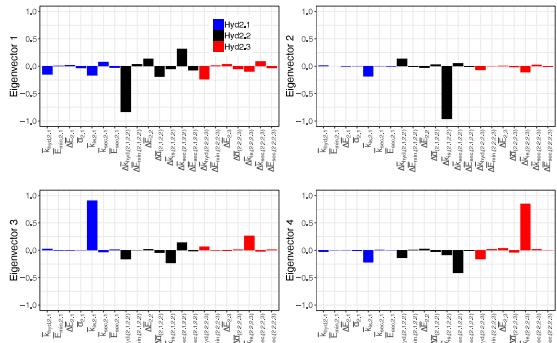
Figure B.9: Results of Scenario 1.4. Figure shows the eigenvectors of the first four eigenvalues.
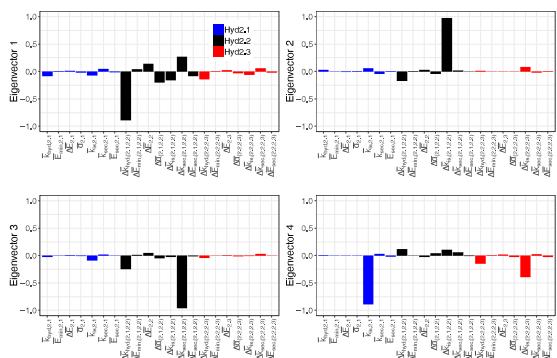
Figure B.10: Results of Scenario 1.5. Figure shows the eigenvectors of the first four eigenvalues.
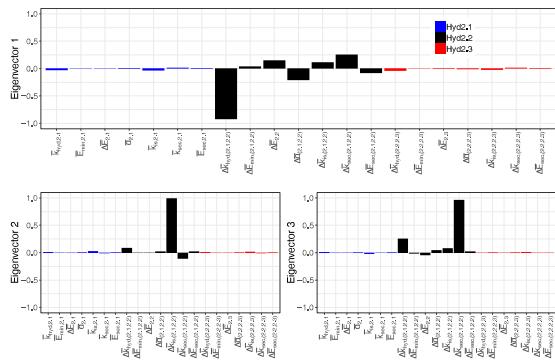
Figure B.11: Results of Scenario 1.7. Figure shows the eigenvectors of the first four eigenvalues.
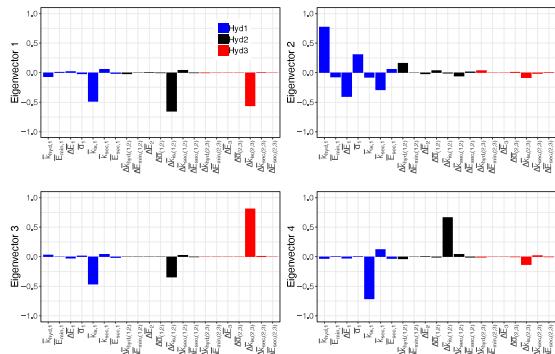
Figure B.12: Results of Scenario 2.1. Figure shows the eigenvectors of the first four eigenvalues.
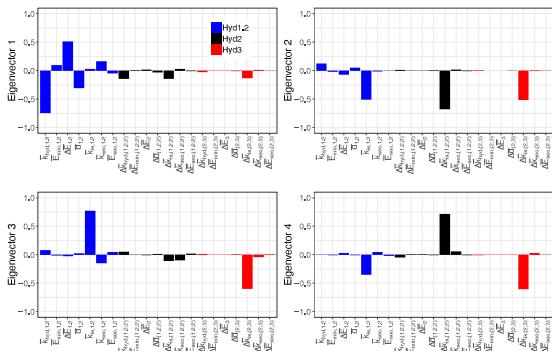
Figure B.13: Results of Scenario 2.3. Figure shows the eigenvectors of the first four eigenvalues.
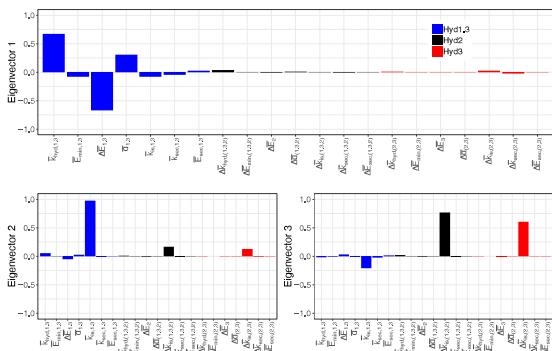

Figure B.14: Results of Scenario 2.4. Figure shows the eigenvectors of the first four eigenvalues.
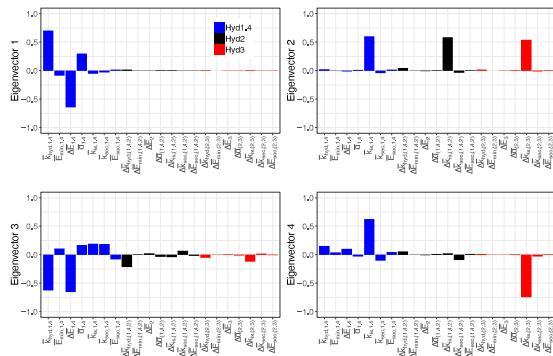
Figure B.15: Results of Scenario 2.5. Figure shows the eigenvectors of the first four eigenvalues.
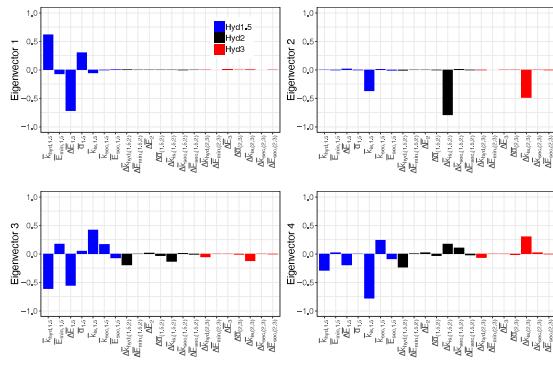
Figure B.16: Results of Scenario 2.6. Figure shows the eigenvectors of the first four eigenvalues.
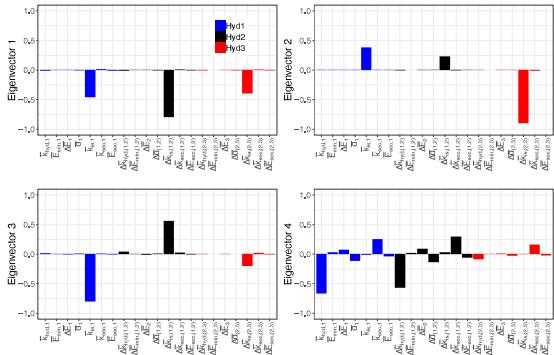
Figure B.17: Results of Scenario 3.2. Figure shows the eigenvectors of the first four eigenvalues.
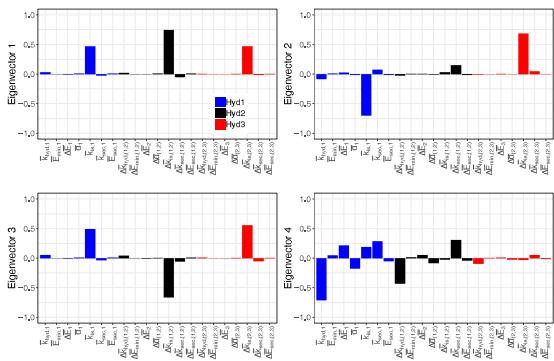

Figure B.18: Results of Scenario 3.3. Figure shows the eigenvectors of the first four eigenvalues.
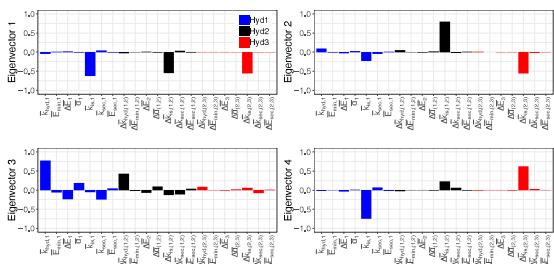

Figure B.19: Results of Scenario 3.4. Figure shows the eigenvectors of the first four eigenvalues.
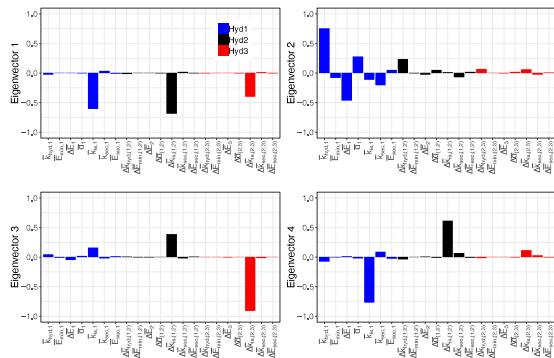
Figure B.20: Results of Scenario 3.5. Figure shows the eigenvectors of the first four eigenvalues.
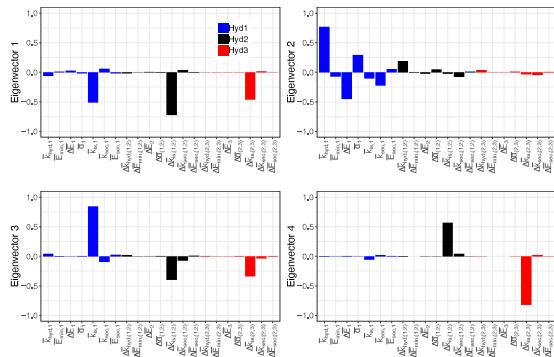

Figure B.21: Results of Scenario 3.6. Figure shows the eigenvectors of the first four eigenvalues.
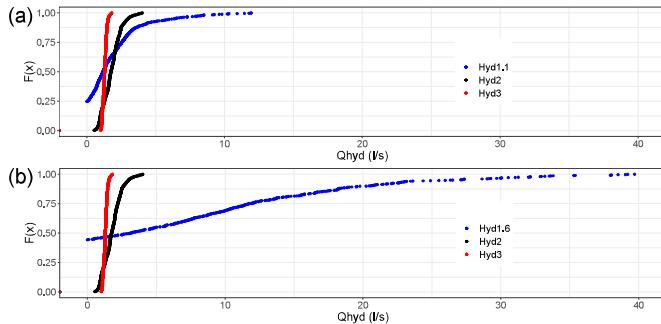
Figure B.22: Empirical cumulative distribution function of the quickflow Q_{hyd} originating from each hydrotope in a) Scenario 2.2 and b) Scenario 2.7.
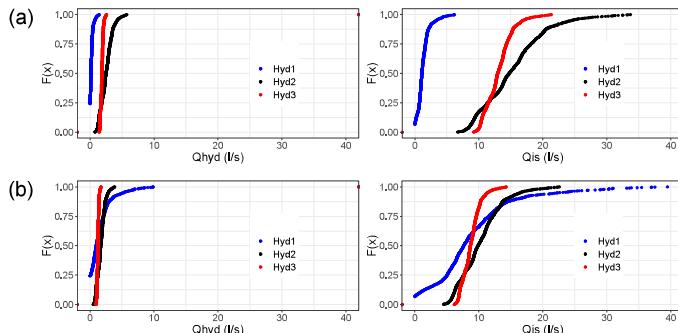

Figure B.23: Empirical cumulative distribution function of the quickflow Q_{hyd} and the recharge Q_{is} originating from each hydrotope in a) Scenario 3.1 and b) Scenario 3.7.

Appendix C

CV

Dr.-Ing. Daniel Bittner, Koblenzer Str. 16, D – 80993 München
daniel.bittner@tum.de, + 49 177 / 33 491 88

CV

Geburtsdatum: 10. November 1987

Geburtsort: Lichtenfels

Familienstand: verheiratet, 1 Kind

Ausbildung:

01.2017 - 05.2020	**Promotion** am Lehrstuhl für Hydrologie und Flussgebietsmanagement der Technischen Universität München

Dissertation: "Uncertainty Quantification in modeling karst water resources and the impacts of land use changes" (mit Auszeichnung bestanden, *summa cum laude*)

10.2013 - 06.2016	**Master of Science** in Geowissenschaften an der Universität Trier, Deutschland

Masterarbeit: "Numerical modeling of coupled surface and ground water flow for the Middle Elbe, Germany" (Note: 1.0)
Endnote: 1.2

10.2010 - 01.2014	**Bachelor of Science** in Angewandter Physischer Geographie an der Universität Trier, Deutschland

Bachelorarbeit: "Evaluierung der Bodenhydrologischen Kartieranleitung der DWA AG HW 1.3" (Note: 1.0)
Endnote: 2.1

06.2009	**Abitur** am Ville Gymnasium Erftstadt, Deutschland

Berufserfahrung:

11.2016 - heute	**Technische Universität München**, Lehrstuhl für Hydrologie und Flussgebietsmanagement, Wissenschaftlicher Mitarbeiter

- Projekt „boDEREC-CE" (seit 2019)

Leitung Interreg Projekt „boDEREC-CE"

Aufgaben: Projekt- und Finanzmanagement, Implementierung und Co-Antragsteller

Inhalte: Erfassung, Bewertung und Modellierung von Pharmazeutika in verschiedenen Grundwassersystemen.
Erarbeitung von Monitoringkonzepten für Pharmazeutika in unterschiedlichen Grundwasserleitern.
Erstellung eines modellgestützten Bewertungsansatzes für Stakeholder zur Ableitung von Handlungsmaßnahmen basierend auf existierenden Studien.

Förderung: 2.300.000 € (gesamt), 241.000 € (TUM), Interreg Central Europe

Projektleitung Grundwasser-bewirtschaftung Waidhofen a.d. Ybbs	• Wasserversorgung Waidhofen a.d. Ybbs (Österreich) (seit 2018)

<u>Aufgaben:</u> Projekt- und Finanzmanagement, Implementierung und Antragsteller

<u>Inhalte:</u> Hydrologische und hydrochemische Zustandsbewertung des Wasserversorgungssystems (Karstgrundwasserleiter). Entwicklung von Bewirtschaftungskonzepten zum Schutz der Grundwasserspender und zur dauerhaften Gewährleistung der Wasserversorgung.

<u>Förderung:</u> 32.000 €, Stadt Waidhofen a.d. Ybbs

Kooperation und Weiterentwicklung von MODFLOW mit USGS

• Forschungsinitiative mit dem United States Geological Survey (USGS) (seit 2018)

<u>Aufgaben:</u> Projektleitung, Finanzmanagement, Antragsteller

<u>Inhalte:</u> Initiierung einer Forschungs- und Lehrkooperation mit den Entwicklern von MODFLOW-OWHM mit Workshops in Deutschland und USA. Modellentwicklung zur physikalisch-basierten und verteilten Simulation von hydraulischen Prozessen in Karst-grundwasserleitern (Testgebiet Barton Springs, Texas).

<u>Förderung:</u> 20.000 €, BaCaTec & TUM Incentive Fund

Leitung Interreg Projekt „PROLINE-CE"

• Projekt „PROLINE-CE" (beendet, 2016 - 2019)

<u>Aufgaben:</u> Projekt- und Finanzmanagement, Implementierung

<u>Inhalte:</u> Konzepte für eine integrierte Grundwasser- und Landbewirtschaftung unter Einbindung von Stakeholdern. Modellgestützte Effektivitätsanalyse der erstellten Konzepte für verschiedene Grundwassersysteme (Karst- und Poren-grundwasserleiter). Entwicklung von modellbasierten Wasserwirtschaftswerkzeugen für Stakeholder.

<u>Förderung:</u> 2.750.000 € (gesamt), 232.000 € (TUM), Interreg Central Europe

01.2016 - 10.2016	**Bundesanstalt für Gewässerkunde (BfG)**, Wissenschaftlicher Mitarbeiter

<u>Aufgaben:</u> Hydrogeologische Beratung des Eisenbahn-Bundesamtes

<u>Inhalte:</u> Statistische Analyse hydrogeologischer und hydrochemischer Daten im Kontext von Schienenbauprojekten (größtenteils Stuttgart 21). Modellbasierte Überprüfung der Wirksamkeit von Wasserhaltungs- und Schutzmaßnahmen vor Aufstieg von Thermalwässern.

Hydrogeologische Beratung in der BfG

01.2014 - 12.2015	**Grundbaulabor Trier, Dipl.-Ing. E. Lehmann**, Geowissenschaftler

<u>Aufgaben:</u> Projektmanagement, Gutachter

<u>Inhalte:</u> Planung und Implementierung von Grundwassermonitoring Konzepten im Rahmen von Baugrunduntersuchungen. Planung, Durchführung und Auswertung von Pumpversuchen. Diverse hydrogeologische und bodenmechanische Feld- und Laborarbeiten.

Hydrogeologische Ingenieurtätigkeit

Auslandsaufenthalte:

01.2019 - 02.2019   **University of Texas at Austin (UT Austin),**
Gastwissenschaftler in der Computational Hydraulics group (Texas, USA)
Modellunsicherheitsquantifizierung mit der „Active Subspace" Methode.
Entwicklung eines Python-basierten Programms zur Kopplung der „Active
Subspace" Methode mit Grundwassermodellen.

06.2018 - 07.2018   **United States Geological Survey (USGS),**
     &   01.2019   Gastwissenschaftler beim California Water Science Center in San Diego
(Kalifornien, USA)
Testen von neu-implementierten numerischen Simulationspaketen in
MODFLOW-OWHM am Beispiel von Salinas Valley (Kalifornien).
Entwicklung von Bewässerungskonzepten und modellgestützte Optimierung
der Grund- und Oberflächenwasserbewirtschaftung im Salinas Valley.

09.2009 - 04.2010   **Work and Travel in Frankreich**
Rezeptionist in verschiedenen Ferienresorts von Pierre & Vacances

Praktika:

07.2015 - 12.2015   **Bundesanstalt für Gewässerkunde (BfG)**, Koblenz (Deutschland)
Erstellung eines numerischen Grundwassermodells für den Bereich der
Mittelelbe zwischen Wittenberg und Aken (Sachsen-Anhalt) zur
Quantifizierung des Austauschs zwischen Oberflächenwasser und
Grundwasser

09.2013 - 10.2013   **Deutsches Luft- und Raumfahrtzentrum (DLR)**, München (Deutschland)
Statistische Analyse von Fernerkundungsdaten des World-View II
Satelliten.
Kalibrierung der Intrakanalzeit zwischen verschiedenen World-View II
Sequenzen.

02.2013 - 03.2013   **Bundesforschungszentrum für Wald, Naturgefahren und Landschaft
(BfW)**, Innsbruck (Österreich)
Statistische Auswertung und Korrektur von alpin beeinflussten
hydrologischen und meteorologischen Daten.
Erstellung von Niederschlags-Abfluss Modellen für Wildbacheinzugsgebiete.
Durchführung bodenphysikalischer Laboruntersuchungen.

07.2012 - 10.2012   **Escuela Politécnica del Ejército (ESPE)**, Quito (Ecuador)
Ermittlung geologischer & geochemischer Parameter im Feld und
topographische Kartierung, sowie quantitative Datenauswertung im Zuge
eines internationalen Geothermieprojekts.
Geochemische Feldarbeit in Karsthöhlen des Amazonas Tieflands.

Ehrenamtliche Tätigkeiten:

01.2020 - heute   **Early Career Karst Hydrologic Modelers**
Gründungsmitglied
Grundwassermodellierer Netzwerk für junge Karsthydrologen.
Diskussion über die Wahl geeigneter Modellansätze für spezifische
Fragestellungen, Weiterentwicklungen und Austausch von Erfahrungen.

06.2019 - heute	**FREEWAT (FREE and open-source tools for WATer management)**, Mitglied des Entwicklerteams
	Entwicklung eines Python-basierten Plug-Ins in QGIS mit freiverfügbaren Analysewerkzeugen für die Wasserwirtschaft.
01.2013 - heute	**Deutsche Vereinigung für Wasserwirtschaft, Abwasser und Abfall (DWA)**, Mitglied in der Arbeitsgruppe HW 1.3
	Erstellung eines bodenhydrologischen Kartierschlüssels, um Abflussprozesse basierend auf bodenphysikalischen Eigenschaften und topographischen Parametern zu kartieren und bewerten. Publizierte Richtlinie DWA M-922 Bodenhydrologische Kartierung und Modellierung.

<u>Lehre:</u>

2020	**Numerical modeling of water demand and supply in arid regions (One-Water, USGS)**, Vorlesung & Seminar
	Hydrologische Statistik, Vorlesung & Seminar
2019	**Numerical modeling of water demand and supply in arid regions (One-Water, USGS)**, Vorlesung & Seminar
	Hydrologische Statistik, Vorlesung & Seminar
2018	**Water management at the catchment scale**, Seminar & Exkursion ins Einzugsgebiet der Etsch
	Hydrologische Statistik, Vorlesung & Seminar

<u>Stipendien:</u>

2020	**PROCOPE** Post-Doc Stipendium der Deutsch-Französischen Botschaft für einen 2-monatigen Forschungsaufenthalt in Frankreich
	Erasmus+, Stipendium für einen Lehraufenthalt an der Universität Paul Sabatier Toulouse III
2019	**Erasmus+**, Stipendium für einen Workshop & IAH Congress in Málaga
2018	**Deutsche Hydrologische Gesellschaft (DHG)**, Feldstipendium
2012	**DAAD Promos**, Reisestipendium für ein 3-monatiges Praktikum in Ecuador

<u>Weitere Qualifikationen:</u>

Weiterbildung (Kurse)	FEFLOW – Introduction and advanced topics, Veranstalter: DHI
	Effizienztraining für Naturwissenschaftler, Veranstalter: TUM Graduate School
	Planung, Durchführung & Auswertung von Pumpversuchen, Veranstalter: Berufsverband Deutscher Geowissenschaftler

Sprachen	Deutsch (Muttersprache), Englisch (fließend), Französisch (fortgeschritten, B2), Spanisch (fortgeschritten, B1)
IT	R (Experte), Python (fortgeschritten), ArcGIS (fortgeschritten), QGIS (fortgeschritten), LATEX (fortgeschritten), MS-Office Anwendungen (Experte), MODFLOW (Experte), FEFLOW (Anfänger)
Führerscheine	B & A (Auto & Motorrad)
Hobbys	Volleyball, Fußball, Bergsteigen, Spielplatz mit meiner Tochter

Artikel (peer-reviewed):

2020   T. Olarinoye, […] **D. Bittner**, […] A. Hartmann (2020, 57 Co-Authors). Global karst springs hydrograph dataset for research and management of the world's fastest flowing groundwater. Nature Scientific Data 7, 59.

D. Bittner, A. Rychlik, T. Klöffel, A. Leuteritz, M. Disse and G. Chiogna (2019). A GIS-based model for simulating the hydrological effects of land use changes on karst systems – The integration of the LuKARS model into FREEWAT. Environmental Modelling & Software 127, 104682.

D. Bittner, M. Teixeira Parente, S. Mattis, B. Wohlmuth and G. Chiogna (2020). Identifying relevant hydrological and catchment properties in active subspaces: An inference study of a lumped karst aquifer model. Adv. in Water Res. 135, 103472.

S. Teschemacher, **D. Bittner** and M. Disse (2020). Automated Location Detection of Retention and Detention Basins for Water Management. Water, 12(5), 1491.

2019   M. Teixeira Parente, **D. Bittner**, S. Mattis, G. Chiogna and B. Wohlmuth (2019). Bayesian calibration and sensitivity analysis for a karst aquifer model using active subspaces. Water Resources Research 55, 7086-7107.

T. Sheikhy Narany, **D. Bittner**, M. Disse and G. Chiogna (2019). Spatial and temporal variability in hydrochemistry of a small scale dolomite karst environment. Environmental Earth Sciences 78, 273.

2018   **D. Bittner**, T. Sheikhy Narany, B. Kohl, M. Disse and G. Chiogna (2018). Modeling the hydrological impacts of land use change in a dolomite-dominated karst system. Journal of Hydrology 567, 267-279.

Konferenzvorträge:

2019   **D. Bittner**, M. Teixeira Parente, S. Mattis, B. Wohlmuth, M. Disse and G. Chiogna (2019). How to model the impacts of land use changes in karstic environments: Model development, parameter dimension reduction and uncertainty quantification. IAH conference, Málaga, Spain.

D. Bittner, M. Teixeira Parente, S. Mattis, B. Wohlmuth and G. Chiogna (2019). Parameter dimension reduction using the active subspace method for a lumped karst aquifer model. EGU conference, Vienna, Austria.

2018   **D. Bittner**, M. Disse, T. Sheikhy Narany and G. Chiogna (2018). Modelling the impact of land use change on drinking water supply in a karstic system. EGU conference, Vienna, Austria.

2016   **D. Bittner** and M. Casper (2016). A coupled modeling approach to assess the surface water - groundwater interactions for the Middle Elbe on regional scale. GeoTirol conference, Innsbruck, Austria.

Gastreferent (eingeladen):

2019   **D. Bittner**, A. Rychlik, T. Klöffel and G. Chiogna (2019). Modeling the hydrological impact of land use change in karst systems using the LuKARS plugin for FREEWAT. 2nd International LIFE REWAT Summer School, Pisa, Italy.

2017   **D. Bittner**, M. Disse and G. Chiogna (2018). Trinkwasserschutz und Landwirtschaft – Wie schützen wir nachhaltig unser Trinkwasser? NABU Vulkaneifel Jahreshauptversammlung, Hillesheim, Germany.